

Universiteit
Leiden
The Netherlands

High-contrast imaging polarimetry of exoplanets and circumstellar disks

Holstein, R.G. van

Citation
Holstein, R. G. van. (2021, October 13). *High-contrast imaging polarimetry of exoplanets and circumstellar disks*. Retrieved from https://hdl.handle.net/1887/3217115

Version:	Publisher's Version
License:	Licence agreement concerning inclusion of doctoral thesis in the Institutional Repository of the University of Leiden
Downloaded from:	https://hdl.handle.net/1887/3217115

Note: To cite this publication please use the final published version (if applicable).

High-contrast imaging polarimetry of exoplanets and circumstellar disks

Rob Gerardus van Holstein

Cover design:
Bottom right: Total-intensity image of the star DH Tau A and its substellar companion DH Tau B. Top left: Linearly polarized intensity image of the same system, revealing the circumstellar disk of DH Tau A and the polarization signal from DH Tau B that indicates the presence of a disk around this companion. The images are presented in Chapter 5 and were taken with SPHERE-IRDIS at ESO's Very Large Telescope located on Cerro Paranal.

High-contrast imaging polarimetry of exoplanets and circumstellar disks

Proefschrift

ter verkrijging van
de graad van doctor aan de Universiteit Leiden,
op gezag van rector magnificus prof. dr. ir. H. Bijl,
volgens besluit van het college voor promoties
te verdedigen op woensdag 13 oktober 2021
klokke 11.15 uur

door

Rob Gerardus van Holstein

geboren te Delft, Nederland
in 1990

Promotor:	Prof. dr. C. U. Keller	
Co-promotor:	Dr. ir. F. Snik	
Promotiecommissie:	Prof. dr. H. J. A. Röttgering (voorzitter)	Universiteit Leiden
	Prof. dr. I. A. G. Snellen (secretaris)	Universiteit Leiden
	Prof. dr. H. M. Schmid	ETH Zürich
	Prof. dr. I. E. E. Kamp	Rijksuniversiteit Groningen
	Prof. dr. M. K. Kupinski	University of Arizona
	Dr. J. Milli	Université Grenoble Alpes

Printed by: Gildeprint

ISBN: 978-94-6419-315-2

An electronic copy of this thesis can be found at https://openaccess.leidenuniv.nl.

© Rob G. van Holstein, 2021

Contents

1 Introduction **1**
- 1.1 Polarimetry to study circumstellar disks and substellar companions 2
- 1.2 High-contrast imaging 6
  - 1.2.1 Components of a high-contrast imager 6
  - 1.2.2 Differential imaging techniques 10
- 1.3 Polarimetry 10
  - 1.3.1 Description of polarized light 11
  - 1.3.2 Polarization measurements with the double difference 11
  - 1.3.3 Instrumental polarization effects and polarization aberrations . . . 12
- 1.4 Outline of this thesis 13
- 1.5 Outlook 16

References 18

2 Polarimetric imaging mode of VLT/SPHERE-IRDIS II: Characterization and correction of instrumental polarization effects **23**
- 2.1 Introduction 24
- 2.2 Conventions and definitions 26
- 2.3 Optical path and instrumental polarization effects of SPHERE-IRDIS . . 27
  - 2.3.1 SPHERE-IRDIS optical path 27
  - 2.3.2 Instrumental polarization effects of optical path 30
- 2.4 Mathematical description of complete optical system 31
- 2.5 Instrumental polarization effects of instrument downstream of M4 35
  - 2.5.1 Calibration measurements and determination of model parameters 35
  - 2.5.2 Results and discussion for internal source calibrations 37
- 2.6 Instrumental polarization effects of telescope and M4 43
  - 2.6.1 Calibration measurements and determination of model parameters 43
  - 2.6.2 Results and discussion for unpolarized star calibrations 44
- 2.7 Polarimetric accuracy of instrument model 48
- 2.8 Correction of science observations 51
  - 2.8.1 Correction method 51
  - 2.8.2 Correction of images of circumstellar disk of T Cha 54
  - 2.8.3 Improvements attained with correction method 55
  - 2.8.4 Limits to and optimization of polarimetric accuracy 58
  - 2.8.5 Data-reduction pipeline including correction method 61
- 2.9 Summary and conclusions 61
- 2.A Computation of parallactic, altitude, HWP, and derotator angles from FITS-headers 62
- 2.B Gradient in flux of internal calibration measurements 63
- 2.C Graphs of model fits of internal calibration measurements 65
- 2.D Determination of normalized Stokes parameters and graphs of model fits of unpolarized star observations 69

2.E Calculation of accuracies of fit and uncertainties in determined parameters 74
References . . . 75

3 Calibration of the instrumental polarization effects of SCExAO-CHARIS' spectropolarimetric mode 79
3.1 Introduction . . . 80
3.2 Mathematical description of complete optical system . . . 81
3.2.1 Optical path of SCExAO-CHARIS . . . 81
3.2.2 Mueller matrix model of optical path . . . 83
3.3 Measurements and data reduction . . . 85
3.4 Results . . . 87
3.4.1 Instrumental polarization effects of the HWP and derotator . . . 87
3.4.2 Instrumental polarization of the telescope . . . 90
3.5 Conclusions and outlook . . . 91
References . . . 92

4 Combining angular differential imaging and accurate polarimetry with SPHERE-IRDIS to characterize young giant exoplanets 95
4.1 Introduction . . . 96
4.2 Measurement technique . . . 98
4.3 Observations . . . 99
4.4 Data reduction . . . 100
4.4.1 Construction of total-intensity I_Q- and I_U-images . . . 102
4.4.2 Construction of Stokes Q- and U-images . . . 104
4.5 Results . . . 108
4.6 Discussion . . . 109
4.7 Conclusions . . . 111
References . . . 111

5 A survey of the linear polarization of directly imaged exoplanets and brown dwarf companions with SPHERE-IRDIS: First polarimetric detections revealing disks around DH Tau B and GSC 6214-210 B 113
5.1 Introduction . . . 114
5.2 Target sample and observations . . . 116
5.2.1 Target sample . . . 116
5.2.2 Observations . . . 117
5.3 Data reduction . . . 120
5.4 Extraction of polarization of companions: Detection of polarization of DH Tau B . . . 122
5.5 Results . . . 129
5.5.1 Detection of intrinsic polarization of DH Tau B . . . 129
5.5.2 Likely detection of intrinsic polarization of GSC 6214 B . . . 134
5.5.3 Detection of interstellar polarization from 1RXS J1609 B . . . 136
5.5.4 Upper limits on polarization of other companions . . . 138

5.5.5 Detection of circumstellar disks of DH Tau, GQ Lup, PDS 70, β Pic, and HD 106906 . . . 140
5.6 Modeling of polarization from circumsubstellar disks . . . 143
5.6.1 Setup of the radiative transfer model . . . 143
5.6.2 Origin of the spatially integrated polarization . . . 144
5.6.3 Dependence on the inner radius and surface density . . . 146
5.7 Discussion . . . 148
5.7.1 Circumsubstellar disks, rotational periods, and formation of DH Tau B, GSC 6214 B, and GQ Lup B . . . 148
5.7.2 Circumsubstellar disks of 1RXS J1609 B, HD 106906 b, and PDS 70 b . . . 150
5.7.3 Atmospheric asymmetries of the companions . . . 151
5.7.4 Confirmation and further characterization of the disks of DH Tau B and GSC 6214 B . . . 152
5.8 Summary and conclusions . . . 153
5.A Cosmetic correction of spurious structure in Q- and U-images . . . 155
5.B Systematic errors due to bad pixels . . . 155
5.C Retrieval of total intensity through ADI: Upper limit on polarization of β Pic b . . . 157
5.D Retrieval of total intensity through PSF fitting: Upper limit on polarization of HD 19467 B . . . 161
5.E Contrast curve of β Pic data . . . 165
References . . . 166

6 Circular polarimetric imaging at planetary system scales by hacking SPHERE-IRDIS: Full-Stokes observations of the asymmetric nebula surrounding VY CMa 171
6.1 Introduction . . . 172
6.2 Observing scheme for measuring circular polarization . . . 174
6.2.1 SPHERE-IRDIS' polarimetric mode for linear polarimetry . . . 175
6.2.2 Observing scheme for measuring circular polarization . . . 178
6.3 Test observations of VY CMa . . . 179
6.4 Instrumental polarization effects of circular-polarization measurements . . . 180
6.4.1 Mueller matrix model and setup of calculations . . . 181
6.4.2 Polarimetric efficiency . . . 181
6.4.3 Instrumental polarization . . . 184
6.4.4 Crosstalk . . . 185
6.4.5 Effect of uncertainty of retardance of UT and M4 . . . 186
6.5 Data reduction . . . 187
6.6 Calibration of crosstalk from data of VY CMa . . . 192
6.6.1 Identification of spurious signals due to uncorrected crosstalk . . . 192
6.6.2 Constraining retardance of UT and M4 from data . . . 193
6.7 Linear and circular polarization of VY CMa and its nebula . . . 196
6.7.1 Spatially unresolved stellar polarization . . . 196
6.7.2 Spatially resolved polarization of nebula . . . 198

6.8 Conclusions . . . 200
6.A Additional figures . . . 202
References . . . 205

7 Polarization-dependent beam shifts upon metallic reflection in high-contrast imagers and telescopes 207
7.1 Introduction . . . 208
7.2 Conventions and definitions . . . 210
7.2.1 Polarization of light . . . 210
7.2.2 Metallic reflection . . . 212
7.3 Beam shifts from polarization ray tracing . . . 215
7.4 Explanation of beam shifts and comparison to polarization ray tracing . . . 218
7.4.1 Spatial Goos-Hänchen shift . . . 220
7.4.2 Angular Goos-Hänchen shift . . . 223
7.4.3 Spatial Imbert-Federov shift . . . 226
7.4.4 Angular Imbert-Federov shift . . . 229
7.5 Discussion . . . 231
7.5.1 Polarization structure in the PSF due to beam shifts . . . 232
7.5.2 Effect of beam shifts on polarimetric measurements . . . 233
7.5.3 Size of beam shifts for various mirror materials and wavelengths . . . 235
7.5.4 Mitigation of beam shifts . . . 237
7.6 Conclusions . . . 238
References . . . 239

English summary 241

Nederlandstalige samenvatting 245

List of publications 249

Curriculum vitae 253

Acknowledgments 255

1 Introduction

In astronomy, the light originating from astrophysical objects is often only studied in terms of its intensity as a function of wavelength through photometry and spectroscopy. However, light is a transverse, electromagnetic wave and therefore has polarization: The electric (and magnetic) fields of the light oscillate or rotate in a certain direction. By performing polarimetry, that is, by measuring the polarization state of the light, we can retrieve much more information about the observed astrophysical objects. Indeed, spectropolarimetry measures the intensity of the light as a function of wavelength and polarization state, and can therefore determine the full information content of the electromagnetic radiation.

Polarimetry is a particularly powerful tool for the direct imaging of circumstellar disks and substellar companions, that is, exoplanets and brown dwarf companions, at near-infrared (NIR) and visible wavelengths. Direct imaging spatially separates the light from the object of interest and the light from the central star. However, this is a very challenging task because circumstellar disks and substellar companions are generally located at angular separations (much) smaller than 1″ from their parent stars and are orders of magnitude fainter than the star. To overcome this challenge, dedicated high-contrast imaging instruments are built that can reach a large contrast very close to the star. Almost all of these instruments operate from the ground and several have polarimetric capabilities.

The first reason that high-contrast imagers employ polarimetric modes is to reach the contrast required to image circumstellar disks and companions. The direct light from the central star is generally unpolarized: The light is a mixture of equal amounts of all possible polarization states. As this starlight scatters off dust grains in the circumstellar disk or off the companion's atmosphere, it becomes linearly polarized. Therefore, when taking an image in linearly polarized light, the direct starlight is strongly suppressed, while the partially polarized light from the circumstellar disk or companion is revealed.

The second reason to perform high-contrast imaging polarimetry is related to characterization; polarimetric images do not only reveal the morphology of circumstellar disks and the architecture of planetary systems, but they also contain information on the physical properties of the scattering particles. Measurements of polarization as a function of wavelength can, for instance, be used to constrain the composition, size, and shape of the dust grains in circumstellar disks and to determine the properties of the atmospheres or surfaces of companions.

The outline of this introductory chapter is as follows. In Sect. 1.1, I discuss the formation and evolution of circumstellar disks and substellar companions and outline what we can learn from polarimetric measurements of these objects. Subsequently, in Sect. 1.2, I describe the components and workings of a high-contrast imaging instrument. In Sect. 1.3, I then outline how polarimetric measurements are taken with a high-contrast imager and describe the instrumental effects that can reduce the performance of the instrument. Finally, I give an outline of the thesis in Sect. 1.4 and present an outlook in Sect. 1.5.

1.1 Polarimetry to study circumstellar disks and substellar companions

The formation of circumstellar disks and substellar companions is closely related to the formation of stars. Stars form inside massive clouds of molecular gas and dust that are located in the interstellar medium (Shu et al., 1987; McKee & Ostriker, 2007). Such a molecular cloud is gravitationally unstable; parts of the cloud fragment and collapse under their own gravity. This results in the formation of dense cores that further collapse to form stars (Shu, 1977; Bate, 1998). Because the collapsing core has a net angular momentum, a rotating disk of dust and gas forms around the forming star from which the star accretes material (Yorke et al., 1993; Nakamoto & Nakagawa, 1994). This disk is called a protoplanetary disk because planets (and brown dwarf companions) are believed to form in this disk (Beckwith & Sargent, 1996; Williams & Cieza, 2011). These substellar companions may form through the coagulation of dust into kilometer-sized planetesimals and the subsequent accretion of planetesimals and gas (Pollack et al., 1996; Chambers, 2004; Bodenheimer et al., 2013), the local collapse of part of the disk due to gravitational instabilities (Cameron, 1978; Boss, 1997; Stamatellos et al., 2007; Kratter et al., 2010), or the direct collapse of a separate core in the molecular cloud (Hennebelle & Chabrier, 2008; Bate, 2009). In all these scenarios the companions are expected to have their own circumsubstellar (accretion) disks (e.g., Stamatellos & Whitworth, 2009; Szulágyi et al., 2017), from which in turn moons may form (Canup & Ward, 2002). As time progresses, the protoplanetary disk disperses due to the formation of companions, accretion onto the star, stellar winds, photoevaporation by ultraviolet radiation, and gravitational interactions with nearby stars (Hollenbach et al., 2000). In some cases, a debris disk remains that consists of second-generation dust produced by the collisions of left-over planetesimals (Wyatt, 2008). Over time, the formed companions cool as they radiate the heat from their formation and continuing contraction (Chabrier et al., 2000; Baraffe et al., 2003), producing a planetary system similar to our own Solar System.

Protoplanetary disks and debris disks are routinely imaged in linearly polarized light with the current high-contrast imaging instruments. These instruments include SPHERE at the Very Large Telescope (see Fig. 1.1; Beuzit et al., 2019), SCExAO at the Subaru Telescope (Jovanovic et al., 2015), and the Gemini Planet Imager (GPI) at the Gemini South Telescope (Macintosh et al., 2014). Whereas GPI (Perrin et al., 2015), the IRDIS subsystem of SPHERE (Dohlen et al., 2008; de Boer et al., 2020; Chapter 2), and the CHARIS subsystem of SCExAO (Groff et al., 2017; Lozi et al., 2020a) perform polarimetric measurements at NIR wavelengths, the ZIMPOL polarimeter of SPHERE (Schmid et al., 2018) operates at visible wavelengths. These instruments principally employ polarimetry as a means to overcome the contrast between the star and the circumstellar disk, which typically is at a disk-to-star contrast of 10^{-2}–10^{-4} in the case of a protoplanetary disk (e.g., Garufi et al., 2020) and at a contrast of 10^{-4}–10^{-6} in the case of a debris disk (e.g., Esposito et al., 2020). After a disk has been detected in polarized light, the measurements are often used to study the extent, orientation, and morphology of the disk. In protoplanetary disks we can observe a wide variety of substructures, such as rings, cavities, gaps, spiral arms, and shadows (see Fig. 1.2, left; e.g., Muto et al., 2012; Quanz et al.,

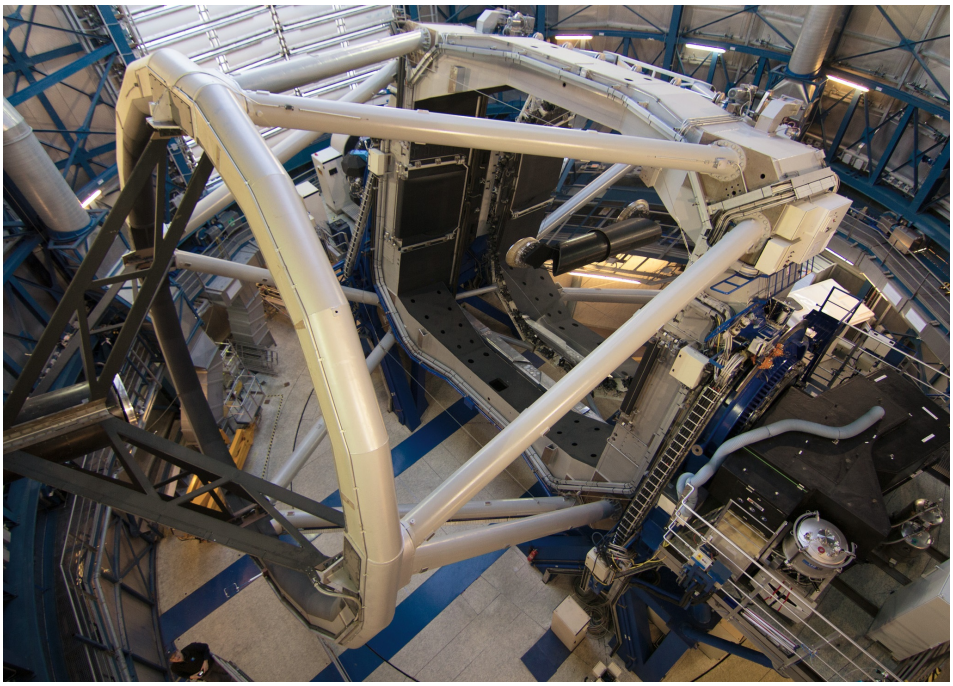


Figure 1.1: Unit Telescope 3 of the Very Large Telescope with SPHERE installed on the Nasmyth platform (bottom right). Image credit: J. H. Girard / ESO.

2013; Benisty et al., 2015; Ginski et al., 2016; Stolker et al., 2016b; de Boer et al., 2016; Benisty et al., 2017; Van Boekel et al., 2017; Pinilla et al., 2018; Garufi et al., 2018), some of which may be caused by companions interacting with the disk (Kley & Nelson, 2012; Dong et al., 2015; Zhu et al., 2015; Dong et al., 2016). The morphology of debris disks is generally simpler and often consists of a single ring (see Fig. 1.2, right; e.g., Engler et al., 2017; Olofsson et al., 2019; Esposito et al., 2020). Linear-polarization measurements are also used to constrain the properties of the dust in the disks by measuring polarized scattering phase functions and performing radiative transfer modeling (e.g., Perrin et al., 2015; Milli et al., 2015; Olofsson et al., 2016; Stolker et al., 2016a; Ginski et al., 2016; Benisty et al., 2017). Measurements of circular polarization could yield additional constraints on the dust properties as well as on scattering asymmetries and magnetic-field geometries (Bastien & Menard, 1990; Gledhill & McCall, 2000), but none of the current high-contrast imagers are designed to measure circular polarization.

Young exoplanets and brown dwarf companions emit the majority of the heat from their formation as NIR radiation. Current high-contrast imaging instruments can directly image these self-luminous companions in NIR total intensity at contrasts of 10^{-2}–10^{-6} (e.g., Bowler, 2016; Nielsen et al., 2019; Langlois et al., 2021). Typically, the companions are studied with photometry and spectroscopy (e.g., Bowler et al., 2014; Bonnefoy et al., 2016; Müller et al., 2018). However, the companions can also be characterized by measuring their NIR linear polarization. This polarization is created as the thermal radiation

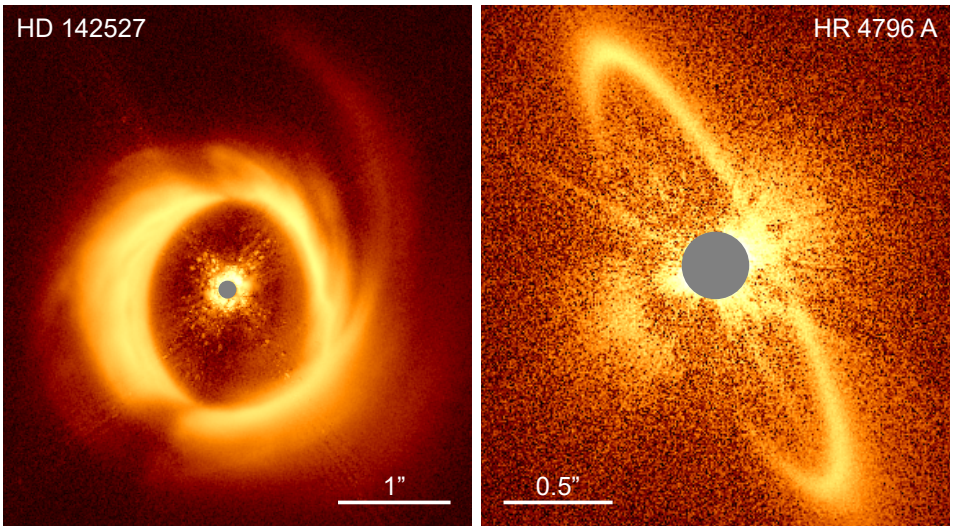


Figure 1.2: Linearly polarized intensity images of the protoplanetary disk of HD 142527 as taken with SPHERE-IRDIS (*left*; Hunziker et al., 2021) and the debris disk of HR 4796 A as taken with SPHERE-ZIMPOL (*right*; Olofsson et al., 2019). Both images are shown on a different logarithmic scale and contain some instrument-induced spurious signal near the center. The gray areas cover the regions where measurements are unreliable.

emanating from within the companion is scattered by dust in the companion's atmosphere (Sengupta & Krishan, 2001). Because the companion is observed as a point source, we only see the polarization integrated over the companion. Whereas for a spherically symmetric companion the integrated signal is zero, a net polarization remains when this symmetry is broken. Examples of these asymmetries are rotation-induced oblateness and an inhomogeneous distribution of atmospheric dust clouds (see Fig. 1.3, left; Sengupta & Marley, 2010; de Kok et al., 2011; Marley & Sengupta, 2011; Stolker et al., 2017). A companion can also be polarized when it has a circumsubstellar disk (see Fig. 1.3, right; Stolker et al., 2017), analogous to how pre-main-sequence stars can be polarized when they host a circumstellar disk (e.g., Rostopchina et al., 1997; Bouvier et al., 1999; Grinin, 2000; Menard et al., 2003). Based on models, the degree of linear polarization due to atmospheric asymmetries and circumsubstellar disks can reach several tenths of a percent, and even up to several percent in favorable cases. The NIR polarization of substellar companions can perhaps be measured with GPI and SPHERE-IRDIS, but attempts to detect these signals with GPI have so far been unsuccessful (Millar-Blanchaer et al., 2015; Jensen-Clem et al., 2016).

Contrary to young companions, most of the flux from evolved, cool exoplanets is reflected, visible starlight. This reflected flux is much smaller than the thermal NIR flux of young companions, with giant exoplanets having contrasts of $\sim 10^{-8}$ (e.g., Hunziker et al., 2020) and rocky exoplanets having contrasts of $\sim 10^{-10}$ (e.g., Traub & Oppenheimer, 2010). However, the reflected flux is expected to be linearly polarized at up to

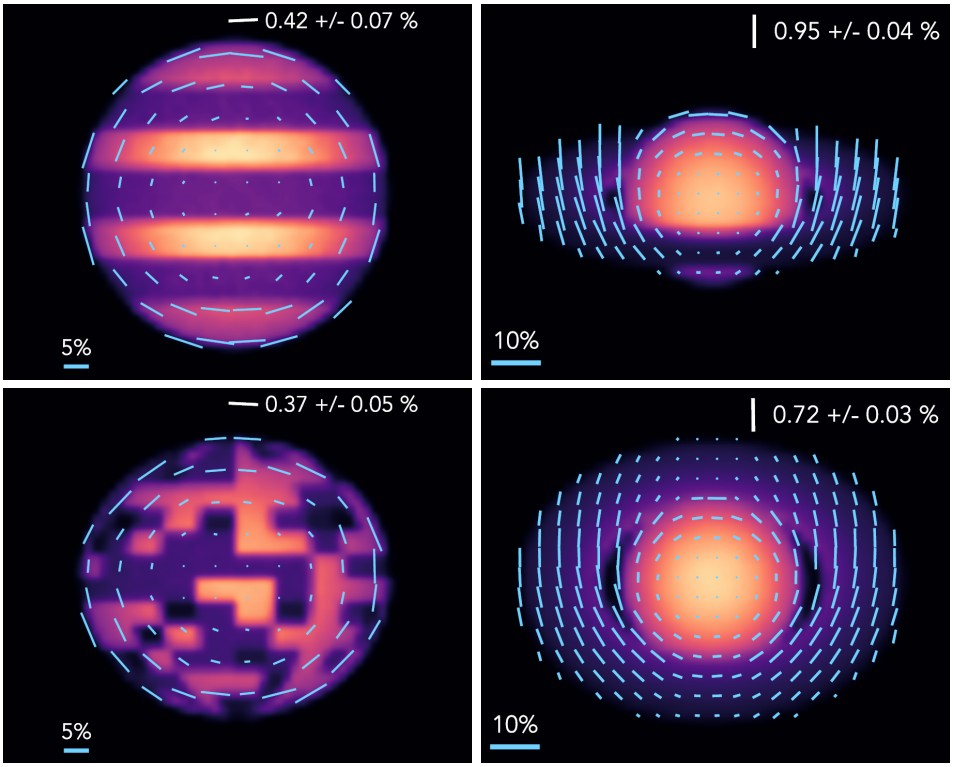


Figure 1.3: Models of the linear polarization of companions from Stolker et al. (2017) showing a companion with banded cloud structure (*top left*), an oblate companion with patchy clouds (*bottom left*), and a companion with a circumsubstellar disk viewed at high inclination (*top right*) as well as low inclination (*bottom right*). The blue lines indicate the local degree and angle of linear polarization. The integrated polarization for each companion is shown in the top right of each panel.

several tens of percent (Stam et al., 2004; Hunziker et al., 2020). Polarimetry is therefore useful to suppress the unpolarized starlight and directly image the planets. In addition, spectropolarimetry at visible wavelengths can be used to characterize these directly imaged exoplanets, at a level beyond that possible with conventional intensity spectroscopy alone. In the case of giant exoplanets, linear spectropolarimetry can be used to constrain the composition and structure of the atmosphere and reveal the presence of atmospheric clouds (Stam et al., 2004; Buenzli & Schmid, 2009). For rocky exoplanets, linear spectropolarimetry can constrain the habitability of the planet by determining the presence of liquid or icy water clouds in the atmosphere (Bailey, 2007; Karalidi et al., 2011, 2012), the type and percentage of cloud cover (Rossi & Stam, 2017), and even the presence of oceans and continents (Stam, 2008; Williams & Gaidos, 2008; Karalidi & Stam, 2012; Trees & Stam, 2019). Circular spectropolarimetry might even reveal the presence of life through the detection of biological homochirality (Sparks et al., 2009; Rossi & Stam,

2018; Patty et al., 2019). Life on Earth largely prefers one of two mirror-image versions of chiral molecules, and this causes the light interacting with chiral biological molecules and structures to become circularly polarized. SPHERE-ZIMPOL is specifically designed to search for the linearly polarized, reflected light of cool, giant exoplanets, but has so far been unsuccessful at detecting them (Hunziker et al., 2020). In the near future, the polarized light of these giant exoplanets could perhaps also be detected with the Nancy Grace Roman Space Telescope (Spergel et al., 2015), although the telescope's polarimetric mode is better suited for the imaging and characterization of circumstellar disks (Bailey et al., 2018; Kasdin et al., 2020). Finally, in the next decade, it should be possible to detect giant and rocky exoplanets in polarized light with ground-based high-contrast imagers such as PCS (or EPICS) at the Extremely Large Telescope (ELT; Kasper et al., 2020) and PSI at the Thirty Meter Telescope (Fitzgerald et al., 2019), as well as with the dedicated polarimetric modes of the proposed space telescopes HabEx (Gaudi et al., 2020) and LUVOIR (LUVOIR Team, 2019).

1.2 High-contrast imaging

Direct imaging of circumstellar disks and substellar companions is challenging because we need to reach extreme contrasts at very small angular separations from the star. Ground-based high-contrast imaging instruments are therefore installed on the largest telescopes and have complex optical systems designed to create near diffraction-limited images and suppress the light from the star. To further suppress the starlight and reach the required contrast, these instruments also employ advanced differential imaging techniques and data-reduction methods.

1.2.1 Components of a high-contrast imager

A schematic of a ground-based high-contrast imaging instrument is shown in Fig. 1.4. For this example, the instrument is located on the Nasmyth platform of a telescope on an alt-azimuth mount, as is the case for SPHERE and SCExAO. The light incident on the telescope is collected by the concave primary mirror and is subsequently refocused by the convex secondary mirror that is suspended at the top of the telescope. The flat tertiary mirror then reflects the light to the Nasmyth platform. When the alt-azimuth telescope mount tracks a target across the sky, the target rotates with the parallactic angle with respect to the telescope pupil, and the telescope rotates with the telescope altitude angle with respect to the Nasmyth platform. To compensate the resulting rotation of the image, the instrument includes an image derotator, which is a rotating assembly of three mirrors (a K-mirror) that can rotate the image to any orientation. The derotator generally has two main operating modes. In field-tracking mode, the derotator keeps the image orientation constant during an observation, allowing for long integrations without smearing of the image. In pupil-tracking mode, the derotator instead keeps the pupil of the telescope fixed, while the target rotates with the parallactic angle around the center of the image. Note that GPI, which is mounted at the Cassegrain focus, does not use a derotator and therefore always observes in pupil-tracking mode.

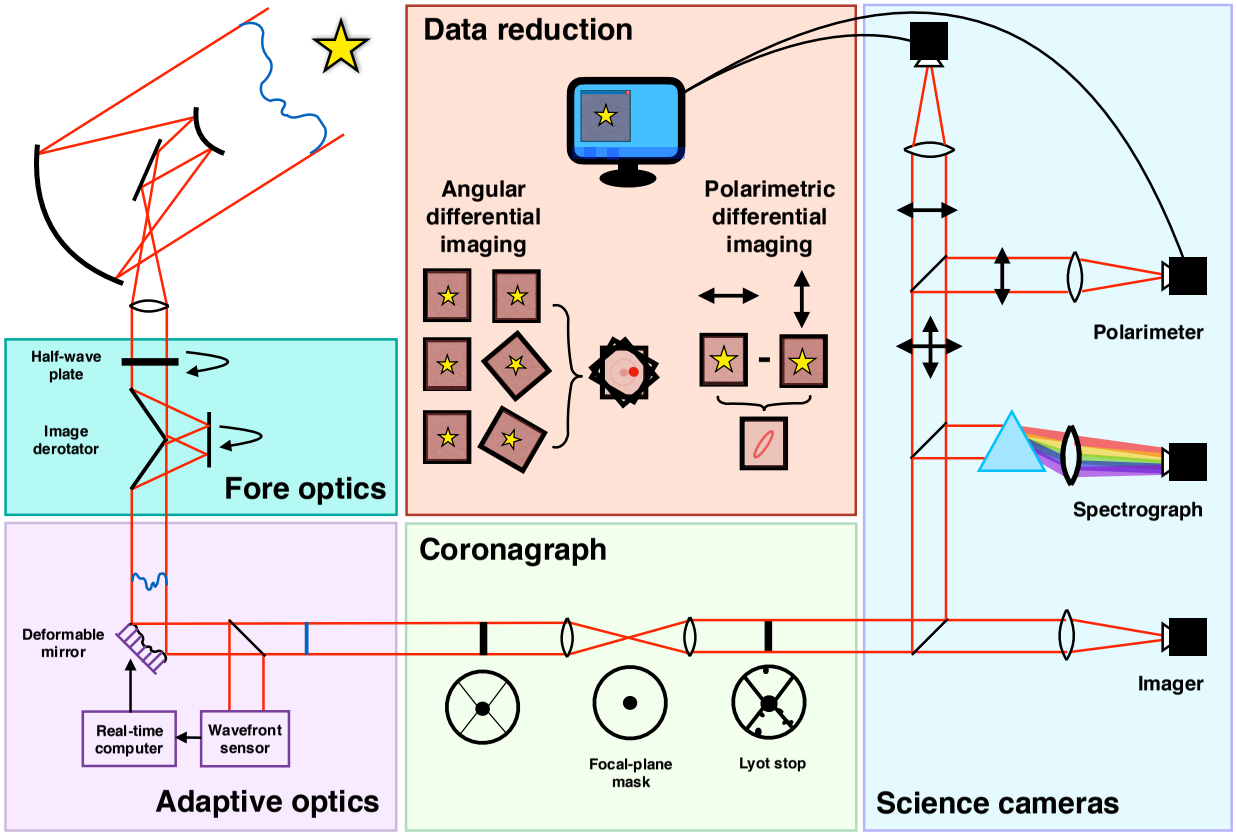


Figure 1.4: Schematic of a ground-based high-contrast imaging instrument installed on a Nasmyth platform, showing the telescope and fore optics, adaptive optics, coronagraphs, science cameras, and data reduction. Image courtesy of David Doelman.

The theoretical angular resolution of the current 8-m class telescopes, as limited by diffraction, is between 12 mas to 80 mas at visible and near-infrared wavelengths. However, for ground-based telescopes the turbulence in the Earth's atmosphere distorts the (initially flat) wavefront of the light arriving from the star (Fried, 1966; Greenwood, 1977). As a result, the angular resolution that these telescopes achieve for typical conditions is much worse, and the full width at half maximum of the point-spread function (PSF) is only on the order of 1″ (see Fig. 1.5, top left). To correct the wavefront distortions, ground-based high-contrast imaging instruments employ adaptive-optics (AO) systems (e.g., Guyon, 2018). These AO systems generally contain a (dichroic) beamsplitter that sends part of the light to a wavefront sensor that measures the distortion in the wavefront (see Fig. 1.4). These measurements are then sent to a computer that calculates the necessary wavefront correction in real-time and controls a deformable mirror that flattens the wavefront. After the AO correction, the PSF is nearly diffraction-limited (see Fig. 1.5, top right).

To overcome the large contrast between the star and the object of interest close to the star, high-contrast imagers use coronagraphs. Coronagraphs are optical devices that remove starlight due to diffraction at the telescope aperture. Many types of coronagraphs act as angular filters: The on-axis transmission is very low whereas the off-axis transmission is high. The simplest coronagraph is the classical Lyot coronagraph invented to study the solar corona outside of eclipses (Lyot, 1939). The Lyot coronagraph consists of a focal-plane mask that blocks the central peak of the PSF of the star and an aperture mask in the subsequent pupil plane, called the Lyot stop, that blocks the light that is diffracted by the focal-plane mask (see Fig. 1.4). Over the years, a wide range of more advanced coronagraphs have been developed (e.g., Guyon et al., 2006; Mawet et al., 2012; Ruane et al., 2018). After the light passes the coronagraph, the starlight is significantly suppressed, thereby enhancing the contrast close to the star. However, remaining wavefront aberrations create speckles in the PSF (see Fig. 1.5, center left) that limit the contrast.

After passing the coronagraph, the light is captured by the detector(s) of one or more science cameras (see Fig. 1.4). The simplest science camera is an imager that use a range of broadband and narrowband filters. SPHERE-IRDIS and SPHERE-ZIMPOL have such imaging modes (Dohlen et al., 2008; Schmid et al., 2018). Another type of science camera is the spectrograph. SCExAO-CHARIS and GPI both employ an integral-field spectrograph (IFS) that uses a lenslet array and a dispersive element to create low-resolution spectra over a 2D field of view (Groff et al., 2017; Larkin et al., 2014). SPHERE-IRDIS also has a long-slit spectroscopy mode that creates a spectrum of the light passing through a slit placed across the field of view (Vigan et al., 2008). Finally, the linear polarization state of the light can be measured with a polarimeter. As discussed in Sect. 1.1, SPHERE-IRDIS, SPHERE-ZIMPOL, SCExAO-CHARIS, and GPI all have linear polarimetric modes. SCExAO-CHARIS combines its polarimetric capability with its IFS to enable low-resolution spectropolarimetry (Lozi et al., 2020a). All these high-contrast imaging polarimeters are of the dual-beam type where a polarizing beamsplitter, or a combination of a nonpolarizing beamsplitter and polarizers, is used to split the beam of light incident on the science camera into two beams with orthogonal linear polarization states (e.g., Snik & Keller, 2013). These beams then fall on the detector(s) to simultaneously create two images. Images in polarized light are then computed as the difference of these

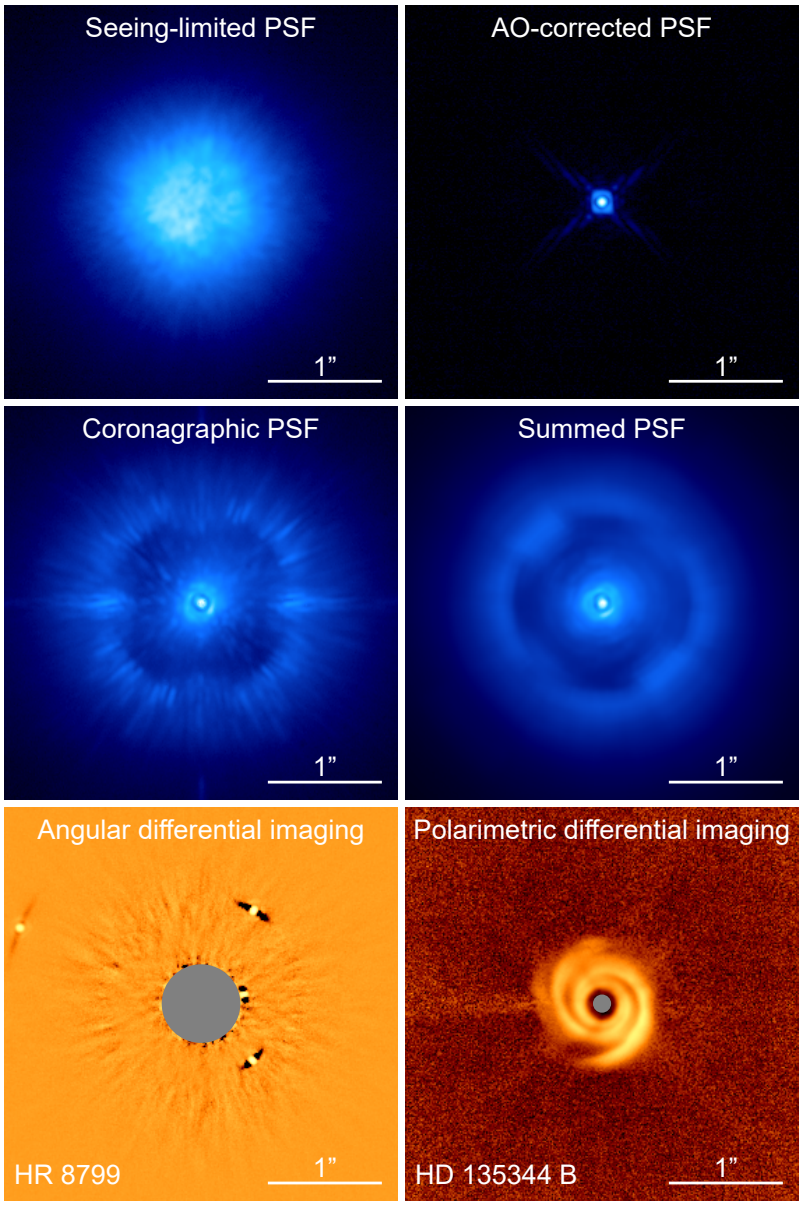


Figure 1.5: Gallery of SPHERE-IRDIS images of the seeing-limited PSF, the AO-corrected PSF, the coronagraphic PSF, the PSF summed over an observation sequence, the total intensity of the four planets of HR 8799 after applying ADI with PCA (Chapter 4), and the linearly polarized intensity of the protoplanetary disk of HD 135344 B after applying PDI (Stolker et al., 2016b). All panels are shown on a (different) logarithmic scale. The angular scales of all panels are the same. The gray areas in the bottom panels cover the regions where measurements are unreliable.

two images. A rotatable half-wave plate (HWP) located at the beginning of the optical path (see Fig. 1.4) is used as a polarization modulator and selects the linear polarization state to be measured.

1.2.2 Differential imaging techniques

When summing the frames of an observation sequence, significant stellar signal remains that can hide substellar companions or a circumstellar disk (see Fig. 1.5, center right). To remove the stellar PSF and further enhance the contrast, a variety of differential imaging techniques, which are applied during the data reduction, have been developed. The two most successful techniques for ground-based high-contrast imaging are angular differential imaging (ADI) and polarimetric differential imaging (PDI).

ADI (see Fig. 1.4; Marois et al., 2006) is primarily used to detect substellar companions in total intensity. To apply ADI, observations are performed in pupil-tracking mode. This way, the stellar PSF and its speckle pattern are stationary on the detector during the observations, while any point sources rotate with the parallactic angle around the center of the image. A model of the stellar PSF is then created during the data reduction by computing the median over all frames. Because any point sources around the star will be at a different position in each frame, their contribution to the PSF model will be very small. We then subtract the PSF model from all frames, derotate these PSF-subtracted frames (i.e., align them such that north is up), and sum the resulting frames. This procedure yields a final image in which the stellar PSF is almost completely removed and any sufficiently bright point sources are visible. To optimize the starlight suppression, the PSF model is often constructed using more advanced algorithms such as principal component analysis (PCA; Soummer et al., 2012; Amara & Quanz, 2012) instead of simply computing the median over the frames (see Fig. 1.5, bottom left).

PDI (see Fig. 1.4; Kuhn et al., 2001) is primarily used to detect the polarized, scattered light from circumstellar disks. In PDI, we use a dual-beam polarimeter to simultaneously take two images of orthogonal polarization states and compute the difference of these two images. Because stars are generally unpolarized (or at least have a very low degree of polarization) and the images are taken under the exact same atmospheric conditions, the intensity of the stellar PSF is virtually the same in both images, and therefore the stellar PSF is strongly suppressed in the difference. At the same time, the polarized light originating from a circumstellar disk has different intensities in the two images and is therefore visible in the difference (see Fig. 1.5, bottom right). With PDI we can thus attain large gains in contrast, but only for objects that are polarized.

1.3 Polarimetry

The performance of high-contrast imaging polarimeters is predominantly limited by two effects (e.g., Keller, 2002; Snik & Keller, 2013). Spurious signals and other noise in the images reduce the polarimetric sensitivity, that is, the noise level in the images above which polarization signals can be detected. In addition, telescope- and instrument-induced changes to the polarization state of light affect the polarimetric accuracy, that is, the dif-

ference between the measured polarization state and the polarization state incident on the telescope. To detect and accurately characterize substellar companions and circumstellar disks, high-contrast imaging polarimeters need to have both a high polarimetric sensitivity and a high polarimetric accuracy.

1.3.1 Description of polarized light

The polarization state of light can be described by the Stokes vector $\boldsymbol{S}$ (e.g., Tinbergen, 2005):

$$\boldsymbol{S} = \begin{bmatrix} I \\ Q \\ U \\ V \end{bmatrix}, \tag{1.1}$$

where I is the total intensity of the light, Q and U describe linearly polarized light, and V describes circularly polarized light. On the sky, positive Q is generally aligned with the north-south direction, and negative Q with the east-west direction (e.g., Hamaker & Bregman, 1996; Snik & Keller, 2013). Positive and negative U are oriented at 45° counterclockwise and clockwise, respectively, from positive Q, and positive and negative V describe circular polarizations of opposite handedness. From these Stokes parameters we can calculate the linearly polarized intensity PI_{L}, the degree of linear polarization P, and the angle of linear polarization χ as:

$$PI_{\mathrm{L}} = \sqrt{Q^2 + U^2}, \tag{1.2}$$

$$P = \frac{PI_{\mathrm{L}}}{I} = \frac{\sqrt{Q^2 + U^2}}{I}, \tag{1.3}$$

$$\chi = \frac{1}{2} \arctan\left(\frac{U}{Q}\right). \tag{1.4}$$

1.3.2 Polarization measurements with the double difference

Using a dual-beam polarimeter, images of Q and U can, in principle, be obtained by taking measurements with the HWP at angles (with respect to some defined reference direction) equal to 0° and 22.5°, respectively, and then computing the difference of the two images of the orthogonal linear polarization states, as described for PDI in Sect. 1.2.2. However, the stellar PSF is not perfectly removed when computing the difference. This is primarily due to the diattenuation of the optical components within the instrument, which causes the two orthogonal linear polarization states to be reflected and transmitted with different efficiencies (Canovas et al., 2011). In addition the two beams of light experience different wavefront aberrations, and the images they create contain different flat-field errors. These differential effects create spurious signals and noise that negatively affect the polarimetric sensitivity, especially at small angular separations from the star, close to the edge of the focal-plane mask of the coronagraph.

To suppress the differential effects and greatly increase the sensitivity, two additional measurements are performed. A total of four measurements are taken with HWP angles equal to 0°, 45°, 22.5°, and 67.5°. At each HWP angle, we compute the difference of the two images and denote the results as Q^+, Q^-, U^+, and U^-, respectively. We then compute the images of Q and U from the so-called double difference (e.g., Bagnulo et al., 2009):

$$Q = \frac{1}{2}\left(Q^+ - Q^-\right), \tag{1.5}$$

$$U = \frac{1}{2}\left(U^+ - U^-\right). \tag{1.6}$$

After computing the double difference, the differential effects are significantly reduced. Some spurious signals and noise still remain because the two measurements used to compute the double difference are not taken simultaneously and therefore experience (slightly) different atmospheric conditions and AO correction. As a result of these variations, the effect of the diattenuation of the components downstream of the HWP is not completely removed.

1.3.3 Instrumental polarization effects and polarization aberrations

After applying the double difference, the measurements are still affected by instrumental polarization effects, which consist of instrumental polarization (IP) and polarization crosstalk. IP is the polarization signal produced by the instrument or telescope and can make unpolarized sources appear to be polarized. It results from the diattenuation of the optical components located upstream of the HWP, which in Fig. 1.4 is the telescope. This diattenuation is not removed in the double difference and creates a halo of polarized light in the Q- and U-images. Crosstalk is the telescope- or instrument-induced mixing of polarization states. It is caused by the retardance of the optical components, which induces a relative phase shift between the two orthogonal linear polarization states. Crosstalk causes an offset of the measured angle of linear polarization and can lead to significant losses of polarization signal. If uncorrected for, the instrumental polarization effects can strongly decrease the polarimetric accuracy of the measurements. Fortunately, the instrumental polarization effects of high-contrast imaging polarimeters can be corrected for through theoretical modeling (e.g., Witzel et al., 2011), or more accurately, with calibration measurements (e.g., de Boer et al., 2014; Wiktorowicz et al., 2014; Millar-Blanchaer et al., 2016).

The coronagraphic performance and achievable contrast of the most sensitive high-contrast imagers are furthermore limited by polarization aberrations (e.g., Chipman, 1989; McGuire & Chipman, 1990; Sanchez Almeida & Martinez Pillet, 1992; McGuire & Chipman, 1994a,b; Breckinridge et al., 2015). Polarization aberrations are minute, polarization-dependent variations of the amplitude and phase of the electromagnetic field across a beam of light that result in polarization structures in the PSF. The diattenuation and retardance, which cause the instrumental polarization effects, can be considered to be zeroth-order polarization aberrations. The first-order polarization aberrations are polarization-dependent wavefront tilts induced by oblique reflection and are connected

to subwavelength-sized shifts of the PSF. Higher-order aberrations, such as polarization-dependent astigmatism, are produced by curved mirrors such as the primary and secondary mirrors of a telescope (see Fig. 1.4). Recently, it was found that the polarimetric speckle suppression of SPHERE-ZIMPOL at small angular separations is limited by reflection-induced beam shifts (Schmid et al., 2018). It is therefore becoming clear that polarization aberrations need to be fully controlled and mitigated for any instrument aiming to achieve the polarimetric sensitivity to detect exoplanets in reflected, polarized light.

1.4 Outline of this thesis

The goals of this thesis are to improve the polarimetric sensitivity, accuracy, and capabilities of high-contrast imaging polarimeters for the detection and characterization of substellar companions and circumstellar disks. In addition, this thesis presents the first direct detections of linear polarization from self-luminous substellar companions. The focus of this thesis is mostly on ground-based high-contrast imaging, in particular with SPHERE-IRDIS. The thesis covers many aspects of high-contrast imaging polarimetry, ranging from theoretical work, calibrations, and the development of new observing techniques to actual scientific polarimetric measurements and astrophysical interpretation.

Chapter 2: Calibration of the instrumental polarization effects of SPHERE-IRDIS

In Chapter 2 we characterize the instrumental polarization effects of SPHERE-IRDIS using measurements with SPHERE's internal light source and observations of unpolarized stars. We find that the IP is almost exclusively produced by the telescope and SPHERE's first mirror, whereas the crosstalk primarily originates from the image derotator. At some orientations, the derotator causes severe loss of signal in the H- and K_s-band as it converts incident linearly polarized light into circularly polarized light. We develop a data-reduction method that corrects the instrumental polarization effects and apply it to observations of a circumstellar disk. With our correction method we reach a polarimetric accuracy of $\lesssim$0.1% in the degree of linear polarization. We have incorporated the correction method in a highly automated end-to-end data-reduction pipeline called `IRDAP`, which is publicly available.

IRDAP enables us to accurately measure the linearly polarized intensity and angle of linear polarization and is currently the go-to pipeline for IRDIS polarimetric data. It is fundamental to the first detections of linear polarization from substellar companions as presented in Chapter 5 and laid the foundation for many scientific publications on circumstellar disks. Among these publications are the detection of non-azimuthal polarization, indicative of multiple scattering, in the circumstellar disk of T Cha (Pohl et al., 2017); the first detection of polarization from a low-mass stellar companion, CS Cha B (Ginski et al., 2018); the detection of the inner circumstellar disk of PDS 70 (Keppler et al., 2018); the discovery of an outer belt and spiral arm in the TWA 7 debris disk (Olofsson et al., 2018); the accurate tracing of the movement of the spiral arms in the MWC 758 disk, which indicates the spiral arms are driven by an unseen planetary perturber (Ren et al., 2020); and many others (Canovas et al., 2018; Bhowmik et al., 2019; Garufi et al.,

2020; Muro-Arena et al., 2020; Boccaletti et al., 2020a; Keppler et al., 2020; Ménard et al., 2020; Kennedy et al., 2020; Rigliaco et al., 2020; Kraus et al., 2020; Ginski et al., 2020; Uyama et al., 2020; Jensen-Clem et al., 2020; Xie et al., 2021; Ginski et al., 2021; Hunziker et al., 2021; Ren et al., 2021; Romero et al., 2021). The developed calibration and data-reduction methods can also be applied to other current and future high-contrast imaging polarimeters, including those on the future extremely large telescopes.

Chapter 3: Calibration of the instrumental polarization effects of SCExAO-CHARIS

In Chapter 3 we present the preliminary results of the characterization of the instrumental polarization effects of the low-resolution spectropolarimetric mode of SCExAO-CHARIS. Similar to Chapter 2, we performed measurements with the internal light source and find that the image derotator produces strong wavelength-dependent crosstalk that can cause significant loss of signal. We calculate the IP, which is almost entirely produced by the telescope, using theoretical models. To complete the calibrations, we plan to measure the IP of the telescope with observations of an unpolarized star and add a data-reduction method that corrects for the instrumental polarization effects to the existing CHARIS post-processing pipeline. Once finished, the calibrations of the spectropolarimetric mode of CHARIS will enable unique quantitative polarimetric studies of circumstellar disks and substellar companions at a spectral resolution beyond that possible with SPHERE-IRDIS' broadband filters.

Chapter 4: Combining polarimetry and ADI for the characterization of substellar companions

In Chapter 4 we introduce an observing scheme that combines high-contrast imaging polarimetry with ADI to reach the polarimetric sensitivity required to characterize substellar companions that are located at small angular separations from their stars. To enable this technique for SPHERE-IRDIS, we have implemented pupil-tracking for IRDIS' polarimetric mode. We develop the corresponding observing strategies and data-reduction approaches, including the correction of the instrumental polarization effects as described in Chapter 2. Using this novel technique, we observed the planets of HR 8799 and the substellar companion PZ Tel B. Although we do not detect NIR polarization from these companions, we reach a polarimetric contrast of $\sim 10^{-7}$ with respect to the star, close to the photon-noise limit. We estimate the 1σ upper limits on the degree of linear polarization to be $\sim 1\%$ for the planets of HR 8799 and $\sim 0.1\%$ for PZ Tel B. The achieved polarimetric sensitivity and sub-percent polarimetric accuracy show that our technique enables the characterization of faint substellar companions located close to their stars.

Chapter 5: First detections of linear polarization from self-luminous substellar companions

In Chapter 5 we use SPHERE-IRDIS to measure the NIR linear polarization of 20 known, directly imaged, self-luminous exoplanets and brown dwarf companions. We reduce the

data using IRDAP (Chapter 2) and retrieve the polarization of the companions using aperture photometry, ADI (Chapter 4), and PSF fitting. We detect polarization signals of several tenths of a percent for DH Tau B and GSC 6214-210 B in H-band. Because these companions have previously measured hydrogen emission lines and red colors, the polarization most likely originates from spatially unresolved circumsubstellar disks. Through radiative transfer modeling, we constrain the position angles of the disks and find that the disks must have high inclinations. For the 18 other companions, we do not detect significant polarization and place subpercent upper limits on their degree of polarization. We also present images of several circumstellar disks, including that of DH Tau. The presence of the disks around DH Tau B and GSC 6214-210 B as well as the misalignment of the disk of DH Tau B with the disk around its host star suggest in-situ formation of the companions. The non-detections of polarization for the other companions may indicate the absence of circumsubstellar disks, a slow rotation rate of young companions, the upper atmospheres containing primarily submicron-sized dust grains, and/or limited cloud inhomogeneity.

The detections of the polarization of DH Tau B and GSC 6214-210 B constitute the first direct detections of polarization from substellar companions. As such, the detections show that the small polarization signals of companions can indeed be detected through high-contrast imaging polarimetry. In addition, our work demonstrates that polarimetry can be used to characterize substellar companions, revealing properties that cannot be deduced through photometry and spectroscopy alone. Finally, the observing strategies, data-reduction methods, and analysis techniques we developed can be used for future NIR polarimetric observations of companions and the search for exoplanets in reflected, polarized light.

Chapter 6: Development of a circular-polarimetric mode for SPHERE-IRDIS

In Chapter 6 we develop the observing scheme, data-reduction methods, and analysis tools to measure NIR circular polarization with SPHERE-IRDIS. We devised an observing scheme that uses the image derotator, which acts as an almost perfect quarter-wave retarder in the H- and K_s-bands (Chapter 2), as a polarization modulator to convert incident circular polarization into measurable linear polarization. We tested the technique with observations of the red hypergiant VY CMa and its surrounding nebula and reduce the data using an adapted version of IRDAP (Chapter 2). We find that the polarimetric accuracy of our measurements is limited by the linear-to-circular crosstalk that is not well calibrated. To more accurately constrain this crosstalk, we use the spatial variation of the linear polarization around VY CMa to distinguish between real, astrophysical circular polarization and crosstalk-induced signal. We find that the light from VY CMa is circularly polarized, in agreement with the literature, but do not conclusively detect spatially resolved circular polarization in the nebula surrounding VY CMa.

The seeing-limited instruments that have so far been used to measure NIR circular polarization cannot reach the high contrast and subarcsecond resolution required to image protoplanetary disks and the nebulae surrounding evolved stars. Our observing scheme therefore enables the first measurements of spatially resolved NIR circular polarization in these systems. Such measurements can yield strong constraints on the distribution of

the scattering material, dust properties, and magnetic-field geometries. In the case of protoplanetary disks, measurements of NIR circular polarization could even shed light on the emergence of homochirality in biomolecules.

Chapter 7: Investigation of polarization-dependent beam shifts in high-contrast imagers and telescopes

In Chapter 7 we investigate polarization aberrations produced by reflection off flat metallic mirrors at the fundamental level. Polarization aberrations are typically modeled with numerical codes, but these codes provide little insight into the full range of effects, their origin, and possible ways to mitigate them. We use polarization ray tracing to numerically compute polarization aberrations and interpret the results in terms of the polarization-dependent spatial and angular Goos-Hänchen and Imbert-Federov shifts of the beam of light as described in the physics literature. We find that all four beam shifts are fully reproduced by polarization ray tracing. We study the origin of the shifts as well as the dependence of their size and direction on the beam intensity profile, incident polarization state, angle of incidence, mirror material, and wavelength. Of the four beam shifts, only the spatial Goos-Hänchen and Imbert-Federov shifts are relevant because they are visible in the focal plane and create polarization structure in the PSF that reduces the performance of coronagraphs and the polarimetric speckle suppression close to the star. The beam shifts in an optical system can be mitigated by keeping the f-numbers large and angles of incidence small as well as by designing mirror coatings to have a retardance close to 180° rather than maximum reflectivity. Our insights can be applied to improve the performance of SPHERE-ZIMPOL and future space- and ground-based high-contrast imagers that aim to reach the extreme contrasts required to directly image exoplanets in reflected, polarized light.

1.5 Outlook

By calibrating the instrumental polarization effects of high-contrast imaging polarimeters with a polarimetric accuracy of $\lesssim$0.1% in the degree of linear polarization, we can now accurately determine the linearly polarized intensity and angle of linear polarization of protoplanetary disks and debris disks. By comparing these observations with accurate radiative transfer models, we can determine the properties of the scattering dust grains. To further characterize the dust grains, the next step is to routinely and accurately determine the degree of linear polarization of disks. For this we need to obtain an image of the disk in total intensity. This is challenging, however, and large uncertainties in the disk's total intensity remain after subtracting the stellar PSF using current methods (such as ADI), thus strongly limiting the accuracy with which we can determine the degree of linear polarization (e.g., Perrin et al., 2015; Hunziker et al., 2021). To routinely measure the degree of linear polarization, we therefore need significant advances in observing strategies and data-reduction techniques (e.g., Wahhaj et al., 2021).

To enable the full characterization of circumstellar disks and the comparison with more refined radiative transfer models, we should work toward enabling full-Stokes, high-

resolution spectropolarimetry on high-contrast imagers. As a first step, we should measure the broadband circular polarization of disks, for which we could add quarter-wave plates to the current instruments. In addition, we should perform spectropolarimetry of disks, initially at low spectral resolution with, for example, SCExAO-CHARIS, and later with higher resolution by, for example, combining the long-slit spectroscopy mode of SPHERE-IRDIS with polarimetry. The latter mode could also enable the measurement of the distribution and abundance of water ice in disks (Clark et al., 2014), which can yield key information on the formation of planets and the delivery of water to rocky exoplanets (e.g., Morbidelli et al., 2000; Kobayashi et al., 2008; D'Angelo et al., 2010; Gundlach & Blum, 2015). All the efforts to characterize circumstellar disks will be aided by future improvements to the current high-contrast imagers, such as those proposed with SPHERE+ (Boccaletti et al., 2020b), GPI 2.0 (Chilcote et al., 2018), and SCExAO (Lozi et al., 2020b).

We have shown that we can measure the NIR linear polarization originating from spatially unresolved disks around young substellar companions. The next step is to detect the polarization signals due to dust scattering in the atmospheres of self-luminous companions. To detect these signals, we most likely need to reach a polarimetric accuracy of <0.01% in the degree of linear polarization, almost an order of magnitude better than the accuracy we attained with SPHERE-IRDIS. Although such a high accuracy is challenging, it has been achieved by Millar-Blanchaer et al. (2020) with their (non-high-contrast) polarimetric measurements of the brown-dwarf binary Luhman 16 using NACO at the Very Large Telescope. The authors could reach this accuracy because they kept the entire instrument at a fixed orientation with respect to the telescope during the observations, thereby stabilizing the instrumental polarization effects. Of the current high-contrast imaging polarimeters, GPI is the only instrument with a similarly stable configuration and may therefore be the most likely instrument to reach the polarimetric accuracy required to detect polarization due to dust scattering in companion atmospheres.

SPHERE-ZIMPOL has so far not been able to detect the reflected, polarized visible light of giant exoplanets (Hunziker et al., 2020). Part of the reason for these non-detections may be polarization aberrations, because the polarimetric speckle suppression of the instrument at small angular separations is limited by polarization-dependent beam shifts (Schmid et al., 2018). We should therefore measure and characterize these beam shifts so that we can devise an observing strategy that minimizes the effect of the beam shifts or can develop a method to accurately correct the shifts in the data reduction. However, it is still unclear whether SPHERE-ZIMPOL can reach a sufficiently high polarimetric sensitivity to detect giant exoplanets after the beam-shift artifacts are mitigated.

During the design of the current high-contrast imagers, polarimetry was often an afterthought and, as a result, the polarimetric sensitivity and accuracy of the instruments are not optimal. To be able to detect rocky exoplanets in reflected, polarized light with future high-contrast imagers, the polarimetric performance should be considered from the start of the design. The design process should particularly focus on minimizing polarization aberrations; instrumental polarization effects can be calibrated with sufficient accuracy and are therefore only of secondary importance. Only by controlling and mitigating the polarization aberrations can future high-contrast imagers and space telescopes such as PCS (or EPICS), PSI, HabEx, and LUVOIR reach the extreme contrasts of 10^{-8}–10^{-10}.

With these instruments and telescopes we may then be able to detect and characterize rocky exoplanets, determine their habitability, and perhaps answer the question whether there is life beyond Earth.

References

Amara, A., & Quanz, S. P. 2012, Monthly Notices of the Royal Astronomical Society, 427, 948

Bagnulo, S., Landolfi, M., Landstreet, J., et al. 2009, Publications of the Astronomical Society of the Pacific, 121, 993

Bailey, J. 2007, Astrobiology, 7, 320

Bailey, V. P., Bottom, M., Cady, E., et al. 2018, in Space Telescopes and Instrumentation 2018: Optical, Infrared, and Millimeter Wave, Vol. 10698, International Society for Optics and Photonics, 106986P

Baraffe, I., Chabrier, G., Barman, T., Allard, F., & Hauschildt, P. 2003, Astronomy & Astrophysics, 402, 701

Bastien, P., & Menard, F. 1990, Astrophysical Journal, 364, 232

Bate, M. R. 1998, Astrophysical Journal Letters, 508, L95

—. 2009, Monthly Notices of the Royal Astronomical Society, 392, 590

Beckwith, S. V., & Sargent, A. I. 1996, Nature, 383, 139

Benisty, M., Juhasz, A., Boccaletti, A., et al. 2015, Astronomy & Astrophysics, 578, L6

Benisty, M., Stolker, T., Pohl, A., et al. 2017, Astronomy & Astrophysics, 597, A42

Beuzit, J.-L., Vigan, A., Mouillet, D., et al. 2019, Astronomy & Astrophysics, 631, A155

Bhowmik, T., Boccaletti, A., Thébault, P., et al. 2019, Astronomy & Astrophysics, 630, A85

Boccaletti, A., Di Folco, E., Pantin, E., et al. 2020a, Astronomy & Astrophysics, 637, L5

Boccaletti, A., Chauvin, G., Mouillet, D., et al. 2020b, arXiv preprint arXiv:2003.05714

Bodenheimer, P., D'Angelo, G., Lissauer, J. J., Fortney, J. J., & Saumon, D. 2013, Astrophysical Journal, 770, 120

Bonnefoy, M., Zurlo, A., Baudino, J.-L., et al. 2016, Astronomy & Astrophysics, 587, A58

Boss, A. P. 1997, Science, 276, 1836

Bouvier, J., Chelli, A., Allain, S., et al. 1999, Astronomy and Astrophysics, 349, 619

Bowler, B. P. 2016, Publications of the Astronomical Society of the Pacific, 128, 102001

Bowler, B. P., Liu, M. C., Kraus, A. L., & Mann, A. W. 2014, Astrophysical Journal, 784, 65

Breckinridge, J. B., Lam, W. S. T., & Chipman, R. A. 2015, Publications of the Astronomical Society of the Pacific, 127, 445

Buenzli, E., & Schmid, H. M. 2009, Astronomy & Astrophysics, 504, 259

Cameron, A. 1978, The Moon and the Planets, 18, 5

Canovas, H., Rodenhuis, M., Jeffers, S., Min, M., & Keller, C. 2011, Astronomy & Astrophysics, 531, A102

Canovas, H., Montesinos, B., Schreiber, M., et al. 2018, Astronomy & Astrophysics, 610, A13

Canup, R. M., & Ward, W. R. 2002, The Astronomical Journal, 124, 3404

Chabrier, G., Baraffe, I., Allard, F., & Hauschildt, P. 2000, Astrophysical Journal, 542, 464

Chambers, J. E. 2004, Earth and Planetary Science Letters, 223, 241

Chilcote, J. K., Bailey, V. P., De Rosa, R., et al. 2018, in Ground-based and Airborne Instrumentation for Astronomy VII, Vol. 10702, International Society for Optics and Photonics, 1070244

Chipman, R. A. 1989, Optical engineering, 28, 280290

Clark, R. N., Swayze, G. A., Carlson, R., Grundy, W., & Noll, K. 2014, Reviews in Mineralogy and Geochemistry, 78, 399

D'Angelo, G., Durisen, R. H., & Lissauer, J. J. 2010, Exoplanets, 319

de Boer, J., Girard, J. H., Mawet, D., et al. 2014, in Ground-based and Airborne Instrumentation for Astronomy V, Vol. 9147, International Society for Optics and Photonics, 914787
de Boer, J., Salter, G., Benisty, M., et al. 2016, Astronomy & Astrophysics, 595, A114
de Boer, J., Langlois, M., van Holstein, R. G., et al. 2020, Astronomy & Astrophysics, 633, A63
de Kok, R., Stam, D., & Karalidi, T. 2011, Astrophysical Journal, 741, 59
Dohlen, K., Langlois, M., Saisse, M., et al. 2008, in Ground-based and Airborne Instrumentation for Astronomy II, Vol. 7014, International Society for Optics and Photonics, 70143L
Dong, R., Fung, J., & Chiang, E. 2016, Astrophysical Journal, 826, 75
Dong, R., Zhu, Z., Rafikov, R. R., & Stone, J. M. 2015, Astrophysical Journal Letters, 809, L5
Engler, N., Schmid, H. M., Thalmann, C., et al. 2017, Astronomy & Astrophysics, 607, A90
Esposito, T. M., Kalas, P., Fitzgerald, M. P., et al. 2020, The Astronomical Journal, 160, 24
Fitzgerald, M., Bailey, V., Baranec, C., et al. 2019, Bulletin of the American Astronomical Society, 51, 251
Fried, D. L. 1966, Journal of the Optical Society of America, 56, 1372
Garufi, A., Benisty, M., Pinilla, P., et al. 2018, Astronomy & Astrophysics, 620, A94
Garufi, A., Avenhaus, H., Pérez, S., et al. 2020, Astronomy & Astrophysics, 633, A82
Gaudi, B. S., Seager, S., Mennesson, B., et al. 2020, arXiv preprint arXiv:2001.06683
Ginski, C., Stolker, T., Pinilla, P., et al. 2016, Astronomy & Astrophysics, 595, A112
Ginski, C., Benisty, M., van Holstein, R., et al. 2018, Astronomy & Astrophysics, 616, A79
Ginski, C., Ménard, F., Rab, C., et al. 2020, Astronomy & Astrophysics, 642, A119
Ginski, C., Facchini, S., Huang, J., et al. 2021, Astrophysical Journal Letters, 908, L25
Gledhill, T., & McCall, A. 2000, Monthly Notices of the Royal Astronomical Society, 314, 123
Greenwood, D. P. 1977, Journal of the Optical Society of America, 67, 390
Grinin, V. 2000, in Disks, Planetesimals, and Planets, Vol. 219, 216
Groff, T., Chilcote, J., Brandt, T., et al. 2017, in Techniques and Instrumentation for Detection of Exoplanets VIII, Vol. 10400, International Society for Optics and Photonics, 1040016
Gundlach, B., & Blum, J. 2015, Astrophysical Journal, 798, 34
Guyon, O. 2018, Annual Review of Astronomy and Astrophysics, 56, 315
Guyon, O., Pluzhnik, E., Kuchner, M. J., Collins, B., & Ridgway, S. 2006, Astrophysical Journal Supplement Series, 167, 81
Hamaker, J., & Bregman, J. 1996, Astronomy and Astrophysics Supplement Series, 117, 161
Hennebelle, P., & Chabrier, G. 2008, Astrophysical Journal, 684, 395
Hollenbach, D. J., Yorke, H. W., & Johnstone, D. 2000, Protostars and planets IV, 401, 12
Hunziker, S., Schmid, H. M., Mouillet, D., et al. 2020, Astronomy & Astrophysics, 634, A69
Hunziker, S., Schmid, H., Ma, J., et al. 2021, Astronomy & Astrophysics, 648, A110
Jensen-Clem, R., Millar-Blanchaer, M., Mawet, D., et al. 2016, Astrophysical Journal, 820, 111
Jensen-Clem, R., Millar-Blanchaer, M. A., van Holstein, R. G., et al. 2020, The Astronomical Journal, 160, 286
Jovanovic, N., Martinache, F., Guyon, O., et al. 2015, Publications of the Astronomical Society of the Pacific, 127, 890
Karalidi, T., & Stam, D. 2012, Astronomy & Astrophysics, 546, A56
Karalidi, T., Stam, D., & Hovenier, J. 2011, Astronomy & Astrophysics, 530, A69
—. 2012, Astronomy & Astrophysics, 548, A90
Kasdin, N. J., Bailey, V., Mennesson, B., et al. 2020, in Space Telescopes and Instrumentation 2020: Optical, Infrared, and Millimeter Wave, Vol. 11443, International Society for Optics and Photonics, 114431U
Kasper, M., Urra, N. C., Pathak, P., et al. 2020, Messenger (182)
Keller, C. U. 2002, Astrophysical Spectropolarimetry, 1, 303
Kennedy, G. M., Ginski, C., Kenworthy, M. A., et al. 2020, Monthly Notices of the Royal Astro-

nomical Society: Letters, 496, L75
Keppler, M., Benisty, M., Müller, A., et al. 2018, Astronomy & Astrophysics, 617, A44
Keppler, M., Penzlin, A., Benisty, M., et al. 2020, Astronomy & Astrophysics, 639, A62
Kley, W., & Nelson, R. 2012, Annual Review of Astronomy and Astrophysics, 50, 211
Kobayashi, H., Watanabe, S.-i., Kimura, H., & Yamamoto, T. 2008, Icarus, 195, 871
Kratter, K. M., Murray-Clay, R. A., & Youdin, A. N. 2010, Astrophysical Journal, 710, 1375
Kraus, S., Kreplin, A., Young, A. K., et al. 2020, Science, 369, 1233
Kuhn, J., Potter, D., & Parise, B. 2001, Astrophysical Journal Letters, 553, L189
Langlois, M., Gratton, R., Lagrange, A.-M., et al. 2021, Astronomy & Astrophysics, 651, A71
Larkin, J. E., Chilcote, J. K., Aliado, T., et al. 2014, in Ground-based and Airborne Instrumentation for Astronomy V, Vol. 9147, International Society for Optics and Photonics, 91471K
Lozi, J., Guyon, O., Kudo, T., et al. 2020a, in Adaptive Optics Systems VII, Vol. 11448, International Society for Optics and Photonics, 114487C
Lozi, J., Guyon, O., Vievard, S., et al. 2020b, in Adaptive Optics Systems VII, Vol. 11448, International Society for Optics and Photonics, 114480N
LUVOIR Team. 2019, arXiv preprint arXiv:1912.06219
Lyot, B. 1939, Monthly Notices of the Royal Astronomical Society, 99, 580
Macintosh, B., Graham, J. R., Ingraham, P., et al. 2014, Proceedings of the National Academy of Sciences, 111, 12661
Marley, M. S., & Sengupta, S. 2011, Monthly Notices of the Royal Astronomical Society, 417, 2874
Marois, C., Lafreniere, D., Doyon, R., Macintosh, B., & Nadeau, D. 2006, Astrophysical Journal, 641, 556
Mawet, D., Pueyo, L., Lawson, P., et al. 2012, in Space Telescopes and Instrumentation 2012: Optical, Infrared, and Millimeter Wave, Vol. 8442, International Society for Optics and Photonics, 844204
McGuire, J. P., & Chipman, R. A. 1990, Journal of the Optical Society of America A, 7, 1614
—. 1994a, Applied optics, 33, 5080
—. 1994b, Applied optics, 33, 5101
McKee, C. F., & Ostriker, E. C. 2007, Annual Review of Astronomy and Astrophysics, 45, 565
Menard, F., Bouvier, J., Dougados, C., Mel'nikov, S. Y., & Grankin, K. N. 2003, Astronomy & Astrophysics, 409, 163
Ménard, F., Cuello, N., Ginski, C., et al. 2020, Astronomy & Astrophysics, 639, L1
Millar-Blanchaer, M. A., Graham, J. R., Pueyo, L., et al. 2015, Astrophysical Journal, 811, 18
Millar-Blanchaer, M. A., Perrin, M. D., Hung, L.-W., et al. 2016, in Ground-based and Airborne Instrumentation for Astronomy VI, Vol. 9908, International Society for Optics and Photonics, 990836
Millar-Blanchaer, M. A., Girard, J. H., Karalidi, T., et al. 2020, Astrophysical Journal, 894, 42
Milli, J., Mawet, D., Pinte, C., et al. 2015, Astronomy & Astrophysics, 577, A57
Morbidelli, A., Chambers, J., Lunine, J., et al. 2000, Meteoritics & Planetary Science, 35, 1309
Müller, A., Keppler, M., Henning, T., et al. 2018, Astronomy & Astrophysics, 617, L2
Muro-Arena, G. A., Ginski, C., Dominik, C., et al. 2020, Astronomy & Astrophysics, 636, L4
Muto, T., Grady, C., Hashimoto, J., et al. 2012, Astrophysical Journal Letters, 748, L22
Nakamoto, T., & Nakagawa, Y. 1994, Astrophysical Journal, 421, 640
Nielsen, E. L., De Rosa, R. J., Macintosh, B., et al. 2019, The Astronomical Journal, 158, 13
Olofsson, J., Samland, M., Avenhaus, H., et al. 2016, Astronomy & Astrophysics, 591, A108
Olofsson, J., van Holstein, R. G., Boccaletti, A., et al. 2018, Astronomy & Astrophysics, 617, A109
Olofsson, J., Milli, J., Thébault, P., et al. 2019, Astronomy & Astrophysics, 630, A142
Patty, C. L., Ten Kate, I. L., Buma, W. J., et al. 2019, Astrobiology, 19, 1221
Perrin, M. D., Duchene, G., Millar-Blanchaer, M., et al. 2015, Astrophysical Journal, 799, 182

Pinilla, P., Benisty, M., de Boer, J., et al. 2018, Astrophysical Journal, 868, 85
Pohl, A., Sissa, E., Langlois, M., et al. 2017, Astronomy & Astrophysics, 605, A34
Pollack, J. B., Hubickyj, O., Bodenheimer, P., et al. 1996, Icarus, 124, 62
Quanz, S. P., Avenhaus, H., Buenzli, E., et al. 2013, Astrophysical Journal Letters, 766, L2
Ren, B., Dong, R., van Holstein, R. G., et al. 2020, Astrophysical Journal Letters, 898, L38
Ren, B., Choquet, É., Perrin, M. D., et al. 2021, Astrophysical Journal, 914, 95
Rigliaco, E., Gratton, R., Kóspál, Á., et al. 2020, Astronomy & Astrophysics, 641, A33
Romero, C., Milli, J., Lagrange, A. M., et al. 2021, Astronomy & Astrophysics, 651, A34
Rossi, L., & Stam, D. 2017, Astronomy & Astrophysics, 607, A57
Rossi, L., & Stam, D. M. 2018, Astronomy & Astrophysics, 616, A117
Rostopchina, A., Grinin, V., Okazaki, A., et al. 1997, Astronomy and Astrophysics, 327, 145
Ruane, G., Riggs, A., Mazoyer, J., et al. 2018, in Space Telescopes and Instrumentation 2018: Optical, Infrared, and Millimeter Wave, Vol. 10698, International Society for Optics and Photonics, 106982S
Sanchez Almeida, J., & Martinez Pillet, V. 1992, Astronomy and Astrophysics, 260, 543
Schmid, H. M., Bazzon, A., Roelfsema, R., et al. 2018, Astronomy & Astrophysics, 619, A9
Sengupta, S., & Krishan, V. 2001, Astrophysical Journal Letters, 561, L123
Sengupta, S., & Marley, M. S. 2010, Astrophysical Journal Letters, 722, L142
Shu, F. H. 1977, Astrophysical Journal, 214, 488
Shu, F. H., Adams, F. C., & Lizano, S. 1987, Annual Review of Astronomy and Astrophysics, 25, 23
Snik, F., & Keller, C. U. 2013, Planets, Stars and Stellar Systems, 2, 175
Soummer, R., Pueyo, L., & Larkin, J. 2012, Astrophysical Journal Letters, 755, L28
Sparks, W., Hough, J., Kolokolova, L., et al. 2009, Journal of Quantitative Spectroscopy and Radiative Transfer, 110, 1771
Spergel, D., Gehrels, N., Baltay, C., et al. 2015, arXiv preprint arXiv:1503.03757
Stam, D. 2008, Astronomy & Astrophysics, 482, 989
Stam, D., Hovenier, J., & Waters, L. 2004, Astronomy & Astrophysics, 428, 663
Stamatellos, D., Hubber, D. A., & Whitworth, A. P. 2007, Monthly Notices of the Royal Astronomical Society: Letters, 382, L30
Stamatellos, D., & Whitworth, A. P. 2009, Monthly Notices of the Royal Astronomical Society, 392, 413
Stolker, T., Dominik, C., Min, M., et al. 2016a, Astronomy & Astrophysics, 596, A70
Stolker, T., Min, M., Stam, D. M., et al. 2017, Astronomy & Astrophysics, 607, A42
Stolker, T., Dominik, C., Avenhaus, H., et al. 2016b, Astronomy & Astrophysics, 595, A113
Szulágyi, J., Mayer, L., & Quinn, T. 2017, Monthly Notices of the Royal Astronomical Society, 464, 3158
Tinbergen, J. 2005, Astronomical polarimetry (Cambridge University Press)
Traub, W. A., & Oppenheimer, B. R. 2010, Direct imaging of exoplanets (University of Arizona Press, Tucson)
Trees, V. J., & Stam, D. M. 2019, Astronomy & Astrophysics, 626, A129
Uyama, T., Ren, B., Mawet, D., et al. 2020, The Astronomical Journal, 160, 283
Van Boekel, R., Henning, T., Menu, J., et al. 2017, Astrophysical Journal, 837, 132
Vigan, A., Langlois, M., Moutou, C., & Dohlen, K. 2008, Astronomy & Astrophysics, 489, 1345
Wahhaj, Z., Milli, J., Romero, C., et al. 2021, Astronomy & Astrophysics, 648, A26
Wiktorowicz, S. J., Millar-Blanchaer, M., Perrin, M. D., et al. 2014, in Ground-based and Airborne Instrumentation for Astronomy V, Vol. 9147, International Society for Optics and Photonics, 914783
Williams, D. M., & Gaidos, E. 2008, Icarus, 195, 927

Williams, J. P., & Cieza, L. A. 2011, Annual Review of Astronomy and Astrophysics, 49, 67
Witzel, G., Eckart, A., Buchholz, R., et al. 2011, Astronomy & Astrophysics, 525, A130
Wyatt, M. C. 2008, Annual Review of Astronomy and Astrophysics, 46, 339
Xie, C., Ren, B., Dong, R., et al. 2021, Astrophysical Journal Letters, 906, L9
Yorke, H. W., Bodenheimer, P., & Laughlin, G. 1993, Astrophysical Journal, 411, 274
Zhu, Z., Dong, R., Stone, J. M., & Rafikov, R. R. 2015, Astrophysical Journal, 813, 88

2 | Polarimetric imaging mode of VLT/SPHERE-IRDIS II: Characterization and correction of instrumental polarization effects

Adapted from

R. G. van Holstein, J. H. Girard, J. de Boer, F. Snik, J. Milli, D. M. Stam, C. Ginski, D. Mouillet, Z. Wahhaj, H. M. Schmid, C. U. Keller, M. Langlois, K. Dohlen, A. Vigan, A. Pohl, M. Carbillet, D. Fantinel, D. Maurel, A. Origné, C. Petit, J. Ramos, F. Rigal, A. Sevin, A. Boccaletti, H. Le Coroller, C. Dominik, T. Henning, E. Lagadec, F. Ménard, M. Turatto, S. Udry, G. Chauvin, M. Feldt, and J.-L. Beuzit

Astronomy & Astrophysics, 633, A64 (2020)

Context. Circumstellar disks and self-luminous giant exoplanets or companion brown dwarfs can be characterized through direct-imaging polarimetry at near-infrared wavelengths. SPHERE-IRDIS at the Very Large Telescope has the capabilities to perform such measurements, but uncalibrated instrumental polarization effects limit the attainable polarimetric accuracy.
Aims. We aim to characterize and correct the instrumental polarization effects of the complete optical system, that is, the telescope and SPHERE-IRDIS.
Methods. We created a detailed Mueller matrix model in the broadband filters Y, J, H, and K_s and calibrated the model using measurements with SPHERE's internal light source and observations of two unpolarized stars. We developed a data-reduction method that uses the model to correct for the instrumental polarization effects, and applied it to observations of the circumstellar disk of T Cha.
Results. The instrumental polarization is almost exclusively produced by the telescope and SPHERE's first mirror and varies with telescope altitude angle. The crosstalk primarily originates from the image derotator (K-mirror). At some orientations, the derotator causes severe loss of signal (>90% loss in the H- and K_s-band) and strongly offsets the angle of linear polarization. With our correction method we reach, in all filters, a total polarimetric accuracy of $\lesssim$0.1% in the degree of linear polarization and an accuracy of a few degrees in angle of linear polarization.
Conclusions. The correction method enables us to accurately measure the polarized intensity and angle of linear polarization of circumstellar disks, and is a vital tool for detecting spatially unresolved (inner) disks and measuring the polarization of substellar companions. We have incorporated the correction method in a highly-automated end-to-end data-reduction pipeline called IRDAP, which we made publicly available online.

2.1 Introduction

The near-infrared (NIR) polarimetric mode of the high-contrast imager SPHERE-IRDIS at the Very Large Telescope (VLT), which we introduced in Paper I (de Boer et al., 2020), has proven to be very successful for the detection of circumstellar disks in scattered light (Garufi et al., 2017) and shows much promise for the characterization of exoplanets and companion brown dwarfs (see Chapter 4). However, studies of circumstellar disks are often limited to analyses of the orientation (position angle and inclination) and morphology (rings, gaps, cavities, and spiral arms) of the disks (e.g., Muto et al., 2012; Quanz et al., 2013; Ginski et al., 2016; de Boer et al., 2016). Quantitative polarimetric measurements of circumstellar disks and substellar companions are currently very challenging because existing data-reduction methods do not account for instrumental polarization effects with a sufficiently high accuracy.

Due to instrumental polarization effects, polarized signal arriving at IRDIS' detector is different from that incident on the telescope. The two predominant effects are instrumental polarization (IP), that is, polarization signals produced by the instrument or telescope, and crosstalk, that is, instrument- or telescope-induced mixing of polarization states. IP not only changes the polarization state of an object, but can also make unpolarized sources appear polarized if not accounted for. For astronomical targets with a relatively low degree of linear polarization, IP can induce a significant rotation of the angle of linear polarization. Crosstalk also causes an offset of the measured angle of linear polarization and can lower the polarimetric efficiency, that is, the fraction of the incident or true linear polarization that is actually measured.We first encountered these instrumental polarization effects when observing the disk around TW Hydrae as described in Paper I.

To derive the true polarization state of the light incident on the telescope, we need to calibrate the instrument so that we know the instrumental polarization effects a priori. This enables us to accurately and quantitatively measure the polarization of circumstellar disks and substellar companions. In addition, it enables accurate mapping of extended objects other than circumstellar disks, such as solar system objects, molecular clouds, and galaxies (e.g., Gratadour et al., 2015), provided the target is sufficiently bright for the adaptive optics correction.

For observations of circumstellar disks (see Paper I), calibrating the instrument yields a multitude of improvements. Firstly, the calibration allows for more accurate studies of the orientation and morphology of the disks, especially at the innermost regions (separation $< 0.5''$). In fact, we are able to deduce the presence of spatially unresolved (inner) disks by measuring the polarization signals of the stars (see e.g., Keppler et al., 2018). Secondly, the calibration enables more accurate measurements of the angle of linear polarization. This in turn allows us to prove the presence of non-azimuthal polarization (Canovas et al., 2015) that can be indicative of multiple scattering or the presence of a binary star, and allows for a more in-depth study of dust properties. Finally, the calibration enables more accurate measurements of the polarized intensity, that is, the polarized surface brightness of the disk.

More accurate measurements of the polarized surface brightness enables us to construct scattering phase functions (e.g., Perrin et al., 2015; Stolker et al., 2016; Ginski et al., 2016; Milli et al., 2017), perform more accurate radiative transfer modeling (e.g.,

Pinte et al., 2009; Min et al., 2009; Pohl et al., 2017a; Keppler et al., 2018), and determine dust particle properties (e.g., Min et al., 2012; Pohl et al., 2017b,a). In addition, it allows for accurate measurements of the degree of linear polarization of the disk, enabling us to further constrain dust properties (e.g., Perrin et al., 2009, 2015; Milli et al., 2015). However, before images of the degree of linear polarization can be constructed, an image of the total intensity of the disk needs to be obtained, for example with reference star differential imaging (RDI; e.g., Canovas et al., 2013) or, for disks viewed edge-on, with angular differential imaging (ADI; Marois et al., 2006).

To measure polarization signals of young self-luminous giant exoplanets or companion brown dwarfs (see Paper I), it is of vital importance to calibrate the instrument. Based on radiative transfer models, the NIR degree of linear polarization of a companion can be a few tenths of a percent up to several percent (de Kok et al., 2011; Marley & Sengupta, 2011; Stolker et al., 2017). Measurements of these small polarization signals therefore need to be performed with a very high accuracy, which is only possible after careful calibration of the instrumental polarization effects.

Polarimetric measurements of substellar companions have already been attempted by Millar-Blanchaer et al. (2015) and Jensen-Clem et al. (2016) with the Gemini Planet Imager (GPI), and in Chapter 4 with SPHERE-IRDIS (using the calibration results presented in this chapter). No polarization signals were detected in these studies. Recently, Ginski et al. (2018) presented the first direct detection of a polarization signal from a substellar companion. Using the calibration results presented in this chapter, they find the companion to CS Cha to have a NIR degree of linear polarization of 14%, which suggests the presence of a spatially unresolved disk and dusty envelope around the companion.

In this chapter, we characterize the instrumental polarization effects of the complete optical system of VLT/SPHERE-IRDIS, that is, the telescope and the instrument, in the four broadband filters Y, J, H, and K_s. Because the complexity of the optical path is comparable to that of solar telescopes and their instruments, we perform a calibration similar to those applied in the field of solar physics (see e.g., Skumanich et al., 1997; Beck et al., 2005; Socas-Navarro et al., 2011). For our calibration, we create a detailed Mueller matrix model of the optical path and determine the parameters of the model from measurements with SPHERE's internal light source and observations of two unpolarized stars. Similar approaches have been adopted for the German Vacuum Tower Telescope (Beck et al., 2005), VLT/NACO (Witzel et al., 2011) and GPI (Wiktorowicz et al., 2014; Millar-Blanchaer et al., 2016). We then develop a data-reduction method to correct science measurements for the instrumental polarization effects using the model, and exemplify this correction method and its advantages with polarimetric observations of the circumstellar disk of T Cha from Pohl et al. (2017a). This chapter is the second part of a larger study in which Paper I discusses IRDIS' polarimetric mode, the data reduction, and recommendations for observations and instrument upgrades.

With our instrument model we aim to achieve in all four broadband filters a total polarimetric accuracy, that is, the uncertainty in the measured polarization signal, of ~0.1% in the degree of linear polarization. In addition, we aim to attain an accuracy of a few degrees in angle of linear polarization in these filters. Reaching these accuracies enables us to measure the linear polarization of substellar companions (we regard the extremely high degree of linear polarization found by Ginski et al. (2018) to be an exception). These

accuracies also readily suffice for quantitative polarimetry of circumstellar disks, because the degree of linear polarization of disks is typically much higher than that of substellar companions: on the order of percents to several ten percent (see e.g., Perrin et al., 2009). To attain a total polarimetric accuracy of ~0.1%, an absolute polarimetric accuracy, that is, the uncertainty in the instrumental polarization (IP), of ≤0.1% and a relative polarimetric accuracy, that is, the uncertainty that scales with the input polarization signal, of <1% is aimed for.

The outline of this chapter is as follows. In Sect. 2.2 we present the conventions and definitions used throughout this chapter. Subsequently, we briefly review the optical path of SPHERE-IRDIS and discuss the expected instrumental polarization effects in Sect. 2.3. We explain the Mueller matrix model describing these effects in Sect. 2.4. In Sects. 2.5 and 2.6 we determine the parameters of the model from measurements with the internal light source and observations of two unpolarized stars, respectively. We then discuss the accuracy of the model in Sect. 2.7. In Sect. 2.8 we present our correction method and exemplify it with polarimetric observations of the circumstellar disk of T Cha. In the same section we describe the improvements we attain with respect to conventional data-reduction methods, discuss the limits to and optimization of the polarimetric accuracy, and introduce our data-reduction pipeline that incorporates the correction method. Finally, we present conclusions in Sect. 2.9. If the reader is only interested in applying our correction method to on-sky data, one could suffice with reading Sects. 2.2, 2.3, 2.8 and 2.9.

2.2 Conventions and definitions

In this section we briefly outline the conventions and definitions used throughout this chapter. The total intensity and polarization state of a beam of light can be described by a Stokes vector $\boldsymbol{S}$ (e.g., Tinbergen, 2005):

$$\boldsymbol{S} = \begin{bmatrix} I \\ Q \\ U \\ V \end{bmatrix}, \tag{2.1}$$

where I is the total intensity (or flux), Q and U describe linear polarization and V represents circular polarization. We define these Stokes parameters with respect to the general reference frame shown in Fig. 2.1. Positive Stokes Q ($+Q$) and negative Stokes Q ($-Q$) correspond to vertical and horizontal linear polarization, respectively. When looking into the beam of light, positive (negative) Stokes U is oriented 45° counterclockwise (clockwise) from positive Stokes Q. Finally, positive (negative) Stokes V is defined as circularly polarized light with clockwise (counterclockwise) rotation when looking into the beam of light.

We can normalize the Stokes vector of Eq. (2.1) by dividing each of its Stokes parameters by the total intensity I:

$$\boldsymbol{S} = [1,\ q,\ u,\ v]^{\mathrm{T}}, \tag{2.2}$$

with q, u, and v the normalized Stokes parameters. From the Stokes parameters we can calculate the linearly polarized intensity (PI_{L}), degree of linear polarization ($DoLP$) and

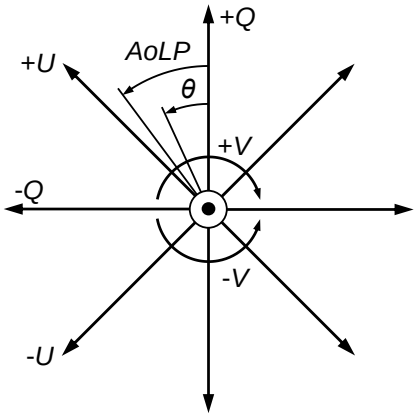


Figure 2.1: Reference frame for the definition of the Stokes parameters describing the oscillation direction of the electric field within a beam of light. The propagation direction of the light beam is out of the paper, toward the reader. Positive and negative Stokes Q are oriented along the vertical ($+Q$) and horizontal ($-Q$) axes, respectively. Looking into the beam of light, positive Stokes U ($+U$) is oriented 45° counterclockwise from positive Stokes Q and positive Stokes V ($+V$) is defined as clockwise rotation. The angle of linear polarization $AoLP$ and the rotation angle θ of an optical component used in the rotation Mueller matrix (see Eqs. (2.15) and (2.16)) are defined counterclockwise when looking into the beam of light.

angle of linear polarization (*AoLP*; see Fig. 2.1) as follows:

$$PI_{\mathrm{L}} = \sqrt{Q^2 + U^2}, \tag{2.3}$$

$$DoLP = \sqrt{q^2 + u^2}, \tag{2.4}$$

$$AoLP = \frac{1}{2}\arctan\left(\frac{U}{Q}\right) = \frac{1}{2}\arctan\left(\frac{u}{q}\right). \tag{2.5}$$

2.3 Optical path and instrumental polarization effects of SPHERE-IRDIS

2.3.1 SPHERE-IRDIS optical path

Before discussing the instrumental polarization effects expected for SPHERE-IRDIS, in this section we first summarize the optical path and the working principle of IRDIS' polarimetric mode. As described in detail in Paper I, SPHERE's optical system is complex and has many rotating components. A simplified version of the optical path is shown in Fig. 2.2. The model parameters, Stokes vectors and the top right part of the image are discussed in Sect. 2.4.

During an observation, light is collected by the altazimuth-mounted Unit Telescope

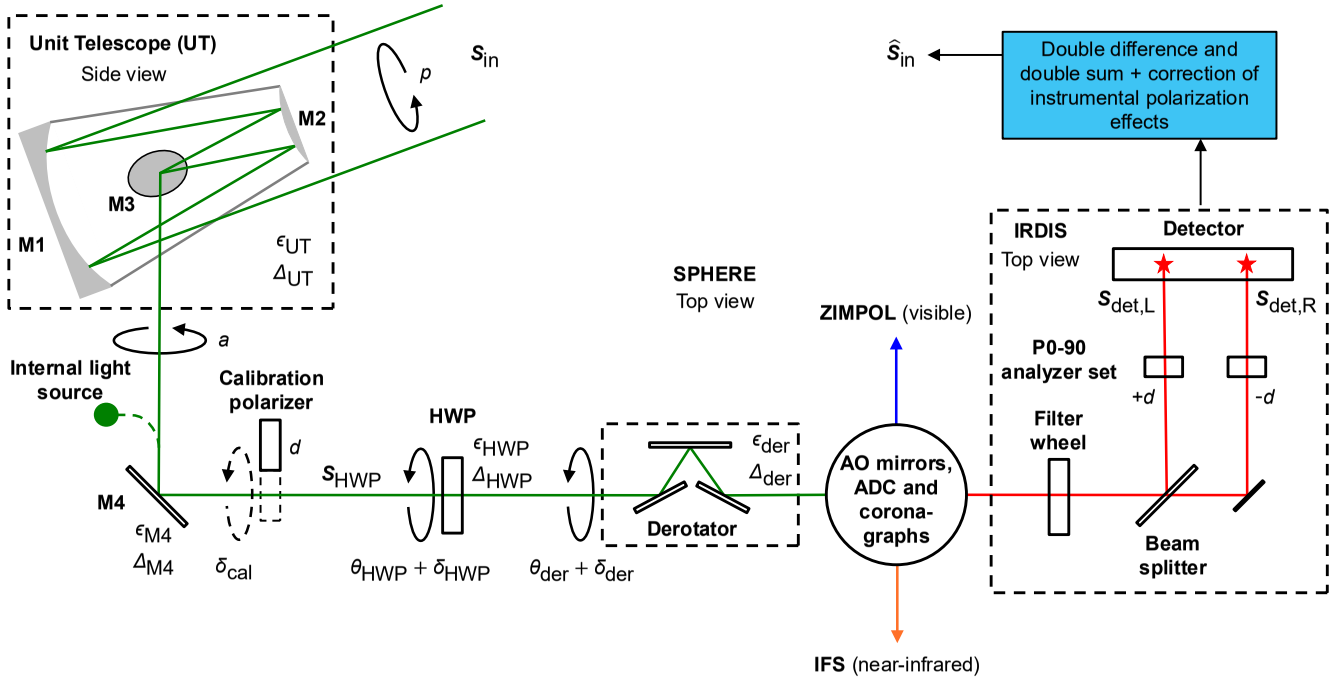


Figure 2.2: Overview of the optical path of the complete optical system, i.e., the Unit Telescope (UT) and SPHERE-IRDIS, showing only the components relevant for polarimetric measurements (image adapted from Fig. 2 of Paper I). The names of the (groups of) components are indicated in boldface. The black circular arrows indicate the astronomical target's parallactic angle p, the telescope's rotation with the altitude angle a, the offset angle of the calibration polarizer δ_{cal}, and the rotation of the HWP and image derotator with the angles $\theta_{HWP} + \delta_{HWP}$ and $\theta_{der} + \delta_{der}$, respectively. Also shown are the parameters describing the instrumental polarization effects of the (groups of) components: the component diattenuations ϵ, retardances Δ and the polarizer diattenuation d. The Stokes vectors $\boldsymbol{S}_{in}$, $\boldsymbol{S}_{HWP}$, $\boldsymbol{S}_{det,L}$, $\boldsymbol{S}_{det,R}$ and $\hat{\boldsymbol{S}}_{in}$ used in the instrument model are indicated as well. Finally, the top right of the image shows the data-reduction process that produces the measured (after calibration) Stokes vector incident on the telescope.

(UT) which consists of three mirrors. The incident light hits the primary mirror (M1) and is subsequently re-focused by the secondary mirror (M2) that is suspended at the top of the telescope tube. The flat tertiary mirror (M3) has an angle of incidence of 45° and reflects the beam of light to the Nasmyth platform where SPHERE is located. When the telescope tracks a target across the sky, the target rotates with the parallactic angle in the pupil of the UT and the UT rotates with the telescope altitude angle with respect to Nasmyth platform.

The light entering SPHERE (Beuzit et al., 2019) passes a system that can feed the instrument with light from an internal light source to enable internal calibrations (Wildi et al., 2009; Roelfsema et al., 2010). Subsequently, the beam of light hits the flat mirror M4 (the pupil tip-tilt mirror) that similarly to M3 is coated with aluminum and has a 45° inclination angle. M4 is the only aluminum mirror in SPHERE; all other mirrors are coated with protected silver. For calibrations, a linear polarizer with its transmission axis aligned vertical, that is, perpendicular to the Nasmyth platform, can be inserted after M4 (Wildi et al., 2009).

The light then reaches the insertable and rotatable half-wave plate (HWP; HWP2 in Paper I) that can rotate the incident angle of linear polarization. The HWP is used to temporally modulate the incident Stokes Q and U and to correct for field rotation so that the polarization direction of the source is kept fixed on the detector. The HWP is followed by the image derotator, which is a rotating assembly of three mirrors (a K-mirror) that rotates both the image and angle of linear polarization for field- or pupil-stabilized observations. Before reaching IRDIS, the light passes the mirrors of the adaptive-optics (AO) common path (Fusco et al., 2006; Hugot et al., 2012), several dichroic mirrors, the rotating atmospheric dispersion corrector (ADC) and the coronagraphs (Carbillet et al., 2011; Guerri et al., 2011).

The light beam entering IRDIS (Dohlen et al., 2008; Langlois et al., 2014) passes a filter wheel containing various color filters. In this work, only the four available broadband filters Y, J, H, and K_s are considered (see Table 1 of Paper I for the central wavelengths and bandwidths). After the filter wheel, the light is split into parallel beams by a combination of a non-polarizing beamsplitter plate and a mirror. The light beams subsequently pass a pair of insertable linear polarizers (the P0-90 analyzer set) with orthogonal transmission axes at 0° (left) and 90° (right) with respect to vertical. Both beams strike the same detector to form two adjacent images, one on the left and one on the right half of the detector.

Images of Stokes Q and U and the corresponding total intensities I (I_Q and I_U) can then be constructed from the single difference and single sum, respectively, of the left and right images on the detector (see Paper I):

$$X^{\pm} = I_{\mathrm{det,L}} - I_{\mathrm{det,R}}, \tag{2.6}$$

$$I_{X^{\pm}} = I_{\mathrm{det,L}} + I_{\mathrm{det,R}}, \tag{2.7}$$

where $X^{\pm}$ is the single-difference Q or U and $I_{X^{\pm}}$ is the single-sum intensity I_Q or I_U. The variables $I_{\mathrm{det,L}}$ and $I_{\mathrm{det,R}}$ are the intensities of the left (L) and right (R) images on the detector, respectively. Stokes Q and I_Q are measured with the HWP angle switched by 0° and U and I_U are measured with the HWP angle switched by 22.5°. We call the resulting

single differences Q^+ and U^+ and the corresponding single-sum intensities I_{Q^+} and I_{U^+}. Additional measurements of Q and I_Q, and of U and I_U, are taken with the HWP angle switched by 45° and 67.5°, respectively. We call the results Q^-, I_{Q^-}, U^-, and I_{U^-}. The set of measurements with HWP switch angles equal to 0°, 45°, 22.5°, and 67.5° are called a HWP or polarimetric cycle. The single differences and single sums are used in Sect. 2.3.2 to calculate the so-called double difference and double sum. Stokes V cannot be measured by IRDIS, as it lacks a quarter-wave plate (however, see the last paragraph of Sect. 2.5.2).

2.3.2 Instrumental polarization effects of optical path

In this section, we discuss the expected instrumental polarization effects of the optical path of SPHERE-IRDIS. Basically all optical components described in Sect. 2.3.1 produce instrumental polarization (IP) and crosstalk. IP is a result of the optical components' (linear) diattenuation, that is, it is caused by the different reflectances (e.g., for the mirrors) or transmittances (e.g., for the beamsplitter or HWP) of the perpendicular linearly polarized components of an incident beam of light. Crosstalk is created by the optical components' retardance (or relative retardation), that is, the relative phase shift of the perpendicular linearly polarized components. Because IRDIS cannot measure circularly polarized light, crosstalk from linearly polarized to circularly polarized light results in a loss of polarization signal and thus a decrease of the polarimetric efficiency. The diattenuation and retardance of an optical component are a function of wavelength and the component's rotation angle.

The diattenuation and retardance are strongest for reflections at large angles of incidence. Therefore the largest effects are expected for M3, M4, the derotator, the two reflections at an angle of incidence of 45° just upstream of IRDIS and IRDIS' beamsplitter-mirror combination (the non-polarizing beamsplitter is in fact ~10% polarizing). The diattenuation and retardance of M1 and M2 are expected to be small, because these mirrors are rotationally symmetric with respect to the optical axis (see e.g., Tinbergen, 2005). Also the diattenuation and retardance of the ADC and the mirrors of the AO common path are likely small, because these components have small angles of incidence (<10°) and stress birefringence in the ADC is expected to be limited. The HWP creates (some) circular polarization because its retardance is not completely achromatic and only approximately half-wave (or 180° in phase).

The IP of the non-rotating components downstream of the HWP can be removed by taking advantage of beam switching with the HWP and computing the Stokes parameters from the double difference (see Paper I; Bagnulo et al. 2009):

$$X = \frac{1}{2}\left(X^+ - X^-\right), \tag{2.8}$$

where X is the double-difference Stokes Q or U, and X^+ and X^- are computed from Eq. (2.6). An additional advantage of the double-difference method is that it suppresses differential effects such as flat-fielding errors and differential aberrations (Tinbergen, 2005; Canovas et al., 2011). The total intensity corresponding to the double-difference Q

or U is computed from the double sum:

$$I_X = \frac{1}{2}\left(I_{X^+} + I_{X^-}\right), \tag{2.9}$$

where I_X is the double-sum intensity I_Q or I_U, and I_{X^+} and I_{X^-} are computed from Eq. (2.7). Finally, we can compute the normalized Stokes parameter q or u (see Eq. (2.2)) as:

$$x = \frac{X}{I_X}. \tag{2.10}$$

All reflections downstream of the derotator lie in the horizontal plane, that is, parallel to the Nasmyth platform that SPHERE is installed on. These reflections can only produce crosstalk between light linearly polarized at ±45° with respect to the horizontal plane and circularly polarized light. Light that is linearly polarized in the vertical or horizontal direction is not affected by crosstalk. Because the P0-90 analyzer set has vertical and horizontal transmission axes and thus only measures the vertical and horizontal polarization components, crosstalk created downstream of the derotator does not affect the measurements. The P45-135 analyzer set is sensitive to this crosstalk and is therefore not discussed in this work. For polarimetric science observations we strongly advice against using the P45-135 analyzer set.

After computing the double difference, IP from the UT (dominated by M3), M4, the HWP, and the derotator remains, because these components are located upstream of the HWP and/or are rotating between the two measurements used in the double difference. In addition, the measurements are affected by the crosstalk created by these components (IP and crosstalk created by the ADC is found to be negligible). We therefore need to calibrate these instrumental polarization effects. To do this, we start by developing a mathematical model of the complete optical system in the next section.

2.4 Mathematical description of complete optical system

Before constructing the mathematical model describing the instrumental polarization effects of the optical system, we define two principal reference frames. In the celestial reference frame, we orient the general reference frame defined in Sect. 2.2 and Fig. 2.1 such that positive Stokes Q is aligned with the local meridian (north up in the sky). In the instrument reference frame, we orient the general reference frame such that positive Stokes Q corresponds to the vertical direction, that is, perpendicular to the Nasmyth platform that SPHERE is installed on.

The goal of our calibration is to obtain a mathematical description of the instrumental polarization effects of the optical system, such that for a given observation we can derive the polarization state of the light incident on the telescope within the required polarimetric accuracy (see Sect. 2.1 and the top right part of Fig. 2.2). In the general case, we can define the polarimetric accuracy with the following equation (Ichimoto et al., 2008; Snik & Keller, 2013):

$$\hat{\boldsymbol{S}}_{\text{in}} = (\mathbb{I} \pm \Delta Z)\boldsymbol{S}_{\text{in}}, \tag{2.11}$$

where $\boldsymbol{S}_{\rm in}$ is the true Stokes vector incident on the telescope, $\hat{\boldsymbol{S}}_{\rm in}$ is the measured incident Stokes vector after calibration (after correction for the instrumental polarization effects), $\mathbb{I}$ is the 4×4 identity matrix and ΔZ is the 4×4 matrix describing the polarimetric accuracy. Both Stokes vectors in Eq. (2.11) are defined in the celestial reference frame. For a perfect measurement, ΔZ equals the zero matrix. In this work, we write ΔZ as:

$$\Delta Z = \begin{bmatrix} - & - & - & - \\ s_{\rm abs} & s_{\rm rel} & - & - \\ s_{\rm abs} & - & s_{\rm rel} & - \\ - & - & - & - \end{bmatrix}, \tag{2.12}$$

with $s_{\rm abs}$ and $s_{\rm rel}$ the absolute and relative polarimetric accuracies, respectively, as defined in Sect. 2.1. The values of $s_{\rm abs}$ and $s_{\rm rel}$ are different for each broadband filter and are established in Sect. 2.7 (we do not directly evaluate Eq. (2.11), however). We do not the determine other elements in Eq. (2.12) because for the calibration only a very limited number of different polarization states can be injected into the optical system, and the total intensity is hardly affected by the instrumental polarization effects.

In the following, we use Mueller calculus (see e.g., Tinbergen, 2005) to construct the model describing the instrumental polarization effects of the complete optical system, that is, the UT and the instrument. The model parameters and Stokes vectors we define in the process are displayed in Fig. 2.2. We express the Stokes vector reaching the left (L) or right (R) half of the detector, $\boldsymbol{S}_{\rm det,L}$ or $\boldsymbol{S}_{\rm det,R}$ (both in the instrument reference frame), in terms of the true Stokes vector incident on the telescope $\boldsymbol{S}_{\rm in}$ (in the celestial reference frame) as:

$$\begin{aligned} \boldsymbol{S}_{\rm det,L/R} &= M_{\rm sys,L/R}\boldsymbol{S}_{\rm in}, \\ \begin{bmatrix} I_{\rm det,L/R} \\ Q_{\rm det,L/R} \\ U_{\rm det,L/R} \\ V_{\rm det,L/R} \end{bmatrix} &= \begin{bmatrix} I\rightarrow I & Q\rightarrow I & U\rightarrow I & V\rightarrow I \\ I\rightarrow Q & Q\rightarrow Q & U\rightarrow Q & V\rightarrow Q \\ I\rightarrow U & Q\rightarrow U & U\rightarrow U & V\rightarrow U \\ I\rightarrow V & Q\rightarrow V & U\rightarrow V & V\rightarrow V \end{bmatrix} \begin{bmatrix} I_{\rm in} \\ Q_{\rm in} \\ U_{\rm in} \\ V_{\rm in} \end{bmatrix}, \end{aligned} \tag{2.13}$$

where $M_{\rm sys,L/R}$ is the 4×4 Mueller matrix describing the instrumental polarization effects of the optical system as seen by the left or right half of the detector. The only difference between $M_{\rm sys,L}$ and $M_{\rm sys,R}$ is the orientation of the transmission axis of the analyzer polarizer. In Eq. (2.13), an element $A\rightarrow B$ describes the contribution of the incident A into the resulting B Stokes parameter. The optical system is comprised of a sequence of optical components that rotate with respect to each other during an observation. To describe the various components and their rotations, we rewrite Eq. (2.13) as a multiplication of Mueller matrices (see e.g., Tinbergen, 2005):

$$\boldsymbol{S}_{\rm det,L/R} = M_n M_{n-1} \cdots M_2 M_1 \boldsymbol{S}_{\rm in}. \tag{2.14}$$

In Eq. (2.14), we do not have to include every separate mirror or component independently. We can combine components which share a fixed reference frame, such as the three mirrors of the derotator. This allows us to create a model with Mueller matrices for only five component groups (see Sect. 2.3 and Fig. 2.2): $M_{\rm UT}$, the three mirrors of the

Unit Telescope (UT); M_{M4}, the first mirror of SPHERE (M4); M_{HWP}, the half-wave plate (HWP); M_{der}, the three mirrors of the derotator; $M_{\mathrm{CI,L/R}}$, the optical path downstream of the derotator including IRDIS and the left or right polarizer of the P0-90 analyzer set. The Mueller matrices M_{M4} and $M_{\mathrm{CI,L/R}}$ are defined in the instrument reference frame, while M_{UT}, M_{HWP} and M_{der} have their own (rotating) reference frames.

The rotations between subsequent reference frames can be described by the rotation matrix $T(\theta)$ (see e.g., Tinbergen, 2005):

$$T(\theta) = \begin{bmatrix} 1 & 0 & 0 & 0 \\ 0 & \cos(2\theta) & \sin(2\theta) & 0 \\ 0 & -\sin(2\theta) & \cos(2\theta) & 0 \\ 0 & 0 & 0 & 1 \end{bmatrix}, \tag{2.15}$$

where the component (group) is rotated counterclockwise by an angle θ when looking into the beam (see Fig. 2.1). After applying the Mueller matrix of the optical component M in its own reference frame, the reference frame can be rotated back to the original frame with the rotation matrix $T(-\theta)$:

$$M_\theta = T(-\theta)MT(\theta), \tag{2.16}$$

where M_θ is the rotated component Mueller matrix.

Taking into account the rotations between the component groups (see Fig. 2.2), the complete optical system can be described by:

$$\begin{aligned} \boldsymbol{S}_{\mathrm{det,L/R}} &= M_{\mathrm{sys,L/R}}\boldsymbol{S}_{\mathrm{in}}, \\ \boldsymbol{S}_{\mathrm{det,L/R}} &= M_{\mathrm{CI,L/R}}T(-\Theta_{\mathrm{der}})M_{\mathrm{der}}T(\Theta_{\mathrm{der}})T(-\Theta_{\mathrm{HWP}})M_{\mathrm{HWP}}T(\Theta_{\mathrm{HWP}}) \\ &\quad M_{\mathrm{M4}}T(a)M_{\mathrm{UT}}T(p)\boldsymbol{S}_{\mathrm{in}}, \end{aligned} \tag{2.17}$$

where p is the astronomical target's parallactic angle, a is the altitude angle of the telescope, and:

$$\Theta_{\mathrm{HWP}} = \theta_{\mathrm{HWP}} + \delta_{\mathrm{HWP}}, \tag{2.18}$$

$$\Theta_{\mathrm{der}} = \theta_{\mathrm{der}} + \delta_{\mathrm{der}}, \tag{2.19}$$

with θ_{HWP} the HWP angle, θ_{der} the derotator angle, and δ_{HWP} and δ_{der} the to-be-determined offset angles (due to misalignments) of the HWP and derotator, respectively. $\theta_{\mathrm{HWP}} = 0°$ when the HWP has its fast or slow optic axis vertical, and $\theta_{\mathrm{der}} = 0°$ when the derotator has its plane of incidence horizontal. The parallactic, altitude, HWP, and derotator angles are obtained from the headers of the FITS-files of the measurements (see Appendix 2.A).

Ideally, all 16 elements of the component group Mueller matrices M_{UT}, M_{M4}, M_{HWP}, M_{der}, and $M_{\mathrm{CI,L/R}}$ would be determined from calibration measurements that inject a multitude of different polarization states into the system. However, IRDIS' non-rotatable calibration polarizer can only inject light that is nearly 100% linearly polarized in the positive Stokes Q-direction (in the instrument reference frame), and polarized standard stars are limited in number and have a low degree of linear polarization at near-infrared

wavelengths. To limit the number of model parameters to determine, we model M_{UT}, M_{M4}, M_{HWP}, and M_{der} as a function of their diattenuation (ϵ) and retardance (Δ) (see Sect. 2.3.2; Keller 2002; Bass et al. 1995):

$$M_{\mathrm{com}} = \begin{bmatrix} 1 & \epsilon & 0 & 0 \\ \epsilon & 1 & 0 & 0 \\ 0 & 0 & \sqrt{1-\epsilon^2}\cos\Delta & \sqrt{1-\epsilon^2}\sin\Delta \\ 0 & 0 & -\sqrt{1-\epsilon^2}\sin\Delta & \sqrt{1-\epsilon^2}\cos\Delta \end{bmatrix}, \tag{2.20}$$

where we have assumed the transmission of the total intensity, which is a scalar multiplication factor to the matrix, equal to 1. The real transmission of the optical system is not important, because we always measure Stokes Q and U relative to the total intensity I and the system transmission cancels out when computing the normalized Stokes parameters and degree and angle of linear polarization (see Eqs. (2.2), (2.4) and (2.5)).

For the HWP, M_{com} is defined with the positive Stokes Q-direction parallel to one of its optic axes. For the other component groups, it is defined with the positive Stokes Q-direction perpendicular to the plane of incidence of the mirrors. The diattenuation ϵ has the range $[-1, 1]$ and creates IP in the positive Stokes Q-direction when $\epsilon > 0$, in the negative Q-direction when $\epsilon < 0$ and no IP when $\epsilon = 0$. Ideally, the retardance $\Delta = 180°$, causing no crosstalk and only changing the signs of Stokes U and V. For other values, an incident Stokes U-signal is converted into Stokes V and vice versa. We use this definition of the retardance for the HWP as well as the other groups containing mirrors, so that we can use the same M_{com} for these component groups. This is only possible because M4, the UT, and the derotator are comprised of an odd number of mirrors; for an even number of mirrors, the signs of Stokes U and V do not change and the ideal Δ would be 0° with our definition. The diattenuation ϵ and retardance Δ depend on the angle of incidence and the wavelength of the light and, for the mirrors, can be computed from the Fresnel equations.

As outlined in Sect. 2.3.2, the effects of the diattenuation and retardance of the optical path downstream of the derotator are negated by the double difference and use of the P0-90 analyzer set, respectively. Therefore, when including the double difference in our mathematical description (see below), $M_{\mathrm{CI,L/R}}$ only needs to describe the combination of the beamsplitter plate and the left or right linear polarizer of the P0-90 analyzer set. To this end, we use Eq. (2.20), but set the transmission of the total intensity equal to $^1/_2$ and the retardance Δ equal to 0°:

$$M_{\mathrm{CI,L/R}} = \frac{1}{2}\begin{bmatrix} 1 & \pm d & 0 & 0 \\ \pm d & 1 & 0 & 0 \\ 0 & 0 & \sqrt{1-d^2} & 0 \\ 0 & 0 & 0 & \sqrt{1-d^2} \end{bmatrix}, \tag{2.21}$$

where d is the diattenuation of the polarizers that accounts for their imperfect extinction ratios. The plus-sign (minus-sign) in Eq. (2.21) is used for the left (right) polarizer with the vertical (horizontal) transmission axis.

Because IRDIS uses a non-polarizing beamsplitter with polarizers, rather than a polarizing beamsplitter or Wollaston prism, the transmission of the total intensity of $M_{\mathrm{CI,L/R}}$

should in reality be set to $^1/_4$ rather than $^1/_2$. However, in practice the reference flux measurements are taken with the polarizers inserted, but are generally not multiplied by a factor 2 to account for the loss of flux. We therefore choose to set the transmission of the total intensity to $^1/_2$ to prevent accidental (relative) photometric errors.

As the final step, we compute the double-difference Stokes Q or U and the corresponding double-sum intensity I_Q or I_U from the Mueller matrix description of the optical path. For this, we first compute $\boldsymbol{S}_{\mathrm{det,L}}$ and $\boldsymbol{S}_{\mathrm{det,R}}$ from Eq. (2.17) using $+d$ and $-d$, respectively, in Eq. (2.21). We then obtain $I_{\mathrm{det,L}}$ and $I_{\mathrm{det,R}}$ from the first element of $\boldsymbol{S}_{\mathrm{det,L}}$ and $\boldsymbol{S}_{\mathrm{det,R}}$. Subsequently, we use $I_{\mathrm{det,L}}$ and $I_{\mathrm{det,R}}$ to compute the single differences $X^{\pm}$ and corresponding single sums $I_{X^{\pm}}$ from Eqs. (2.6) and (2.7), respectively. After computing the single difference and single sum for two measurements, we compute the double-difference X and corresponding double-sum I_X (see Eqs. (2.8) and (2.9), respectively) as:

$$X = \frac{1}{2}\left[X^{+}(p^{+}, a^{+}, \theta^{+}_{\mathrm{HWP}}, \theta^{+}_{\mathrm{der}}) - X^{-}(p^{-}, a^{-}, \theta^{-}_{\mathrm{HWP}}, \theta^{-}_{\mathrm{der}})\right], \tag{2.22}$$

$$I_X = \frac{1}{2}\left[I_{X^{+}}(p^{+}, a^{+}, \theta^{+}_{\mathrm{HWP}}, \theta^{+}_{\mathrm{der}}) + I_{X^{-}}(p^{-}, a^{-}, \theta^{-}_{\mathrm{HWP}}, \theta^{-}_{\mathrm{der}})\right], \tag{2.23}$$

where we explicitly show that $X^{\pm}$ and $I_{X^{\pm}}$ are functions of the parallactic, altitude, HWP, and derotator angles of the first (superscript +) and second (superscript −) measurement. Finally, we compute the normalized Stokes parameter x from Eq. (2.10).

The rotation laws of the derotator and HWP in field- and pupil-tracking mode are such that for an ideal optical system, X (or x) in the instrument reference frame would correspond to Q_{in} (q_{in}) and U_{in} (u_{in}) in the celestial reference frame for HWP switch angle combinations $[0°, 45°]$ and $[22.5°, 67.5°]$, respectively[1]. However, the optical system is not ideal. We therefore need to determine the model parameters of the five component group Mueller matrices (ϵ's, Δ's, and d) and the HWP and derotator offset angles δ_{HWP} and δ_{der} (see Fig. 2.2). When we have the values of these model parameters, we can mathematically describe any measurement and invert the equations to derive $\hat{\boldsymbol{S}}_{\mathrm{in}}$, the estimate of the true incident Stokes vector $\boldsymbol{S}_{\mathrm{in}}$.

2.5 Instrumental polarization effects of instrument downstream of M4

2.5.1 Calibration measurements and determination of model parameters

With the Mueller matrix model of the telescope and instrument defined, we can now determine the model parameters describing the optical path downstream of M4. To this end, we have taken measurements with the internal light source (see Fig. 2.2) using the Y-, J-, H-, and K_s-band filters. On August 15, 2015, a total of 528 exposures were taken with the calibration polarizer inserted, injecting light that is nearly 100% linearly polarized

[1]For pupil-tracking observations this is true since January 22, 2019, when the new HWP rotation law was implemented (see also Chapter 4).

in the vertical direction (in the positive Q-direction in the instrument reference frame). The derotator and HWP were rotated between the exposures with $\theta_{\rm der}$ ranging from 0° to 90° and $\theta_{\rm HWP}$ ranging from 0° to 101.25° (varying step sizes). This data, hereafter called the polarized source measurements, is used to determine for each broadband filter the retardances of the derotator and HWP ($\Delta_{\rm der}$ and $\Delta_{\rm HWP}$), the offset angles of the derotator and HWP ($\delta_{\rm der}$ and $\delta_{\rm HWP}$), and the diattenuation of the polarizers (d).

In addition, on June 12 and 13, 2016, a total of 400 exposures were taken without the calibration polarizer inserted, so that almost completely unpolarized light was injected. The derotator and HWP were rotated between the exposures with $\theta_{\rm der}$ and $\theta_{\rm HWP}$ ranging from 0° to 101.25° with a step size of 11.25°. This data, hereafter called the unpolarized source measurements, is used to fit for each broadband filter the diattenuations of the derotator and HWP ($\epsilon_{\rm der}$ and $\epsilon_{\rm HWP}$). The light injected is actually weakly polarized, because it is reflected off M4 before reaching the HWP. We therefore also fit the injected normalized Stokes parameters $q_{\rm in,unpol}$ and $u_{\rm in,unpol}$.

We pre-process the data by applying dark subtraction, flat fielding, and bad-pixel correction according to Paper I. Subsequently, we construct double-difference and double-sum images from Eqs. (2.8) and (2.9), respectively, using pairs of exposures with the same $\theta_{\rm der}$ and with $\theta^{+}_{\rm HWP}$ (first measurement) and $\theta^{-}_{\rm HWP}$ (second measurement) differing 45°. In this case the images do not always correspond to Q-, U-, I_Q-, and I_U-images in the instrument reference frame, because HWP angles different from 0°, 45°, 22.5°, and 67.5° have been used as well. The only model parameter that cannot be determined from these double-difference and double-sum images is the derotator diattenuation $\epsilon_{\rm der}$, because with the constant derotator angle the derotator's induced polarization is removed in the double difference. Therefore, the unpolarized source measurements are used to create additional double-difference and double-sum images by pairing exposures with the same $\theta_{\rm HWP}$ (rather than $\theta_{\rm der}$) and with $\theta^{+}_{\rm der}$ (first measurement) and $\theta^{-}_{\rm der}$ (second measurement) differing 45°.

The flux in most of the produced images is not uniform, but displays a gradient (for a detailed description see Appendix 2.B). To take into account the resulting uncertainty in the normalized Stokes parameters, we compute the median of the double-difference and double-sum images in nine apertures (100 pixel radii, arranged 3×3) located throughout almost the complete frame. Subsequently, we calculate the normalized Stokes parameters according to Eq. (2.10). This yields a total of 6696 data points with nine data points for every derotator and HWP angle combination. We determine the model parameters based on all of these data points together so that our model is valid over the complete field of view.

To describe the measurements, we use Eq. (2.10) and insert the model equations of Sect. 2.4. This set of equations comprises the model function. We apply only the part of Eq. (2.17) without the UT and M4:

$$\begin{aligned} \boldsymbol{S}_{\rm det,L/R} = {} & M_{\rm CI,L/R}\, T(-\Theta_{\rm der})\, M_{\rm der}\, T(\Theta_{\rm der}) \\ & T(-\Theta_{\rm HWP})\, M_{\rm HWP}\, T(\Theta_{\rm HWP})\, \boldsymbol{S}_{\rm HWP}, \end{aligned} \tag{2.24}$$

where $\boldsymbol{S}_{\rm HWP}$ is the Stokes vector injected upstream of the HWP (in the instrument reference frame; see Fig. 2.2). For the polarized source measurements, it is difficult to discern

the diattenuation (due to the imperfect extinction ratio) of the calibration polarizer from that of the analyzer polarizers. Therefore, we assume the diattenuations of the calibration and analyzer polarizers to be identical and write $\boldsymbol{S}_{\mathrm{HWP}} = T(-\delta_{\mathrm{cal}})\,[1, d, 0, 0]^{\mathrm{T}}$, with δ_{cal} the offset angle of the calibration polarizer that we also fit from the measurements (see Fig. 2.2). For the unpolarized source measurements, the incident light is weakly polarized due to the reflection off M4. We therefore write $\boldsymbol{S}_{\mathrm{HWP}} = [1, q_{\mathrm{in,unpol}}, u_{\mathrm{in,unpol}}, 0]^{\mathrm{T}}$, with $q_{\mathrm{in,unpol}}$ and $u_{\mathrm{in,unpol}}$ the to-be-determined injected normalized Stokes parameters, assuming that no circularly polarized light is produced. We note that there are no degeneracies among the model parameters with the above definitions of $\boldsymbol{S}_{\mathrm{HWP}}$ because the derotator, HWP, calibration polarizer, and M4 each have their own independent (local) references frames.

With the description of the measurements complete, we determine the model parameters by fitting the model function to the data points using nonlinear least squares (for which we use sequential least squares programming as implemented in the Python function *scipy.optimize.minimize*). The HWP and derotator angles required for this are obtained from the headers of the FITS-files of the measurements (see Appendix 2.A). To prevent the values of ϵ_{HWP} and ϵ_{der} from being dominated by the polarized source measurements (which have larger residuals), we fit the data of the polarized and unpolarized source measurements sequentially and repeat the two fits until convergence. The graphs of the model fits including the residuals can be found in Appendix 2.C.

2.5.2 Results and discussion for internal source calibrations

The resulting values for the model parameters are shown in Table 2.1. The 1σ-uncertainties of the parameters are also tabulated and are computed from the residuals of fit using a linear approximation (see Appendix 2.E). For this calculation it was necessarily assumed that the determined model parameters are uncorrelated and that they do not contain systematic errors. The systematic errors are likely very small, because the residuals of fit are close to normally distributed (see Figs. 2.18–2.20).

To visualize the effect of the parameters determined from the polarized source measurements, we plot the measured and fitted degree of linear polarization of the H-band polarized source measurements as a function of HWP and derotator angle in Fig. 2.3. We recall that the data points created in Sect. 2.5.1 are normalized Stokes parameters computed from the double difference and double sum using pairs of exposures with $\theta^{+}_{\mathrm{HWP}}$ (first exposure) and $\theta^{-}_{\mathrm{HWP}}$ (second exposure) differing 45°. The degree of linear polarization (see Eq. (2.4)) is computed from pairs of data points with values for $\theta^{+}_{\mathrm{HWP}}$ (and therefore also values for $\theta^{-}_{\mathrm{HWP}}$) that differ 22.5° or 67.5° from each other. The effect of the gradient in the measured flux (see Appendix 2.B) appears to be limited, because the nine data points of each HWP and derotator angle combination in Fig. 2.3 are relatively close together, within a few percent. For these polarized source measurements, which have nearly 100% polarized light incident, we interpret the degree of linear polarization as the polarimetric efficiency, that is, the fraction of the incident or true linear polarization that is actually measured.

For an ideal instrument, the polarimetric efficiency is 100%. However, in Fig. 2.3 a dramatic decrease in polarimetric efficiency is seen around $\theta_{\mathrm{der}} = 45°$, reaching values as

Table 2.1: Determined parameters and their errors of the part of the model describing the instrument downstream of M4 in the *Y*-, *J*-, *H*-, and K_s-band. The retardances of the derotator and HWP (Δ_{der} and Δ_{HWP}, respectively) cause the strongest instrumental polarization effects (i.e., crosstalk) and are indicated in red. The polarizer diattenuations d correspond to extinction ratios (computed as $(1+d)/(1-d)$) of 100:1, 189:1, 447:1, and 126:1 in the *Y*-, *J*-, *H*-, and K_s-band, respectively.

Parameter		BB_Y	BB_J	BB_H	BB_K_s
ϵ_{HWP}		$-0.00021 \pm 2 \cdot 10^{-5}$	$-0.000433 \pm 4 \cdot 10^{-6}$	$-0.000297 \pm 7 \cdot 10^{-6}$	$-0.000415 \pm 8 \cdot 10^{-6}$
Δ_{HWP}	(°)	184.2 ± 0.2	177.5 ± 0.2	170.7 ± 0.1	177.6 ± 0.1
δ_{HWP}	(°)	-0.6132 ± 0.0007	-0.6132 ± 0.0007	-0.6132 ± 0.0007	-0.6132 ± 0.0007
ϵ_{der}		$-0.00094 \pm 2 \cdot 10^{-5}$	$-0.008304 \pm 6 \cdot 10^{-6}$	$-0.002260 \pm 7 \cdot 10^{-6}$	$0.003552 \pm 7 \cdot 10^{-6}$
Δ_{der}	(°)	126.1 ± 0.1	156.1 ± 0.1	99.32 ± 0.06	84.13 ± 0.05
δ_{der}	(°)	$0.50007 \pm 6 \cdot 10^{-5}$	$0.50007 \pm 6 \cdot 10^{-5}$	$0.50007 \pm 6 \cdot 10^{-5}$	$0.50007 \pm 6 \cdot 10^{-5}$
d		0.9802 ± 0.0004	0.9895 ± 0.0002	0.9955 ± 0.0002	0.9842 ± 0.0003
$q_{\mathrm{in,unpol}}$	(%)	1.789 ± 0.001	1.2150 ± 0.0003	0.9480 ± 0.0005	0.8352 ± 0.0006
$u_{\mathrm{in,unpol}}$	(%)	0.061 ± 0.002	0.0585 ± 0.0004	0.0406 ± 0.0007	0.0589 ± 0.0008
δ_{cal}	(°)	-1.542 ± 0.001	-1.542 ± 0.001	-1.542 ± 0.001	-1.542 ± 0.001

low as 5%. This low efficiency indicates severe loss of polarization signal and is due to the derotator retardance strongly deviating from the ideal value of 180°. With $\Delta_{\rm der} = 99.32°$, the derotator acts almost as a quarter-wave plate for which $\Delta = 90°$. Around $\theta_{\rm der} = 45°$, the derotator therefore produces strong crosstalk and almost all incident linearly polarized light is converted into circularly polarized light to which the P0-90 analyzer set is not sensitive. We already encountered the strongly varying polarimetric efficiency in Fig. 3 of Paper I.

The retardance of the HWP has a much smaller effect on the polarimetric efficiency than the retardance of the derotator because $\Delta_{\rm HWP} = 170.5°$ in the H-band, relatively close to the ideal value of 180°. In Fig. 2.3 the effect of the HWP retardance is visible as the changing skewness of the fitted curves for different HWP angles. The offset angles $\delta_{\rm HWP}$, $\delta_{\rm der}$, and $\delta_{\rm cal}$ also contribute a small shift of the curves. Finally, the diattenuation of the polarizers d determines the maximum values of the curves around $\theta_{\rm der} = 0°$ and $\theta_{\rm der} = 90°$.

The crosstalk produced by the derotator and HWP not only deteriorates the polarimetric efficiency, but also induces an offset in the measurement of the angle of linear polarization, as is illustrated by the varying Stokes Q- and U-images in Fig. 3 of Paper I. Figure 2.4 shows the measured and fitted offsets of the angle of linear polarization corresponding to the curves of Fig. 2.3. The offsets are computed as the actually measured angle of linear polarization (see Eq. (2.5)) minus the angle that would be measured in case the optical system were ideal. Figure 2.4 shows that the measured angle of linear polarization varies around the ideal angle, with a maximum deviation of 34° and the strongest rotation rate around $\theta_{\rm der} = 45°$.

Fig. 2.5 shows the polarimetric efficiency in the four broadband filters Y, J, H, and K_s. The curves displayed are for $\theta^+_{\rm HWP} = 0°$ and 22.5° and the derotator angle ranges from 0° to 180° (the curves repeat for $\theta_{\rm der} > 180°$). We have also taken measurements in the range $0° \leq \theta_{\rm der} \leq 180°$ (not shown) that confirm the curves for $\theta_{\rm der} > 90°$. However, we do not use these measurements to determine the model parameters, because neutral density filters were inserted which appear to depolarize the light by a few percent. Because the nine data points of each HWP and derotator angle combination are relatively close together, we conclude that the effect of the gradient in the measured flux is small for all filters.

From Fig. 2.5 it follows that for all filters, the efficiency is minimum around $\theta_{\rm der} = 45°$ and $\theta_{\rm der} = 135°$. The minimum values of the curves differ substantially among the filters, because the derotator retardance varies strongly with wavelength (see Table 2.1). The exact shape and minimum values of the curves depend on the HWP angles used (see Fig. 2.3) because the HWP retardance deviates slightly from the ideal value of 180° in all filters (strongest in the H-band; see Table 2.1). The asymmetry with respect to $\theta_{\rm der} = 90°$ visible in Fig. 2.5 is also due to the non-ideal HWP retardance.

The absolute minimum polarimetric efficiency is lowest in the H-band for which it is 5%. Also the K_s-band (efficiency $\geq$ 7%) shows a strongly varying performance, while in the Y-band ($\geq$54%) and especially in the J-band ($\geq$89%) the polarimetric efficiency is much less affected by the derotator angle. The polarimetric efficiency during science observations, and an observation strategy in which the derotator angle is optimized to prevent observing at a low polarimetric efficiency are discussed in Paper I.

Figure 2.6 shows the offsets of the angle of linear polarization corresponding to the

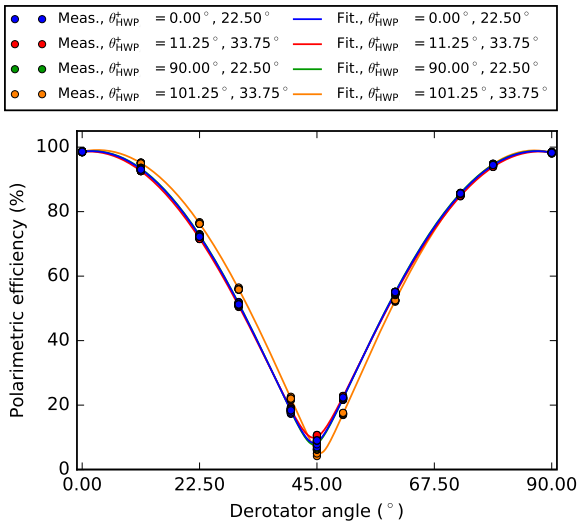


Figure 2.3: Measured and fitted polarimetric efficiency of the instrument downstream of M4 as a function of HWP and derotator angle in the *H*-band. The legend only shows the θ^+_{HWP}-values of each data point or curve; it is implicit that the corresponding values for θ^-_{HWP} differ 45° from those of θ^+_{HWP}. The measurement points and fitted curves for $\theta^+_{\mathrm{HWP}} = 0.00°, 22.50°$ (blue) and $\theta^+_{\mathrm{HWP}} = 90.00°, 22.50°$ (green) overlap.

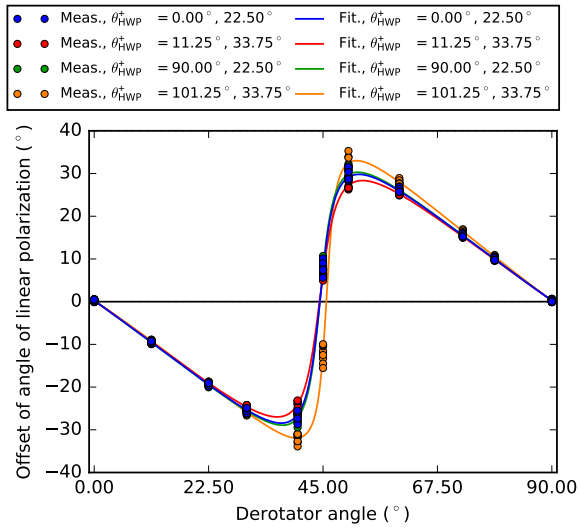


Figure 2.4: Measured and fitted offset of the angle of linear polarization induced by the instrument downstream of M4 as a function of HWP and derotator angle in the *H*-band. The legend only shows the θ^+_{HWP}-values of each data point or curve; it is implicit that the corresponding values for θ^-_{HWP} differ 45° from those of θ^+_{HWP}. The measurement points and fitted curves for $\theta^+_{\mathrm{HWP}} = 0.00°, 22.50°$ (blue) and $\theta^+_{\mathrm{HWP}} = 90.00°, 22.50°$ (green) overlap.

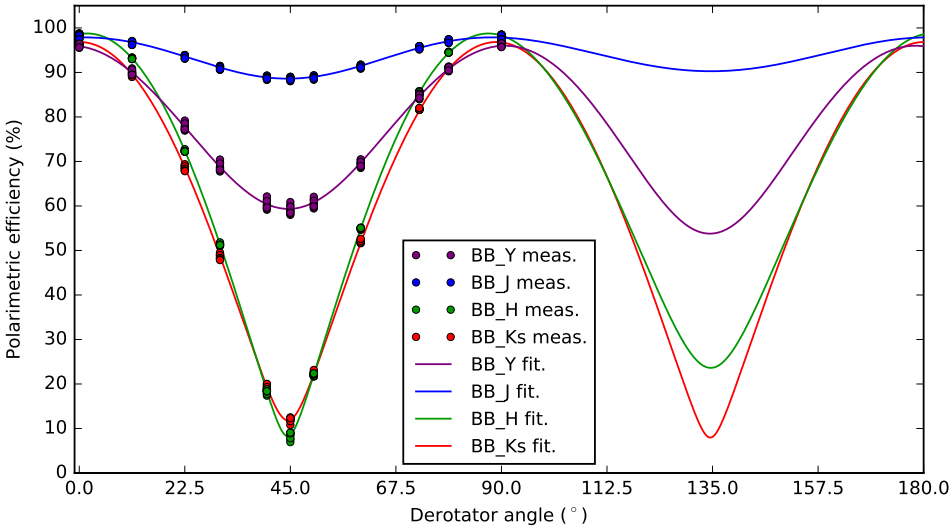


Figure 2.5: Measured and fitted polarimetric efficiency of the instrument downstream of M4 with $\theta^{+}_{\mathrm{HWP}} = 0°, 22.5°$ (and therefore $\theta^{-}_{\mathrm{HWP}} = 45°, 67.5°$) as a function of derotator angle in the Y-, J-, H-, and K_s-band.

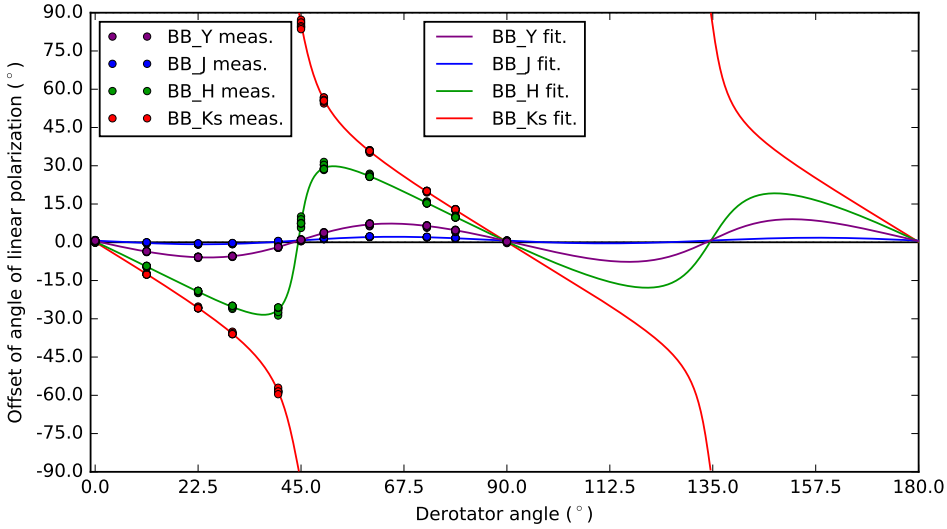


Figure 2.6: Measured and fitted offset of angle of linear polarization induced by the instrument downstream of M4 with $\theta^{+}_{\mathrm{HWP}} = 0°, 22.5°$ (and therefore $\theta^{-}_{\mathrm{HWP}} = 45°, 67.5°$) as a function of derotator angle in the Y-, J-, H-, and K_s-band.

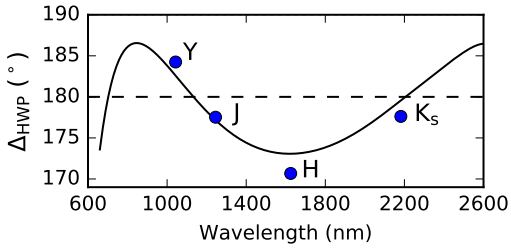


Figure 2.7: HWP retardance as a function of wavelength as specified by the manufacturer[2] compared to the determined HWP retardance ($\Delta_{\rm HWP}$) in the Y-, J-, H-, and K_s-band.

polarimetric efficiency curves of Fig. 2.5. Also in this case the non-ideal HWP retardance causes an asymmetry with respect to $\theta_{\rm der} = 90°$ and variations of the exact shape and maximum values of the curves with HWP angle (see Fig. 2.4). While the variation around the ideal value is marginal in the J-band, with a maximum deviation of 4°, the offset of the angle of linear polarization is $\leq 11°$ in the Y-band and $\leq 34°$ in the H-band. For the K_s-band, the angle of linear polarization does not even return to the ideal value around $\theta_{\rm der} = 45°$ and $\theta_{\rm der} = 135°$, but continues rotating beyond $\pm 90°$ (where a rotation of $+90°$ is indistinguishable from $-90°$).

To validate the determined HWP retardances in the four filters, the values are compared to the retardance as specified by the manufacturer in Fig. 2.7. The error bars on the determined HWP retardances are smaller than the size of the symbols used. It follows that the determined HWP retardances are accurate, since they follow the general shape of the curve and are well within the 4% manufacturing tolerance as specified by the manufacturer[2].

For the unpolarized source measurements, the light incident on the HWP is primarily linearly polarized in the positive Q-direction as follows from the determined values of $q_{\rm in,unpol}$ and $u_{\rm in,unpol}$. The degree of linear polarization decreases with increasing wavelength (from the Y- to K_s-band). This polarization signal must be IP from M4 that is in between the internal light source and the HWP (see Fig. 2.2). The determined values of $q_{\rm in,unpol}$ are also in good agreement with the determined diattenuations of M4 (see Fig. 2.10 and the discussion in Sect. 2.6.2), and shows that the light from the internal light source is almost completely unpolarized until it reaches M4.

The polarization signals induced by the HWP and the derotator are very small, since $\epsilon_{\rm HWP}$ and $\epsilon_{\rm der}$ are very close to the ideal value of 0 in all filters (with the largest deviation for the derotator in the J-band; see Table 2.1). The low diattenuation of the derotator is as expected, because its main surface coating is protected silver that is highly reflective. However, considering that the derotator has its plane of incidence horizontal when $\theta_{\rm der} = 0°$, one would naively expect $\epsilon_{\rm der}$ to be positive in all filters (producing polarization in the positive Q-direction) while it turns out to be negative (producing polarization in the negative Q-direction) in three of the four filters. This behavior of the diattenuation with

[2] B. Halle Nachfl. GmbH, http://www.b-halle.de/products/Retarders/Achromatic_Retarders.html, consulted November 21, 2017.

wavelength is likely due to the complex combination of coatings on the derotator mirrors.

The strong crosstalk produced by the derotator in the H- and K_s-band can also be used to our advantage. In these filters, the retardance of the derotator is close to that of a quarter-wave plate (close to 90°; see Table 2.1). At $\theta_{\rm der} = 45°$ and 135°, the derotator does not only convert almost all incident linearly polarized into circularly polarized light (problematic for the polarimetric efficiency), but it also converts almost all incident circularly polarized light into linearly polarized light that can then be measured by the P0-90 analyzer set. Hence by using the derotator as a quarter-wave plate to modulate Stokes V, we can measure circularly polarized light, for example from molecular clouds. The development of a technique to measure circularly polarized light with IRDIS is beyond the scope of this chapter and is left for future work (see Chapter 6).

2.6 Instrumental polarization effects of telescope and M4

2.6.1 Calibration measurements and determination of model parameters

Now that we have a validated description of the optical path downstream of M4, we can complete our instrument model by determining the model parameters describing the UT and M4 (see Fig. 2.2). On June 15, 2016, we therefore observed the unpolarized standard star HD 176425 (Turnshek et al. 1990; $0.020 \pm 0.009\%$ polarized in the B-band) at different telescope altitude angles using the four broadband filters Y, J, H, and K_s under program ID 60.A-9800(S). Because M1 and M3 were re-aluminized between April 3 and April 16, 2017, we repeated the calibration measurements on August 21, 2018 with the unpolarized star HD 217343 under program ID 60.A-9801(S). Although HD 217343 is not an unpolarized standard star, it is located at only 31.8 pc from Earth (Gaia Collaboration et al., 2018) and therefore the probability of it being polarized by interstellar dust is very low (Leroy, 1993, 1999).

The two data sets are used to determine the diattenuations of the UT and M4 ($\epsilon_{\rm UT}$ and $\epsilon_{\rm M4}$) before and after the re-aluminization of M1 and M3. The retardances of the UT and M4 ($\Delta_{\rm UT}$ and $\Delta_{\rm M4}$) are assumed to be equal for both data sets and are computed analytically because their limited effect does not justify dedicated calibration measurements (see Sect. 2.6.2). In addition the degree of linear polarization of polarized standard stars at near-infrared wavelengths is too low to accurately determine the retardances, and observations of the polarized daytime sky (see e.g., Harrington et al., 2011; de Boer et al., 2014; Harrington et al., 2017) are very time consuming.

During the observations of HD 176425 (2016), the derotator was fixed with its plane of incidence horizontal ($\theta_{\rm der} = 0°$) to ensure a polarimetric efficiency close to 100%. The adaptive optics were turned off (open-loop) to reach a large total photon count per detector integration time, minimizing read-out noise. The calibration polarizer was out of the beam. For every filter, 10 HWP cycles (measurements with $\theta_{\rm HWP} = 0°$ and 45° for Stokes Q, and with $\theta_{\rm HWP} = 22.5°$ and 67.5° for Stokes U; see Sect. 2.3.1) were taken at different altitude and parallactic angle combinations. In this way, the effect of the

diattenuations of the UT and M4 and a possible (but unlikely) stellar polarization signal can be distinguished when fitting the data to the model. The HWP cycles were kept short (~140 s) to limit the parallactic and altitude angle variations of the data points themselves.

For the observations of HD 217343 (2018) we took 12 HWP cycles per filter with a similar instrument setup as used for HD 176425. The most important difference between the two setups is that this time we (accidentally) observed in field-tracking mode. In this mode the derotator is rotating continuously and therefore the polarimetric efficiency varies during the measurements. Because we did not optimize the derotator angle as recommended (see Paper I), the polarimetric efficiency reached a value as low as 31% for the last measurement in the K_s-band.

Both data sets are processed by applying dark subtraction, flat fielding, bad-pixel correction, and centering with a Moffat function as described in Paper I. Subsequently, we construct the double-difference Q- and U-images from Eq. (2.8) and the double-sum I_Q- and I_U-images from Eq. (2.9). Finally, we calculate the normalized Stokes parameters q and u by dividing the sum in an aperture in the Q- and U-images by the sum in the same aperture in the corresponding I_Q- and I_U-images (see Eq. (2.10)). For an elaboration on the extraction of the normalized Stokes parameters and the selected aperture sizes see Appendix 2.D.

To describe the measurements, we use Eq. (2.10) with the model equations of Sect. 2.4 inserted (together the model function). We use the complete Eq. (2.17) and fill in the values of the determined parameters ϵ_{HWP} to d from Table 2.1. We compute the retardances of the UT (actually M3 since M1 and M2 are rotationally symmetric) and M4 using the Fresnel equations with the complex refractive index of aluminum obtained from Rakić (1995). This computation needs to be performed before determining the diattenuations, because the retardance of M4 affects the measurement of the IP produced by the UT. Because we observed unpolarized (standard) stars, we write $\boldsymbol{S}_{\mathrm{in}} = [1, 0, 0, 0]^{\mathrm{T}}$.

We determine the diattenuations of the UT and M4 independently for both data sets by fitting the model function to the data points using nonlinear least squares. The parallactic, altitude, HWP, and derotator angles required for this are obtained from the headers of the FITS-files of the measurements (see Appendix 2.A). We have tested fitting the incident Stokes vectors in addition to the diattenuations (writing $\boldsymbol{S}_{\mathrm{in}} = [1, q_{\mathrm{in}}, u_{\mathrm{in}}, 0]^{\mathrm{T}}$), and found that the degree of linear polarization of the stars is indeed insignificant ($< 0.1\%$) in all filters. We therefore choose not to fit the incident Stokes vectors and assume the stars to be completely unpolarized. Graphs of the model fits and the residuals can be found in Appendix 2.D.

2.6.2 Results and discussion for unpolarized star calibrations

The determined diattenuations and calculated retardances of the UT and M4 for both data sets are shown in Table 2.2. The listed 1σ-uncertainties of the diattenuations are computed from the residuals of fit (see Appendix 2.E) under the same assumptions as described in Sect. 2.5.2.

The calculated values of Δ_{UT} and Δ_{M4} are close to the ideal value of 180° and therefore the crosstalk produced by the UT and M4 is very limited. In all filters, the combined polarimetric efficiency of the UT and M4 is $> 98\%$ and the corresponding offset of the

Table 2.2: Determined diattenuations with their errors and computed retardances of the part of the model describing the telescope and M4 in the Y-, J-, H-, and K_s-band. The second column shows when the parameters are valid, i.e., before and/or after the re-aluminization of M1 and M3 that took place between April 3 and April 16, 2017. The diattenuations of the UT and M4 that are valid before April 16, 2017 are determined from the observations of HD 176425 in 2016, and those valid after April 16, 2017 are determined from the observations of HD 217343 in 2018.

Parameter	Valid before or after April 16, 2017	BB_Y	BB_J	BB_H	BB_K_s
ϵ_{UT}	before	0.0236 ± 0.0002	0.0167 ± 0.0001	$0.01293 \pm 8 \cdot 10^{-5}$	0.0106 ± 0.0003
	after	0.0175 ± 0.0003	0.0121 ± 0.0002	0.0090 ± 0.0001	0.0075 ± 0.0005
ϵ_{M4}	before	0.0182 ± 0.0002	0.0128 ± 0.0001	$0.00985 \pm 8 \cdot 10^{-5}$	0.0078 ± 0.0003
	after	0.0182 ± 0.0003	0.0130 ± 0.0002	0.0092 ± 0.0001	0.0081 ± 0.0005
Δ_{UT} (°)	before and after	171.9	173.4	175.0	176.3
Δ_{M4} (°)	before and after	171.9	173.4	175.0	176.3

angle of linear polarization is at most a few tenths of a degree (largest effect in the Y-band). Due to the limited crosstalk, any realistic deviation of the real retardances from the computed ones results in very small errors only. This also implies that the systematic error on $\epsilon_{\rm UT}$ due to using an analytical rather than a measured value of $\Delta_{\rm M4}$ is very small.

To understand the effect of the determined diattenuations, we plot the measured and fitted degree of linear polarization (see Eq. (2.4)) as a function of telescope altitude angle for the observations of HD 176425 (2016) and HD 217343 (2018) in Fig. 2.8 and 2.9, respectively. The degree of linear polarization can in this case be interpreted as the IP of the UT and M4. The figures also show analytical curves that are constructed by computing the diattenuations from the Fresnel equations and assuming that the aluminum coatings of the UT (M3) and M4 have the same properties. The error bars on the measurements are calculated as half the difference between the degree of linear polarization determined from apertures with radii 50 pixels larger and smaller than that used for the data points themselves (see Appendix 2.D). The error bars show the uncertainty in the degree of linear polarization due to the dependency of the measured values on the chosen aperture radius. The uncertainty is small for all measurements except for those of HD 176425 (2016) taken in the K_s-band. The latter measurements are less certain because of difficulties in removing the thermal background signal (see Appendix 2.D). We note that for science observations the telescope altitude angle is restricted to $30° \leq a \leq 87°$.

Figure 2.8 shows that the IP increases with decreasing altitude angle and that before the re-aluminization of M1 and M3 the maximum IP (at $a = 30°$) is equal to approximately 3.5%, 2.5%, 1.9%, and 1.5% in the Y-, J-, H-, and K_s-band, respectively. The corresponding minimum values (at $a = 87°$) are 0.58%, 0.42%, 0.33%, and 0.29%, respectively. Ideally, we would expect the IP of M3 to completely cancel that of M4 when the reflection planes of the mirrors are crossed at $a = 90°$ (analytical curves). However, because the determined $\epsilon_{\rm UT}$ and $\epsilon_{\rm M4}$ are not identical, this is not the case. This discrepancy is probably caused by differences in the coating or aluminum oxide layers of the mirrors (see van Harten et al., 2009).

Figure 2.9 shows that the IP after the re-aluminization of M1 and M3 is significantly smaller than before. The maximum values (at $a = 30°$) are now equal to approximately 3.0%, 2.1%, 1.5%, and 1.3% in the Y-, J-, H-, and K_s-band, respectively, and the corresponding minimum values (at $a = 87°$) are 0.18%, 0.12%, 0.07%, and 0.06%, respectively. This decrease of IP is due to the lower diattenuation of the UT (see Table 2.2). In fact, after re-aluminization the diattenuation of the UT is comparable to that of M4, leading to almost complete cancellation of the IP at 90° altitude angle[3]. Because the measurements were taken in field-tracking mode, the data points shown have been corrected for the polarimetric efficiency (the residuals for the two data points in the K_s-band close to $a = 30°$ are considerably enhanced because of this correction). Finally, during the observations of HD 217343 we did not switch filter after every HWP cycle as we did

[3]ZIMPOL (Schmid et al., 2018), the visible imaging polarimeter of SPHERE, has an additional HWP in between M3 and M4 that is used to rotate the IP produced by M3 such that it is ideally completely canceled by M4 at any altitude angle (Roelfsema et al., 2010). However, also at visible wavelengths the diattenuations of M3 and M4 were probably not equal before the re-aluminization of M1 and M3, so that some IP originating from the UT and M4 must have remained for ZIMPOL. After the re-aluminization, the IP of ZIMPOL is most likely close to zero because the diattenuations are much more comparable.

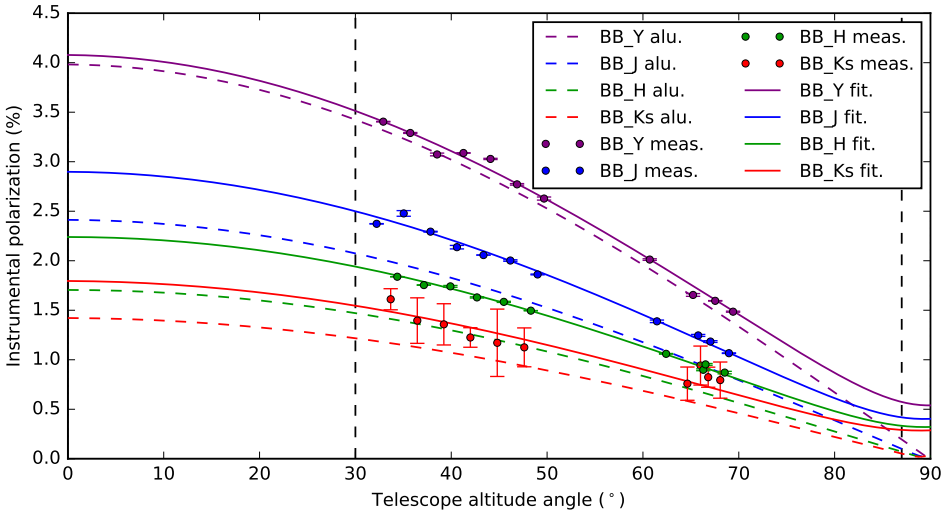


Figure 2.8: Analytical (aluminum), measured (including error bars), and fitted instrumental polarization (IP) of the telescope and M4 as a function of telescope altitude angle in the Y-, J-, H-, and K_s-band from the measurements of HD 176425 taken in 2016 before the re-aluminization of M1 and M3. For science observations the telescope altitude angle is restricted to $30° \leq a \leq 87°$.

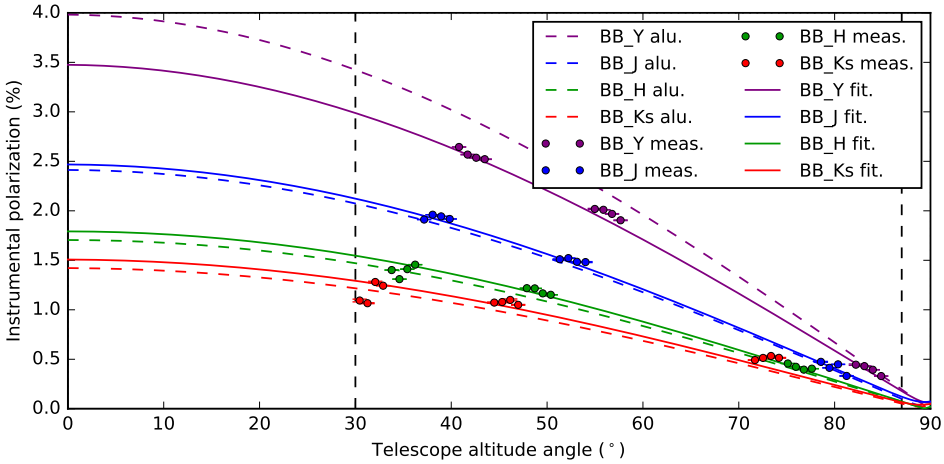


Figure 2.9: Analytical (aluminum), measured (including error bars) and fitted instrumental polarization (IP) of the telescope and M4 as a function of telescope altitude angle in the Y-, J-, H-, and K_s-band from the measurements of HD 217343 taken in 2018 after the re-aluminization of M1 and M3. For science observations the telescope altitude angle is restricted to $30° \leq a \leq 87°$.

for HD 176425 (compare Figs. 2.8 and 2.9). Therefore the measurement points are less spread out over the range of altitude angles, making them constrain the model function somewhat less.

The IP created by the UT or M4 separately, as determined from the various measurements, is shown as a function of central wavelength of the Y-, J-, H-, and K_s-band in Fig. 2.10. The IP created is equal to the diattenuation of the mirror(s) when assuming that the incident light is completely unpolarized (see Eq. (2.20)). Figure 2.10 shows that before the re-aluminization of M1 and M3, the IP of the UT is significantly larger than that of M4 (on-sky 2016). After the re-aluminization, the IP of the UT has decreased and differs less than 0.1% from that of M4 in all filters (on-sky 2018). This indicates that the coatings of M3 and M4 are much more similar after the re-aluminization. Between the observations of the unpolarized stars in 2016 and 2018, the IP of M4 (which has not been re-aluminized) differs less than 0.07% in all filters, showing that the diattenuation does not significantly change in time.

Figure 2.10 also shows the IP of M4 as determined from the unpolarized source measurements, that is, $q_{\text{in,unpol}}$ from Table 2.1 (ignoring $u_{\text{in,unpol}}$, which is close to zero in all filters). Clearly, the observations of the unpolarized stars are in good agreement with the measurements with the internal light source. The small differences among the values determined from the measurements of the unpolarized stars and the internal light source could be due to the different spectra of the stars and the internal light source, the calibration unit producing some polarization, or the finite precision of the measurements. Finally, Fig. 2.10 shows the IP produced by the UT or M4 as computed from the Fresnel equations (aluminum analytical). We conclude that the determined IP agrees well with the theoretical expectation.

2.7 Polarimetric accuracy of instrument model

In this section we determine for each broadband filter the total polarimetric accuracy of our completed instrument model and compare it to the aims we set in Sect. 2.1. As the first step to calculate the accuracy of the model, we compute the accuracies of fitting the model parameters to the calibration data. These accuracies of fit are calculated as the corrected sample standard deviation of the residuals in Appendix 2.E and show the random errors of the measurements. The systematic errors of the model fits are likely small, because the residuals of fit are close to normally distributed (see Figs. 2.18–2.20 and 2.23–2.25).

To compute the total polarimetric accuracy from the residuals of fit, we need to compute the absolute and relative polarimetric accuracies s_{abs} and s_{rel} (see Eqs. (2.11) and (2.12)). For the absolute polarimetric accuracy we compute separate values before and after the re-aluminization of M1 and M3. The absolute polarimetric accuracy is calculated as $s_{\text{abs}} = \sqrt{(s_{\text{unpol}}^2 + s_{\text{star}}^2)}$, with s_{unpol} the accuracy of fit of the unpolarized source measurements and s_{star} the accuracy of fit of the observations of the unpolarized star under consideration (see Appendix 2.E). We take the relative polarimetric accuracy s_{rel} (valid before and after the re-aluminization) equal to the accuracy of fit of the polarized source measurements. The resulting absolute and relative polarimetric accuracies in the Y-, J-, H-, and K_s-band are shown in Table 2.3.

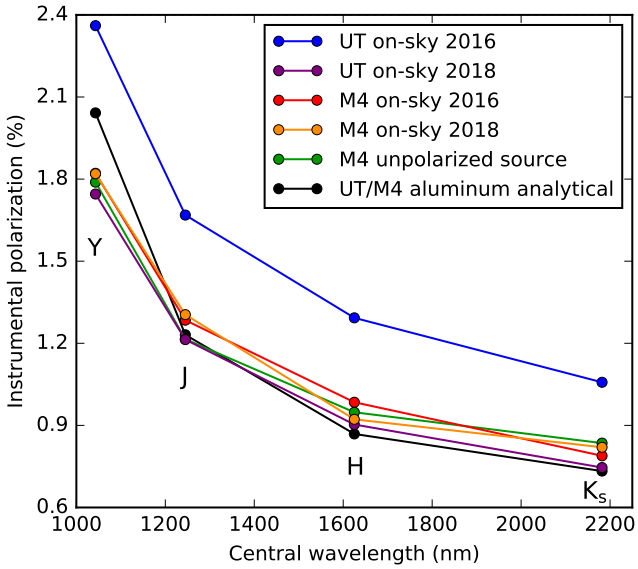


Figure 2.10: Instrumental polarization (IP) of the UT and M4 separately, as determined from the various measurements, versus central wavelength of the Y-, J-, H-, and K_s-band. The curves show the IP of the UT and M4 from the observations of the unpolarized stars HD 176425 (on-sky 2016) and HD 217343 (on-sky 2018), the IP of M4 from the unpolarized source measurements and the IP of the UT and M4 computed from the Fresnel equations (aluminum analytical).

From Table 2.3 we conclude that the absolute polarimetric accuracies before and after the re-aluminization of M1 and M3 are comparable and that the requirements on the absolute and relative polarimetric accuracies (≤0.1% and <1%, respectively) are met for all filters. The values of $s_{\rm abs}$ are consistent with the ~0.05% absolute difference among the independent estimates of the IP of M4 from the observations of the unpolarized stars and the unpolarized source measurements (see Fig. 2.10). Because the residuals of fit are close to normally distributed, the absolute and relative polarimetric accuracies can probably be improved by obtaining calibration measurements with a higher signal-to-noise ratio. However, the accuracy we attain when correcting science observations appears to be limited by systematic errors (see Sect. 2.8.4).

With the absolute and relative polarimetric accuracies calculated, we can now compute the total polarimetric accuracies in Stokes Q and U, $s_{\rm Q}$ and $s_{\rm U}$, respectively, as:

$$s_{\rm Q} = s_{\rm abs}\hat{I}_{Q,{\rm in}} + s_{\rm rel}\left|\hat{Q}_{\rm in}\right|, \tag{2.25}$$

$$s_{\rm U} = s_{\rm abs}\hat{I}_{U,{\rm in}} + s_{\rm rel}\left|\hat{U}_{\rm in}\right|, \tag{2.26}$$

where $\hat{I}_{Q,{\rm in}}$, $\hat{I}_{U,{\rm in}}$, $\hat{Q}_{\rm in}$, and $\hat{U}_{\rm in}$ are the measured Stokes I_Q, I_U, Q, and U incident on the telescope after correcting the instrumental polarization effects with the model (see

Table 2.3: Absolute and relative polarimetric accuracies in the Y-, J-, H-, and K_s-band. For the absolute polarimetric accuracy separate values have been calculated before and after the re-aluminization of M1 and M3 that ended on April 16, 2017.

Filter	$s_{\rm abs}$ (%) (before April 16, 2017)	$s_{\rm abs}$ (%) (after April 16, 2017)	$s_{\rm rel}$ (%)
BB_Y	0.062	0.068	0.73
BB_J	0.047	0.072	0.41
BB_H	0.026	0.030	0.58
BB_K_s	0.10	0.093	0.54

Sect. 2.8.1). Eqs. (2.25) and (2.26) are derived from Eqs. (2.11) and (2.12) by substituting $\hat{Q}_{\rm in}$ and $\hat{U}_{\rm in}$ for the true incident $Q_{\rm in}$ and $U_{\rm in}$. We can determine the total polarimetric accuracy in the degree and angle of linear polarization ($s_{\rm DoLP}$ and $s_{\rm AoLP}$) as:

$$s_{\rm DoLP} = \sqrt{\frac{\hat{q}_{\rm in}^2 {s_{\rm q}}^2 + \hat{u}_{\rm in}^2 {s_{\rm u}}^2}{\hat{q}_{\rm in}^2 + \hat{u}_{\rm in}^2}}, \tag{2.27}$$

$$s_{\rm AoLP} = \frac{\sqrt{\hat{u}_{\rm in}^2 {s_{\rm q}}^2 + \hat{q}_{\rm in}^2 {s_{\rm u}}^2}}{2\left(\hat{q}_{\rm in}^2 + \hat{u}_{\rm in}^2\right)}, \tag{2.28}$$

where $\hat{q}_{\rm in} = \hat{Q}_{\rm in} / \hat{I}_{Q,{\rm in}}$, $s_{\rm q} = s_{\rm Q} / \hat{I}_{Q,{\rm in}}$, $\hat{u}_{\rm in} = \hat{U}_{\rm in} / \hat{I}_{U,{\rm in}}$, and $s_{\rm u} = s_{\rm U} / \hat{I}_{U,{\rm in}}$. We have derived Eqs. (2.27) and (2.28) from Eqs. (2.4), (2.5), (2.25), and (2.26) by applying standard error propagation and assuming Gaussian statistics, zero uncertainty in $\hat{I}_{Q,{\rm in}}$ and $\hat{I}_{U,{\rm in}}$, and no correlation between $s_{\rm Q}$ and $s_{\rm U}$. In case $\hat{I}_{Q,{\rm in}}$ and $\hat{I}_{U,{\rm in}}$ contain substantial flux from the central star, $\hat{Q}_{\rm in}$, $\hat{U}_{\rm in}$, $s_{\rm Q}$, and $s_{\rm U}$ should be divided by the intensity from the source we are interested in (e.g., a circumstellar disk or substellar companion) when computing $s_{\rm DoLP}$ and $s_{\rm AoLP}$. We note that corrections need to be applied to Eqs. (2.27) and (2.28) in case the signal-to-noise ratio in the degree of linear polarization is very low, that is, lower than ~3 (see Sparks & Axon, 1999; Patat & Romaniello, 2006).

Table 2.4 shows the polarimetric accuracies of measuring the degree and angle of linear polarization of a 1% polarized substellar companion and a 30% polarized circumstellar disk in the Y-, J-, H-, and K_s-band before the re-aluminization of M1 and M3 (the results after the aluminization are comparable). The accuracies are computed from Eqs. (2.27) and (2.28) under the assumption that $\hat{I}_{Q,{\rm in}}$ and $\hat{I}_{U,{\rm in}}$ contain no starlight. The accuracies weakly depend on the angle of linear polarization of the incident light (the specific values of $\hat{q}_{\rm in}$ and $\hat{u}_{\rm in}$) and so the worst case is shown. From Table 2.4 it follows that for increasing degrees of linear polarization of the source, the error on the degree of linear polarization increases. For sources with a low degree of linear polarization (up to a few percent) the error is nearly equal to the absolute polarimetric accuracy $s_{\rm abs}$, while for sources with a high degree of linear polarization (several tens of percent) the contribution of the relative polarimetric accuracy $s_{\rm rel}$ dominates. Table 2.4 also shows that the error on the angle of linear polarization decreases with an increasing degree of linear polarization

Table 2.4: Polarimetric accuracy of measuring the degree and angle of linear polarization of a 1% polarized substellar companion and a 30% polarized circumstellar disk in the Y-, J-, H-, and K_s-band before the re-aluminization of M1 and M3. The results after the re-aluminization are comparable.

Filter	s_{DoLP} (%) 1% pol. companion	s_{AoLP} (°) 1% pol. companion	s_{DoLP} (%) 30% pol. disk	s_{AoLP} (°) 30% pol. disk
BB_Y	0.069	1.9	0.28	0.21
BB_J	0.051	1.4	0.17	0.13
BB_H	0.032	0.86	0.20	0.14
BB_K_s	0.11	3.0	0.26	0.20

of the source, because the polarization components Q and U are measured with a higher relative accuracy. This also means that for sources with a very low degree of linear polarization (~0.1%) the error on the angle of linear polarization can be as large as 10° or more.

Assuming that Gaussian statistics apply and that systematic errors are small, Table 2.4 shows that the polarization signal of a 1% polarized substellar companion can be measured in all filters with the required total polarimetric accuracy of ~0.1% in the degree of linear polarization and an accuracy of a few degrees in angle of linear polarization. For the 30% polarized circumstellar disk, the attainable accuracies in degree of linear polarization are below 0.3% in all filters, which is amply sufficient for quantitative polarimetry. For real measurements the attained accuracies are generally somewhat worse because of for example measurement noise and varying atmospheric conditions (see Sect. 2.8.4). In addition, the accuracy of measuring a circumstellar disk's degree of linear polarization itself is limited by the accuracy with which the total intensity of the disk can be obtained.

2.8 Correction of science observations

2.8.1 Correction method

In this section, we explain the data-reduction method we have developed to correct science measurements for the instrumental polarization effects of the complete optical system using our instrument model. The goal of the correction method is to obtain from the measurements the $\hat{Q}_{\mathrm{in}}$- and $\hat{U}_{\mathrm{in}}$-images, that is, the estimates of the true Q_{in}- and U_{in}-images incident on the telescope (see top right part of Fig. 2.2). A flow diagram of our correction method for field-tracking observations is shown in Fig. 2.11.

Before applying our correction method, we pre-process the raw data by performing dark subtraction, flat fielding, bad-pixel correction, and centering (see Sect. 2.8.2 and Paper I). Subsequently, we construct for each HWP cycle the Q- and U-images from the double difference (Eq. (2.8)) and the corresponding I_Q- and I_U-images from the double sum (Eq. (2.9)). We denote the n double-difference images (Q or U) by X_i and the cor-

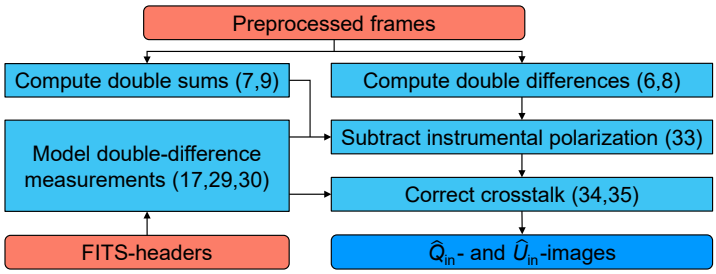


Figure 2.11: Flow diagram showing the steps to construct the incident $\hat{Q}_{\rm in}$- and $\hat{U}_{\rm in}$-images from field-tracking observations using the instrument model. The numbers of the equations used for the various steps are indicated in parentheses.

responding double-sum images (I_Q or I_U) by $I_{X,i}$, with $i = 1, 2, \ldots, n$. We construct the $\hat{I}_{Q,\rm in}$-and $\hat{I}_{U,\rm in}$-images, that is, the I_Q- and I_U-images incident on the telescope, simply by computing the mean (or median) of the double-sum $I_{Q,i}$- and $I_{U,i}$-images, respectively.

To construct the $\hat{Q}_{\rm in}$- and $\hat{U}_{\rm in}$-images we use our instrument model. The instrumental polarization effects are different for each measurement, because the parallactic, altitude, HWP, and derotator angles change continuously as the telescope tracks the target. To describe these changing instrumental polarization effects, we compute the vector equivalents of the single and double difference (Eqs. (2.6) and (2.22)) using our instrument model. To this end, we obtain the date, filter, and the parallactic, altitude, HWP, and derotator angles of each measurement from the headers of the FITS-files of the data (see Appendix 2.A). We then take the model parameters corresponding to the filter from Tables 2.1 (parameters $\epsilon_{\rm HWP}$ to d) and 2.2, taking into account the date of the observations for the latter. For each measurement, we compute $M_{\rm sys,L}$ and $M_{\rm sys,R}$ from Eq. (2.17) using $+d$ and $-d$ in $M_{\rm CI,L/R}$ (Eq. (2.21)), respectively. Similar to Sect. 2.4, where we computed the single difference from the top elements of $\boldsymbol{S}_{\rm det,L}$ and $\boldsymbol{S}_{\rm det,R}$ (i.e., $I_{\rm det,L}$ and $I_{\rm det,R}$), we now compute the single difference from the top rows of $M_{\rm sys,L}$ and $M_{\rm sys,R}$ (which we call $\boldsymbol{I}_{\rm sys,L}$ and $\boldsymbol{I}_{\rm sys,R}$):

$$\boldsymbol{D}^{\pm} = \boldsymbol{I}_{\rm sys,L} - \boldsymbol{I}_{\rm sys,R}, \tag{2.29}$$

where $\boldsymbol{D}^{\pm}$ is the single-difference row vector. Subsequently, we compute for every double-difference image X_i the double-difference row vector $\boldsymbol{D}_i$ as:

$$\begin{aligned}\boldsymbol{D}_i &= \frac{1}{2}\left[\boldsymbol{D}^{+}\left(p_i^{+}, a_i^{+}, \theta_{{\rm HWP},i}^{+}, \theta_{{\rm der},i}^{+}\right) - \boldsymbol{D}^{-}\left(p_i^{-}, a_i^{-}, \theta_{{\rm HWP},i}^{-}, \theta_{{\rm der},i}^{-}\right)\right], \\ &= \left[(I\to X)_i \quad (Q\to X)_i \quad (U\to X)_i \quad (V\to X)_i\right],\end{aligned} \tag{2.30}$$

where $\boldsymbol{D}^{+}$ and $\boldsymbol{D}^{-}$ are a function of the parallactic, altitude, HWP, and derotator angles of the first (superscript +) and second (superscript −) measurements used to compute the double difference, respectively.

To describe the i-th double-difference measurement, we can write:

$$\begin{aligned}X_i &= \boldsymbol{D}_i \cdot \boldsymbol{S}_{\rm in}, \\ &= (I\to X)_i\, I_{\rm in} + (Q\to X)_i\, Q_{\rm in} + (U\to X)_i\, U_{\rm in} + (V\to X)_i\, V_{\rm in}.\end{aligned} \tag{2.31}$$

We can ignore the element $(V \rightarrow X)_i$, that is, assume $V_{\rm in} = 0$, because we do not expect circularly polarized signals from the targets we are interested in. In addition, we can assume that the measured double-sum intensities $I_{X,i}$ are equal to the incident intensity $I_{\rm in}$ (the resulting maximum relative error is $\sim 10^{-4}$). Therefore, we can describe the i-th double-difference measurement as:

$$X_i = (I \rightarrow X)_i \, I_{X,i} + (Q \rightarrow X)_i \, Q_{\rm in} + (U \rightarrow X)_i \, U_{\rm in}. \tag{2.32}$$

The elements $(I \rightarrow X)_i$ describe the instrumental polarization (IP) of the complete optical system for each measurement. We remove the IP from each double-difference image X_i by scaling the corresponding double-sum intensity image $I_{X,i}$ with this element and subtracting the result from the double-difference image:

$$X_{{\rm IPS},i} = X_i - (I \rightarrow X)_i \, I_{X,i}, \tag{2.33}$$

where $X_{{\rm IPS},i}$ is the i-th IP-subtracted double-difference image.

The elements $(Q \rightarrow X)_i$ and $(U \rightarrow X)_i$ in Eq. (2.32) account for the crosstalk (and thus for the polarimetric efficiency and offset of the angle of linear polarization) of the complete optical system for each measurement. To correct for the crosstalk, we set up a system of equations as follows:

$$\boldsymbol{Y} = A \, [Q_{\rm in}, U_{\rm in}]^T \,,$$

$$\begin{bmatrix} X_{{\rm IPS},1} \\ X_{{\rm IPS},2} \\ \vdots \\ X_{{\rm IPS},n} \end{bmatrix} = \begin{bmatrix} (Q \rightarrow X)_1 & (U \rightarrow X)_1 \\ (Q \rightarrow X)_2 & (U \rightarrow X)_2 \\ \vdots & \vdots \\ (Q \rightarrow X)_n & (U \rightarrow X)_n \end{bmatrix} \begin{bmatrix} Q_{\rm in} \\ U_{\rm in} \end{bmatrix}, \tag{2.34}$$

with $\boldsymbol{Y}$ a column vector containing the $i = 1, 2, \ldots, n$ IP-subtracted double-difference images, $Q_{\rm in}$ and $U_{\rm in}$ the true Q- and U-images incident on the telescope and A the $n \times 2$ system matrix containing the elements $(Q \rightarrow X)_i$ and $(U \rightarrow X)_i$ of each double difference. We obtain the $\hat{Q}_{\rm in}$- and $\hat{U}_{\rm in}$-images, that is, the estimates of the true incident $Q_{\rm in}$- and $U_{\rm in}$-images, by solving for every pixel the system of equations using linear least squares:

$$\left[\hat{Q}_{\rm in}, \hat{U}_{\rm in}\right]^T = (A^{\rm T} A)^{-1} A^{\rm T} \boldsymbol{Y}. \tag{2.35}$$

Alternatively, we can obtain the incident $\hat{Q}_{\rm in}$- and $\hat{U}_{\rm in}$-images by solving the system of equations for each pair of IP-subtracted double-difference Q- and U-images (each HWP cycle) separately, and then computing the median or trimmed mean over all resulting $\hat{Q}_{\rm in}$- and $\hat{U}_{\rm in}$-images. Computing the median or trimmed mean has the advantage that any bad pixels still visible in the images are removed, but using Eq. (2.35) is expected to generally yield more accurate results. In place of Eq. (2.35) we can also use weighted linear least squares, wherein the weight matrix takes into account the signal-to-noise ratio of the images or the polarimetric efficiency as predicted by the instrument model. We note that the correction method (using Eq. (2.35)) can be applied to data sets having an unequal number of double-difference Q and U measurements.

The instrument model is valid for any combination of parallactic, altitude, HWP, and derotator angles and does not require the use of a particular rotation control law for the HWP and derotator. However, for observations not taken in field-tracking mode (e.g., pupil-tracking mode), the derotator does not keep the image orientation constant. We therefore need to derotate with our pipeline the images after subtracting the IP and before correcting the crosstalk. The adapted correction method for pupil-tracking observations, which in addition combines polarimetry with angular differential imaging (ADI), is presented in Chapter 4.

2.8.2 Correction of images of circumstellar disk of T Cha

The correction method presented in Sect. 2.8.1 has already been successfully applied to over a hundred polarimetric data sets, including HR 8799 and PZ Tel (Chapter 4), TW Hydrae (Paper I), T Cha (Pohl et al., 2017a), DZ Cha (Canovas et al., 2018), TWA7 (Olofsson et al., 2018), PDS 70 (Keppler et al., 2018), and CS Cha (Ginski et al., 2018). In this section, we demonstrate our correction method with the H-band polarimetric observations of the circumstellar disk of T Chamaeleontis (T Cha) as published in Pohl et al. (2017a). The transition disk around T Cha consists of a coplanar inner and outer disk separated by a large gap, and is viewed close to edge-on with an inclination of ~69° (Olofsson et al., 2013; Pohl et al., 2017a; Hendler et al., 2018). While the outer disk can easily be spatially resolved with SPHERE, the very narrow and close-in inner disk cannot (its extent is only <0.2 pixel on the IRDIS detector).

The data of T Cha was taken on February 20, 2016 under program ID 096.C-0248(C). It consists of a total of 30 HWP cycles with HWP switch angles 0°, 45°, 22.5°, and 67.5° to measure Stokes Q and U (see Sect. 2.3.1). During the observations, the parallactic and altitude angles varied from 5.8° to 27.3°, and from 35.1° to 34.1°, respectively. We preprocess the raw data by performing dark subtraction, flat fielding, bad-pixel correction, and centering with the star center frames as described in Paper I and Pohl et al. (2017a). We then construct the Q- and U-images from the double difference (Eq. (2.8)) and the I_Q- and I_U-images from the double sum (Eq. (2.9)). The Q- and U-images show a weak detector artifact comprised of continuous vertical bands. We remove this artifact by subtracting, for every pixel column, the median value of the 60 pixels at the top and bottom of that column (see Paper I). The resulting double-difference U-images of the first and last (30th) HWP cycle are shown in the left column of Fig. 2.12. The pronounced differences between the two images are predominantly caused by IP that evolves from negative to positive U during the 78 min total observing time.

We now apply our correction method (using the diattenuations of the UT and M4 valid before April 16, 2017) and subtract the IP from the double-difference Q- and U-images (see Eq. (2.33)). The resulting IP-subtracted U-images of the first and last HWP cycle are shown in the center column of Fig. 2.12. The resulting images are much more similar compared to the original double-difference images (left column). However, the optical system's crosstalk makes the disk brighter in Stokes U and fainter in Stokes Q during the course of the observations. This is because the crosstalk transfers part of the flux in Stokes Q to Stokes U or vice versa, that is, it introduces an offset in the angle of linear polarization (see Fig. 2.4). In addition the crosstalk converts part of the linearly polarized

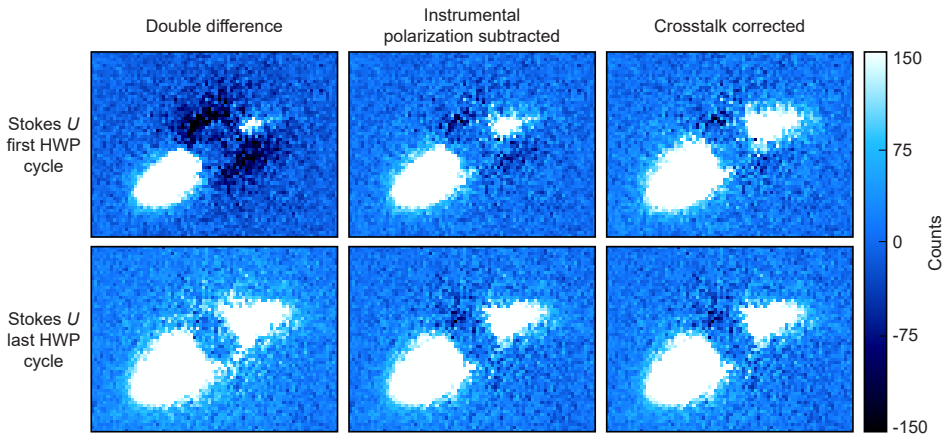


Figure 2.12: Effect of the data-reduction steps of our correction method on the Stokes U-images of the first and last (30th) HWP cycle of the observations of the circumstellar disk of T Cha.

light into circularly polarized light that the P0-90 analyzer set is not sensitive to, entailing a loss of signal as quantified by the polarimetric efficiency (see Fig. 2.3). These two effects are also seen in Fig. 3 of Paper I as variations in the Stokes Q- and U-images. Although the polarimetric efficiency during the observations of T Cha is not very low (minimum of 88%), the offset of the angle of linear polarization reaches values as large as 13°. This shows that even for observations taken at a reasonably high polarimetric efficiency, there is still significant transfer of signal between the Stokes Q- and U-images (we recall that the orientations of Q and U differ by 45°).

We correct for the crosstalk using linear least squares (see Eq. (2.35)), directly yielding the $\hat{Q}_{\rm in}$- and $\hat{U}_{\rm in}$-images. The right column of Fig. 2.12 shows the resulting $\hat{U}_{\rm in}$-images of the first and last HWP cycle after solving the system of equations for each HWP cycle separately. It follows that after crosstalk correction the disk has a very similar surface brightness distribution in all images. The integrated signal of the disk only varies by a few percent among the images, which is due to varying atmospheric conditions during the observations (e.g., seeing and sky transparency). Although by correcting the crosstalk we compensate for the polarimetric efficiency, this does not increase the signal-to-noise ratio (as clearly visible in Fig. 8 of Paper I). Next, we subtract the constant polarized background in the $\hat{Q}_{\rm in}$- and $\hat{U}_{\rm in}$-images after determining it from a large star-centered annulus with inner and outer radii of 360 and 420 pixels, respectively. Finally, we use the resulting images and Eqs. (2.3) and (2.5) to compute the polarized intensity and angle of linear polarization of the disk as shown in Fig. 2.13.

2.8.3 Improvements attained with correction method

In this section we show the improvements attained with our correction method by comparing the model-corrected $\hat{Q}_{\rm in}$- and $\hat{U}_{\rm in}$-images of T Cha with Q- and U-images generated

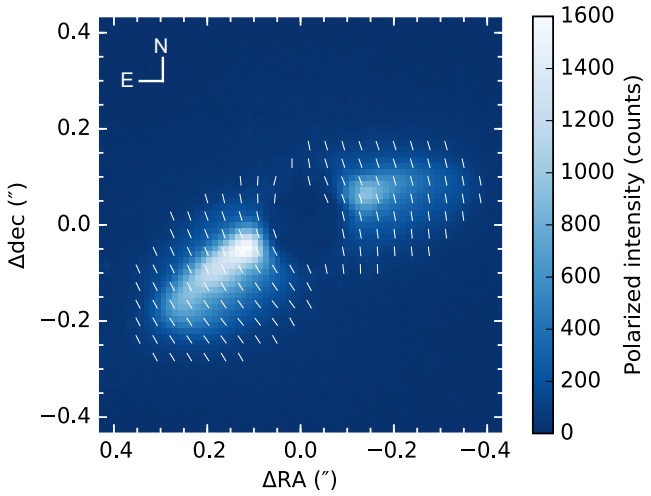


Figure 2.13: Polarized intensity and angle of linear polarization of the circumstellar disk of T Cha after applying the correction method. The white lines indicating the angle of linear polarization have arbitrary length and are only shown where the polarized intensity is higher than 50 counts.

with the conventional IP-subtraction method as presented by Canovas et al. (2011). In Paper I we made a similar comparison using data of the (nearly) face-on viewed disk of TW Hydrae. While that data set could in principle be reduced using conventional data-reduction methods, in this section we show that the correction method is essential to accurately reduce data of an inclined disk and that it enables us to detect non-azimuthal polarization and the polarization of the starlight.

To construct the Q- and U-images with the conventional IP-subtraction method, we compute the mean of the double-difference Q- and U- and double-sum I_Q- and I_U-images, and subtract the IP following the steps described in Sect. 4.1 of Paper I. We convert these and the model-corrected images into images of the azimuthal Stokes parameters Q_ϕ and U_ϕ (see Sect. 4.2 and Eqs. 15 to 17 of Paper I) to ease the comparison and interpretation of the images. The resulting images are shown in Fig. 2.14.

The model-corrected images are more accurate than the images generated with the conventional IP-subtraction method. With our correction method the instrumental polarization effects are known a priori and are corrected with an absolute polarimetric accuracy of ~0.1% or better (see Table 2.3 and Sect. 2.8.4). The conventional IP-subtraction method on the other hand does not correct the crosstalk and estimates the IP from the science data under the assumption that the starlight is unpolarized, resulting in errors in the polarized intensity and angle of linear polarization.

Comparing the left and right columns of Fig. 2.14, it follows that the disk in the model-corrected Q_ϕ-image is ~20% brighter. This increase in brightness is largely due to the crosstalk correction, that is, the correction of the polarimetric efficiency and transfer of signal between the Q_ϕ- and U_ϕ-images (or Q- and U-images). As a result of the cor-

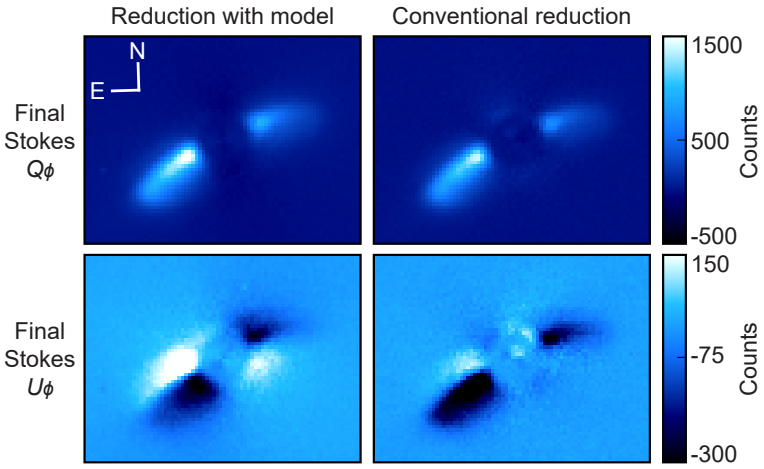


Figure 2.14: Final azimuthal Stokes Q_ϕ- and U_ϕ-images of the circumstellar disk of T Cha after applying our correction method compared to the images generated with the conventional IP-subtraction method from Canovas et al. (2011). Positive Q_ϕ indicates linear polarization in the azimuthal direction and U_ϕ shows the linear polarization at ±45° from this direction. The color scales of the top and bottom row are different, i.e., the signals in Q_ϕ are almost 10 times larger than the signals in U_ϕ.

rection, the polarized surface brightness distribution, orientation and morphology of the disk are more accurately retrieved in the model-corrected images.

Fig. 2.14 also shows that both reduction methods yield non-zero U_ϕ-signals, but with significant differences. Our correction method corrects for the IP and crosstalk without an assumption on the polarization of the star (as in the conventional IP-subtraction method) or the angle of linear polarization over the disk (as in the U_ϕ-minimization method, see Paper I). Therefore our correction method is truly sensitive to non-azimuthal polarization and yields the accurate U_ϕ-image. From Fig. 2.13 and the model-corrected U_ϕ-image of Fig. 2.14, we can conclude that away from the brightness region of the disk the angle of linear polarization deviates from the azimuthal direction. Pohl et al. (2017a) primarily attribute this non-azimuthal polarization to multiple scattering starting in the inner disk.

A clear disadvantage of the conventional IP-subtraction method is that it substantially over-subtracts the IP when the star is polarized, because it cannot discern IP from polarized starlight. Figure 2.15 shows for each individual HWP cycle the polarization signal as measured from the AO residuals in the model-corrected $\hat{Q}_{\rm in}$- and $\hat{U}_{\rm in}$-images. The figure shows that the measured polarization signal, and therefore the angle of linear polarization, is constant in time. This indicates that the starlight is polarized, because any uncorrected IP would have changed with the variation in parallactic and altitude angle during the observations.

From Fig. 2.15, and using the variation in the data points for the uncertainties, we find that the star has a degree and angle of linear polarization of 0.94 ± 0.07% and 17 ± 2°, respectively. This stellar polarization signal is most likely not caused by interstellar dust,

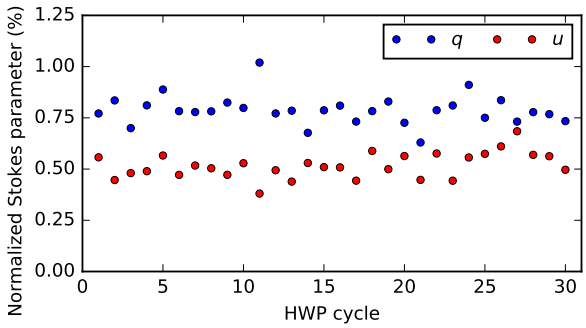


Figure 2.15: Normalized Stokes parameters of the measured stellar polarization of T Cha as function of HWP cycle after applying our correction method.

because T Cha is located in front of, and not in, the Cha I dark cloud (Murphy et al., 2013; Gaia Collaboration et al., 2018) and the angle of linear polarization differs by ~80° with respect to the average in the cloud (Covino et al., 1997). Because the measured angle of linear polarization is approximately perpendicular to the position angle of the outer circumstellar disk (see the top left image of Fig. 2.13), the stellar polarization signal most likely originates from the coplanar, spatially unresolved inner disk and/or part of the outer disk viewed close to the star. Indeed, the model-corrected images of Fig. 2.14, which still contain the stellar polarization signal, correspond much better to radiative transfer models than the images generated with the conventional IP-subtraction method (see Pohl et al. 2017a; also Keppler et al. 2018).

It appears to be quite common for stars that host a circumstellar disk to be polarized, because in at least half of the more than hundred data sets we have applied our correction method to we measure significant stellar polarization. If interstellar dust can be excluded as the origin, the stellar polarization can indicate the presence of a spatially unresolved (inner) disk, in particular for a circumstellar disk with a low to moderate inclination (see e.g., Keppler et al., 2018). The position angle of an inner disk can then be determined from the measured angle of linear polarization. For a detailed example on how to determine whether the stellar polarization is caused by interstellar dust, see Ginski et al. (2018). We note that to measure the small polarization signals of substellar companions, measuring the polarization of the star is imperative to prove that the companion's polarization is intrinsic and is not caused by over-subtraction of disk-induced stellar polarization or interstellar dust.

2.8.4 Limits to and optimization of polarimetric accuracy

The polarimetric accuracy of measuring Stokes Q and U and the degree and angle of linear polarization after applying our correction method can be computed from Eqs. (2.25)–(2.28). However, with real measurements the uncertainty on these physical quantities is generally somewhat worse than the computed accuracies. The accuracies of Table 2.3 should therefore be considered lower limits. In general, for stars that are not polarized

because of their circumstellar disk or interstellar dust, a polarization signal of ~0.1% remains after applying our correction method. The higher uncertainty on the measured polarization is likely due to limitations of the instrument model, measurement noise, and varying atmospheric conditions. In this section we elaborate on these limiting factors and discuss means to optimize the polarimetric accuracy.

A first limitation of the instrument model is that we assume the instrumental polarization effects to be fixed for a given broadband filter. However, because the instrumental polarization effects vary with wavelength (see e.g., Figs. 2.5 and 2.8), any spectral differences between the science object and the calibration sources used to determine the model parameters introduce small errors in the correction of the IP and crosstalk. We can limit these errors by comparing the spectra of the science object and calibration sources and interpolating the values of the model parameters over the wavelength domain. Such an interpolation is quite accurate for the diattenuations of the UT and M4 and the retardance of the HWP, because their spectral dependency is smooth and is known from theory and the manufacturer, respectively (see e.g., Fig. 2.7). The largest interpolation errors are expected for the retardance of the derotator, because we need to guess the shape of the function from the four measured data points. By interpolating the model parameters we are also able to correct measurements taken with the narrowband filters.

A second limitation of the instrument model is that the instrumental polarization effects are taken constant over the field of view. We know the instrumental polarization effects have spatial dependence, because the images of the internal calibration measurements display a gradient (see Appendix 2.B). However, contrary to the polarimetric imaging mode of FORS (Patat & Romaniello, 2006), this spatial dependence is very small as demonstrated by the relative proximity of the nine data points taken throughout the image for each HWP and derotator angle combination in Figs. 2.3–2.6 and 2.18–2.20. The main reason for the limited spatial dependence is that the light beams within SPHERE have much larger f-numbers than those within FORS, that is, the beams converge and diverge much more slowly within SPHERE. Because we have determined the model parameters from all these data points together (see Sect. 2.5.1), the spatial dependence downstream of M4 is accounted for in the polarimetric accuracy of the model. Nevertheless, we can increase the accuracy of the model by determining a separate set of model parameters from each of the nine apertures used, because the nine data points do not vary randomly around their average value but show a relation with position on the detector. We do not expect the diattenuations and retardances of the UT and M4 to be strongly spatially dependent, because spatial variations generally originate from transmissive optics near a focal plane.

A third limitation of the model is that the instrumental polarization effects are assumed to be constant in time. At least some temporal variation is expected for the diattenuation and retardance of the UT, because the UT is open to the atmosphere and therefore the amount of contamination (e.g., dust) on the mirrors varies (see Snik & Keller, 2013). However, as M1 and M3 are cleaned with CO_2 on a monthly basis, this variation is most likely small. For the other optical components we do not expect temporal variations due to contamination because they are located within SPHERE. Aging of these components is most likely also limited, because the model parameters describing the optical path downstream of M4 seem not to have changed since the internal calibration measurements of 2016, and the determined diattenuation of M4 has not significantly changed between the

observations of the unpolarized stars in 2016 and 2018 (see Sect. 2.6.2). To optimize the accuracy of our correction, we can recalibrate the diattenuation of the UT and M4 during the same night as the science observations, preferably with an unpolarized star that has a spectrum as similar as possible to that of the science object(s).

To keep the instrument model accurate over time, new calibration measurements need to be taken when a modification is made to the optical path that affects the polarimetry. Examples of such modifications are the insertion of a new optical component, the replacement or removal of an existing component, or the re-coating of a mirror (e.g., the re-aluminization of M1 and M3 as performed between April 3 and April 16, 2017). Because the mathematical description of our model includes the double difference, changes to the optical path downstream of the derotator generally do not require new calibration measurements.

The polarimetric accuracy we can really attain is also affected by measurement noise. In Eq. (2.11), the polarimetric accuracy is defined for infinite sensitivity, that is, without any noise or spurious signals present in the data. However, in general the combined photon, speckle, (sky) background, and read-out noise of a measurement is much larger than the polarimetric accuracy of the instrument model. Therefore, when stating uncertainties of measured polarization signals, we recommend to always compare the polarimetric accuracy as computed from Eqs. (2.25)–(2.28) with the measurement noise. The criteria to reach a polarimetric sensitivity, in addition to a polarimetric accuracy, of $\leq$0.1% with IRDIS for the measurement of polarization signals of substellar companions are discussed in Chapter 4.

With the double-difference method, spurious polarization signals created when the atmospheric seeing or sky transparency changes between measurements is removed to first order. Some spurious signals remain, because these atmospheric variations prevent the effect of the diattenuation of the components downstream from the derotator to be completely removed. When the variations in seeing and sky transparency are large, the spurious signals can be suppressed by computing Stokes Q and U from the 'normalized' double difference (compare to Eq. (2.8)):

$$X = \frac{1}{2}\left(\frac{X^+}{I_{X^+}} - \frac{X^-}{I_{X^-}}\right) \cdot I_X, \tag{2.36}$$

with I_X computed from Eq. (2.9).

The accurate polarized intensity images that we obtain with our correction method enable the construction of images of the degree of linear polarization of circumstellar disks. To construct such an image, an image of the total intensity of the disk is required. In principle such an image can be obtained by subtracting the point spread function of a reference star (e.g., Canovas et al., 2013) or by using angular differential imaging for disks seen close to edge-on (e.g., Perrin et al., 2015). However, these techniques have proven to be challenging and residual speckles from the star remain in the total intensity image of the disk. Therefore the accuracy of measuring the degree of linear polarization of circumstellar disks is limited by the accuracy of the total intensity image rather than the accuracy of the instrument model.

2.8.5 Data-reduction pipeline including correction method

We have incorporated our correction method in a highly-automated end-to-end data-reduction pipeline called IRDAP (IRDIS Data reduction for Accurate Polarimetry). IRDAP is publicly available and handles data taken both in field- and pupil-tracking mode and using the broadband filters Y, J, H, and K_s. Data taken with the narrowband filters can be reduced as well, although with a lower accuracy, by using the correction method of the broadband filters. For pupil-tracking observations IRDAP can additionally apply angular differential imaging.

Reducing data with IRDAP is very straightforward and does not require the user to do any coding. IRDAP is simply run from a terminal with only a few commands and uses a configuration file with a limited number of input parameters. For an average-sized data set and using a modern computer, IRDAP performs a complete data reduction from raw data to final data products within a few minutes.

The documentation of IRDAP, including the installation and user instructions, can be found online[4]. We plan to regularly add functionalities and make improvements to IRDAP. Among others, we plan to calibrate the instrument in the narrowband filters to also enable the accurate reduction of data taken in these filters.

2.9 Summary and conclusions

We have created a detailed Mueller matrix model describing the instrumental polarization effects of the Unit Telescope (UT) and SPHERE-IRDIS in the broadband filters Y, J, H, and K_s. To determine the parameters of the model, we have taken measurements with SPHERE's internal light source and have observed two unpolarized stars. We have developed a data-reduction method that uses the model to correct for the instrumental polarization and crosstalk. We have exemplified this correction method with observations of the circumstellar disk of T Cha and have shown the improvements compared to conventional data-reduction and analysis methods.

The instrumental polarization (IP) of the optical system primarily originates from the UT and SPHERE's first mirror (M4) and increases with decreasing telescope altitude angle. The IP is different for observations taken before and after the re-aluminization of the primary and tertiary mirrors of the UT (M1 and M3). Before the re-aluminization (i.e., before April 16, 2017), the maximum IP (at an altitude angle of 30°) is approximately equal to 3.5%, 2.5%, 1.9%, and 1.5% in the Y-, J-, H-, and K_s-band, respectively. After the re-aluminization (i.e., after April 16, 2017), the maximum IP in the same filters is approximately 3.0%, 2.1%, 1.5%, and 1.3%, respectively.

The crosstalk of the optical system is strongly wavelength dependent and is primarily produced by the derotator (K-mirror). The crosstalk decreases the polarimetric efficiency, because it converts linearly polarized light into circularly polarized light that IRDIS cannot measure. The polarimetric efficiency is lowest when the reflection plane of the derotator is at approximately ±45° from the vertical direction and has minimum values equal to 54%, 89%, 5%, and 7% in the Y-, J-, H-, and K_s-band, respectively. The crosstalk

[4] https://irdap.readthedocs.io

also causes an offset of the angle of linear polarization in these filters, with maximum deviations equal to 11°, 4°, 34°, and 90°, respectively. In Paper I, we present a strategy to prevent observing at a low polarimetric efficiency by optimizing the derotator angle.

In all broadband filters, the instrument model has an absolute and relative polarimetric accuracy of ≤0.1% and <1%, respectively. With these accuracies we can measure the polarization signals of substellar companions with a total polarimetric accuracy of ∼0.1% in the degree of linear polarization and an accuracy of a few degrees in angle of linear polarization. These accuracies are amply sufficient for quantitative polarimetry of circumstellar disks, because these objects are typically polarized a few tens of percent. The uncertainty on the measured polarization after applying our correction method to science observations is generally somewhat worse than the accuracies of the model itself due to limitations of the model, varying atmospheric conditions, and measurement noise.

With our correction method the IP and crosstalk are known a priori and for weakly polarized sources are corrected with an absolute polarimetric accuracy of ∼0.1% or better. This is contrary to conventional data-reduction methods that do not correct the crosstalk and estimate the IP from the (noisy) science data. Using our correction method we can therefore more accurately measure the polarized intensity and angle of linear polarization. With the correction method we can also measure the polarization of the star, which enables us to detect spatially unresolved (inner) disks and prove that the measured polarization signal of a substellar companion is intrinsic to the companion. The method can be applied to measurements taken both in field- and pupil-tracking mode.

We have incorporated our correction method in a highly-automated end-to-end data-reduction pipeline called IRDAP (IRDIS Data reduction for Accurate Polarimetry). IRDAP is publicly available and the documentation, including the installation and user instructions, can be found online[5]. To achieve the highest polarimetric accuracy, it is recommended to always use IRDAP for the reduction of IRDIS polarimetric data. Even for observations of nearly face-on circumstellar disks or measurements taken at a high polarimetric efficiency (e.g., when the derotator is kept at a favorable angle or observations are performed in the J-band), our correction method makes a significant correction to the angle of linear polarization and increases the signal-to-noise ratio in the final images.

2.A Computation of parallactic, altitude, HWP, and derotator angles from FITS-headers

The parallactic, altitude, HWP, and derotator angles needed for the instrument model can be retrieved from the headers of the FITS-files of the measurements. However, even during a measurement these angles are continuously changing as the telescope tracks the target. For each measurement, we therefore compute the mean value of these angles from the start and end values specified in the FITS-headers. We note that for angles we cannot simply use the arithmetic mean, and instead use the mean of circular quantities:

$$\text{mean}\,(\theta_\text{s},\ \theta_\text{e}) = \text{atan2}\,(\sin\theta_\text{s} + \sin\theta_\text{e}, \cos\theta_\text{s} + \cos\theta_\text{e})\,, \tag{2.37}$$

[5] https://irdap.readthedocs.io

where θ_s and θ_e are the angles at the start and end of the measurement, respectively.

The parallactic angle p and HWP angle θ_{HWP} are obtained from the FITS-headers as:

$$p = \text{mean}\,(\text{TEL PARANG START},\ \text{TEL PARANG END})\,, \tag{2.38}$$

$$\theta_{HWP} = \text{mean}\,(\text{INS4 DROT3 BEGIN},\ \text{INS4 DROT3 END}) - 152.15°. \tag{2.39}$$

For observations in field-tracking mode, the derotator angle θ_{der} is computed as:

$$\theta_{der} = \text{mean}\,(\text{INS4 DROT2 BEGIN},\ \text{INS4 DROT2 END})\,. \tag{2.40}$$

For pupil-tracking observations (see Chapter 4), the derotator angle is calculated as:

$$\theta_{der} = \text{mean}\,(\text{INS4 DROT2 BEGIN},\ \text{INS4 DROT2 END}) + \frac{1}{2}\eta_{pupil}, \tag{2.41}$$

where $\eta_{pupil} = 135.99 \pm 0.11°$ is the fixed position angle offset of the image (see Maire et al., 2016). This offset is used to align a mask added to the Lyot stop (the 'spider mask') with the diffraction pattern of the support structure of the UT's secondary mirror. For the altitude angle a, only the start value is available from the header TEL ALT. Therefore we use spline interpolation to compute the mean altitude angle during a measurement.

2.B Gradient in flux of internal calibration measurements

The flux in most of the images taken with the internal light source is not uniform, but shows a gradient. This structure appears to consist of two components: a gradient that depends on the total intensity of the incident light and a gradient that depends on the polarization state of the incident light. The total-intensity-dependent gradient (see Fig. 2.16) has a different strength and orientation for every broadband filter, and is most prominent in the K_s-band. It must originate downstream of the derotator, since it does not depend on the derotator or HWP angle. The gradient may be due to imperfect alignment of optical components or differences in transmission or reflectivity over the surface of the components. As the gradient is also present in the lamp flat frames, the flat-field correction applied to the exposures suppresses the gradient. In the double-difference images (actually already in the single-difference images), the total-intensity-dependent gradient is completely removed (see Fig. 2.17, left). However, it is still visible in the double-sum images. Therefore, the normalized Stokes parameters determined from these images depend on the position of the apertures from which they are computed.

In the polarized source measurements, the computation of the double difference removes the total-intensity-dependent gradient, but a polarization-dependent-gradient remains (see Fig. 2.17, right). This gradient is different in strength and orientation for each exposure and therefore seems to depend on the orientation of the HWP and/or derotator.

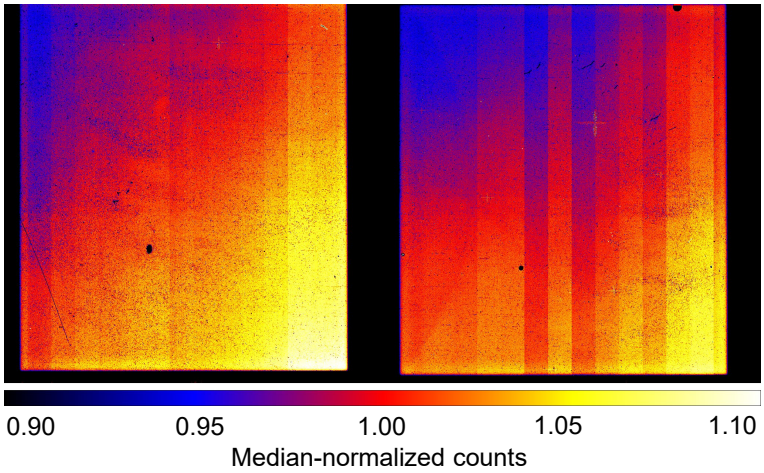


Figure 2.16: Dark-subtracted and bad-pixel-filtered flat-field frame in the K_s-band showing the total-intensity-dependent gradient in the left and right images on the detector.

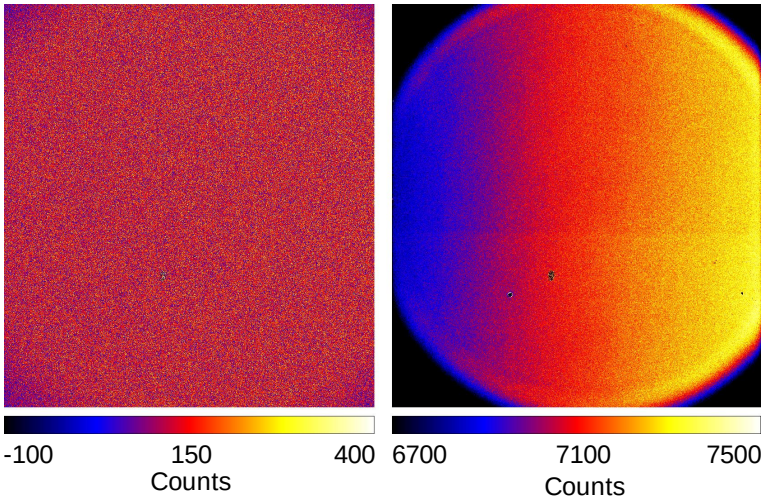


Figure 2.17: Double-difference images of the unpolarized source (*left*) and polarized source measurements (*right*) in the K_s-band showing that the double difference completely removes the total-intensity-dependent gradient, but does not remove the polarization-dependent-gradient.

Because the HWP is close to a focal plane, a likely cause of the polarization-dependent-gradient is that the retardance of the HWP varies over the surface of the HWP. The gradient is not visible in the unpolarized source measurements, because the incident light is only very weakly polarized in that case.

2.C Graphs of model fits of internal calibration measurements

Figure 2.18 shows the ideal, measured, and fitted normalized Stokes parameters of the polarized source measurements in the H-band as a function of HWP and derotator angle, including the residuals of fit. The ideal curves are computed with the HWP and derotator retardances equal to 180°, no angle offsets and the diattenuation of the polarizers equal to 1. The measured and fitted normalized Stokes parameters of the unpolarized source measurements in the H-band are displayed in Figs. 2.19 (normal double difference) and 2.20 (modified double difference with the derotator angles, rather than the HWP angles, differing 45° between the two exposures). These figures also show the corresponding residuals of fit. The ideal curves (completely unpolarized light incident on the HWP, the diattenuations of the HWP, derotator, and polarizers equal to 1, and no angle offsets) coincide with the x-axes of the graphs and are therefore not shown.

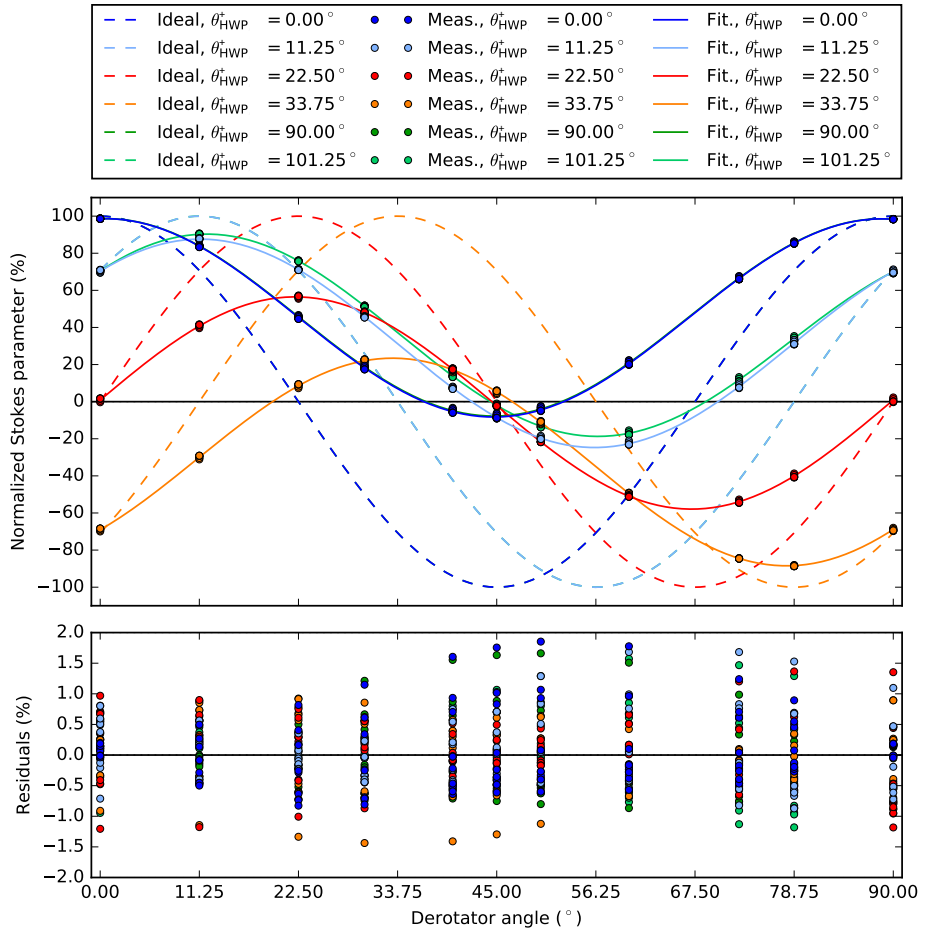


Figure 2.18: Ideal, measured, and fitted normalized Stokes parameters of the polarized source measurements in the H-band as a function of HWP and derotator angle. The legend only shows the θ^+_{HWP}-value of each data point or curve; it is implicit that the corresponding value for θ^-_{HWP} differs 45° from that of θ^+_{HWP}.

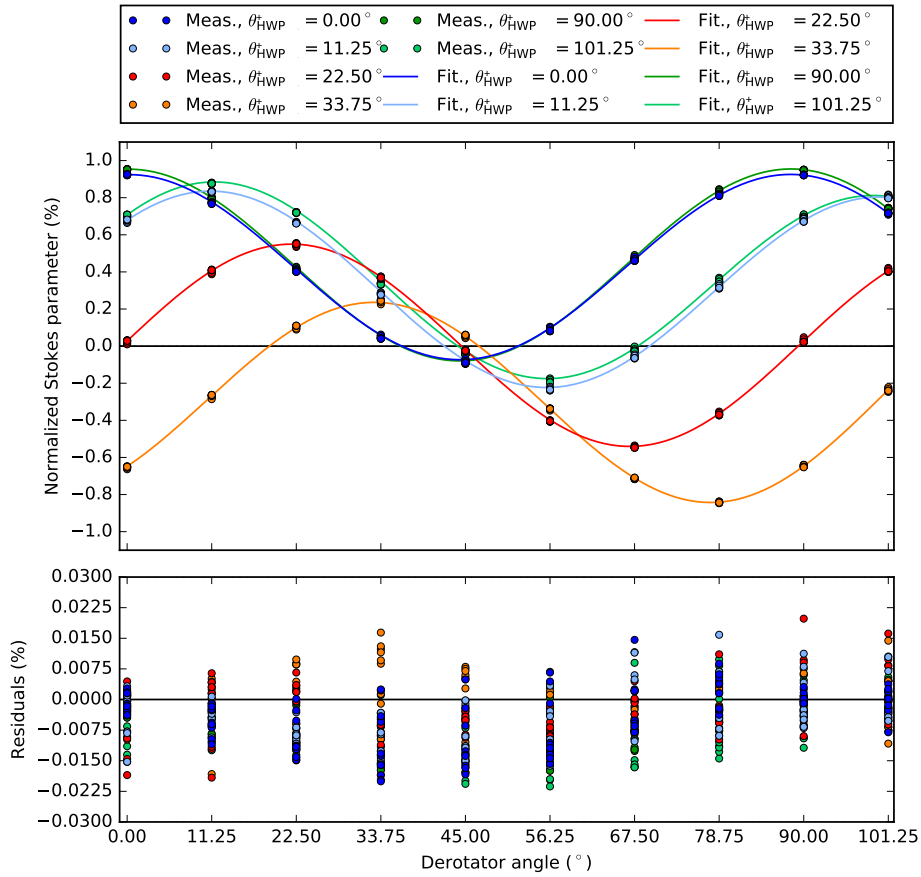


Figure 2.19: Measured and fitted normalized Stokes parameters of the unpolarized source measurements in the H-band (normal double difference with the two HWP angles differing 45°) as a function of HWP and derotator angle. The legend only shows the θ^+_{HWP}-value of each data point or curve; it is implicit that the corresponding value for θ^-_{HWP} differs 45° from that of θ^+_{HWP}.

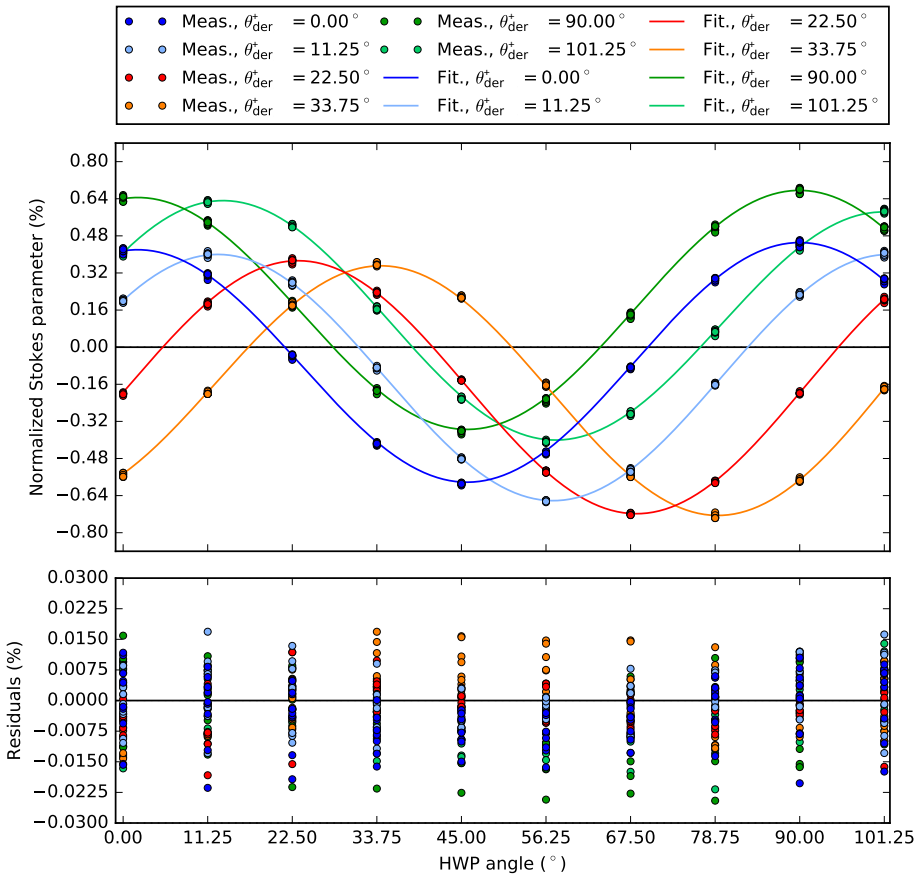


Figure 2.20: Measured and fitted normalized Stokes parameters of the unpolarized source measurements in the *H*-band (modified double difference with the two derotator angles, rather than the HWP angles, differing 45°) as a function of derotator and HWP angle. The legend only shows the θ^+_{der}-value of each data point or curve; it is implicit that the corresponding value for θ^-_{der} differs 45° from that of θ^+_{der}. The x-axis displays the HWP angle and not the derotator angle as in Figs. 2.18 and 2.19.

2.D Determination of normalized Stokes parameters and graphs of model fits of unpolarized star observations

The normalized Stokes parameters of the observations of the unpolarized stars are determined from apertures in the Q-, U-, I_Q-, and I_U-images. For the data of HD 217343 (2018), we compute the signal in these images as the mean in an aperture minus the median of the background signal in a concentric annulus. We then calculate the normalized Stokes parameter q or u by dividing the signal from the Q- or U-image by that from the corresponding I_Q- or I_U-image according to Eq. (2.10). The radii of the apertures used are determined from plots of the normalized Stokes parameters as a function of aperture radius (see Fig. 2.21). In all filters an aperture radius of 220 pixels is used, because at this radius the curves have approached a constant value. The annulus to compute the background signal from starts at the outer radius of the aperture and has a width of 40 pixels.

For the data of HD 176425 (2016) we use the same method to compute the normalized Stokes parameters, but we do not subtract the background signal. This is because almost the complete image is filled with signal from the star and therefore there is no location to accurately determine the background signal from. In the Y-, J-, and H-band, where we use an aperture radius of 200 pixels, this is no problem because the background signal is very small.

In the K_s-band however (see Fig. 2.22), the curves of q and u versus aperture radius do not approach a constant value, but decrease with increasing aperture radii due to the much stronger background signal that most likely originates from thermal emission of the UT and SPHERE's uncooled optics upstream from IRDIS. Because the intensity of the star's point spread function (PSF) decreases with increasing distance from the center, the thermal background becomes more prominent for larger aperture radii. Although the thermal background is removed after computing the double difference (Q- and U-images), it is not removed after computing the double sum (I_Q- and I_U-images), and therefore the normalized Stokes parameters decrease with increasing aperture radius. An aperture radius of 125 pixels is selected for the measurements in the K_s-band, because at this radius: 1) the curves of the other filters start to approach a constant value, 2) the thermal background starts to become visible in the raw frames, and 3) the determined diattenuations of the UT and M4 are in line with expectations based on the determined diattenuations in the other filters and their deviation from the analytical values (see Fig. 2.10).

Figs. 2.23 and 2.24 show the analytical, measured, and fitted normalized Stokes parameters q and u of the observations of HD 176425 (2016) as a function of telescope altitude angle in the H- and K_s-band, respectively. Figure 2.25 shows the same graph for the observations of HD 217343 (2018) in the H-band. The residuals of fit are also included in these figures. The analytical curves are computed from the Fresnel equations using the complex refractive index of aluminum. The error bars are calculated as half the difference between the normalized Stokes parameters determined from apertures with radii 50 pixels larger and smaller than the radius of the aperture used to calculate q and u used for determining the diattenuations (see Figs. 2.21 and 2.22). The error bars show the

uncertainty in the normalized Stokes parameters due to the dependency of the measured values on the chosen aperture radius. These uncertainties are small for all measurement except those of HD 176425 (2016) in the K_s-band because the thermal background could not be subtracted. Finally, because we did not keep the derotator fixed with its plane of incidence horizontal for the observations of HD 217343 (2018), crosstalk from the derotator causes the shape of the curves in Fig. 2.25 to be different from those of Figs. 2.23 and 2.24.

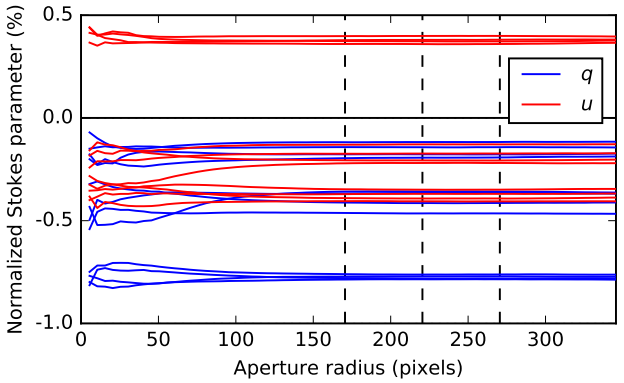


Figure 2.21: Normalized Stokes parameters q and u as a function of aperture radius for the observations of the unpolarized star HD 217343 (2018) in the H-band. The central and outer dashed lines indicate the radii of the apertures from which the normalized Stokes parameters and their error bars (see Figs. 2.9 and 2.25) have been determined, respectively.

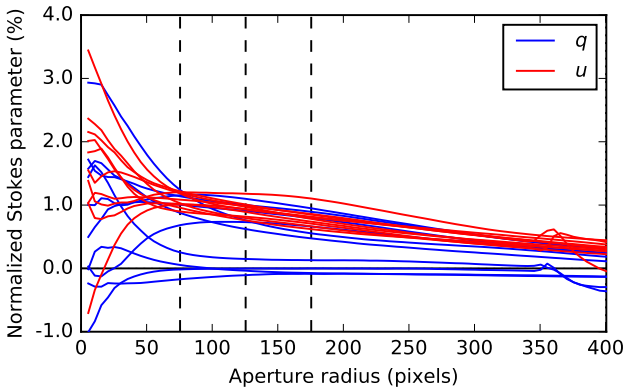


Figure 2.22: Normalized Stokes parameters q and u as a function of aperture radius for the observations of the unpolarized standard star HD 176425 (2016) in the K_s-band. The central and outer dashed lines indicate the radii of the apertures from which the normalized Stokes parameters and their error bars (see Figs. 2.8 and 2.24) have been determined, respectively.

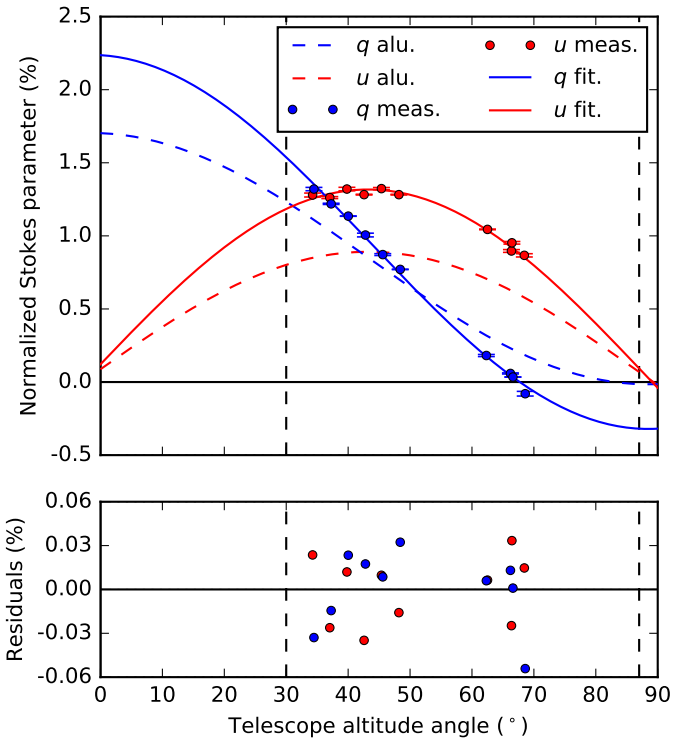


Figure 2.23: Analytical (aluminum), measured (including error bars), and fitted normalized Stokes parameters q and u as a function of telescope altitude angle for the observations of the unpolarized standard star HD 176425 (2016) in the H-band. For science observations the telescope altitude angle is restricted to $30° \leq a \leq 87°$.

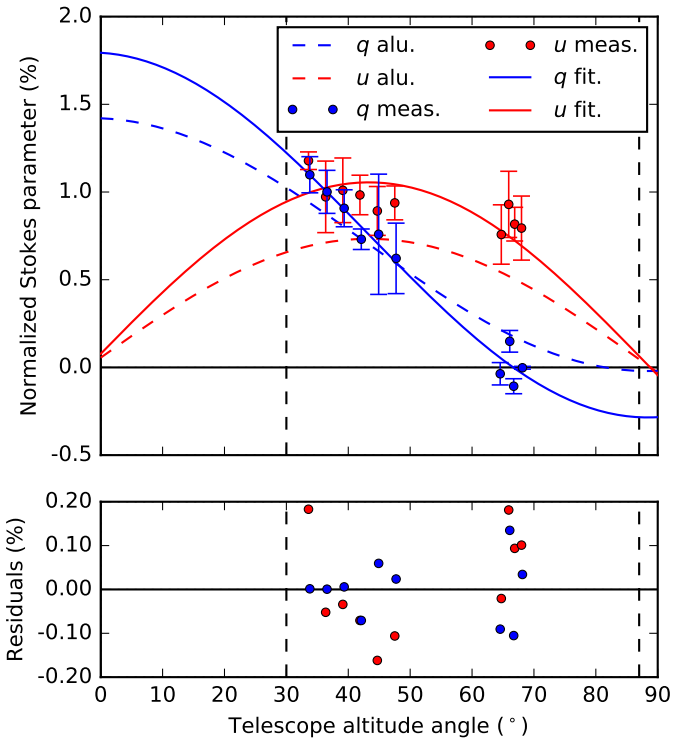


Figure 2.24: Analytical (aluminum), measured (including error bars), and fitted normalized Stokes parameters q and u as a function of telescope altitude angle for the observations of the unpolarized standard star HD 176425 (2016) in the K_s-band. For science observations the telescope altitude angle is restricted to $30° \leq a \leq 87°$.

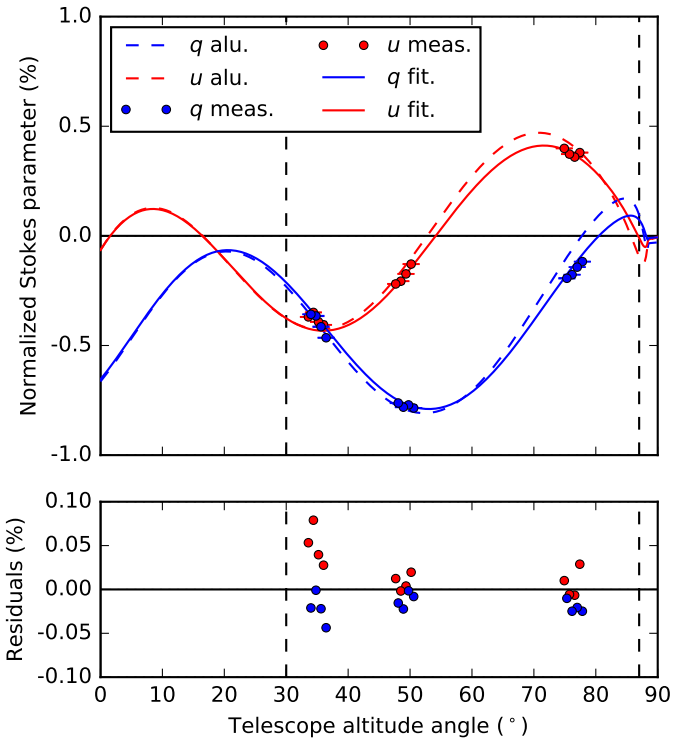


Figure 2.25: Analytical (aluminum), measured (including error bars), and fitted normalized Stokes parameters q and u as a function of telescope altitude angle for the observations of the unpolarized star HD 217343 (2018) in the H-band. For science observations the telescope altitude angle is restricted to $30° \leq a \leq 87°$.

2.E Calculation of accuracies of fit and uncertainties in determined parameters

To estimate the polarimetric accuracy of the instrument model, we calculate for each broadband filter the accuracies of fitting the model parameters to the calibration data. We compute these accuracies of fit as the corrected sample standard deviation of the residuals s_{res}:

$$s_{\mathrm{res}} = \sqrt{\frac{\sum_{i=1}^{n} r_i^2}{n-k}}, \tag{2.42}$$

with r_i the residuals of fit, n the number data points, and k the number of parameters determined from the data set. The accuracies of fit are calculated separately for the polarized source measurements, the unpolarized source measurements, and the two observations of unpolarized stars (denoted s_{rel}, s_{unpol}, and s_{star}, respectively, in Sect. 2.7). The results are shown in Table 2.5.

To compute the uncertainties of the determined model parameters, we approximate the covariance matrix of the model parameters Σ as:

$$\Sigma = \tau (J^{\mathrm{T}} J)^{-1} \tau, \tag{2.43}$$

where J is the Jacobian matrix:

$$J = \begin{bmatrix} \frac{\partial x_1}{\partial \beta_1} & \cdots & \frac{\partial x_1}{\partial \beta_m} \\ \vdots & \ddots & \vdots \\ \frac{\partial x_n}{\partial \beta_1} & \cdots & \frac{\partial x_n}{\partial \beta_m} \end{bmatrix}, \tag{2.44}$$

with β_1 to β_m the m determined model parameters and x_1 to x_n the model functions describing the n measurements (Eq. (2.10) with the model equations and the parallactic, altitude, derotator, and HWP angles of the measurements substituted). The matrix τ has dimensions $m \times m$ and contains on its diagonal for each model parameter the accuracy of fit (s_{res}) of the measurements from which that parameter is determined (see Table 2.5). For example, the diagonal element of τ corresponding to the model parameter Δ_{der} in the H-band is equal to s_{res} of the polarized source measurements in the same filter. Finally, we compute the 1σ-errors (1 times the standard deviation) of the model parameters as the square root of the diagonal elements of Σ, and list them behind the $\pm$-signs in Tables 2.1 and 2.2.

By taking the diagonal values of Σ as the uncertainties of the parameters, it is assumed that the parameter values are not correlated. However, in reality all the parameters are weakly correlated, in particular because the offset angles δ_{HWP}, δ_{der}, and δ_{cal} are determined from the complete set of polarized source measurements. In addition, the uncertainties of the parameters are computed using a linear approximation through the Jacobian. Therefore the uncertainties should be considered first order estimates only.

Table 2.5: Accuracies of fit of the polarized source measurements, the unpolarized source measurements, and the observations of the unpolarized stars HD 176425 (2016) and HD 217343 (2018) in the Y-, J-, H-, and K_s-band.

Filter	s_{res} (%) polarized source	s_{res} (%) unpolarized source	s_{res} (%) unpolarized star 2016	s_{res} (%) unpolarized star 2018
BB_Y	0.73	0.023	0.058	0.064
BB_J	0.41	0.0070	0.047	0.072
BB_H	0.58	0.0083	0.025	0.029
BB_K_s	0.54	0.0085	0.10	0.092

References

Bagnulo, S., Landolfi, M., Landstreet, J. D., et al. 2009, Publications of the Astronomical Society of the Pacific, 121, 993

Bass, M., Stryland, E. W. V., Williams, D. R., & Wolfe, W. L. 1995, Handbook of Optics Volume II Devices, Measurements, and Properties 2nd edition

Beck, C., Schlichenmaier, R., Collados, M., Bellot Rubio, L., & Kentischer, T. 2005, Astronomy & Astrophysics, 443, 1047

Beuzit, J. L., Vigan, A., Mouillet, D., et al. 2019, Astronomy & Astrophysics, 631, A155

Canovas, H., Ménard, F., de Boer, J., et al. 2015, Astronomy & Astrophysics, 582, L7

Canovas, H., Ménard, F., Hales, A., et al. 2013, Astronomy & Astrophysics, 556, A123

Canovas, H., Rodenhuis, M., Jeffers, S. V., Min, M., & Keller, C. U. 2011, Astronomy & Astrophysics, 531, A102

Canovas, H., Montesinos, B., Schreiber, M. R., et al. 2018, Astronomy & Astrophysics, 610, A13

Carbillet, M., Bendjoya, P., Abe, L., et al. 2011, Experimental Astronomy, 30, 39

Covino, E., Palazzi, E., Penprase, B. E., Schwarz, H. E., & Terranegra, L. 1997, Astronomy & Astrophysics Supplement, 122, 95

de Boer, J., Girard, J. H., Mawet, D., et al. 2014, in Proceedings of the SPIE, Vol. 9147, Ground-based and Airborne Instrumentation for Astronomy V, 914787

de Boer, J., Salter, G., Benisty, M., et al. 2016, Astronomy & Astrophysics, 595, A114

de Boer, J., Langlois, M., van Holstein, R. G., et al. 2020, Astronomy & Astrophysics, 633, A63

de Kok, R. J., Stam, D. M., & Karalidi, T. 2011, Astrophysical Journal, 741, 59

Dohlen, K., Langlois, M., Saisse, M., et al. 2008, in Proceedings of the SPIE, Vol. 7014, Ground-based and Airborne Instrumentation for Astronomy II, 70143L

Fusco, T., Rousset, G., Sauvage, J.-F., et al. 2006, Optics Express, 14, 7515

Gaia Collaboration, Brown, A. G. A., Vallenari, A., et al. 2018, Astronomy & Astrophysics, 616, A1

Garufi, A., Benisty, M., Stolker, T., et al. 2017, The Messenger, 169, 32

Ginski, C., Stolker, T., Pinilla, P., et al. 2016, Astronomy & Astrophysics, 595, A112

Ginski, C., Benisty, M., van Holstein, R. G., et al. 2018, Astronomy & Astrophysics, 616, A79

Gratadour, D., Rouan, D., Grosset, L., Boccaletti, A., & Clénet, Y. 2015, Astronomy & Astrophysics, 581, L8

Guerri, G., Daban, J.-B., Robbe-Dubois, S., et al. 2011, Experimental Astronomy, 30, 59

Harrington, D. M., Kuhn, J. R., & Ariste, A. L. 2017, Journal of Astronomical Telescopes, Instru-

ments, and Systems, 3, 018001
Harrington, D. M., Kuhn, J. R., & Hall, S. 2011, Publications of the Astronomical Society of the Pacific, 123, 799
Hendler, N. P., Pinilla, P., Pascucci, I., et al. 2018, Monthly Notices of the Royal Astronomical Society, 475, L62
Hugot, E., Ferrari, M., El Hadi, K., et al. 2012, Astronomy & Astrophysics, 538, A139
Ichimoto, K., Lites, B., Elmore, D., et al. 2008, Solar Physics, 249, 233
Jensen-Clem, R., Millar-Blanchaer, M., Mawet, D., et al. 2016, Astrophysical Journal, 820, 111
Keller, C. U. 2002, in Astrophysical Spectropolarimetry, ed. J. Trujillo-Bueno, F. Moreno-Insertis, & F. Sánchez, 303–354
Keppler, M., Benisty, M., Müller, A., et al. 2018, Astronomy & Astrophysics, 617, A44
Langlois, M., Dohlen, K., Vigan, A., et al. 2014, in Proceedings of the SPIE, Vol. 9147, Ground-based and Airborne Instrumentation for Astronomy V, 91471R
Leroy, J. L. 1993, Astronomy & Astrophysics, 274, 203
—. 1999, Astronomy & Astrophysics, 346, 955
Maire, A.-L., Langlois, M., Dohlen, K., et al. 2016, in Proceedings of the SPIE, Vol. 9908, Ground-based and Airborne Instrumentation for Astronomy VI, 990834
Marley, M. S., & Sengupta, S. 2011, Monthly Notices of the Royal Astronomical Society, 417, 2874
Marois, C., Lafrenière, D., Doyon, R., Macintosh, B., & Nadeau, D. 2006, Astrophysical Journal, 641, 556
Millar-Blanchaer, M. A., Graham, J. R., Pueyo, L., et al. 2015, Astrophysical Journal, 811, 18
Millar-Blanchaer, M. A., Perrin, M. D., Hung, L.-W., et al. 2016, in Proceedings of the SPIE, Vol. 9908, Ground-based and Airborne Instrumentation for Astronomy VI, 990836
Milli, J., Mawet, D., Pinte, C., et al. 2015, Astronomy & Astrophysics, 577, A57
Milli, J., Vigan, A., Mouillet, D., et al. 2017, Astronomy & Astrophysics, 599, A108
Min, M., Canovas, H., Mulders, G. D., & Keller, C. U. 2012, Astronomy & Astrophysics, 537, A75
Min, M., Dullemond, C. P., Dominik, C., de Koter, A., & Hovenier, J. W. 2009, Astronomy & Astrophysics, 497, 155
Murphy, S. J., Lawson, W. A., & Bessell, M. S. 2013, Monthly Notices of the Royal Astronomical Society, 435, 1325
Muto, T., Grady, C. A., Hashimoto, J., et al. 2012, Astrophysical Journal Letters, 748, L22
Olofsson, J., Benisty, M., Le Bouquin, J.-B., et al. 2013, Astronomy & Astrophysics, 552, A4
Olofsson, J., van Holstein, R. G., Boccaletti, A., et al. 2018, Astronomy & Astrophysics, 617, A109
Patat, F., & Romaniello, M. 2006, Publications of the Astronomical Society of the Pacific, 118, 146
Perrin, M. D., Schneider, G., Duchene, G., et al. 2009, Astrophysical Journal Letters, 707, L132
Perrin, M. D., Duchene, G., Millar-Blanchaer, M., et al. 2015, Astrophysical Journal, 799, 182
Pinte, C., Harries, T. J., Min, M., et al. 2009, Astronomy & Astrophysics, 498, 967
Pohl, A., Sissa, E., Langlois, M., et al. 2017a, Astronomy & Astrophysics, 605, A34
Pohl, A., Benisty, M., Pinilla, P., et al. 2017b, Astrophysical Journal, 850, 52
Quanz, S. P., Avenhaus, H., Buenzli, E., et al. 2013, Astrophysical Journal Letters, 766, L2
Rakić, A. D. 1995, Applied Optics, 34, 4755
Roelfsema, R., Schmid, H. M., Pragt, J., et al. 2010, in Proceedings of the SPIE, Vol. 7735, Ground-based and Airborne Instrumentation for Astronomy III, 77354B
Schmid, H. M., Bazzon, A., Roelfsema, R., et al. 2018, Astronomy & Astrophysics, 619, A9
Skumanich, A., Lites, B. W., Pillet, V. M., & Seagraves, P. 1997, Astrophysical Journal Supplement, 110, 357
Snik, F., & Keller, C. U. 2013, Astronomical Polarimetry: Polarized Views of Stars and Planets, ed. T. D. Oswalt & H. E. Bond, 175

Socas-Navarro, H., Elmore, D., Asensio Ramos, A., & Harrington, D. M. 2011, Astronomy & Astrophysics, 531, A2
Sparks, W. B., & Axon, D. J. 1999, Publications of the Astronomical Society of the Pacific, 111, 1298
Stolker, T., Dominik, C., Min, M., et al. 2016, Astronomy & Astrophysics, 596, A70
Stolker, T., Min, M., Stam, D. M., et al. 2017, Astronomy & Astrophysics, 607, A42
Tinbergen, J. 2005, Astronomical Polarimetry
Turnshek, D. A., Bohlin, R. C., Williamson, II, R. L., et al. 1990, Astronomical Journal, 99, 1243
van Harten, G., Snik, F., & Keller, C. U. 2009, Publications of the Astronomical Society of the Pacific, 121, 377
Wiktorowicz, S. J., Millar-Blanchaer, M., Perrin, M. D., et al. 2014, in Proceedings of the SPIE, Vol. 9147, Ground-based and Airborne Instrumentation for Astronomy V, 914783
Wildi, F., Mouillet, D., Beuzit, J.-L., et al. 2009, in Proceedings of the SPIE, Vol. 7440, Techniques and Instrumentation for Detection of Exoplanets IV, 74400Q
Witzel, G., Eckart, A., Buchholz, R. M., et al. 2011, Astronomy & Astrophysics, 525, A130

3 | Calibration of the instrumental polarization effects of SCExAO-CHARIS' spectropolarimetric mode

Adapted from

R. G. van Holstein, S. P. Bos, J. Ruigrok, J. Lozi, O. Guyon, B. Norris, F. Snik, J. Chilcote, T. Currie, T. D. Groff, G .J .J. 't Hart, N. Jovanovic, J. Kasdin, T. Kudo, F. Martinache, B. Mazin, A. Sahoo, M. Tamura, S. Vievard, A. Walter, and J. Zhang

Ground-based and Airborne Instrumentation for Astronomy VIII, Proceedings of the SPIE, 11447, 114475B (2020)

SCExAO at the Subaru telescope is a visible and near-infrared high-contrast imaging instrument employing extreme adaptive optics and coronagraphy. The instrument feeds the near-infrared light (JHK) to the integral field spectrograph CHARIS. Recently, a Wollaston prism was added to CHARIS' optical path, giving CHARIS a spectropolarimetric capability that is unique among high-contrast imaging instruments. We present a detailed Mueller matrix model describing the instrumental polarization effects of the complete optical path, thus the telescope and instrument. The 22 wavelength bins of CHARIS provide a unique opportunity to investigate in detail the wavelength dependence of the instrumental polarization effects. From measurements with the internal light source, we find that the image derotator (K-mirror) produces strong wavelength-dependent crosstalk, in the worst case converting ~95% of the incident linear polarization to circularly polarized light that cannot be measured. Theoretical calculations show that the magnitude of the instrumental polarization of the telescope varies with wavelength between approximately 0.5% and 0.7%, and that its angle is exactly equal to the altitude angle of the telescope. We plan to more accurately determine the instrumental polarization of the telescope with observations of a polarization standard star, and fit more comprehensive physical models to all experimental data. In addition, we plan to integrate the complete Mueller matrix model into the existing CHARIS post-processing pipeline, with the aim to achieve a polarimetric accuracy of <0.1% in the degree of linear polarization. Our calibrations of CHARIS' spectropolarimetric mode will enable unique quantitative polarimetric studies of circumstellar disks and planetary and brown dwarf companions.

3.1 Introduction

The near-infrared (NIR) polarimetric modes of the high-contrast imaging instruments SPHERE-IRDIS (Beuzit et al., 2019; Dohlen et al., 2008; de Boer et al., 2020; Chapter 2) at the Very Large Telescope, Gemini Planet Imager (GPI; Macintosh et al., 2014; Perrin et al., 2015) at the Gemini South Telescope, and HiCIAO (Hodapp et al., 2008) at the Subaru Telescope have been very successful at imaging circumstellar disks of various ages (Garufi et al., 2017; Avenhaus et al., 2018; Esposito et al., 2020; Hashimoto et al., 2011; Muto et al., 2012) using polarimetric differential imaging (PDI). GPI and SPHERE-IRDIS have also been used to search for polarization from planetary and brown dwarf companions (Millar-Blanchaer et al., 2015; Jensen-Clem et al., 2016, 2020; Chapter 4), leading to the detection of polarization from the stellar companion CS Cha B (Ginski et al., 2018; Haffert et al., 2020), and more recently, the first detection of polarization from a planetary mass companion (Chapter 5). In 2017, the Subaru telescope lost its high-spatial resolution NIR imaging polarimetric capability when HiCIAO was decommissioned. The current high-contrast imager is the Subaru Coronagraphic Extreme Adaptive Optics (SCExAO) system (Jovanovic et al., 2015; Lozi et al., 2018). While initially SCExAO had no NIR polarimetric capabilities, recently a spectropolarimetric mode (Lozi et al., 2019b), which is unique among high-contrast imagers, was implemented for its Coronagraphic High Angular Resolution Imaging Spectrograph (CHARIS) subsystem (Groff et al., 2017).

SCExAO is located on the NIR Nasmyth platform of the Subaru telescope, behind the AO188 system (Minowa et al., 2010), which provides an initial low-order wavefront correction. The extreme adaptive optics system of SCExAO consists of a pyramid wavefront sensor that operates at wavelengths in the range 600-900 nm (Lozi et al., 2019a), a deformable mirror with 45 actuators over the pupil, and the real-time control software Compute and Control for Adaptive Optics (Guyon et al., 2018). SCExAO feeds light to several science instruments, among which is CHARIS that provides low-resolution spectra with a resolving power $R = 18$ over the JHK-bands with a field-of-view (FOV) of $2'' \times 2''$. To enable the spectropolarimetric capability, a Wollaston prism, which splits the light into two orthogonal linear polarization states, has been placed directly upstream of CHARIS. The existing half-wave plate (HWP) located upstream of AO188, that was originally implemented for HiCIAO, is used to modulate the incident polarization to be measured.

The accuracy of the CHARIS spectropolarimetric measurements is currently limited by instrumental polarization effects of the telescope and instrument. The dominant effects are instrumental polarization (IP) and polarimetric crosstalk, which both cause the measured polarization state to differ from the true polarization state incident on the telescope. IP is the introduction of polarization signals by the telescope or instrument, and can make an unpolarized target appear to be polarized. It is caused by the diattenuation of an optical component, which is the difference in reflectance or transmission of the two orthogonal linear polarization states. Crosstalk is the conversion of linear to circular polarization (and vice versa) by optical components, and can lower the polarimetric efficiency (the fraction of the incident linear polarization that is actually measured) and can cause an offset of the measured angle of linear polarization. Crosstalk is the result of retardance, which is the

difference in acquired phase between two orthogonal linear polarization states when light reflects of a mirror or transmits through an optic.

To enable unique and highly accurate quantitative polarimetry of circumstellar disks, planets, and brown dwarf companions with the spectropolarimetric mode of CHARIS, we are developing a detailed and fully validated Mueller matrix model that describes the instrumental polarization effects of the telescope and instrument. For this work we follow the methodology and definitions from Chapter 2 as used for the polarimetric calibration of SPHERE-IRDIS. We calibrate the Mueller matrix model with measurements from SCExAO's internal light source and observations of polarization standard stars. For these calibrations, the 22 wavelength bins of CHARIS provide a unique opportunity to investigate in detail the wavelength dependence of the instrumental polarization effects. After completing the calibrations, we will use the model for the post-processing of science observations to correct for the IP and crosstalk. In this chapter, we present the first results of this project.

The outline of this chapter is as follows. In Sect. 3.2 we describe the optical path of SCExAO-CHARIS and explain the Mueller matrix model that describes the instrumental polarization effects of the telescope and instrument. Subsequently, in Sect. 3.3, we outline the calibration measurements we performed with the internal light source, the data reduction, and the fitting of the model parameters to the calibration data. In Sect. 3.4, we then present the results of fitting the model parameters of the HWP and derotator, and discuss theoretical computations of the instrumental polarization introduced by the telescope. Finally, in Sect. 3.5 we present conclusions and a brief outlook on future steps for this project.

3.2 Mathematical description of complete optical system

3.2.1 Optical path of SCExAO-CHARIS

A simplified optical path showing only the components that are relevant for the SCExAO-CHARIS polarimetric mode is presented in Fig. 3.1. The Subaru telescope is an 8-m class, altazimuth-mounted Ritchey-Chrétien telescope located at 4.2 km altitude on the summit of Mauna Kea. During observations the incident light is collected by the primary mirror (M1) and reflected to the secondary mirror (M2) that is suspended at the top of the telescope. The M2 subsequently reflects the light down toward the flat tertiary mirror (M3) that has an angle of incidence of 45° to reflect the light to the Nasmyth platform where SCExAO is located. This M3 is coated with silver for high reflectivity in the NIR wavelength range. While the object moves across the sky during the night, it rotates with the parallactic angle in the pupil of the telescope, and the telescope rotates with respect to the Nasmyth platform to track the altitude angle of the object.

When the light reaches the Nasmyth platform it passes a system that can be inserted into the light beam to perform calibration measurements. This calibration system consists of an internal (calibration) light source, a flat mirror with a 45° angle of incidence, and a manually rotatable linear polarizer. After the calibration system the light reaches an insertable and rotatable broadband half-wave plate (HWP), which is used to temporally

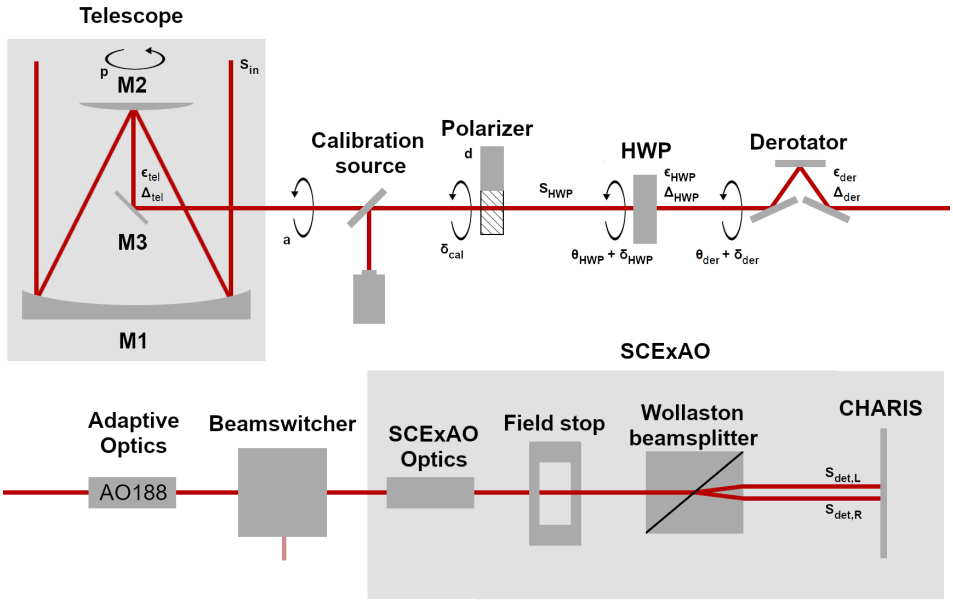


Figure 3.1: Overview of the optical path from the Subaru telescope to SCExAO-CHARIS, showing only the components relevant for polarimetric measurements. Circular arrows next to a component indicate that it is rotatable. The symbols next to the components indicate their model parameters and rotation (offset) angles. Also shown are the Stokes vectors incident on the telescope, the HWP, and the detector. Note that the beam switcher that is included in this figure has not been built at the moment of writing.

modulate the polarization state of the incident light. Following the HWP there is an image derotator, which consists of a three-mirror assembly (K-mirror) on a rotation stage. When the K-mirror rotates, it rotates both the image and the angle of linear polarization. For observations with SCExAO, the image derotator operates in pupil-stabilized mode. The derotator is followed by the adaptive optics of AO188, which includes a deformable mirror to correct for wavefront aberrations and a dichroic beamsplitter to feed the wavefront sensor. All reflections in AO188 are in the horizontal plane (i.e., parallel to the Nasmyth platform).

Currently, SCExAO is located directly behind AO188, and this location is shared by other instruments. Therefore, SCExAO has to be regularly craned in and out of this position for observations. As this process is very cumbersome, a beam switcher with multiple output ports to serve all the instruments on the Nasmyth platform is considered for a future upgrade (Lozi et al., 2017). SCExAO will then be located behind the beam switcher at one of these ports and the need for craning is eliminated. The reflections within the current beam switcher design are exclusively in the horizontal and vertical planes.

Within SCExAO the light has multiple reflections in the horizontal plane before a field stop limits the FOV to 2″×1″. The field stop is followed by a Wollaston prism that splits the light into the orthogonal horizontal and vertical linear polarization states before

it enters CHARIS. Within CHARIS, the light passes a lenslet array and a prism to create a field of spectra in each of the two orthogonal linear polarization states, which then strike the detector side by side.

SCExAO hosts many different coronagraphs to suppress starlight, and most are not expected to affect polarimetric measurements. Two exceptions are the vector vortex coronagraph (Kühn et al., 2018) and the vector-Apodizing Phase Plate (Doelman et al., 2017). However, with their current implementation these coronagraphs cannot be combined with polarimetry (Snik et al., 2014).

To measure the Stokes parameters Q and U and the corresponding total intensities I_Q and I_U, a HWP cycle is performed which consists of four consecutive measurements with HWP switch angles equal to 0°, 45°, 22.5°, and 67.5°. For each wavelength bin, we then compute from the resulting left (L) and right (R) intensities on the detector of each measurement, $I_{\mathrm{det,L}}$ and $I_{\mathrm{det,R}}$, the single difference and single sum as:

$$X^{\pm} = I_{\mathrm{det,L}} - I_{\mathrm{det,R}}, \tag{3.1}$$

$$I_{X^{\pm}} = I_{\mathrm{det,L}} + I_{\mathrm{det,R}}, \tag{3.2}$$

with $X^{\pm}$ the single-difference Q^{+}, Q^{-}, U^{+}, and U^{-} (taken at HWP switch angles 0°, 45°, 22.5°, and 67.5°), and $I_{X^{\pm}}$ the corresponding single-sum intensities $I_{Q^{+}}$, $I_{Q^{-}}$, $I_{U^{+}}$, and $I_{U^{-}}$. We then compute the double difference and double sum as:

$$X = \frac{1}{2}\left(X^{+} - X^{-}\right), \tag{3.3}$$

$$I_X = \frac{1}{2}\left(I_{X^{+}} + I_{X^{-}}\right), \tag{3.4}$$

with X the double-difference Q or U and I_X the double-sum I_Q or I_U.

3.2.2 Mueller matrix model of optical path

To mathematically describe the instrumental polarization effects of the optical system of SCExAO-CHARIS, we create a Mueller matrix model similar to that of Chapter 2 for SPHERE-IRDIS. We use the same definitions of the Stokes parameters, reference frames, and Mueller matrices as described in that work. The relevant Stokes vectors and model parameters describing the components are shown in Fig. 3.1. Because the optical setups of SPHERE-IRDIS and SCExAO-CHARIS are quite similar, the Mueller matrix models of both instruments show many similarities.

The Stokes vectors reaching the left and right halves of the detector, $\boldsymbol{S}_{\mathrm{det,L}}$ and $\boldsymbol{S}_{\mathrm{det,R}}$, can be written in terms of the true Stokes vector incident on the telescope $\boldsymbol{S}_{\mathrm{in}}$ as:

$$\begin{aligned} \boldsymbol{S}_{\mathrm{det,L/R}} &= M_{\mathrm{sys,L/R}}\boldsymbol{S}_{\mathrm{in}}, \\ \begin{bmatrix} I_{\mathrm{det,L/R}} \\ Q_{\mathrm{det,L/R}} \\ U_{\mathrm{det,L/R}} \\ V_{\mathrm{det,L/R}} \end{bmatrix} &= \begin{bmatrix} I\to I & Q\to I & U\to I & V\to I \\ I\to Q & Q\to Q & U\to Q & V\to Q \\ I\to U & Q\to U & U\to U & V\to U \\ I\to V & Q\to V & U\to V & V\to V \end{bmatrix} \begin{bmatrix} I_{\mathrm{in}} \\ Q_{\mathrm{in}} \\ U_{\mathrm{in}} \\ V_{\mathrm{in}} \end{bmatrix}, \end{aligned} \tag{3.5}$$

where $M_{\mathrm{sys,L/R}}$ is the Mueller matrix that describes the instrumental polarization effects of the images on the left or right half of the detector. We can further express $M_{\mathrm{sys,L/R}}$ in terms of the separate components and their rotations as:

$$\begin{aligned} \boldsymbol{S}_{\mathrm{det,L/R}} &= M_{\mathrm{sys,L/R}}\boldsymbol{S}_{\mathrm{in}}, \\ \boldsymbol{S}_{\mathrm{det,L/R}} &= M_{\mathrm{W,L/R}}T(-\Theta_{\mathrm{der}})M_{\mathrm{der}}T(\Theta_{\mathrm{der}})T(-\Theta_{\mathrm{HWP}})M_{\mathrm{HWP}}T(\Theta_{\mathrm{HWP}}) \\ &\quad T(-a)M_{\mathrm{tel}}T(p)\boldsymbol{S}_{\mathrm{in}}, \end{aligned} \tag{3.6}$$

where p is the parallactic angle, a is the telescope altitude angle, and:

$$\Theta_{\mathrm{HWP}} = \theta_{\mathrm{HWP}} + \delta_{\mathrm{HWP}}, \tag{3.7}$$

$$\Theta_{\mathrm{der}} = \theta_{\mathrm{der}} + \delta_{\mathrm{der}}, \tag{3.8}$$

with θ_{HWP} the HWP angle, θ_{der} the derotator angle, δ_{HWP} the HWP offset angle, and δ_{der} the derotator offset angle. The rotations of the components and Stokes vectors are described with the rotation matrix $T(\theta)$:

$$T(\theta) = \begin{bmatrix} 1 & 0 & 0 & 0 \\ 0 & \cos(2\theta) & \sin(2\theta) & 0 \\ 0 & -\sin(2\theta) & \cos(2\theta) & 0 \\ 0 & 0 & 0 & 1 \end{bmatrix}. \tag{3.9}$$

The Mueller matrices M_{tel}, M_{HWP}, and M_{der} describe the three mirrors of the telescope, the HWP, and the three mirrors of the image derotator, respectively, and are defined as the component Mueller matrix M_{com}:

$$M_{\mathrm{com}} = \begin{bmatrix} 1 & \epsilon & 0 & 0 \\ \epsilon & 1 & 0 & 0 \\ 0 & 0 & \sqrt{1-\epsilon^2}\cos\Delta & \sqrt{1-\epsilon^2}\sin\Delta \\ 0 & 0 & -\sqrt{1-\epsilon^2}\sin\Delta & \sqrt{1-\epsilon^2}\cos\Delta \end{bmatrix}, \tag{3.10}$$

where ϵ is the diattenuation and Δ is the retardance of the component. The optical components downstream of the derotator, except for the Wollaston prism, to first order do not affect our measurements (see Chapter 2). All reflections downstream of the derotator lie in the horizontal (and vertical) plane, and therefore these components do not produce crosstalk affecting the horizontal or linear polarization states that pass the Wollaston prism. In addition, because we compute the Stokes parameters Q and U from the double difference, any diattenuation produced downstream of the derotator is removed. The matrix $M_{\mathrm{W,L/R}}$ therefore only describes the left and right channels of the Wollaston prism:

$$M_{\mathrm{W,L/R}} = \frac{1}{2}\begin{bmatrix} 1 & \pm 1 & 0 & 0 \\ \pm 1 & 1 & 0 & 0 \\ 0 & 0 & 0 & 0 \\ 0 & 0 & 0 & 0 \end{bmatrix}, \tag{3.11}$$

where the plus- and minus-signs are used for the left and right detector halves, respectively. This Mueller matrix represents a perfect polarizing beamsplitter, because the extinction ratio of Wollaston prisms exceeds 100.000:1 (King & Talim, 1971).

To model the measurement of a Stokes parameter and the corresponding total intensity from a pair of measurements, we calculate for each measurement $\boldsymbol{S}_{\mathrm{det,L}}$ and $\boldsymbol{S}_{\mathrm{det,R}}$ from Eq. (3.6) and retrieve $I_{\mathrm{det,L}}$ and $I_{\mathrm{det,R}}$ from the first element of these vectors. Subsequently, we compute the single differences $X^{\pm}$ and single sums $I_{X^{\pm}}$ from Eqs. (3.1) and (3.2), and the double-difference X and double-sum I_X from Eqs. (3.3) and (3.4). Finally, we compute the normalized Stokes parameter x, as:

$$x = \frac{X}{I_X}. \tag{3.12}$$

We note that only for measurement pairs using HWP switch angles equal to 0°, 45°, 22.5°, and 67.5° the Stokes parameters X and x correspond to Q, U, q, and u.

3.3 Measurements and data reduction

With the Mueller matrix model of the optical system defined, we can now experimentally determine the model parameters describing the optical path downstream of the telescope. To this end, we took a total of 340 calibration measurements with the internal (calibration) light source on February 19, 2020. The calibration polarizer, which is located downstream of the light source (see Fig. 3.1), was inserted in the optical path with its transmission axis at 45° to the horizontal. This setup therefore injected almost 100% positive U-polarized light into the system. The measurements were taken at many combinations of HWP and derotator angles, with the HWP angle ranging from 0° to 78.75° with steps of 11.25°, and the derotator angle ranging from 45° to 127.5° in steps of 7.5°. The aim of these measurements is to fit the retardances and offset angles of the HWP and the derotator. We cannot use these measurements to fit the diattenuations of the HWP and the derotator, because for that we would need measurements without the calibration polarizer inserted. However, because these diattenuations are expected to be very small (as is the case for SPHERE-IRDIS; Chapter 2) we did not take such measurements.

We preprocess the raw data with the CHARIS data-reduction pipeline[1] (Brandt et al., 2017) using the standard settings (given by the examples in the documentation) for the wavelength calibration and data extraction. The result is a three-dimensional data cube with two spatial axes and one spectral axis with 22 wavelength bins. One of the images resulting from the preprocessing (for a single wavelength bin) is shown in Fig. 3.2. The square 2″×2″ image is divided into a left and right 2″×1″ rectangular image, corresponding to the two orthogonal linear polarization states.

After the preprocessing is completed, we retrieve the normalized Stokes parameters from the images for each of the 22 wavelength bins. To this end, we define eight square apertures on both the left and right halves of each image (see Fig. 3.2), and sum the flux in each of the apertures. We then compute eight values for the single difference and single sum (following Eqs. (3.1) and (3.2)) by respectively subtracting and adding the summed flux in apertures marked by the same number in Fig. 3.2. Subsequently, we compute values for the double difference and double sum (following Eqs. (3.3) and (3.4)) from the single-difference and single-sum values computed from images that were taken at the

[1] http://princetonuniversity.github.io/charis-dep

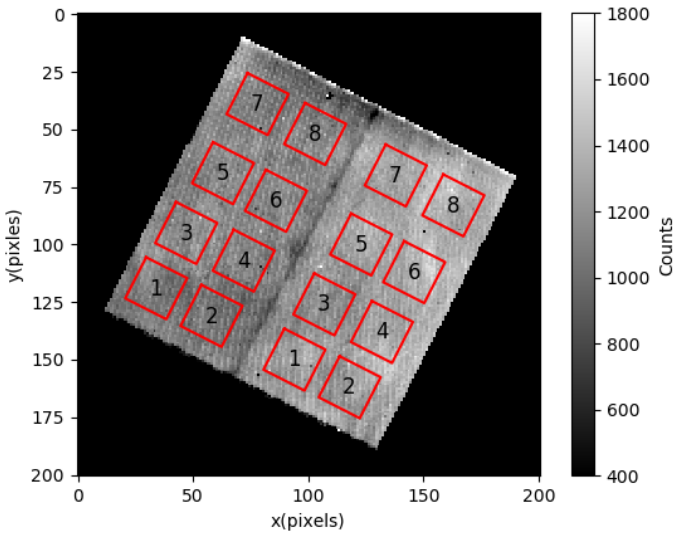


Figure 3.2: Preprocessed image of a single wavelength bin showing the left and right 2″×1″ rectangular images of the two orthogonal linear polarization states. Eight square apertures, which are used to compute the single-difference and single-sum values, are shown in red on each rectangular image.

same derotator angle and at HWP angles that differ by 45°. Finally, we compute the normalized Stokes parameters by dividing the resulting double-difference values by the corresponding double-sum values (following Eq. (3.12)).

To describe the measurements, we apply Eq. (3.12) and insert Eqs. (3.1)–(3.11). We only use the part of Eq. (3.6) downstream of the telescope:

$$\boldsymbol{S}_{\mathrm{det,L/R}} = M_{\mathrm{W,L/R}} T(-\Theta_{\mathrm{der}}) M_{\mathrm{der}} T(\Theta_{\mathrm{der}}) T(-\Theta_{\mathrm{HWP}}) M_{\mathrm{HWP}} T(\Theta_{\mathrm{HWP}}) \boldsymbol{S}_{\mathrm{HWP}}, \tag{3.13}$$

where $\boldsymbol{S}_{\mathrm{HWP}} = T(45° - \delta_{\mathrm{cal}})[1, d, 0, 0]^T$ is the Stokes vector incident on the HWP, with δ_{cal} and d respectively the offset angle and diattenuation of the calibration polarizer.

We now fit our model to the data points using non-linear least squares. We use the Powell algorithm as implemented in the Python function `scipy.optimize.minimize`. For each of the 22 wavelength bins we fit the retardance of the HWP Δ_{HWP}, the retardance of the derotator Δ_{der}, the HWP angle offset δ_{HWP}, and the diattenuation of the calibration polarizer d. For the angle offsets of the derotator and the calibration polarizer, δ_{der} and δ_{cal}, we fit only a single value valid for all wavelength bins. Because we cannot accurately determine the diattenuations of the derotator and HWP from these measurements with the calibration polarizer inserted, we set ϵ_{HWP} and ϵ_{der} to their ideal values of 0.

3.4 Results

3.4.1 Instrumental polarization effects of the HWP and derotator

The fitted values for the retardance of the derotator and the HWP as a function of wavelength are shown in Fig. 3.3. The derotator retardance Δ_{der} ideally has a constant value of 180°. However, as shown in Fig. 3.3 (left), the retardance strongly varies with wavelength. At $\lambda = 1180$ nm the retardance has a value of $\Delta_{\mathrm{der}} \approx 250°$, then rapidly drops off to $\Delta_{\mathrm{der}} \approx 70°$ for $\lambda = 1800$ nm, and stabilizes around values between 60° and 65° for wavelengths between 1800 and 2400 nm. Around $\lambda = 1600$ nm, the retardance is close to 90°, which means that the derotator acts as an almost perfect quarter-wave plate (QWP) and thus converts almost all incident linear polarization to circular polarization. For the derotator offset angle, we assumed a constant value with wavelength and find $\delta_{\mathrm{der}} = -0.42°$.

The HWP retardance Δ_{HWP} is plotted in Fig. 3.3 (right). As with the derotator, the HWP retardance would ideally have a constant value of 180°. However, we find that Δ_{HWP} varies between 167.5° and 185° for the measured wavelength range, and that it is exactly half wave around $\lambda = 2200$ nm. The measured retardance curve is very similar to that of commercially available achromatic HWPs[2]. For $\lambda < 1400$ nm, the fitted retardance values are very noisy and do not follow a smooth curve as we would expect from the physics of wave plates. We have not yet determined the exact cause for this behavior. For our fit of the model parameters, we have allowed the HWP offset angle δ_{HWP} to vary with wavelength and find that it indeed varies between −0.4° and −0.8°. However, the orientation of the optic axis of an achromatic HWP cannot vary with wavelength due to the relatively simple design of such a wave plate. Therefore the wavelength variations of the HWP offset angle are most likely not physical and we adopt the mean value of −0.6° as the HWP offset angle for all wavelength bins.

In Fig. 3.4 we show the fitted values for the diattenuation of the calibration polarizer d as a function of wavelength. It shows that the diattenuation is relatively constant ($0.98 < d \leq 1$) between 1180 and 2200 nm and drops sharply for $\lambda > 2200$ nm. This sharp drop can be explained by a sudden decrease in optical performance or, more likely, by a measurement bias due to the increasing thermal background of the instrument at these longer wavelengths. For the offset angle of the calibration polarizer, we assumed a constant value with wavelength and find $\delta_{\mathrm{cal}} = 0.76°$.

By comparing the measured degree of linear polarization $P = \sqrt{(q^2 + u^2)}$ and angle of linear polarization $\chi = {}^1/_2 \arctan(u/q)$ with the values these quantities would have if the optical components were ideal, we can calculate the polarimetric efficiency and offset of the angle of linear polarization. The results of these calculations for various wavelengths are shown as a function of derotator angle in Fig. 3.5. In the ideal case, the polarimetric efficiency would be 100% for all derotator angles and wavelengths. However, as shown in Fig. 3.5 (left), the polarimetric efficiency shows strong variations with derotator angle. The polarimetric efficiency is minimized for derotator angles around 45° and 135°, and is maximized for derotator angles close to 0°, 90° and 180°. This behaviour is due to the derotator having a retardance that is not equal to 180° (see Fig. 3.3, left). For derotator

[2] https://www.thorlabs.com/newgrouppage9.cfm?objectgroup_id=2193

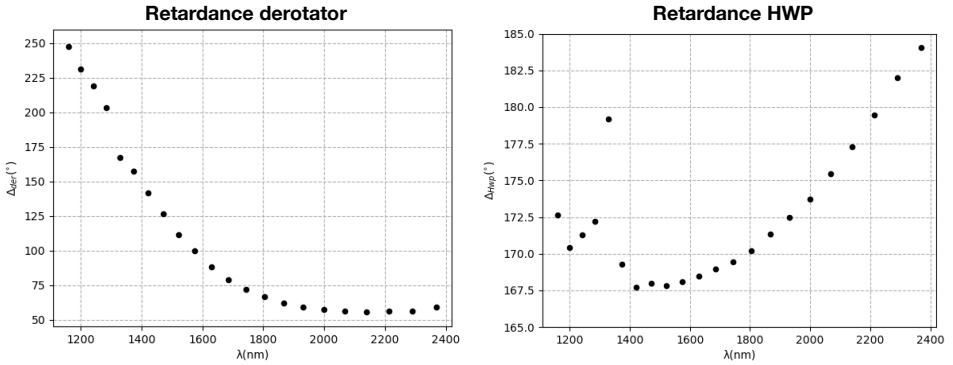


Figure 3.3: Fitted retardances of the derotator (*left*) and the HWP (*right*) as a function of wavelength. Ideally, the derotator and HWP would have a retardance of 180° for all wavelengths.

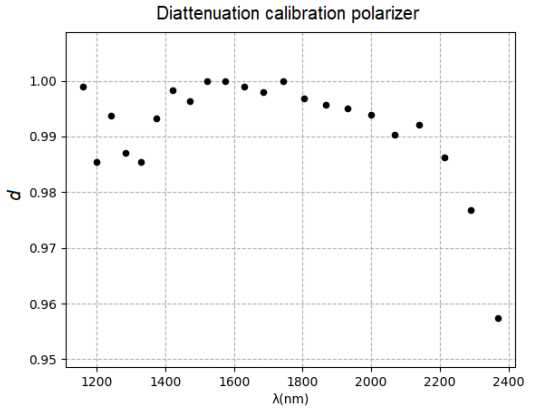


Figure 3.4: Fitted diattenuation of the calibration polarizer as a function of wavelength. Ideally, the diattenuation would have a value of 1 for all wavelengths.

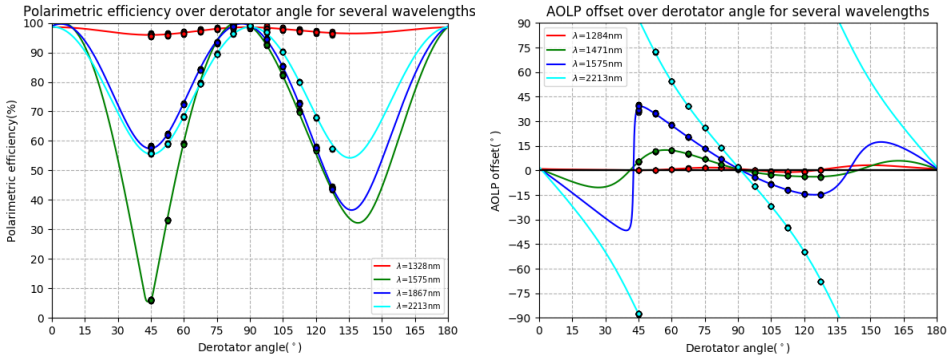


Figure 3.5: Measured polarimetric efficiency (*left*) and offset of the angle of linear polarization (AOLP; *right*) as a function of derotator angle for various wavelengths. Ideally, the polarimetric efficiency would be 100% and the offset of the angle of linear polarization 0° for all wavelengths and derotator angles. We note that the two panels show slightly different wavelength bins.

angles close to 45° and 135°, the derotator is optimally oriented to convert the horizontal and vertical polarization states to circular polarization, which cannot be measured using the Wollaston prism. The asymmetry between the minima of the polarimetric efficiency at derotator angles of 45° and 135° is caused by the HWP retardance being offset from 180°.

From Fig. 3.5 (left), we also see that the derotator retardance varies strongly with wavelength. For $\lambda = 1575$ nm the polarimetric efficiency even drops to a value close to 5% at a derotator angle of 45°. An overview of the minimum polarimetric efficiency as a function of wavelength is plotted in Fig. 3.6. This figure shows that the polarimetric efficiency peaks around $\lambda = 1300$ nm, when the derotator retardance is closest to 180° (see Fig. 3.3, left). We also see that at wavelengths around $\lambda = 1600$ nm the lowest polarimetric efficiency can be reached, because at these wavelengths the derotator acts as an almost perfect QWP.

For an ideal instrument, there would be no offset of the angle of linear polarization for all derotator angles and wavelengths. However, as shown in Fig. 3.5 (right), the derotator retardance does not only decrease the polarimetric efficiency, but also introduces a non-zero offset of the angle of linear polarization. The offset is strongest for derotator angles close to 45° and 135° where the polarimetric efficiency is lowest, and is close to zero for derotator angles around 0°, 90°, and 180°. Similar to the curves of the polarimetric efficiency, the curves for the angle offset show an asymmetry between derotator angles of 45° and 135° that is caused by the non-ideal value of the HWP retardance. As with the polarimetric efficiency, we find that the angle offset strongly varies with wavelength. For several wavelength bins the offset angle can even be as large as ±90°.

Finally, we note that the results discussed in this subsection are very similar to those presented for SPHERE-IRDIS in Chapter 2. One reason for this is that the optical setups of SPHERE-IRDIS and SCExAO-CHARIS are quite similar. However, the results also suggests that the design of the HWP and the coating of the derotator are comparable to those used for SPHERE.

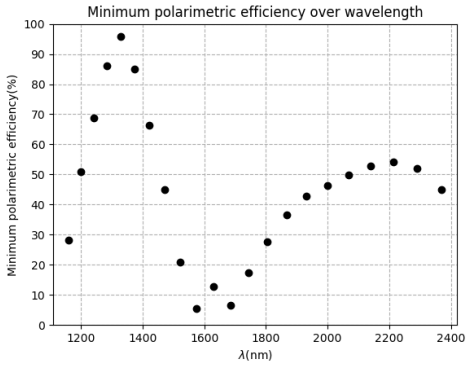


Figure 3.6: Minimum polarimetric efficiency as a function of wavelength.

3.4.2 Instrumental polarization of the telescope

The instrumental polarization (IP) of the telescope is almost completely created by the telescope's tertiary mirror (M3). This silver-coated mirror has an angle of incidence of 45° and deflects the light arriving from the secondary mirror to the Nasmyth platform where SCExAO is located. The first and secondary mirror of the telescope are axisymmetric and therefore do not create significant instrumental polarization (Tinbergen, 2005).

We can theoretically predict the IP of the telescope by computing the diattenuation ϵ of M3 for each wavelength bin with the Fresnel equations. For this calculation we obtain the refractive indices of silver from Rakić et al. (1998). We describe the measurements with only the part of Eq. (3.6) upstream of the HWP:

$$\boldsymbol{S}_{\mathrm{HWP}} = T(-a)M_{\mathrm{tel}}T(p)\boldsymbol{S}_{\mathrm{in}}. \tag{3.14}$$

We set $\boldsymbol{S}_{\mathrm{in}} = [1, 0, 0, 0]^T$, and retrieve the normalized Stokes parameters q and u from the second and third elements of $\boldsymbol{S}_{\mathrm{HWP}}$.

Figure 3.7 (left) shows the resulting q and u as a function of telescope altitude angle for four of the wavelength bins, including the bins of the shortest and longest wavelengths. The shape of the curves can be explained as follows. M3 produces IP that is oriented perpendicular to the plane of incidence of the mirror, and this plane of incidence rotates with respect to the instrument when the telescope altitude angle is changed. Whereas the degree of linear polarization $P = \epsilon$ of this IP signal does not change with altitude angle, the angle of linear polarization is exactly equal to the altitude angle: $\chi = a$. The normalized Stokes parameters thus vary as $q = \epsilon\cos(2a)$ and $u = \epsilon\sin(2a)$. We note that the shape of the curves for q and u differ from those determined for SPHERE-IRDIS in Chapter 2 because in that case the IP of both the telescope and the first mirror of SPHERE (M4) are considered.

From Fig. 3.7 (left) we also see that the IP is different for the various wavelength bins plotted. In Fig. 3.7 (right) we therefore show the IP (the diattenuation) for each of the 22 wavelength bins. The IP is largest for the shortest wavelength (~0.7%), and decreases monotonically for longer wavelengths to a value of ~0.5%. This behavior is exactly the

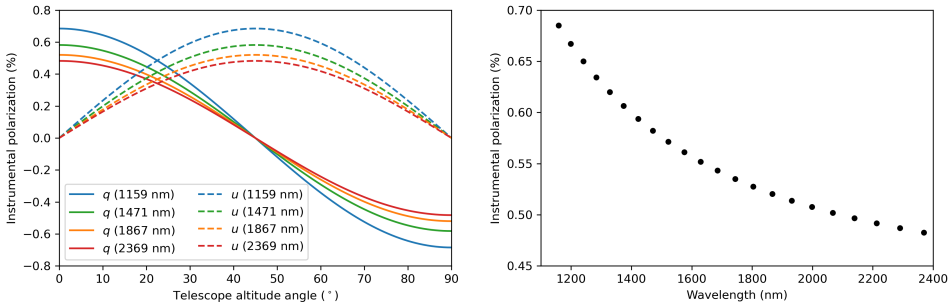


Figure 3.7: Theoretically predicted instrumental polarization of the telescope expressed as the normalized Stokes parameters q and u as a function of telescope altitude angle for four wavelength bins (*left*) and as the diattenuation for the 22 wavelength bins (*right*).

same as that found for the telescope of SPHERE-IRDIS in Chapter 2. However, in that case the IP is overall larger, because the M3 of the Very Large Telescope is coated with aluminum rather than silver.

Although the results presented in Fig. 3.7 are qualitatively accurate, the exact values for the diattenuation at each wavelength bin will differ in reality. We have therefore observed the polarization standard star HD 283809 (Messinger et al., 1997) during the SCExAO engineering nights on 31 January, and 9 February 2020. This polarization standard star has a well-measured degree and angle of linear polarization that we will use to accurately calibrate the IP of the telescope as a function of wavelength.

3.5 Conclusions and outlook

In this chapter we have presented the first results of our efforts to characterize the instrumental polarization effects of the spectropolarimetric mode of SCExAO-CHARIS. We have created a detailed Mueller matrix model describing the telescope and instrument. Using measurements with the internal light source and a calibration polarizer, we have determined the retardance of the derotator and the HWP for each of the 22 wavelength bins. We find that the retardance of the derotator strongly varies with wavelength (with values between 50° and 250°), and that it acts as an almost perfect quarter-wave plate (QWP) at wavelengths around 1600 nm. The retardance of the HWP varies between 167.5° and 185° over the wavelength range considered. The curve of the retardance versus wavelength suggests that the HWP is an achromatic wave plate, similar to those commercially available. The non-ideal values of the derotator retardance results for some wavelengths in very low polarimetric efficiencies at derotator angles around 45° and 135°. In the worst case, at wavelengths close to 1600 nm, ~95% of the incident linear polarization is converted to circular polarization that cannot be measured. The variations in the polarimetric efficiency are accompanied by offsets of the angle of linear polarization that can be as large as ±90°. These results are very similar to those obtained with calibrations of SPHERE-IRDIS as presented in Chapter 2.

To estimate the instrumental polarization (IP) of the telescope, we have performed theoretical calculations for each wavelength bin using the Fresnel equations. We find that the degree of linear polarization of the IP does not vary with the telescope altitude angle. This degree of linear polarization is largest (~0.7%) for the shortest wavelengths, and decreases monotonically for longer wavelengths to a value of ~0.5%. The angle of linear polarization of the IP is exactly equal to the altitude angle of the telescope.

In the future, we plan to accurately determine the IP of the telescope with measurements of the polarization standard star HD 283809 that we recently obtained. We will also fit comprehensive physical models to all calibration data, including models that accurately describe the design of the HWP and the coating of the derotator. Subsequently, we will perform a careful error analysis to determine the polarimetric accuracy of our model. Finally, we will integrate the complete Mueller matrix model into the existing CHARIS post-processing pipeline (Currie et al., 2011; Currie et al., 2012, 2018), with the aim to achieve a polarimetric accuracy of <0.1% in the degree of linear polarization. This pipeline will be comparable to the IRDAP pipeline[3] (Chapter 2) for SPHERE-IRDIS, and will be made publicly available to the community.

The spectropolarimetric mode of CHARIS is one of three polarimetric modes currently available at SCExAO. A fast polarimetry mode combined with non-redundant aperture masking interferometry is offered in the visible (600-800 nm) by the VAMPIRES instrument (Norris et al., 2015). Currently under development is a fast NIR polarimetry mode employing a ferroelectric liquid crystal that provides fast polarization modulation (up to a ~1 kHz) in synchronisation with a C-RED ONE camera (Feautrier et al., 2017), and a Wollaston prism to split the orthogonal linear polarization states. Compared to CHARIS, these two additional modes operate with different polarization-sensitive components, and use either different wavelength ranges or different bandwidths. To enable accurate polarimetry with these modes as well, separate polarimetric calibration measurements need to be performed. Our calibrations of CHARIS' spectropolarimetric mode will enable unique quantitative polarimetric studies of circumstellar disks and planetary and brown dwarf companions.

References

Avenhaus, H., Quanz, S. P., Garufi, A., et al. 2018, The Astrophysical Journal, 863, 44
Beuzit, J.-L., Vigan, A., Mouillet, D., et al. 2019, Astronomy & Astrophysics, 631, A155
Brandt, T. D., Rizzo, M., Groff, T., et al. 2017, Journal of Astronomical Telescopes, Instruments, and Systems, 3, 048002
Currie, T., Burrows, A., Itoh, Y., et al. 2011, The Astrophysical Journal, 729, 128
Currie, T., Debes, J., Rodigas, T. J., et al. 2012, The Astrophysical Journal Letters, 760, L32
Currie, T., Brandt, T. D., Uyama, T., et al. 2018, The Astronomical Journal, 156, 291
de Boer, J., Langlois, M., van Holstein, R. G., et al. 2020, Astronomy & Astrophysics, 633, A63
Doelman, D. S., Snik, F., Warriner, N. Z., & Escuti, M. J. 2017, in Techniques and Instrumentation for Detection of Exoplanets VIII, Vol. 10400, International Society for Optics and Photonics, 104000U

[3] https://irdap.readthedocs.io

Dohlen, K., Langlois, M., Saisse, M., et al. 2008, in Ground-based and Airborne Instrumentation for Astronomy II, Vol. 7014, International Society for Optics and Photonics, 70143L
Esposito, T. M., Kalas, P., Fitzgerald, M. P., et al. 2020, The Astronomical Journal, 160, 24
Feautrier, P., Gach, J.-L., Greffe, T., et al. 2017, in Image Sensing Technologies: Materials, Devices, Systems, and Applications IV, Vol. 10209, International Society for Optics and Photonics, 102090G
Garufi, A., Benisty, M., Stolker, T., et al. 2017, arXiv preprint arXiv:1710.02795
Ginski, C., Benisty, M., van Holstein, R., et al. 2018, Astronomy & Astrophysics, 616, A79
Groff, T., Chilcote, J., Brandt, T., et al. 2017, in Techniques and Instrumentation for Detection of Exoplanets VIII, Vol. 10400, International Society for Optics and Photonics, 1040016
Guyon, O., Sevin, A., Gratadour, D., et al. 2018, in Adaptive Optics Systems VI, Vol. 10703, International Society for Optics and Photonics, 107031E
Haffert, S., van Holstein, R., Ginski, C., et al. 2020, Astronomy & Astrophysics, 640, L12
Hashimoto, J., Tamura, M., Muto, T., et al. 2011, The Astrophysical Journal Letters, 729, L17
Hodapp, K. W., Suzuki, R., Tamura, M., et al. 2008, in Ground-based and Airborne Instrumentation for Astronomy II, Vol. 7014, International Society for Optics and Photonics, 701419
Jensen-Clem, R., Millar-Blanchaer, M., Mawet, D., et al. 2016, The Astrophysical Journal, 820, 111
Jensen-Clem, R., Millar-Blanchaer, M. A., van Holstein, R. G., et al. 2020, The Astronomical Journal, 160, 286
Jovanovic, N., Martinache, F., Guyon, O., et al. 2015, Publications of the Astronomical Society of the Pacific, 127, 890
King, R., & Talim, S. 1971, Journal of Physics E: Scientific Instruments, 4, 93
Kühn, J., Serabyn, E., Lozi, J., et al. 2018, Publications of the Astronomical Society of the Pacific, 130, 035001
Lozi, J., Jovanovic, N., Guyon, O., et al. 2019a, Publications of the Astronomical Society of the Pacific, 131, 044503
Lozi, J., Guyon, O., Jovanovic, N., et al. 2017, Proceedings of Adaptive Optics for Extremely Large Telescopes 5 (AO4ELT5)
Lozi, J., Guyon, O., Jovanovic, N., et al. 2018, in Adaptive Optics Systems VI, Vol. 10703, International Society for Optics and Photonics, 1070359
Lozi, J., Guyon, O., Jovanovic, N., et al. 2019b, in 6th International Conference on Adaptive Optics for Extremely Large Telescopes, AO4ELT 2019
Macintosh, B., Graham, J. R., Ingraham, P., et al. 2014, Proceedings of the National Academy of Sciences, 111, 12661
Messinger, D., Whittet, D., & Roberge, W. 1997, The Astrophysical Journal, 487, 314
Millar-Blanchaer, M. A., Graham, J. R., Pueyo, L., et al. 2015, The Astrophysical Journal, 811, 18
Minowa, Y., Hayano, Y., Oya, S., et al. 2010, in Adaptive Optics Systems II, Vol. 7736, International Society for Optics and Photonics, 77363N
Muto, T., Grady, C., Hashimoto, J., et al. 2012, The Astrophysical Journal Letters, 748, L22
Norris, B., Schworer, G., Tuthill, P., et al. 2015, Monthly Notices of the Royal Astronomical Society, 447, 2894
Perrin, M. D., Duchene, G., Millar-Blanchaer, M., et al. 2015, The Astrophysical Journal, 799, 182
Rakić, A. D., Djurišić, A. B., Elazar, J. M., & Majewski, M. L. 1998, Applied optics, 37, 5271
Snik, F., Otten, G., Kenworthy, M., Mawet, D., & Escuti, M. 2014, in Ground-based and Airborne Instrumentation for Astronomy V, Vol. 9147, International Society for Optics and Photonics, 91477U
Tinbergen, J. 2005, Astronomical polarimetry (Cambridge University Press)

4 | Combining angular differential imaging and accurate polarimetry with SPHERE-IRDIS to characterize young giant exoplanets

Adapted from

R. G. van Holstein, F. Snik, J. H. Girard, J. de Boer, C. Ginski, C. U. Keller, D. M. Stam, J.-L. Beuzit, D. Mouillet, M. Kasper, M. Langlois, A. Zurlo, R. J. de Kok, and A. Vigan

Techniques and Instrumentation for Detection of Exoplanets VIII, Proceedings of the SPIE, 10400, 1040015 (2017)

Young giant exoplanets emit infrared radiation that can be linearly polarized up to several percent. This linear polarization can trace: 1) the presence of atmospheric cloud and haze layers, 2) spatial structure, for example cloud bands and rotational flattening, 3) the spin axis orientation and 4) particle sizes and cloud top pressure. We introduce a novel high-contrast imaging scheme that combines angular differential imaging (ADI) and accurate near-infrared polarimetry to characterize self-luminous giant exoplanets. We implemented this technique at VLT/SPHERE-IRDIS and developed the corresponding observing strategies, the polarization calibration and the data-reduction approaches. The combination of ADI and polarimetry is challenging, because the field rotation required for ADI negatively affects the polarimetric performance. By combining ADI and polarimetry we can characterize planets that can be directly imaged with a very high signal-to-noise ratio. We use the IRDIS pupil-tracking mode and combine ADI and principal component analysis to reduce speckle noise. We take advantage of IRDIS' dual-beam polarimetric mode to eliminate differential effects that severely limit the polarimetric sensitivity (flat-fielding errors, differential aberrations and seeing), and thus further suppress speckle noise. To correct for instrumental polarization effects, we apply a detailed Mueller matrix model that describes the telescope and instrument and that has an absolute polarimetric accuracy $\leq$0.1%. Using this technique we have observed the planets of HR 8799 and the (substellar) companion PZ Tel B. Unfortunately, we do not detect a polarization signal in a first analysis. We estimate preliminary 1σ upper limits on the degree of linear polarization of $\sim$1% and $\sim$0.1% for the planets of HR 8799 and PZ Tel B, respectively. The achieved sub-percent sensitivity and accuracy show that our technique has great promise for characterizing exoplanets through direct-imaging polarimetry.

4.1 Introduction

Direct imaging enables the characterization of the atmospheres of self-luminous, hot, massive planets with photometry and spectroscopy. With these methods, the planets' luminosity and atmospheric composition, structure and temperature can be constrained (see e.g., Lafrenière et al., 2008; Ingraham et al., 2014; Chilcote et al., 2015; Macintosh et al., 2015; Zurlo et al., 2016). Additional information on the composition and structure of planetary (or substellar companion) atmospheres can be deduced with polarimetry.

Not only the starlight that an exoplanet reflects is expected to be linearly polarized (Seager et al., 2000; Stam et al., 2004), but also the thermal emission of a planet (or brown dwarf), as this radiation from inside the atmosphere will be scattered by cloud and haze particles on its way up (Sengupta & Marley, 2010; de Kok et al., 2011; Stolker et al., 2017). If the companion is spherically symmetric, polarization signals from different parts on its surface will cancel each other and the integrated degree of linear polarization will be zero (de Kok et al., 2011). Therefore, for a net polarization signal to arise in the thermally emitted radiation, the companion must feature asymmetries such as equatorial flattening due to rapid rotation, patchy clouds or spots in the atmosphere (de Kok et al., 2011), or an obscuring moon (Sengupta & Marley, 2016) or a circumplanetary disk (Stolker et al., 2017). The degree of linear polarization at near-infrared wavelengths of hot exoplanets featuring such asymmetries is expected to be generally larger than 0.1% and could be up to several percent in some cases (de Kok et al., 2011; Stolker et al., 2017).

Measurements of the polarized thermal emission of exoplanets could provide information on the presence and patchiness of atmospheric clouds and hazes, the cloud top pressure, spatial structure (the asymmetries mentioned above), and the surface gravity and mass of the companion (de Kok et al., 2011; Marley & Sengupta, 2011). To disentangle the various possible causes of the polarization, polarimetric follow-up observations are needed. By determining the angle of linear polarization, the planet's projected spin axis could be constrained (de Kok et al., 2011). If the polarization signal is periodic, it could indicate the presence of persistent storms, such as Jupiter's Great Red Spot, and reveal atmospheric rotation rates. Finally, combining polarimetric measurements with flux measurements could reveal atmospheric particle properties, such as albedo and size. The information on the atmospheric composition and structure revealed through polarimetry will significantly increase the accuracy of fitting atmospheric models based on known spectra of field brown dwarfs and substellar companions to spectroscopic exoplanet observations, which currently results in errors of at least 10% (Ingraham et al., 2014; Chilcote et al., 2015; Bonnefoy et al., 2016).

Near-infrared polarimetry has already been successfully performed for dozens of field brown dwarfs, yielding degrees of linear polarization between 0.1 to 2.5% in the I-band (Sengupta & Marley, 2010) and up to 0.8% in the Z- and J-bands (Miles-Páez et al., 2013). For these field dwarfs, the polarization likely arises from patchy clouds. The polarization signals of exoplanets are expected to be stronger, because exoplanets have a lower surface gravity, hence a stronger flattening for a given rotation rate, and a lower effective atmospheric temperature can yield stronger polarization signals for a given temperature gradient (de Kok et al., 2011). With the recently comissioned high-contrast imaging polarimeters SPHERE and GPI, detecting these polarization signals is now technically

feasible. Measurements of the thermal polarization signals of the planets of HR 8799 have already been attempted with VLT/NACO by Juan Ovelar (2013) and recently of HD 19467 B with GPI by Jensen-Clem et al. (2016), but the contrasts attained were insufficient for a detection. The first direct measurement of exoplanetary polarization signals has therefore yet to be performed.

SPHERE (Spectro-Polarimetric High-contrast Exoplanet REsearch) is a high-contrast imaging instrument employing extreme adaptive optics, stellar coronagraphs and three imagers to directly image and characterize giant exoplanets orbiting nearby stars (Beuzit et al., 2008). It is installed on the Nasmyth platform of UT3 of the Very Large Telescope (VLT). One of the imagers, the InfraRed Dual-band Imager and Spectrograph (IRDIS; Dohlen et al., 2008) is primarily designed for detecting hot young exoplanets. It also has a dual-beam polarimetric mode that is mainly used for high-contrast imaging of circumstellar disks (Langlois et al., 2014; de Boer et al., 2020). Since IRDIS has detected exoplanets with huge signal-to-noise ratio (S/N > 200 for some planets of HR 8799; Zurlo et al., 2016), exoplanetary polarization signals could be detected for the first time with this polarimetric mode. Because the expected polarization signals are at most a small fraction (<1%) of the total thermal signal of a planet, we need to achieve a polarimetric sensitivity, that is, the noise level in the degree of linear polarization, and an absolute polarimetric accuracy, that is, the uncertainty in the measured polarization signal, of ~0.1%.

In an attempt at measuring polarization signals of substellar companions, we have observed the four young giant planets HR 8799 bcde (Marois et al., 2008, 2010) and the (substellar) companion PZ Tel B (Biller et al., 2010; Mugrauer et al., 2010) with SPHERE-IRDIS. The planets of HR 8799 could be polarized, because recent spectral measurements have revealed sub-micron dust particles in their atmospheres (Bonnefoy et al., 2016). In addition, temporal variations in near-infrared gaseous absorption features, such as those of CH_4, strongly suggest the presence of patchy clouds (Oppenheimer et al., 2013). PZ Tel B is a very bright companion in an eccentric orbit seen edge-on (Ginski et al., 2014; Maire et al., 2016). If its spin axis is perpendicular to its orbital plane, polarization due to rotational flattening could be detected.

To achieve the required polarimetric sensitivity and accuracy, we combine angular differential imaging (ADI; Marois et al., 2006) with IRDIS' dual-beam polarimetric mode (see Juan Ovelar, 2013) and correct for instrumental polarization effects with the detailed Mueller matrix model described in Chapter 2. In comparison to the recent attempt to measure near-infrared exoplanetary polarization with GPI (Jensen-Clem et al., 2016), we observe longer time sequences to take full advantage of ADI and apply more advanced ADI and polarimetric demodulation techniques. In Sects. 4.2 and 4.3, we describe the measurement technique and observations, respectively. Subsequently, we discuss the data-reduction scheme we developed for the observations in Sect. 4.4. In Sect. 4.5 we then present the results and in Sect. 4.6 we discuss the measurement technique and possible improvements to the data-reduction. Finally, we present conclusions in Sect. 4.7.

4.2 Measurement technique

The polarization signals of young giant exoplanets are expected to be a few tenths of a percent to a percent of the total intensity of the planets. To detect these polarization signals, we need to observe planets that can be directly imaged with a very high signal-to-noise ratio. IRDIS uses a (non-polarizing) beamsplitter and a pair of polarizers with orthogonal transmission axes to simultaneously create two adjacent images on the detector (Langlois et al., 2014; de Boer et al., 2020). This dual-beam system allows us to perform beam switching with the half wave plate (HWP) and to compute the Stokes parameters Q and U from the double difference (see Sect. 4.4.2; Bagnulo et al., 2009), thereby eliminating differential effects that severely limit polarimetric sensitivity, such as flat-fielding errors, differential aberrations and seeing (see e.g., Canovas et al., 2011). To attain the high contrast required for polarimetry of exoplanets, we observe in pupil-tracking mode and construct both the total intensity and polarization images by combining ADI with principal component analysis (PCA; Amara & Quanz, 2012; Soummer et al., 2012; Meshkat et al., 2014) to significantly reduce speckle noise, the principle noise component. The combination of ADI and polarimetry further suppresses speckle noise (especially at small angular separations from the star), because stars, and therefore the speckles, are generally unpolarized.

To accurately derive a planet's polarization state from a measurement, it is paramount to correct for instrumental polarization (IP) and cross-talk of the complete optical system, that is, telescope and instrument. To this end, we use the Mueller matrix model for VLT/SPHERE-IRDIS described in Chapter 2. This model has been validated by taking measurements of an unpolarized standard star and with SPHERE's internal source, reaching an absolute polarimetric accuracy $\leq$0.1% in all broadband filters (Y-, J-, H- and K_s-band; see Table 4.1). The polarimetric accuracy is particularly affected by the IP, which can make unpolarized sources appear a few percent polarized when unaccounted for. With the model, the IP can be subtracted more accurately than with regular IP-subtraction techniques, because no assumptions on the stellar polarization are needed.

To enable the application of ADI + PCA, we have commissioned pupil-tracking for IRDIS' polarimetric mode. In this mode, the derotator (K-mirror) only compensates for the altitude angle of the telescope, so that the pupil (and the quasi-static speckle pattern) is kept fixed with respect to the detector, while the image (the planet) rotates with the parallactic angle. Unfortunately we could not implement a new HWP rotation control law to keep the polarization direction of the source fixed on the detector during pupil-tracking[1]. Therefore Stokes Q and U are measured by performing beam switching with the HWP relative to the vertical (perpendicular to the Nasmyth platform; STATIC mode)

[1]For this, the following HWP control law should be implemented:

$$\theta_{\mathrm{HWP}} = a + \frac{1}{2}\left(-p + \gamma + \eta_{\mathrm{pupil}}\right) \tag{4.1}$$

with θ_{HWP} the HWP angle, a the altitude angle of the telescope, p the parallactic angle of the target, γ an offset of the angle of linear polarization due to a user-defined HWP offset and η_{pupil} the fixed position angle offset of the image to align the 'spider mask' with the diffraction pattern of the support structure of the telescope's secondary mirror (see below). Beam switching with the HWP (to measure Stokes Q and U) is performed relative to this HWP angle. The HWP control law for field-tracking mode is described in Chapter 2.

Table 4.1: Central wavelength and bandwidth of the broadband filters available for IRDIS polarimetry (Wahhaj et al., 2017).

Filter	Central wavelength (nm)	Bandwidth (nm)
BB_Y	1042.5	139
BB_J	1257.5	197
BB_H	1625.5	291
BB_K_s	2181.3	313.5

with HWP switch angles 0° and 45° to measure Q, and 22.5° and 67.5° to measure U (a so-called polarimetric or HWP cycle). The disadvantage is that the polarization direction of the source rotates with the parallactic angle on the detector while tracking a target, but this can readily be accounted for with the Mueller matrix model of Chapter 2. Pupil-tracking with IRDIS' polarimetric mode is officially offered since P100.

As described in Chapter 2 and de Boer et al. (2020), the derotator can produce very strong cross-talk at specific derotator angles, resulting in severe loss of polarization signal. For field-tracking observations, de Boer et al. (2020) recommend to apply an offset to the derotator angle to prevent this signal loss. Such an offset cannot be applied in pupil-tracking mode, because the support structure of the secondary mirror of the telescope (the 'spider') will then not be aligned with a mask added to the Lyot stop (the 'spider mask'), resulting in (locally) much higher speckle noise. Fortunately, the polarimetric efficiency, that is, the fraction of the linearly polarized light entering the system that is actually measured, happens to be sufficiently high for a large range of altitude angles in all broadband filters. Figure 4.1 shows the polarimetric efficiency in pupil-tracking mode as a function of parallactic and altitude angle in H-band and is constructed using the Mueller matrix model of Chapter 2. The efficiency is >80% for altitude angles between 20° and 75°, but goes down to 64% for altitude angles larger than 75°. The polarimetric efficiency plots in Y-, J-, and K_s-band look similar, but with the minima at altitude angles between 20° and 75° equal to 87%, 96% and 83%, respectively. At altitude angles larger than 75°, the minima are equal to 76%, 94% and 67%, respectively.

4.3 Observations

During the nights starting on October 10 and 12, 2016, we observed the four young giant planets HR 8799 bcde and the (substellar) companion PZ Tel B with the measurement technique described in Sect. 4.2. An overview of the observations is shown in Table 4.2. PZ Tel was observed twice for almost 40 min during twilight using the broadband H- and J-filters, while HR 8799 was observed twice for ~2.5 h during nighttime in H-band. All measurements were taken with the apodized pupil Lyot coronagraph ALC_YJH_S (mask diameter = 185 mas). The first three observing sequences had good to medium seeing conditions. However, the HR 8799 observations of 13-10-2016 are not considered in this work, as the seeing and coherence time were very poor and the control loop of the adaptive optics system opened many times. PZ Tel and HR 8799 were observed at

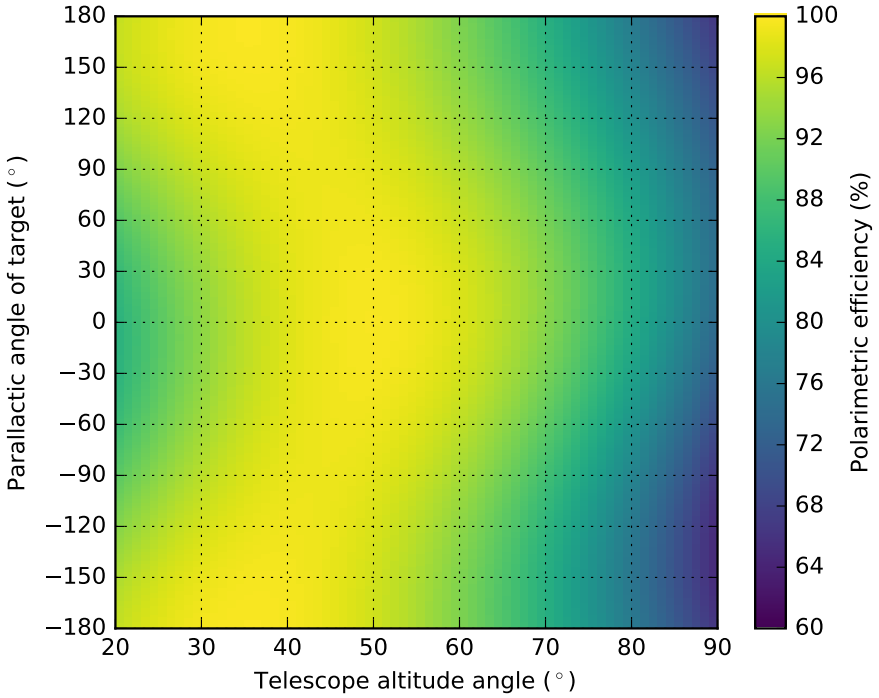


Figure 4.1: Polarimetric efficiency of SPHERE-IRDIS in H-band as a function of parallactic angle of the target and telescope altitude angle in pupil-tracking mode.

an average altitude angle of ~57° (air mass ~1.2) and ~41° (air mass ~1.5), respectively. From Fig. 4.1, it follows that the polarimetric efficiency of the observations in H-band at these altitude angles is always higher than ~86%.

4.4 Data reduction

To explain the data-reduction, we will primarily discuss the reduction of the HR 8799 data of 11-10-2016 and only mention the details of the reduction of the PZ Tel datasets that deviate from this first description. We prepare the raw frames by applying dark-subtraction, flat-fielding and bad pixel filtering. Subsequently, we center the frames with the four satellite spots of the star center frames (see Zurlo et al., 2016). From these prepared frames, we create images of Stokes Q and U and the corresponding total intensity images I_Q and I_U to determine the degree and angle of linear polarization of the planets. We will now first describe the creation of the total intensity images.

Table 4.2: Overview of the polarimetric observations of the (substellar) companion PZ Tel B and the four giant planets around HR 8799. DIT = Detector Integration Time; NDIT = Number of Detector Integration Times; ToT = Time on Target; m_V = apparent magnitude of central star in V-band.

Date	Target	Filter	DIT (s)	HWP cycles	NDIT	ToT (min)	Parallactic rotation (°)	Altitude angle (°)	m_V	Seeing (″)	Coherence time (ms)
10-10-2016	PZ Tel	BB_H	12	10	4	39	14	55 - 60	8.34	0.6 - 1.0	2.8 - 6.4
11-10-2016	HR 8799	BB_H	16	43	3	164	50	38 - 44	5.95	0.4 - 0.9	2.4 - 6.0
12-10-2016	PZ Tel	BB_J	12	10	4	37	13	53 - 58	8.34	0.9 - 1.2	2.8 - 6.1
13-10-2016	HR 8799	BB_H	16	39	3	145	45	40 - 44	5.95	0.9 - 2.8	1.0 - 4.0

4.4.1 Construction of total-intensity I_Q- and I_U-images

To create the total intensity images, we start by adding the images of the simultaneously recorded orthogonal polarization states on the left and right halves of the detector (single sum images I_Q^+, I_Q^-, I_U^+ and I_U^-) for all the prepared frames. After that, for each HWP cycle, we compute the double sum, that is, the mean of the single sum images with HWP switch angles 0° and 45° for I_Q and 22.5° and 67.5° for I_U. To show the sensitivity we attain, we look at the contrast curve displayed in Fig. 4.2. The curves in this figure are computed as the mean or 1× the standard deviation (1σ) over 1 pixel wide annuli centered on the star, normalized with the maximum intensity of the star. The purple solid curve in Fig. 4.2 shows the mean intensity profile of the coronagraphic stellar point spread function (PSF) when we compute the mean of the cube of the I_Q-frames. Comparing this curve to the non-coronagraphic stellar PSF profile (top black solid curve) obtained from the flux calibration image (see Zurlo et al., 2016) clearly demonstrates the effect of the adaptive optics and coronagraph close to the star. The dark blue solid curve shows the standard deviation (1σ) over the I_Q-frames, which can be regarded as a measure of the speckle noise. It follows that we can detect planet b from the double sum images, but that the inner three planets remain hidden. Indeed, planet b is (marginally) visible in a single raw frame.

To increase the contrast, we combine ADI with PCA using the software package PynPoint (Amara & Quanz, 2012; Amara et al., 2015) to subtract 5 principle components from the cubes of the I_Q- and I_U-frames separately. We then derotate the frames with the parallactic angle and compute their mean to obtain the final I_Q- and I_U-images. The resulting I_Q-image is shown in Fig. 4.3 (left). The light blue solid curve in Fig. 4.2 shows the standard deviation over this image and the four lower black solid curves show the PSF profiles of the planets[2]. After applying ADI + PCA, the speckle noise is substantially suppressed and all planets are clearly detected. This is also evident from Fig. 4.3 (left), as all planets and the Airy rings surrounding planet b and c (and perhaps d) are clearly visible.

For the reduction of the PZ Tel data, we do not perform ADI + PCA when creating the total intensity images, because the parallactic rotation is limited (see Table 4.2). Instead we derotate the double sum I_Q- and I_U-frames with the parallactic angle and compute the mean of the cube of these derotated frames. The resulting I_Q-image of the H-band observations is displayed in Fig. 4.3 (right). The first Airy ring and the diffraction pattern of the support structure of the telescope's secondary mirror are clearly visible around the companion. To suppress the halo of starlight, which shows radial symmetry, we subtract 180°-rotated versions of the I_Q- and I_U-images from the originals. Remaining background will be removed when computing the total intensity of the companion from apertures. The contrast curve of the PZ Tel observations in H-band is shown in Fig. 4.4. The PSF profile of the companion (lower solid black curve) is obtained from the halo-subtracted images. The light blue solid curve in Fig. 4.4 shows that the companion is detected very clearly.

[2]The PSF profiles of the planets are not extracted from the final I_Q-image, because we have not accounted for the ADI self-subtraction, for example by injecting fake negative planets (Marois et al., 2010; Bonnefoy et al., 2011; Zurlo et al., 2014). Instead, we obtained them by scaling the non-coronagraphic stellar PSF of the flux calibration image with the planet contrasts reported in Zurlo et al. (2016).

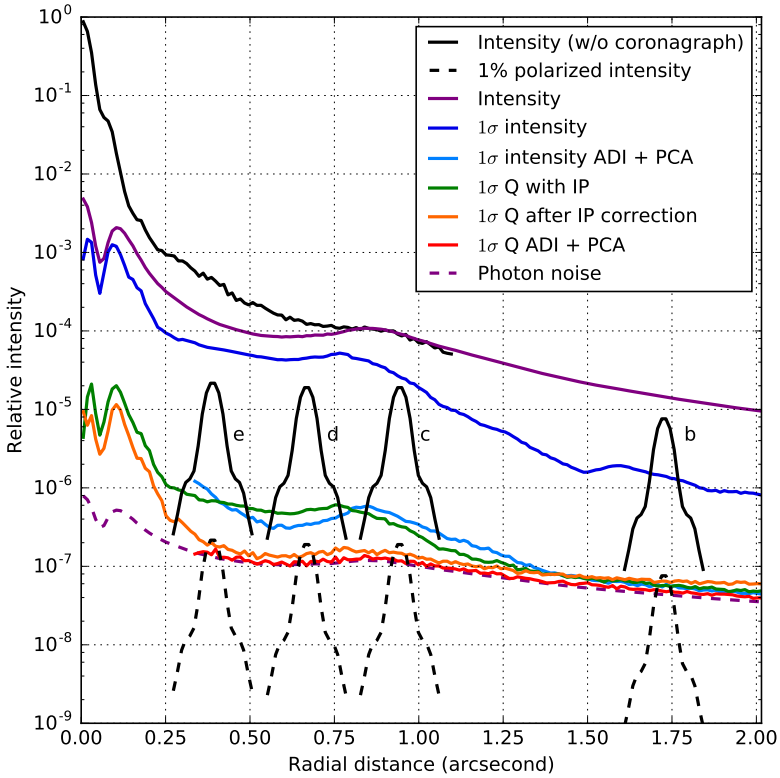


Figure 4.2: Contrast curve of the HR 8799 observations of 11-10-2016 in H-band showing the effect of the various data-reduction steps.

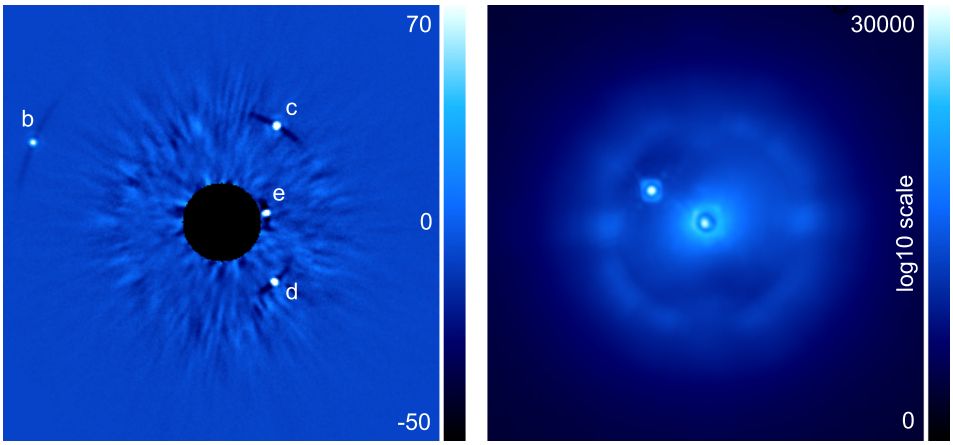


Figure 4.3: *Left*: Total intensity I_Q-image of the planets of HR 8799 in H-band created using ADI + PCA. *Right*: I_Q-image of PZ Tel B in H-band (without ADI + PCA).

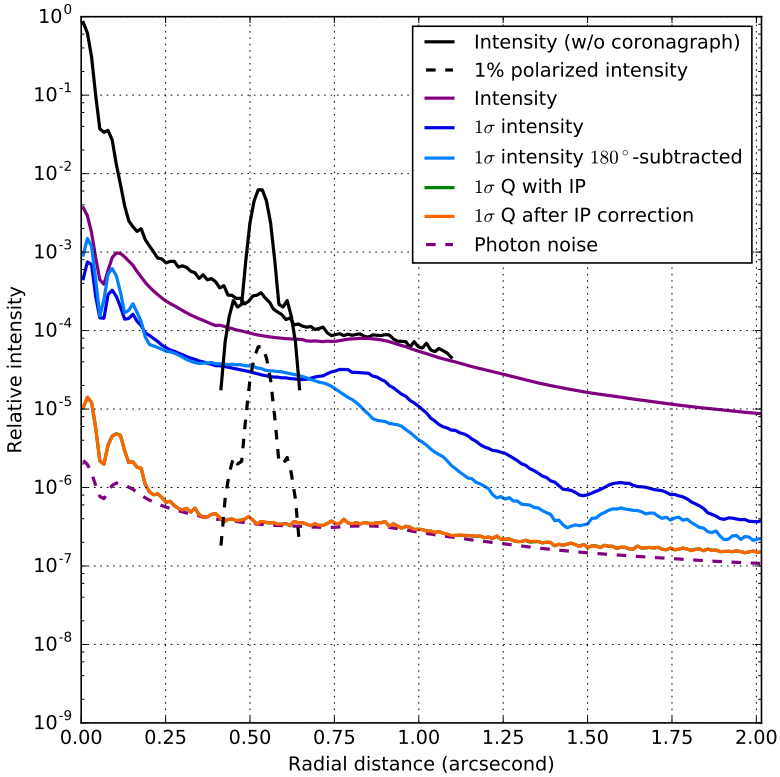


Figure 4.4: Contrast curve of the PZ Tel observations of 10-10-2016 in H-band showing the effect of the various data-reduction steps. The orange curve overlaps with the green curve, because the average of the IP in Stokes Q happened to be zero.

4.4.2 Construction of Stokes Q- and U-images

In the contrast curve of the HR 8799 observations shown in Fig. 4.2, the tops of the planets' PSF profiles (four lower black solid curves) are at a contrast of $\sim 10^{-5}$. If these planets are 1% polarized, their polarization signals will correspond to the four black dashed curves. This clearly shows the challenge at hand: since the planets are expected to be at most a few tenths of a percent to a percent polarized, we need to reach a contrast in polarized light of at least 10^{-7}. In the following we will present and justify the order of data-reduction steps to construct the Stokes Q- and U-images. A flow diagram of the data-reduction steps is shown in Fig. 4.5.

We start by computing the difference between the images of simultaneously recorded orthogonal polarization states on the left and right halves of the detector (single difference images Q^+, Q^-, U^+ and U^-) for all the prepared frames. For each HWP cycle, we then compute the double difference, that is, half the difference between the single difference images with HWP switch angles 0° and 45° for Q, and 22.5° and 67.5° for U. We choose not to derotate the frames with the parallactic angle before computing the double differ-

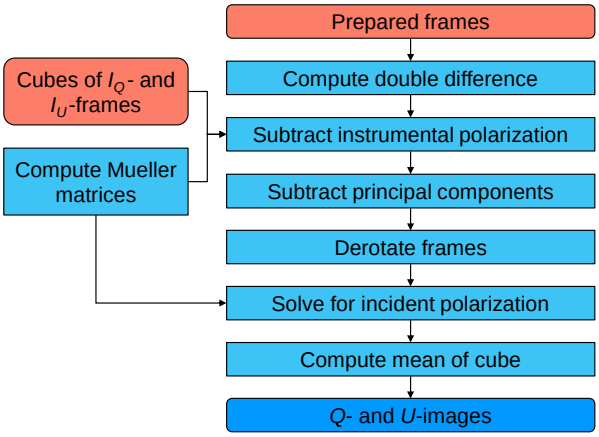


Figure 4.5: Flow diagram of the data-reduction steps to construct the images of Stokes Q and U.

ence, because this way we most effectively remove the quasi-static speckles and the IP downstream of the HWP, and suppress differential effects that limit the polarimetric sensitivity, including flat-fielding errors. The disadvantage is that we create some spurious polarization signal, because the planet positions have changed slightly between subsequent exposures. However, this rotation-induced signal cancels out when we integrate the polarization signal over a sufficiently large aperture. The double difference frames show a weak detector read-out artifact that has a continuous vertical band structure. Similarly to de Boer et al. (2016), we remove this structure by subtracting, for every column of pixels, the median value of the top and bottom 60 pixels. Since starlight shows little to no polarization (in general), computing the double difference strongly suppresses the halo of starlight. The green solid curve in Fig. 4.2 shows that we reach approximately the same contrast as that attained using ADI + PCA on the total intensity images.

The IP created by SPHERE's first mirror (M4) and the telescope are not removed by computing the double difference, because they are located upstream of the HWP. Therefore a residual stellar speckle halo is visible in all double difference frames as shown in Fig. 4.6 (top left). To remove this residual speckle halo and correct the planets' polarization signals for the IP, we use the Mueller matrix model of Chapter 2 to describe the contribution of the telescope and instrument for every measurement. With the model we compute the IP for each double difference Q- or U-frame from the corresponding parallactic, telescope altitude, HWP and derotator angle. The IP predicted by the model is shown in Fig. 4.7 (left). We remove the IP in the Q- and U-frames by scaling their corresponding double sum intensity I_Q- and I_U-frames with the predicted IP and subtracting the result from the Q- and U-frames. The removed residual speckle halo in Fig. 4.6 (top right) illustrates that this procedure effectively removes close to all IP from the Q- and U-frames. As a result, the orange solid curve in Fig. 4.2 shows a significant increase in contrast close to the star.

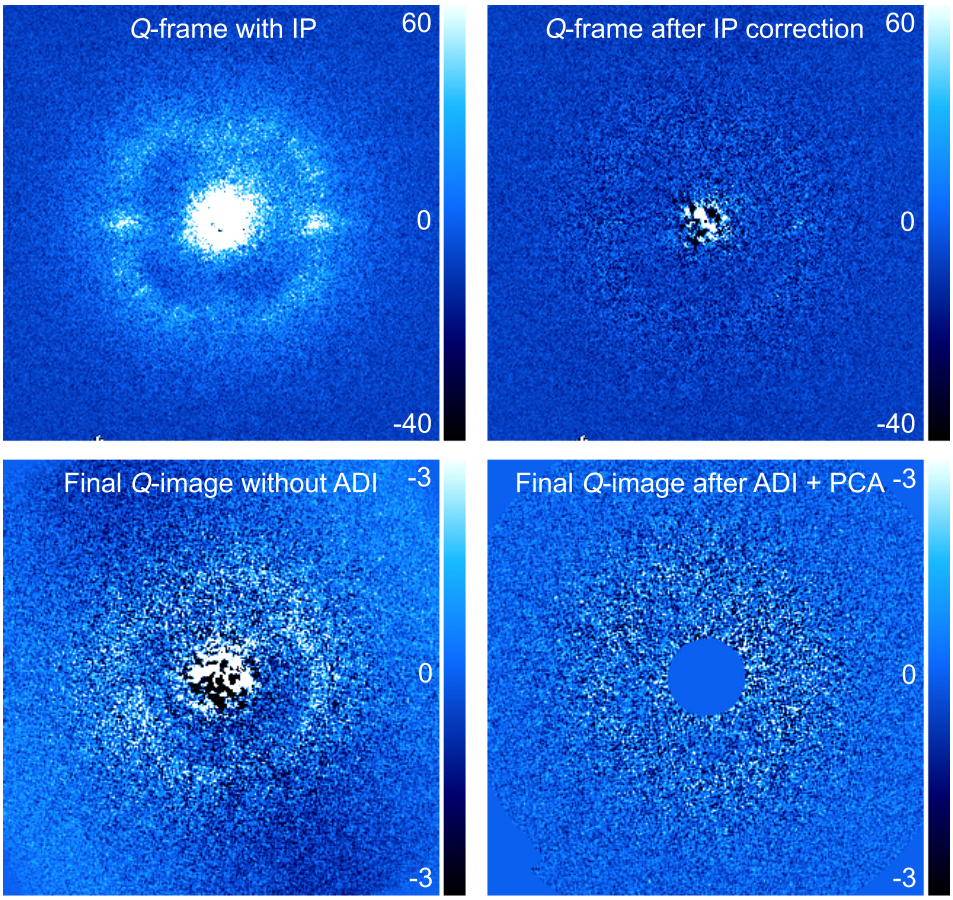


Figure 4.6: *Top left*: Double difference Q-frame showing the instrumental polarization of SPHERE's first mirror (M4) and the telescope. *Top right*: Q-frame after removing the IP by subtracting the corresponding I_Q-frame scaled with the IP predicted by the Mueller matrix model. *Bottom left*: Q-image after computing the mean of the cube of IP-corrected Q-frames showing remaining structure. Note that the range of values is much smaller than that in the frames at the top. *Bottom right*: Final Q-image after removing the structure by subtracting three principle components and correcting for efficiency and cross-talk with the Mueller matrix model.

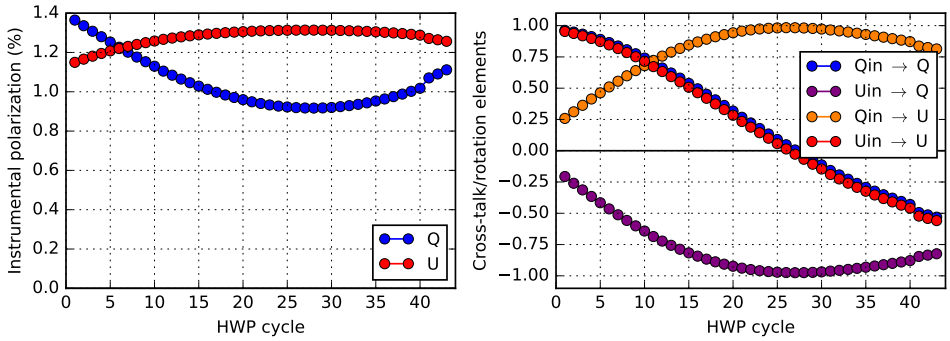


Figure 4.7: *Left*: Instrumental polarization predicted by the Mueller matrix model for each double difference Q- or U-frame. *Right*: The four elements describing the transmission ($Q_{\rm in} \rightarrow Q$ and $U_{\rm in} \rightarrow U$) and exchange between the polarization components ($U_{\rm in} \rightarrow Q$ and $Q_{\rm in} \rightarrow U$) as predicted by the Mueller matrix model for each pair of Q- and U-frames. Because we briefly interrupted the observing sequence to take calibration measurements, there is a small discontinuity after the 40th HWP cycle in both plots.

When we compute the mean of the cubes of the IP-corrected Q- and U-frames, some structure remains, as shown in Fig. 4.6 (bottom left). This structure likely arises because the speckle field changes in time and the orthogonal polarization states are treated slightly differently by the instrument. In addition, there might be some stellar and background polarization or residual IP, because the Mueller matrix model has a finite accuracy. To remove the structure, we apply ADI + PCA to the cubes of the IP-corrected Q- and U-frames separately, subtracting three principle components for each. The ADI + PCA step cannot be performed before removing the IP with the Mueller matrix model, because in that case the IP will be partly removed with ADI + PCA and then over-subtracted with the modeled IP value. Also, applying ADI + PCA alone would never suffice to remove the IP at the planet position, because it cannot discriminate between planet signal and IP and the planets are moving between exposures.

After performing ADI + PCA, we derotate the frames so that the images are aligned with North up and the planets are at the same position in all frames. Since the HWP control law for pupil-tracking has not yet been implemented (see Sect. 4.2), the polarization direction of the planets on the detector rotates between HWP cycles. In addition, the cross-talk produced by the instrument (in particular by the derotator) results in a time-varying transmission of and exchange between the polarization components Q and U. As a result, the polarization signal of the planets is different in each pair of Q- and U-frames and we cannot simply compute the mean of the cubes of the Q- and U-frames. To correct for the rotation and the cross-talk, we use the Mueller matrix model to derive for each pair of Q- and U-frames (each HWP cycle) two linear equations describing the measurements. For every pixel, we solve these equations for the polarization signal incident on the telescope ($Q_{\rm in}$ and $U_{\rm in}$). The four elements describing the transmission ($Q_{\rm in} \rightarrow Q$ and $U_{\rm in} \rightarrow U$) and exchange between the polarization components ($U_{\rm in} \rightarrow Q$ and $Q_{\rm in} \rightarrow U$) are plotted in Fig. 4.7 (right). Finally, we compute the mean of the cubes of the $Q_{\rm in}$- and

$U_{\rm in}$-frames to obtain the final Q and U-images incident on the telescope.

Figure 4.6 (bottom right) shows the final Q-image. The structure seen in Fig. 4.6 (bottom left) is clearly removed. The red solid curve in Fig. 4.2 shows that the final contrast achieved is $\sim 10^{-7}$ at the position of the three inner planets and a bit better at the position of planet b. As illustrated by the black dashed curves in Fig. 4.2, we should be able to detect the polarization signals from the planets if they are 1% polarized. The contrast reached is very close to the photon limit (purple dashed curve), that is computed as the square root of the total intensity (solid purple curve). Applying ADI + PCA does not increase the contrast in case of planet b, since it is at a large separation from the star and not speckle noise limited. At the position of the three inner planets, applying ADI + PCA has improved the contrast only by a factor of ~2, because IRDIS' dual-beam polarimetric mode already substantially suppresses speckles and we have reached the photon noise limit (i.e., the fundamental lower contrast limit for a given dataset). If we would observe longer, the contrast will likely benefit more from ADI + PCA.

Reaching the contrast required to measure a ~1% polarization signal of PZ Tel B in the data sets of 10-10-2016 (H-band) and 12-10-2016 (J-band) is less challenging. In the contrast curve of the H-band measurements of PZ Tel shown in Fig. 4.4, the top of the companion's PSF profile (lower black solid curve) is at a contrast of $\sim 6 \cdot 10^{-3}$. Hence to measure a 1% polarized signal (black dashed curve), the contrast required is ~300 times lower than for the inner three planets around HR 8799.

To create the Q- and U-images of the PZ Tel data, we omit the ADI + PCA step and instead derotate the frames after correcting the IP with the model. The solid orange curve in Fig. 4.4 shows that we achieve a contrast of $\sim 3 \cdot 10^{-7}$ at the position of the companion, also close to the photon limit. This contrast is sufficient to detect polarization signals <0.1%. Note that because the average of the IP in Stokes Q happened to be zero, the contrast curves with IP (solid green curve) and without IP (solid orange curve) are overlapping in Fig. 4.4.

4.5 Results

The final Stokes Q-images of the H-band observations of HR 8799 and PZ Tel are shown in Figs. 4.8 (left) and 4.8 (right), respectively. By visual inspection, we do not detect a polarization signal for any of the companions in our measurements. Based on the contrasts achieved in Stokes Q (see Figs. 4.2 and 4.4) and U, we estimate preliminary 1σ upper limits on the degree of linear polarization of ~1% and ~0.1% for the planets of HR 8799 (H-band) and PZ Tel B (H- and J-band), respectively. The upper limits on the polarization of PZ Tel B would be lower based on the contrast curves alone, but is limited by the accuracy of the Mueller matrix model. As we will make a few improvements to the data-reduction (see Sect. 4.6), we leave the accurate determination of the polarization signals or upper limits and the interpretation of these results for future work.

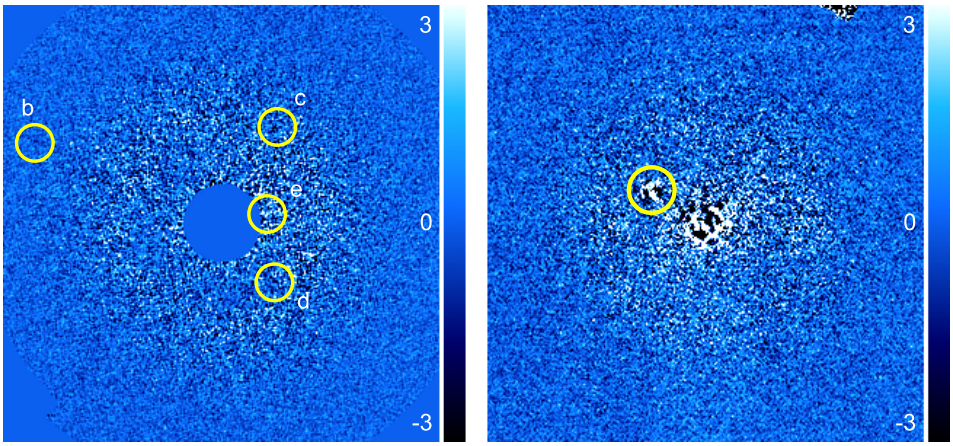


Figure 4.8: Final Stokes Q-images of the observations of HR 8799 (*left*) and PZ Tel (*right*) in H-band. By visual inspection, no polarization signals are detected.

4.6 Discussion

Although we have not detected a polarization signal, our technique of combining ADI and accurate polarimetry shows that it is possible to measure realistic polarization degrees for planetary and brown dwarf companions. While for PZ Tel B we have reached a sufficiently high contrast to detect a polarization signal of a few tenths of a percent, we would need to observe the planets of HR 8799 for several nights at good seeing conditions to detect such a signal. To detect polarization signals of (substellar) companions without requiring an excessive amount of observing time (maximum ~2.5 hr), several criteria need to be kept in mind. We would in general need (approximate numbers for the criteria are given in parentheses):

- a brighter companion in absolute terms (H-band apparent magnitude of ~16 or brighter)
- a lower companion-to-star contrast (H-band magnitude difference of at most ~9)
- a larger separation from the central star (at least 0.6")
- good seeing conditions (seeing ~0.6″ and coherence time ~4 ms)
- a brighter central star for good adaptive optics performance (R-band magnitude of ~11 or brighter)

The first two criteria are connected: if a companion is brighter in absolute terms, a higher companion-to-star contrast is acceptable and vice versa. When taking all these criteria into account, only a few dozen known targets are feasible. To increase the chance of a detection, we should observe targets that are more likely to be polarized (see Stolker et al., 2017). Examples are companions with evidence for dust, hazes or patchy clouds in their atmospheres, companions that are known to rotate rapidly or that have the same spectral

type and temperature as field brown dwarfs that are known to rotate rapidly (see Miles-Páez et al., 2013), companions with low surface gravities in orbits seen edge-on (higher polarization signal if rotationally flattened; de Kok et al., 2011; Stolker et al., 2017) or companions that show evidence for accretion.

Since IRDIS' polarimetric mode alone (without ADI) is already so powerful for the detection of companion polarization signals, one might think to prefer the simpler field-tracking mode over the pupil-tracking mode. However, for close-in and/or relatively faint planets such as the planets of HR 8799, accurate determination of their total intensity (which is required to compute the degree of linear polarization) is not possible in field-tracking mode, because the PSF of the star washes out that of the planets. Pupil-tracking observations on the other hand allow the application of advanced ADI techniques (e.g., PCA) to effectively remove the halo of starlight and accurately determine the total intensity. In addition, pupil-tracking mode enables the use of the spider mask, so that the speckle noise due to the support structure of the telescope's secondary mirror is suppressed. Also, because the speckles are quasi-static in pupil-tracking mode, these speckles and the IP downstream of the HWP are more effectively removed when computing the double difference. For long observations, applying ADI + PCA on the Q- and U-frames can possibly yield a large increase in sensitivity. Finally, since the planet moves over the detector during an observing sequence, flat-fielding errors are averaged out and the effect of an inconveniently located bad pixel will be limited (dithering is not yet implemented for IRDIS polarimetry).

When performing polarimetric measurements in pupil-tracking, one should consider the effect of the parallactic rotation. More parallactic rotation will be beneficial to the ADI performance and the suppression of flat-fielding errors. However, when the parallactic rotation is fast, more spurious polarization signal will be created and the accuracy of the measured angle of linear polarization will diminish, because the polarization direction rotates during a single exposure with the current rotation law of the HWP (see Sect. 4.2). To limit these effects, one could avoid observing at the meridian or keep the exposure time and the duration of the HWP cycles short.

Before accurately computing (upper limits on) the polarization signals of the companions, we will make a few improvements to the data-reduction. Firstly, we will improve the centering of the frames. The position of the central star obtained from the star center frames differs by approximately half a pixel between the start and the end of the HR 8799 observations. To account for this drift, we can interpolate between the start and end coordinates of the central star and center the science frames with the interpolated coordinates. After that, we can further improve the centering by cross-correlating the frames. For the ADI + PCA data-reduction step, different PCA algorithms can be tried out. Most importantly, we will account for the self-subtraction of ADI + PCA, for example by using the method of fake negative planets (Marois et al., 2010; Bonnefoy et al., 2011; Zurlo et al., 2014). Alternatively, we could use the PCA code by Meshkat et al. (2014) to construct for each frame to be reduced a separate stellar PSF model from only those frames where the companion PSF does not overlap with the companion PSF in the to-be-reduced frame (see Juan Ovelar, 2013). Finally, we will attempt to reduce the noise in our final images by applying a matched filter, similarly to Juan Ovelar (2013). When these improvements have been implemented, we will determine the degree and angle of linear polarization

of the companions by performing aperture photometry on the final I_Q-, I_U-, Q- and U-frames. In case of a non-detection, we will determine upper limits on the polarization by estimating the random noise in the images.

4.7 Conclusions

We have introduced a novel high-contrast imaging scheme that combines angular differential imaging (ADI) and accurate near-infrared polarimetry to characterize self-luminous giant exoplanets. The combination of ADI and polarimetry is challenging, because the field rotation required for ADI negatively affects the polarimetric performance. By combining ADI and polarimetry we can characterize planets that can be directly imaged with a very high signal-to-noise ratio. We use the IRDIS pupil-tracking mode and combine ADI and principal component analysis to reduce speckle noise. We take advantage of IRDIS' dual-beam polarimetric mode to eliminate differential effects that severely limit the polarimetric sensitivity (flat-fielding errors, differential aberrations and seeing), and thus further suppress speckle noise. To correct for instrumental polarization effects, we apply a detailed Mueller matrix model that describes the telescope and instrument and that has an absolute polarimetric accuracy $\leq$0.1%. As the technique is still in development, further improvements will be made in future work.

With our observing technique, we have observed the planets of HR 8799 and the (substellar) companion PZ Tel B. Even though by visual inspection we do not detect a polarization signal, we reach a contrast of $\sim 10^{-7}$, close to the photon noise limit. Based on the contrast achieved, we estimate a preliminary 1σ upper limit on the degree of linear polarization of PZ Tel B equal to $\sim$0.1% in H- and J-band. The planets of HR 8799 are much fainter however, and we estimate an upper limit of $\sim$1% on their degrees of linear polarization in H-band. We leave the accurate determination of the polarization signals or upper limits and the interpretation of these results for future work. The achieved sub-percent sensitivity and accuracy show that our technique has great promise to characterize exoplanets through direct-imaging polarimetry.

References

Amara, A., & Quanz, S. P. 2012, Monthly Notices of the Royal Astronomical Society, 427, 948
Amara, A., Quanz, S. P., & Akeret, J. 2015, Astronomy and Computing, 10, 107
Bagnulo, S., Landolfi, M., Landstreet, J. D., et al. 2009, Publications of the Astronomical Society of the Pacific, 121, 993
Beuzit, J.-L., Feldt, M., Dohlen, K., et al. 2008, in Ground-based and airborne instrumentation for astronomy II, Vol. 7014, International Society for Optics and Photonics, 701418
Biller, B. A., Liu, M. C., Wahhaj, Z., et al. 2010, Astrophysical Journal Letters, 720, L82
Bonnefoy, M., Lagrange, A.-M., Boccaletti, A., et al. 2011, Astronomy & Astrophysics, 528, L15
Bonnefoy, M., Zurlo, A., Baudino, J. L., et al. 2016, Astronomy & Astrophysics, 587, A58
Canovas, H., Rodenhuis, M., Jeffers, S. V., Min, M., & Keller, C. U. 2011, Astronomy & Astrophysics, 531, A102
Chilcote, J., Barman, T., Fitzgerald, M. P., et al. 2015, Astrophysical Journal Letters, 798, L3
de Boer, J., Salter, G., Benisty, M., et al. 2016, Astronomy & Astrophysics, 595, A114

de Boer, J., Langlois, M., van Holstein, R. G., et al. 2020, Astronomy & Astrophysics, 633, A63
de Kok, R. J., Stam, D. M., & Karalidi, T. 2011, Astrophysical Journal, 741, 59
Dohlen, K., Langlois, M., Saisse, M., et al. 2008, in Ground-based and Airborne Instrumentation for Astronomy II, Vol. 7014, International Society for Optics and Photonics, 70143L
Ginski, C., Schmidt, T. O. B., Mugrauer, M., et al. 2014, Monthly Notices of the Royal Astronomical Society, 444, 2280
Ingraham, P., Marley, M. S., Saumon, D., et al. 2014, Astrophysical Journal Letters, 794, L15
Jensen-Clem, R., Millar-Blanchaer, M., Mawet, D., et al. 2016, Astrophysical Journal, 820, 111
Juan Ovelar, M. d. 2013, Ph.D. Thesis, Leiden Observatory, Faculty of Science, Leiden University
Lafrenière, D., Jayawardhana, R., & van Kerkwijk, M. H. 2008, Astrophysical Journal Letters, 689, L153
Langlois, M., Dohlen, K., Vigan, A., et al. 2014, in Ground-based and Airborne Instrumentation for Astronomy V, Vol. 9147, International Society for Optics and Photonics, 91471R
Macintosh, B., Graham, J. R., Barman, T., et al. 2015, Science, 350, 64
Maire, A.-L., Bonnefoy, M., Ginski, C., et al. 2016, Astronomy & Astrophysics, 587, A56
Marley, M. S., & Sengupta, S. 2011, Monthly Notices of the Royal Astronomical Society, 417, 2874
Marois, C., Lafrenière, D., Doyon, R., Macintosh, B., & Nadeau, D. 2006, Astrophysical Journal, 641, 556
Marois, C., Macintosh, B., Barman, T., et al. 2008, Science, 322, 1348
Marois, C., Macintosh, B., & Véran, J.-P. 2010, in Adaptive Optics Systems II, Vol. 7736, International Society for Optics and Photonics, 77361J
Marois, C., Zuckerman, B., Konopacky, Q. M., Macintosh, B., & Barman, T. 2010, Nature, 468, 1080
Meshkat, T., Kenworthy, M. A., Quanz, S. P., & Amara, A. 2014, Astrophysical Journal, 780, 17
Miles-Páez, P. A., Zapatero Osorio, M. R., Pallé, E., & Peña Ramírez, K. 2013, Astronomy & Astrophysics, 556, A125
Mugrauer, M., Vogt, N., Neuhäuser, R., & Schmidt, T. O. B. 2010, Astronomy & Astrophysics, 523, L1
Oppenheimer, B. R., Baranec, C., Beichman, C., et al. 2013, Astrophysical Journal, 768, 24
Seager, S., Whitney, B. A., & Sasselov, D. D. 2000, Astrophysical Journal, 540, 504
Sengupta, S., & Marley, M. S. 2010, Astrophysical Journal Letters, 722, L142
—. 2016, Astrophysical Journal, 824, 76
Soummer, R., Pueyo, L., & Larkin, J. 2012, Astrophysical Journal Letters, 755, L28
Stam, D. M., Hovenier, J. W., & Waters, L. B. F. M. 2004, Astronomy & Astrophysics, 428, 663
Stolker, T., Min, M., Stam, D. M., et al. 2017, Astronomy & Astrophysics
Wahhaj, Z., Girard, J., Milli, J., et al. 2017, ESO SPHERE User Manual Issue P100 Phase 2
Zurlo, A., Vigan, A., Mesa, D., et al. 2014, Astronomy & Astrophysics, 572, A85
Zurlo, A., Vigan, A., Galicher, R., et al. 2016, Astronomy & Astrophysics, 587, A57

5 A survey of the linear polarization of directly imaged exoplanets and brown dwarf companions with SPHERE-IRDIS: First polarimetric detections revealing disks around DH Tau B and GSC 6214-210 B

Adapted from

R. G. van Holstein, T. Stolker, R. Jensen-Clem, C. Ginski, J. Milli, J. de Boer, J. H. Girard, Z. Wahhaj, A. J. Bohn, M. A. Millar-Blanchaer, M. Benisty, M. Bonnefoy, G. Chauvin, C. Dominik, S. Hinkley, C. U. Keller, M. Keppler, M. Langlois, S. Marino, F. Ménard, C. Perrot, T. O. B. Schmidt, A. Vigan, A. Zurlo, and F. Snik

Astronomy & Astrophysics, 647, A21 (2021)

Context. Young giant planets and brown dwarf companions emit near-infrared radiation that can be linearly polarized up to several percent. This polarization can reveal the presence of an (unresolved) circumsubstellar accretion disk, rotation-induced oblateness of the atmosphere, or an inhomogeneous distribution of atmospheric dust clouds.

Aims. We aim to measure the near-infrared linear polarization of 20 known directly imaged exoplanets and brown dwarf companions.

Methods. We observed the companions with the high-contrast imaging polarimeter SPHERE-IRDIS at the Very Large Telescope. We reduced the data using the IRDAP pipeline to correct for the instrumental polarization and crosstalk of the optical system with an absolute polarimetric accuracy <0.1% in the degree of polarization. We employed aperture photometry, angular differential imaging, and point-spread-function fitting to retrieve the polarization of the companions.

Results. We report the first detection of polarization originating from substellar companions, with a polarization of several tenths of a percent for DH Tau B and GSC 6214-210 B in H-band. By comparing the measured polarization with that of nearby stars, we find that the polarization is unlikely to be caused by interstellar dust. Because the companions have previously measured hydrogen emission lines and red colors, the polarization most likely originates from circumsubstellar disks. Through radiative transfer modeling, we constrain the position angles of the disks and find that the disks must have high inclinations. For the 18 other companions, we do not detect significant polarization and place subpercent upper limits on their degree of polarization. We also present images of the circumstellar disks of DH Tau, GQ Lup, PDS 70, β Pic, and HD 106906. We detect a highly asymmetric disk around GQ Lup and find evidence for multiple scattering in the disk of PDS 70. Both disks show spiral-like features that are potentially induced by GQ Lup B and PDS 70 b, respectively.

Conclusions. The presence of the disks around DH Tau B and GSC 6214-210 B as well as the misalignment of the disk of DH Tau B with the disk around its primary star suggest in situ formation of the companions. The non-detections of polarization for the other companions may indicate the absence of circumsubstellar disks, a slow rotation rate of young companions, the upper atmospheres containing primarily submicron-sized dust grains, and/or limited cloud inhomogeneity.

5.1 Introduction

Understanding the formation and evolution of young, self-luminous exoplanets and brown dwarf companions is one of the main goals of high-contrast imaging at near-infrared wavelengths (e.g., Nielsen et al., 2019; Vigan et al., 2021). Only a few of these directly imaged substellar companions have been detected close to the parent star and within a circumstellar disk (e.g., Lagrange et al., 2010; Keppler et al., 2018; Haffert et al., 2019); most companions are found at much larger separations ($\gtrsim$100 au; see e.g., Bowler, 2016). Close-in planets and companions are generally believed to form through core accretion (Pollack et al., 1996; Alibert et al., 2005) or gravitational instabilities in the circumstellar disk (Cameron, 1978; Boss, 1997). Companions at larger separations may form through direct collapse in the molecular cloud (Bate, 2009) or disk gravitational instabilities at an early stage (Kratter et al., 2010). Alternatively, companions may form close to the star and subsequently scatter to wide orbits through dynamical encounters with other companions (e.g., Veras et al., 2009).

In all formation scenarios, the companion is generally expected to form its own circumsubstellar accretion disk (e.g., Stamatellos & Whitworth, 2009; Szulágyi et al., 2017). Indeed, a handful of substellar companions show evidence for the presence of an accretion disk through hydrogen emission lines, red near-infrared colors, and excess emission at mid-infrared wavelengths (e.g., Seifahrt et al., 2007; Bowler et al., 2011; Bailey et al., 2013; Kraus et al., 2014; Zhou et al., 2014; Haffert et al., 2019). Interestingly, whereas ALMA and other radio interferometers have been successful at detecting the dust and gas of disks around isolated substellar objects (e.g., Ricci et al., 2014; van der Plas et al., 2016; Bayo et al., 2017), attempts to detect such disks around substellar companions have almost exclusively yielded non-detections (Bowler et al., 2015; MacGregor et al., 2017; Wu et al., 2017a,b; Wolff et al., 2017; Ricci et al., 2017; Pérez et al., 2019; Wu et al., 2020). The only detection of a disk around a substellar companion at mm-wavelengths is that of PDS 70 c with ALMA by Isella et al. (2019). ALMA has also detected a disk around FW Tau C (Kraus et al., 2015; Caceres et al., 2015), but, from models of the Keplerian rotation of the gas, the companion appears to be a $\sim$0.1$M_\odot$ star (Wu & Sheehan, 2017; Mora et al., 2020). To explain their non-detections, Wu et al. (2017a) and Wu et al. (2020) suggest that the disks around substellar companions must be very compact ($\lesssim$1000 $R_{\rm Jup}$ or $\lesssim$0.5 au) and optically thick to be able to sustain several million years of accretion. Alternatively, there might be a dearth of large dust grains in circumsubstellar disks because the observed mid-infrared excess could also be explained by a gaseous disk with small micron-sized dust grains.

Although compact circumsubstellar disks cannot be spatially resolved with current 8-m class telescopes, they can create a measurable, integrated linear polarization at near-infrared wavelengths (Stolker et al., 2017). The polarization can be introduced through scattering of the companion's thermal photons by dust within the disk, (partial) obscuration of the companion's atmosphere by the disk, or self-scattering in the case of a high-temperature disk. In all cases, the disk must have a nonzero inclination because the polarization of a face-on viewed, rotationally symmetric disk integrates to zero and a low-inclination disk cannot obscure the companion's atmosphere. Measuring polarization originating from circumsubstellar disks enables us to study the structure and physical properties of the disks.

Planets and brown dwarf companions without a disk can also be linearly polarized at near-infrared wavelengths. Late-M- to mid-L-type dwarfs are expected to have dusty atmospheres because their temperatures are sufficiently low for refractory material to condense (Allard et al., 2001; Ackerman & Marley, 2001). This atmospheric dust scatters the thermal radiation emanating from within the object, linearly polarizing the light. Whereas the spatially integrated polarization signal of a spherical, horizontally homogeneous dusty atmosphere is zero, a net polarization remains when this symmetry is broken (Sengupta & Krishan, 2001). Examples of these asymmetries are rotation-induced oblateness and an inhomogeneous distribution of atmospheric dust clouds (Sengupta & Marley, 2010; de Kok et al., 2011; Marley & Sengupta, 2011; Stolker et al., 2017), or even a large transiting moon (Sengupta & Marley, 2016). Based on the models, the degree of linear polarization due to circumsubstellar disks and atmospheric asymmetries can be several tenths of a percent up to several percent in favorable cases.

Spatially unresolved polarimetric observations have already been used to study disks around pre-main sequence stars (e.g., Rostopchina et al., 1997; Bouvier et al., 1999; Grinin, 2000; Ménard et al., 2003). In addition, optical and near-infrared polarization has been detected for dozens of field brown dwarfs (Ménard et al., 2002; Zapatero Osorio et al., 2005; Tata et al., 2009; Zapatero Osorio et al., 2011; Miles-Páez et al., 2013, 2017). In most cases, the polarization of these brown dwarfs is interpreted as being caused by rotation-induced oblateness or circumsubstellar disks, whereas an inhomogeneous cloud distribution has appeared harder to prove. However, Millar-Blanchaer et al. (2020) recently measured the near-infrared polarization of the two L/T transition dwarfs of the Luhman 16 system and found evidence for banded clouds on the hotter, late-L-type object.

With the adaptive-optics-fed high-contrast imaging instruments Gemini Planet Imager (GPI; Macintosh et al., 2014) and SPHERE-IRDIS (Beuzit et al., 2019; Dohlen et al., 2008) at the Very Large Telescope (VLT), we now have access to the spatial resolution and sensitivity required to measure the near-infrared polarization of substellar companions at small separations. After correction for instrumental polarization effects, the polarimetric modes of both instruments can reach absolute polarimetric accuracies of $\lesssim$0.1% in the degree of polarization (Wiktorowicz et al., 2014; Millar-Blanchaer et al., 2016; Chapter 2). Early attempts to measure the polarization of substellar companions by Millar-Blanchaer et al. (2015) and Jensen-Clem et al. (2016) with GPI and in Chapter 4 with SPHERE-IRDIS have been unsuccessful. Nevertheless, in Chapter 4 it is shown that SPHERE-IRDIS can achieve a polarimetric sensitivity close to the photon noise limit at

angular separations >0.5″. Ginski et al. (2018) detected a companion to CS Cha using SPHERE-IRDIS and measured the companion's polarization to be 14%, suggesting that it is surrounded by a highly inclined and vertically extended disk. However, recent optical spectroscopic observations with MUSE show that the companion is not substellar in nature, but is a mid M-type star that is obscured by its disk (Haffert et al., 2020).

In this chapter, we present the results of a survey of 20 planetary and brown dwarf companions with SPHERE-IRDIS, aiming to detect linear polarization originating from both circumsubstellar disks and atmospheric asymmetries. Our study is complemented by a similar survey of seven companions using GPI and SPHERE by Jensen-Clem et al. (2020).

The outline of this chapter is as follows. In Sect. 5.2 we present the sample of companions and the observations. Subsequently, we describe the data reduction in Sect. 5.3 and explain the extraction of the polarization signals in Sect. 5.4. In Sect. 5.5 we discuss our detections of polarization and the upper limits on the polarization for the non-detections. In the same section, we present images of five circumstellar disks that we detected in our survey. Because the most plausible explanation for the polarization of the companions is the presence of circumsubstellar disks, we perform radiative transfer modeling of a representative example of such a disk in Sect. 5.6. Finally, we discuss the implications of our measurements in Sect. 5.7 and present conclusions in Sect. 5.8.

5.2 Target sample and observations

5.2.1 Target sample

The sample of this study consists of 20 known directly imaged planetary and brown dwarf companions, out of the approximately 140 such companions that are currently known[1]. Because the expected polarization of the companions is around a few tenths of a percent or less, our primary selection criterion was whether SPHERE-IRDIS can reach a high signal-to-noise ratio (S/N) in total intensity without requiring an excessive amount of observing time. Therefore, the selected companions are relatively bright, are at a moderate companion-to-star contrast, are at a large angular separation from the star, and/or have a bright star for good adaptive-optics (AO) performance (see Chapter 4). Our sample contains the majority of the approximately two dozen known companions that match these requirements. Three of the remaining companions have been observed by Jensen-Clem et al. (2020) in their survey of seven companions.

An overview of the properties of the companions of our sample is shown in Fig. 5.1, with the full details presented in Table 5.1[2]. The sample is diverse, with the companions spanning spectral types from T5.5 to M7, masses between approximately 6 and 70 M_{Jup}, and ages between approximately 2 Myr and 11 Gyr. The companions orbit stars of spectral types A5 to M1. Six companions show evidence of hosting a circumsubstellar disk,

[1] From The Extrasolar Planets Encyclopaedia, `http://exoplanet.eu`, (Schneider et al., 2011), consulted on January 5, 2021.

[2] Throughout this chapter we use the short names GSC 8047, GSC 6214, 1RXS J1609, and TYC 8998 for the stars GSC 08047-00232, GSC 06214-00210 (or GSC 6214-210), 1RXS J160929.1-210524, and TYC 8998-760-1, respectively.

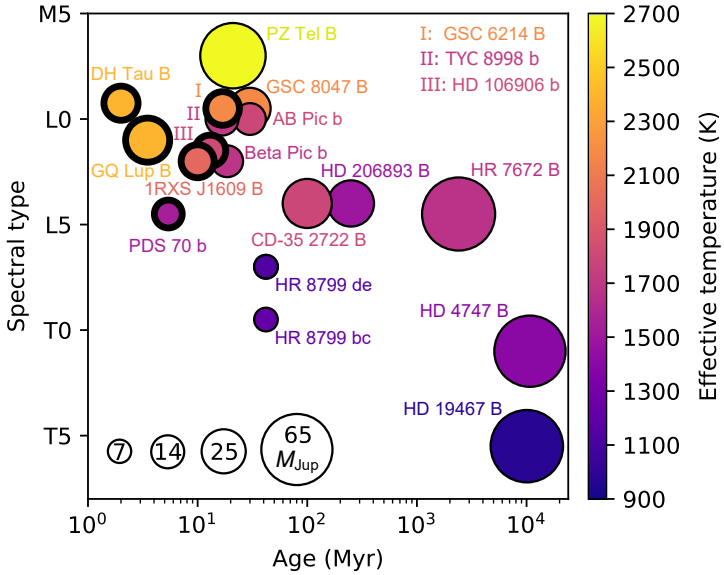


Figure 5.1: Properties of the companions of our sample showing the age, spectral type, mass (surface area of data points), effective temperature, and possible existence of a circumsubstellar disk (thick border). The data points of HR 8799 b and c, and of HR 8799 d and e, overlap.

mostly in the form of red near-infrared colors, excess emission at mid-infrared wavelengths, and hydrogen emission lines that reveal ongoing accretion. As can be seen particularly well from Fig. 5.1, the overall sample ranges from young, hot, accreting companions with spectral types between late M and early L, to old, cold, and massive companions of later spectral types. For the six companions that show evidence of hosting a circumsubstellar disk, we expect any polarization to be primarily due to this (spatially unresolved) disk, whereas for the other companions polarization would most likely be due to an inhomogeneous cloud distribution or rotation-induced oblateness.

5.2.2 Observations

All our observations were performed with the dual-beam polarimetric imaging (DPI) mode of SPHERE-IRDIS (de Boer et al., 2020; Chapter 2). In this mode, linear polarizers are inserted in the left and right optical channels of IRDIS to simultaneously create images of the two orthogonal linear polarization states on the detector. A rotatable half-wave plate (HWP) modulates the incident linear polarization with switch angles 0°, 45°, 22.5°, and 65.5° (a HWP cycle) to measure Stokes Q and U. The observations were carried out between October 10, 2016, and February 16, 2020, under generally good to excellent atmospheric conditions. An overview of the observations is shown in Table 5.2.

The observation strategy was as follows. We generally observed each target multiple times with typically over 30 min of on-source exposure time per visit. However, for some

Table 5.1: Properties of the companions of our sample.

Target	d (pc)	SpT star	Age	ρ ($''$)	Mass ($M_{\rm Jup}$)	SpT companion	$T_{\rm eff}$ (K)	log g	Evidence CSD	References
HR 8799 b	41.2	A5	42^{+6}_{-4} Myr	1.7	5.8 ± 0.5	~L/T	1175 ± 125	~3.5	-	1,2,3
HR 8799 c	41.2	A5	42^{+6}_{-4} Myr	0.9	$7.2^{+0.6}_{-0.7}$	~L/T	1225 ± 125	3.5 - 3.9	-	1,2,3
HR 8799 d	41.2	A5	42^{+6}_{-4} Myr	0.7	$7.2^{+0.6}_{-0.7}$	L7 ± 1	1200 ± 100	3.0 - 4.5	-	1,2,3
HR 8799 e	41.2	A5	42^{+6}_{-4} Myr	0.4	$7.2^{+0.6}_{-0.7}$	L7 ± 1	1150 ± 50	4.3 ± 0.3	-	1,2,3,4
PZ Tel B	47.0	G9	21 ± 4 Myr	0.5	38 - 72	M7 ± 1	2700 ± 100	$<$4.5	-	5,6
HR 7672 B	17.7	G0	$2.4^{+0.6}_{-0.7}$ Gyr	0.8	$68.7^{+2.4}_{-3.1}$	L4.5 ± 1.5	1510 - 1850	5.0 - 5.5	-	7,8,9,10
GSC 8047 B	86.0	K2	~30 Myr	3.2	22^{+4}_{-7}	M9.5 ± 0.5	2200 ± 100	4.0 ± 0.5	-	5,11,12,13
HD 19467 B	32.0	G3	10 ± 1 Gyr	1.6	$67.4^{+0.9}_{-1.5}$	T5.5 ± 1	978^{+20}_{-43}	~5	-	14,15,16
GQ Lup B	151.2	K7	2 - 5 Myr	0.7	~10 - 40	L1 ± 1	2400 ± 100	4.0 ± 0.5	H,N	17,18,19,20
HD 206893 B	40.8	F5	250^{+450}_{-200} Myr	0.3	15 - 40	L3 - L5	1300 - 1700	3.5 - 5.0	-	7,21,22
HD 4747 B	18.8	G9	11 ± 7 Gyr	0.6	$65.3^{+4.4}_{-3.3}$	T1 ± 2	1407^{+134}_{-140}	$5.2^{+0.5}_{-0.6}$	-	15,23,24
CD-35 2722 B	22.4	M1	100 ± 50 Myr	3.1	31 ± 8	L4 ± 1	1700 - 1900	4.5 ± 0.5	-	5,25
AB Pic b	50.0	K1	~30 Myr	5.5	13^{+1}_{-2}	L0 ± 1	1800^{+100}_{-200}	4.5 ± 0.5	-	5,13,26,27
HD 106906 b	103.0	F5	13 ± 2 Myr	7.1	12.5 ± 1.5	L1.5 ± 1.0	1820 ± 240	~3.5	N,P	28,29,30
GSC 6214 B	108.5	K5	17^{+2}_{-3} Myr	2.2	14.5 ± 2.0	M9.5 ± 1	2200 ± 100	...	H,N,M	19,31
PDS 70 b	113.0	K7	5.4 ± 1.0 Myr	0.2	~10	~L	1500 - 1600	~4	H	32,33,34,35,36
1RXS J1609 B	139.1	M0	~10 Myr	2.2	14.0 ± 1.5	L2 ± 1	2000 ± 100	~4	N,M,A_V	19,37,38
DH Tau B	134.8	M1	~2 Myr	2.3	15^{+7}_{-4}	M9.25 ± 0.25	2400 ± 100	3.5 ± 0.5	H,N	13,19,39
β Pic b	19.7	A6	$18.5^{+2.0}_{-2.4}$ Myr	0.3	13 ± 3	L2 ± 1	1694 ± 40	$4.17^{+0.10}_{-0.13}$	-	40,41,42,43,44
TYC 8998 b	94.6	K3	16.7 ± 1.4 Myr	1.7	14 ± 3	~L0	1727^{+172}_{-127}	$3.91^{+1.59}_{-0.41}$	-	32,45

Notes. d is the distance from Earth, SpT stands for spectral type, ρ is the approximate angular separation of the companion from the host star at the time of observation, $T_{\rm eff}$ is the effective temperature, and log g is the surface gravity. The second column from the right indicates the evidence for the existence of a circumsubstellar disk (CSD), which includes hydrogen emission lines (H), red near-infrared colors (N), excess emission at mid-infrared wavelengths (M), a radially extended point spread function in Hubble Space Telescope images (P), and significant extinction by dust (A_V). HR 7672 B, HD 19467 B, HD 4747 B, and β Pic b have also been observed by Jensen-Clem et al. (2020).

References. Distances from Gaia DR2 (Gaia Collaboration et al., 2018; Bailer-Jones et al., 2018). Other properties from: (1) Gray et al. (2003), (2) Wang et al. (2018), (3) Bonnefoy et al. (2016), (4) Gravity Collaboration et al. (2019), (5) Torres et al. (2006), (6) Maire et al. (2016a), (7) Gray et al. (2006a), (8) Crepp et al. (2012), (9) Liu et al. (2002), (10) Boccaletti et al. (2003), (11) Chauvin et al. (2005a), (12) Ginski et al. (2014), (13) Bonnefoy et al. (2014), (14) Crepp et al. (2014), (15) Wood et al. (2019), (16) Crepp et al. (2015), (17) Kharchenko & Roeser (2009), (18) Donati et al. (2012), (19) Wu et al. (2017a) and references therein, (20) Wu et al. (2017b) and references therein, (21) Delorme et al. (2017), (22) Milli et al. (2017), (23) Montes et al. (2001), (24) Crepp et al. (2018), (25) Wahhaj et al. (2011), (26) Bonnefoy et al. (2010), (27) Chauvin et al. (2005b), (28) Houk & Cowley (1975), (29) Kalas et al. (2015), (30) Daemgen et al. (2017), (31) Pearce et al. (2019), (32) Pecaut & Mamajek (2016), (33) Müller et al. (2018), (34) Keppler et al. (2018), (35) Christiaens et al. (2019), (36) Haffert et al. (2019), (37) Rizzuto et al. (2015), (38) Wu et al. (2015), (39) Herbig (1977), (40) Gray et al. (2006b), (41) Miret-Roig et al. (2020), (42) Stolker et al. (2020), (43) Chilcote et al. (2017), (44) Dupuy et al. (2019), (45) Bohn et al. (2020).

Table 5.2: Overview of the observations performed.

Target	Date	Tracking mode	Filter	DIT (s)	NDIT	t_{exp} (min)	Parallactic rotation (°)	Seeing (")	Coherence time (ms)
HR 8799	2016-10-11	Pupil	BB_H	16	3	137.6	50.5	0.41 - 0.93	2.4 - 6.1
PZ Tel	2016-10-10	Pupil	BB_H	12	4	32.0	14.3	0.57 - 1.21	3.6 - 6.4
	2016-10-12	Pupil	BB_J	12	4	32.0	12.9	0.86 - 1.24	2.8 - 6.1
HR 7672	2018-06-08	Pupil	BB_H	4	1	12.8	9.8	0.51 - 0.68	3.5 - 5.9
	2018-07-13	Pupil	BB_H	4	1	12.8	11.0	0.36 - 0.46	7.2 - 11.0
	2018-07-14	Pupil	BB_H	4	1	12.8	10.9	0.44 - 0.56	11.7 - 15.2
GSC 8047	2018-08-07	Pupil	BB_H	64	1	42.7	13.0	0.40 - 0.65	3.9 - 6.8
	2018-08-09A	Pupil	BB_H	64	1	42.7	13.7	0.43 - 0.82	3.1 - 7.3
	2018-08-09B	Pupil	BB_H	32	2	38.4	17.7	0.39 - 0.56	4.0 - 9.2
HD 19467	2018-08-07	Field	BB_H	12	1	25.6		0.47 - 0.66	2.2 - 3.9
	2018-08-10A	Field	BB_H	12	1	25.6		0.42 - 0.53	6.4 - 11.2
	2018-08-10B	Field	BB_H	12	1	32.0		0.52 - 0.78	4.3 - 9.5
GQ Lup	2018-08-15	Pupil	BB_H	32	1	38.4	6.0	0.48 - 0.72	3.9 - 7.9
HD 206893	2018-09-06	Pupil	BB_K_s	32	1	36.3	31.6	0.46 - 0.64	6.5 - 10.4
	2018-09-08	Pupil	BB_K_s	32	1	40.5	39.3	0.48 - 0.84	11.2 - 19.5
HD 4747	2018-09-10	Pupil	BB_K_s	12	1	25.6	1.1	1.19 - 1.77	2.0 - 3.5
	2018-09-11	Pupil	BB_K_s	12	1	25.6	1.2	0.53 - 0.75	2.2 - 4.4
CD-35 2722	2018-11-22	Pupil	BB_H	16	1	16.0	3.3	0.56 - 0.68	2.7 - 5.1
AB Pic	2019-01-12	Field	BB_H	32	1	46.9		0.59 - 0.91	2.7 - 5.3
HD 106906	2019-01-17	Field	BB_H	32	1	29.9		0.40 - 0.86	5.1 - 11.8
	2019-01-18	Field	BB_H	32	1	29.9		0.40 - 0.96	8.4 - 14.4
	2019-01-20	Field	BB_H	32	1	29.9		0.44 - 0.78	11.5 - 16.7
	2019-01-26	Field	BB_H	32	1	29.9		0.36 - 0.48	13.9 - 20.1
GSC 6214	2019-02-22	Pupil	BB_H	32	1	29.9	1.3	0.43 - 0.99	11.2 - 21.0
	2019-08-06	Pupil	BB_H	32	1	33.1	1.6	0.34 - 0.53	5.1 - 11.4
	2019-08-07	Pupil	BB_H	32	1	29.9	0.8	0.43 - 0.58	5.8 - 8.8
PDS 70	2019-07-12	Pupil	BB_K_s	64	1	135.5	85.2	0.37 - 0.79	2.8 - 5.4
	2019-08-09	Pupil	BB_H	64	1	38.4	13.5	1.28 - 1.67	1.8 - 2.5
1RXS J1609	2019-08-06	Pupil	BB_H	32	1	29.9	1.5	0.33 - 0.50	8.0 - 13.2
	2019-08-29	Field	BB_H	64	1	46.9		0.55 - 0.81	2.6 - 3.6
	2019-08-31	Field	BB_H	64	1	11.7		0.89 - 1.13	2.2 - 3.0
	2019-09-17A	Field	BB_H	64	1	12.8		0.58 - 0.73	3.4 - 4.1
	2019-09-17B	Field	BB_H	64	1	38.4		0.52 - 0.80	2.7 - 3.9
	2019-09-23	Field	BB_H	64	1	38.4		0.71 - 1.03	3.0 - 5.1
DH Tau	2019-08-17	Pupil	BB_H	32	1	14.9	4.3	0.48 - 0.56	3.9 - 4.8
	2019-09-16	Field	BB_H	64	1	38.4		0.90 - 1.60	1.6 - 2.9
	2019-10-24	Field	BB_H	64	1	38.4		0.20 - 0.32	5.5 - 12.0
	2019-10-25A	Field	BB_H	64	1	38.4		0.50 - 0.99	5.9 - 10.4
	2019-10-25B	Field	BB_H	64	1	38.4		0.47 - 0.64	5.3 - 11.7
β Pic	2019-10-29	Pupil	BB_H	4	8	29.9	20.9	0.34 - 0.60	3.3 - 5.8
	2019-11-26	Pupil	BB_H	4	8	29.9	19.8	0.37 - 0.53	2.9 - 7.8
TYC 8998	2020-02-16	Pupil	BB_H	32	4	34.1	12.8	0.46 - 0.75	7.1 - 11.2

Notes. The date is in the format year-month-day, DIT stands for detector integration time, NDIT is the number of detector integrations per HWP switch angle and t_{exp} is the total on-source exposure time. The parallactic rotation is only indicated for observations performed in pupil-tracking mode. The seeing and coherence time are retrieved from measurements by the DIMM (Differential Image Motion Monitor) and from the MASS-DIMM (Multi-Aperture Scintillation Sensor), respectively.

targets a single visit was enough to detect the companion with high S/N in total intensity. We mainly observed in broadband H, but sometimes used broadband J or K_s when we wanted to obtain data in an additional filter or in the case the companion was brighter in K_s than H. We used the apodized Lyot coronagraph with a mask diameter of 185 mas (for J and H) or 240 mas (for K_s) to suppress the starlight (Carbillet et al., 2011; Guerri et al., 2011). This allowed us to use longer integration times per frame to minimize the effects of read noise. However, we did not use integration times longer than 64 s to limit the effect of changing atmospheric conditions during a HWP cycle. In addition to the polarimetric science frames, we took star center frames to accurately determine the position of the star behind the coronagraph and star flux frames to measure the total stellar flux. We also took sky frames with the same instrument setup as the science and star flux frames to subtract the sky background from the respective frames.

For the majority of the observations, we used the pupil-tracking mode (see Chapter 4). In this mode the image derotator (K-mirror) rotates such that the telescope pupil is kept fixed with respect to the detector while the on-sky field of view rotates with the parallactic angle. The pupil-tracking mode has numerous advantages. With sufficient parallactic rotation we can apply angular differential imaging (ADI; Marois et al., 2006) to suppress speckle noise and accurately determine the total intensity of the companions located at small angular separations from the star. Furthermore, because the speckles are quasistatic, they are more effectively removed in the polarimetric data-reduction steps (and can be further suppressed by applying ADI to the polarimetric images). In addition, the diffraction spikes created by the support structure of the telescope's secondary mirror are suppressed by a mask added to the Lyot stop. Finally, the loss of signal due to the crosstalk produced by the image derotator is limited (see Chapter 2). As a result, the polarimetric efficiency, that is, the fraction of the linearly polarized light incident on the telescope that is actually measured, is always high (typically $\gtrsim 90\%$).

For a few targets, we used the field-tracking mode to be able to offset the derotator position angle and control the orientation of the image on the detector. For instance, the companions of AB Pic and HD 106906 are at such large angular separations (see Table 5.1) that we needed to place them in one of the corners of the $11'' \times 11''$ field of view to make them visible. In the case of 1RXS J1609 and DH Tau we switched to field-tracking mode after we discovered that both companions crossed a cluster of bad pixels during the pupil-tracking observations. In all cases, we chose the orientation of the image derotator such that the polarimetric efficiency was high (see de Boer et al., 2020).

5.3 Data reduction

We reduced the data with the publicly available and highly automated pipeline `IRDAP`[3] (IRDIS Data reduction for Accurate Polarimetry), version 1.2.2 (Chapter 2). IRDAP pre-processes the raw data by subtracting the sky background, flat fielding, correcting for bad pixels, extracting the images of IRDIS' left and right optical channels, and centering using the star center frames. It then subtracts the right images from the left images (the single difference) for each of the measurements taken at HWP switch angles equal to 0°,

[3] `https://irdap.readthedocs.io`

45°, 22.5°, and 67.5° to obtain the Q^+-, Q^--, U^+-, and U^--images, respectively. IRDAP also adds these same left and right images (the single sum) to obtain the total-intensity I_{Q^+}-, I_{Q^-}-, I_{U^+}-, and I_{U^-}-images. Subsequently, IRDAP computes cubes of Q- and U-images from the double difference and the corresponding cubes of total-intensity I_Q- and I_U-images from the double sum, as:

$$Q = \frac{1}{2}\left(Q^+ - Q^-\right), \tag{5.1}$$

$$I_Q = \frac{1}{2}\left(I_{Q^+} + I_{Q^-}\right), \tag{5.2}$$

and similar for U and I_U. For the two data sets of HD 4747 and the data set of PZ Tel in J-band, strongly varying atmospheric seeing prevents the double difference from fully removing the signal created by transmission differences between the two orthogonal polarization directions downstream of the image derotator. To remove this spurious polarization, we used the normalized double difference (see Chapter 2) instead of the conventional double difference for these three data sets.

After computing the double difference and double sum, IRDAP uses a fully validated Mueller matrix model to correct for the instrumental polarization (created upstream of the image derotator) and crosstalk of the telescope and instrument with an absolute polarimetric accuracy of $\lesssim$0.1% in the degree of polarization. IRDAP also derotates the images and corrects them for true north (see Maire et al., 2016b). This results in a total of four images: Q, U, I_Q, and I_U, that constitute our best estimate of the linear polarization state incident on the telescope. Finally, IRDAP computes images of the linearly polarized intensity $PI = \sqrt{(Q^2 + U^2)}$, and, following the definitions of de Boer et al. (2020), images of Q_ϕ and U_ϕ. Positive (negative) Q_ϕ indicates linear polarization in the azimuthal (radial) direction, and U_ϕ shows the linear polarization at ±45° from these directions. In Sect. 5.5.5 we use the polarized intensity and Q_ϕ- and U_ϕ-images to show the five circumstellar disks that we detected.

The model-corrected Q- and U-images often contain a halo of polarized light from the star. This polarization can originate from interstellar dust, (unresolved) circumstellar material, and spurious or uncorrected instrumental polarization. With IRDAP we can therefore determine the stellar polarization from the I_Q-, I_U-, and model-corrected Q- and U-images by measuring the flux in these images in a user-defined region that contains only starlight and no signal from a companion, background star, or circumstellar disk. For most data sets we measured the stellar polarization using a star-centered annulus placed over the AO residuals, or in the case that region contains little flux, a large aperture centered on the star. IRDAP then determines the corresponding uncertainty by measuring the stellar polarization for each HWP cycle individually and computing the standard error of the mean over the measurements. Finally, IRDAP creates an additional set of Q- and U-images with the stellar polarization subtracted. To this end, it scales the I_Q- and I_U-images with the measured fractional stellar polarization and subtracts the resulting images from the model-corrected Q- and U-images. Whenever discussing data in this chapter, we always mean the reduction without the stellar polarization subtracted, unless explicitly stated.

For the observations taken in pupil-tracking mode, IRDAP additionally performs classical ADI and ADI with principal component analysis (PCA; Soummer et al., 2012; Amara & Quanz, 2012) to suppress the stellar speckle halo and detect the companions in total intensity. IRDAP also processes the star flux frames by performing sky subtraction, flat fielding, bad-pixel correction, and registering through fitting the frames to a 2D Gaussian function. We obtained the final images of the stellar point spread function (PSF) by mean-combining the left and right processed star flux frames and scaling the pixel values to the integration time and system transmission (i.e., due to neutral-density filters) of the science frames. We separately reduced the data sets of targets that we observed multiple times and then used IRDAP to mean-combine the final images produced in each reduction.

The final Q- and U-images of most data sets still contain a small amount of speckle noise close to the star. For the data sets of HR 8799, HD 206893 and β Pic, which have companions at small separations from the star, we therefore performed additional reductions in which we apply classical ADI on the polarimetric images to further suppress these speckles (see Chapter 4). To this end, we added a reduction step to IRDAP in which we median-combine the instrumental-polarization-subtracted Q-frames (and U-frames) and subtract the resulting median image from each of the frames before derotating them. In these reductions we skip the later step of determining and subtracting the stellar polarization because the ADI step has already removed the halo of polarized starlight.

5.4 Extraction of polarization of companions: Detection of polarization of DH Tau B

With the data of all targets reduced, we can determine the polarization of the companions, or, in the case we do not detect significant polarization, place upper limits on the degree of polarization of the companions. For this we have developed a method similar to that employed by Jensen-Clem et al. (2020), which, in turn, is based on the method used by Jensen-Clem et al. (2016). In this method, we use aperture photometry to estimate the probability distributions of the companion signals in the I_Q-, I_U-, Q-, and U-images. We then use these distributions to calculate the probability distributions of the degree and angle of linear polarization, from which we retrieve the median values, uncertainties, and upper limits. We applied this method to the data sets of GSC 8047, CD-35 2722, AB Pic, HD 106906, GSC 6214, 1RXS J1609, DH Tau, and TYC 8998. In this section, we demonstrate the method using the 2019-10-24 H-band data set of DH Tau and exemplify the detection of the polarization of DH Tau B, a companion at a large angular separation from its star. For companions at close separations or with large star-to-companion contrasts, we have slightly adapted the method and determine the distributions in I_Q and I_U through ADI with negative PSF injection or fitting of the companion PSF. In Appendices 5.C and 5.D we demonstrate the two respective methods and show how we set upper limits on the polarization of β Pic b and HD 19467 B.

To start the analysis of the 2019-10-24 data set of DH Tau, we determine the center coordinates of the companion DH Tau B by mean-combining the I_Q- and I_U-images and fitting a 2D Moffat function to the resulting image at the position of the companion. We

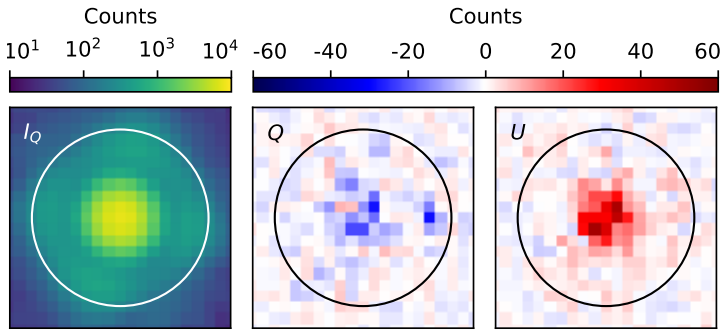


Figure 5.2: Reduced I_Q-, Q-, and U-images (after applying the cosmetic correction described in Appendix 5.A) at the position of the companion DH Tau B of the 2019-10-24 data set of DH Tau, showing an aperture of radius 8 pixels centered on the companion. The I_U-image, which is not shown, is very similar to the I_Q-image.

then make a cosmetic correction to the Q- and U-images (if necessary) to remove spurious structures that result from imperfect relative centering of the images, image motion, and parallactic rotation (see Appendix 5.A). The I_Q-, Q-, and U-images (after the cosmetic correction) at the companion position are shown in Fig. 5.2. The signals in Q and (in particular) in U are clear indications that DH Tau B is polarized.

To determine the probability distributions of the companion signals in I_Q, I_U, Q, and U, we define a range of aperture radii from 1 to 10 pixels to be used for the photometry. For each aperture radius we perform the following five steps, after which we select the final aperture radius to be used for our results. Because at the end of this section we select a final aperture radius of 8 pixels, we use this radius in the examples of the five steps below.

As the first step, we place an aperture of the given radius at the position of the companion in each of the I_Q-, I_U-, Q-, and U-images (see Fig. 5.2) and sum the flux in the aperture. In the same images we then place a ring of comparison apertures around the star at the same separation as the companion to sample the background. We exclude those apertures that contain the first Airy ring of the companion, diffraction spikes from the star and the companion, and clusters of bad pixels. The resulting ring of apertures for an aperture radius of 8 pixels is shown superimposed on the I_Q-image in Fig. 5.3. In this figure the first Airy ring and the diffraction spikes created by the Lyot stop mask are clearly visible at the companion position, which is evidence of the extremely good atmospheric conditions during the observations (see Table 5.2). Finally, we sum the flux in each of the comparison apertures and compute the mean background as the mean of the aperture sums.

In step two, we calculate the probability density function (PDF) of the companion signal in I_Q, I_U, Q, and U, taking into account only the photon noise of the companion. To this end, we compute the companion signals in I_Q, I_U, Q, and U by subtracting the mean background from the summed flux of the companion aperture. We then compute the PDFs of I_Q and I_U from a Gaussian distribution with the mean and variance equal to the respective companion signals, while accounting for the conversion from counts

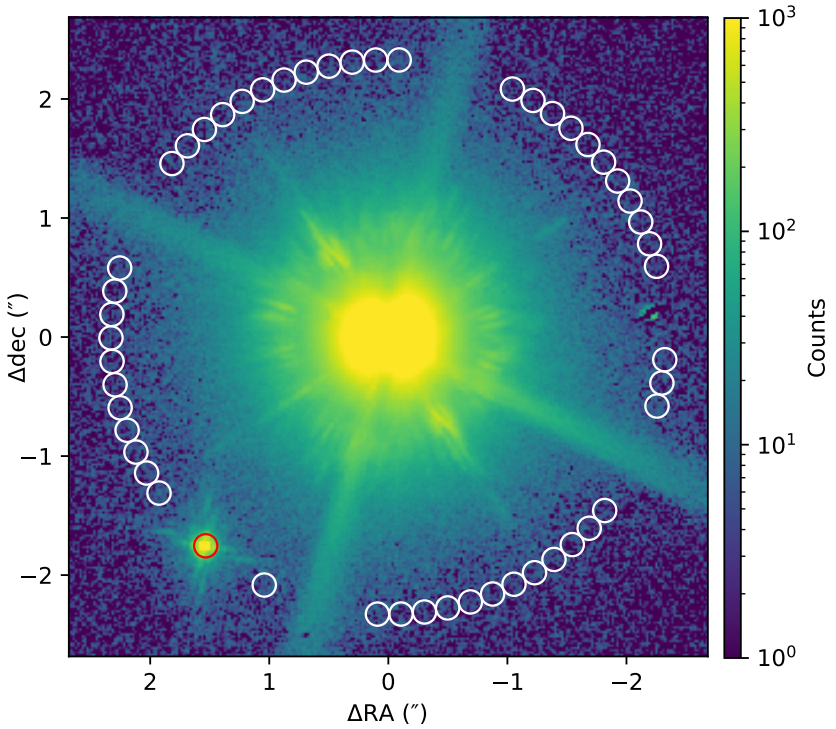


Figure 5.3: Reduced I_Q-image of the 2019-10-24 data set of DH Tau, showing an aperture of radius 8 pixels at the position of the companion DH Tau B (red) and the ring of comparison apertures of the same radius around the star (white).

to total number of detected photoelectrons and back to counts (using a detector gain of 1.75 e^-/count). The resulting PDF of I_Q for an aperture radius of 8 pixels is shown in Fig. 5.4 (left). For large number of photons, the photon noise in Q and U is the same as that in I_Q and I_U. We therefore construct the PDFs of Q and U from a Gaussian distribution with the mean equal to the companion signals in Q and U, but the variance equal to that of the PDFs of I_Q and I_U. Figure 5.4 (right) shows the resulting PDF in Q.

For the third step, we estimate the PDF of the background in I_Q, I_U, Q, and U using the comparison aperture sums obtained in the first step. To not a priori assume a specific functional form of the PDF, we use kernel density estimation (KDE). In this method, the PDF is obtained by placing a Gaussian kernel of a given bandwidth (i.e., a Gaussian distribution with a given standard deviation) at each data point of the sample and summing the resulting kernels. We compute the bandwidth of the Gaussian kernel using Scott's rule (Scott, 2015), in this case yielding a bandwidth of ~84 counts for I_Q and I_U, and ~18 counts for Q and U. Histograms of the background samples and the PDFs as estimated via KDE for an aperture radius of 8 pixels are shown in Fig. 5.5. We note that for very close-in companions such as PDS 70 b, the number of comparison apertures is low enough that KDE does not produce accurate results. When there are fewer than 21

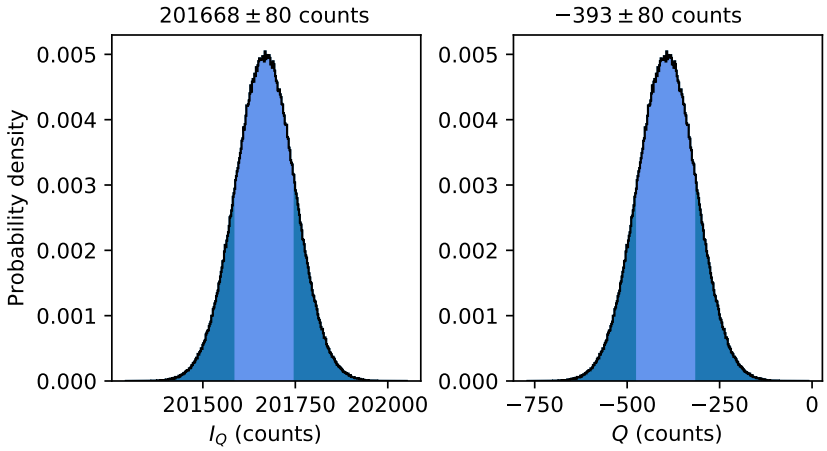


Figure 5.4: PDF of the signal of DH Tau B in I_Q (*left*) and Q (*right*) from the 2019-10-24 data set of DH Tau, using an aperture radius of 8 pixels and taking into account only the photon noise of the companion. The mean and standard deviation of the distributions are shown above the graphs, with the latter also indicated by the light-blue shaded area.

comparison apertures, we therefore account for the small-sample statistics by fitting the background samples with a Student's t-distribution with the empirical standard deviation equal to $s = s_{\mathrm{bg}}\sqrt{(1 + 1/n)}$, with s_{bg} the standard deviation of the comparison aperture sums and n the number of comparison apertures (see Mawet et al., 2014).

In step four, we compute the final probability distributions in I_Q, I_U, Q, and U that include both the photon noise of the companion and the uncertainty of the background. For this, we draw 10^6 random samples from the previously constructed PDFs of the companion signal (step two) and the background (step three). Because we already subtracted the background when computing the PDF of the companion signal, we first subtract the mean background from the drawn background samples. We then compute the final distribution by subtracting the resulting background samples from the samples of the companion signal. Next, we compute the median values of the final distributions and determine the uncertainties from the two-sided 68.27% equal-tailed interval around the median, corresponding to the 1σ (one standard deviation) confidence interval of the Gaussian distribution. The resulting probability distributions for an aperture radius of 8 pixels, including the median values, uncertainties, and S/Ns (i.e., the median value divided by the largest uncertainty), are shown in Fig. 5.6 (top row). The data are clearly photon-noise limited in Q and U because the distributions are nearly Gaussian and the uncertainties are close to the standard deviation shown in Fig. 5.4 (right). It follows that we detect DH Tau B with a very high S/N in total intensity and also have significant detections of polarization, especially in Stokes U.

As the fifth and final step, we use the I_Q-, I_U-, Q-, and U-samples to compute the distributions of normalized Stokes $q = Q/I_Q$, normalized Stokes $u = U/I_U$, the degree of linear polarization $P = \sqrt{(q^2 + u^2)}$, and the angle of linear polarization $\chi = {}^1/_2 \arctan(u/q)$. We compute the median values and uncertainties in the same way as we did for I_Q, I_U, Q,

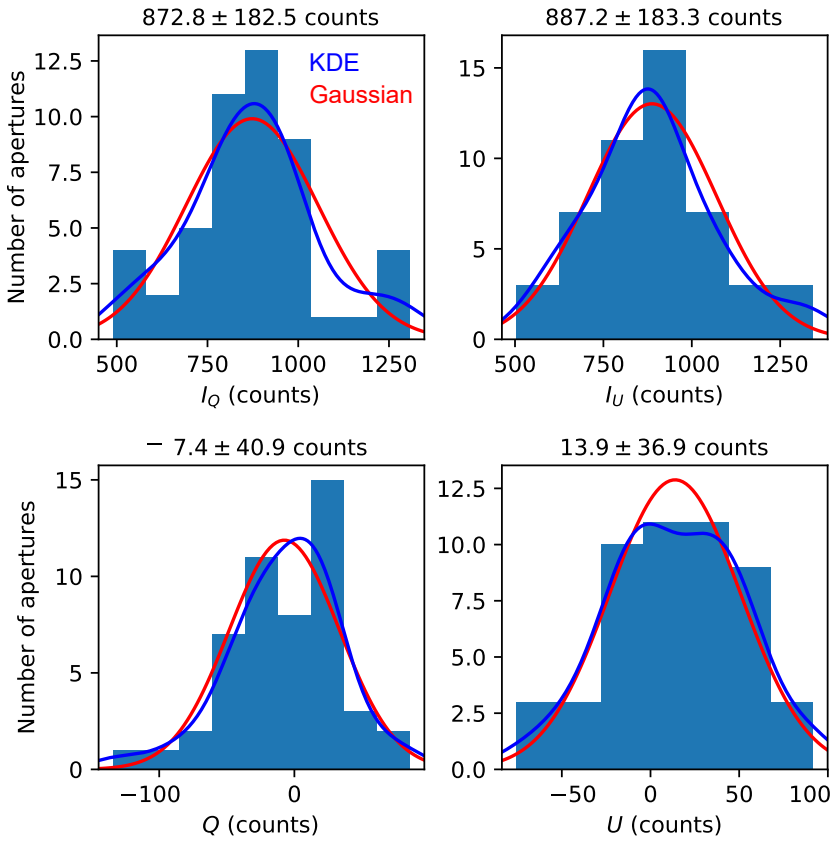


Figure 5.5: Histograms of the background in I_Q, I_U, Q, and U of the 2019-10-24 data set of DH Tau, as obtained through summing the flux in the 8-pixel-radius comparison apertures of Fig. 5.3. The mean and standard deviation of the samples are shown above the histograms. The blue curves show the PDFs as estimated through KDE and the red curves show the best-fit Gaussian distributions for comparison.

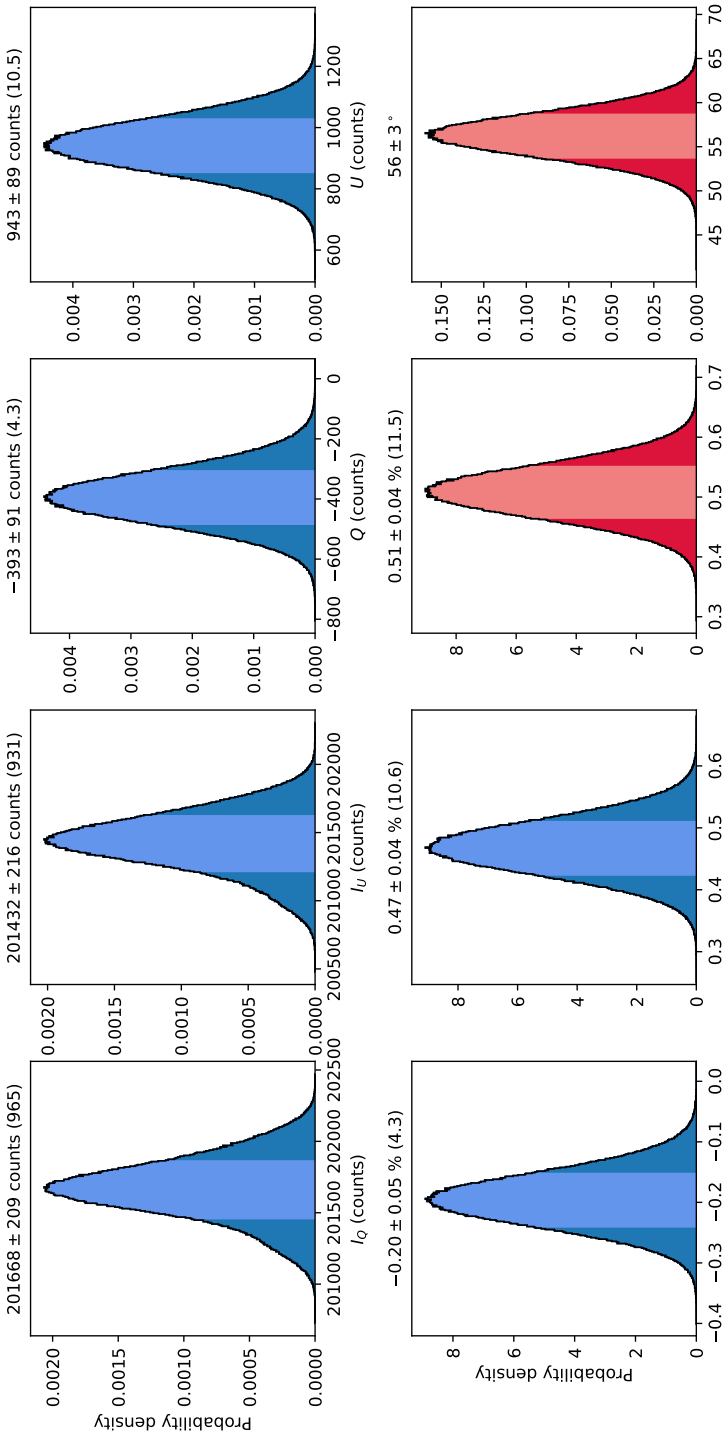


Figure 5.6: Final probability distributions of the signals of DH Tau B in I_Q, I_U, Q, and U (*top row*), and in normalized Stokes q and u, degree of linear polarization, and angle of linear polarization (*bottom row*) from the 2019-10-24 data set of DH Tau, using an aperture radius of 8 pixels. The median values of the distributions, as well as the uncertainties computed from the two-sided 68.27% equal-tailed interval around the median, are shown above the graphs. The S/N, i.e., the median value divided by the largest uncertainty, is shown within parentheses. The 68.27% intervals are also indicated by the light-blue and light-red shaded areas.

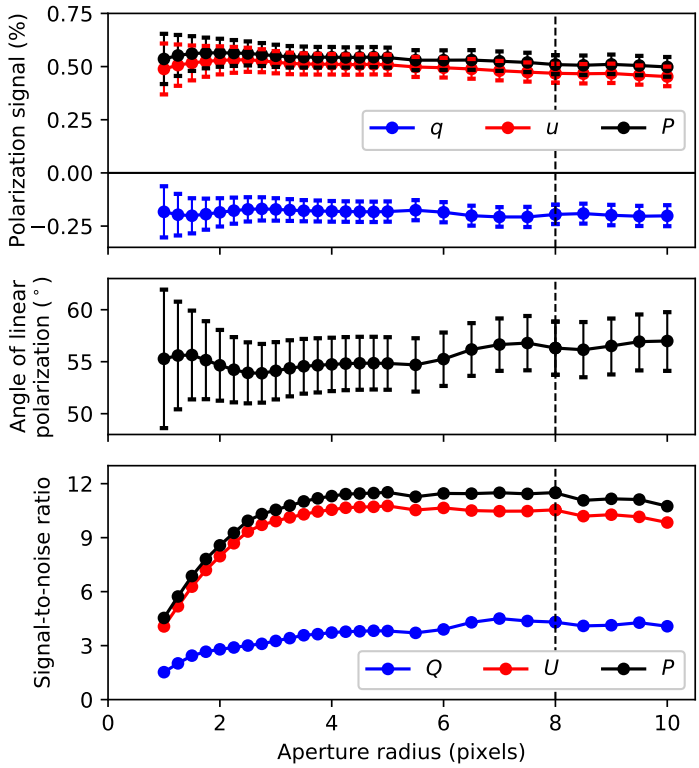


Figure 5.7: Normalized Stokes parameters q and u and degree of linear polarization (*top*), angle of linear polarization (*center*), and S/N in q, u, and the degree of linear polarization (*bottom*) of DH Tau B as a function of aperture radius for the 2019-10-24 data set of DH Tau. The uncertainties of the measured values are shown with error bars. The final selected aperture radius of 8 pixels is indicated with the dashed vertical lines.

and U. The results of these computations for an aperture radius of 8 pixels are shown in Fig. 5.6 (bottom row).

After performing the five steps above for each defined aperture radius, we plot the median values and uncertainties of q, u, the degree and angle of polarization, and the S/N in q, u, and the degree of polarization as a function of aperture radius in Fig. 5.7. From this figure we see that, within the uncertainties, the polarization of the companion is constant with changing aperture radius. We select a final aperture radius of 8 pixels, as indicated by the vertical dashed lines in Fig. 5.7, because at this radius the S/N in q and u is maximized and the aperture is sufficiently large to suppress (average out) the spurious signals resulting from incompletely removed bad pixels (see Appendix 5.B). We conclude that for this 2019-10-24 data set, we measure DH Tau B to have a degree of polarization of 0.51 ± 0.04% and an angle of polarization of 56 ± 3° (east of north) in H-band.

5.5 Results

After careful analysis of our data with the methods as described in Sect. 5.4 and Appendices 5.C and 5.D, we detected unresolved polarization originating from DH Tau B and GSC 6214 B. We consider these measurements detections because the measured polarization signals are significant (i.e., have an S/N of at least 5 in q or u) and are very likely intrinsic to the companions (i.e., are not due to interstellar dust). We present these results in Sects. 5.5.1 and 5.5.2. We also marginally detected polarization from 1RXS J1609 B, but we show in Sect. 5.5.3 that this polarization is best explained by interstellar dust. For the other 17 companions we do not detect significant polarization. In Sect. 5.5.4, we place upper limits on the degree of polarization of 1RXS J1609 B and these other companions. Finally, in Sect. 5.5.5, we briefly describe five circumstellar disks that we detected in our survey and of which two had not been imaged in polarized scattered light before.

5.5.1 Detection of intrinsic polarization of DH Tau B

In this section we present the detection of polarization originating from DH Tau B. Table 5.3 shows the measured H-band degree and angle of polarization of DH Tau B, including the uncertainties and the attained S/Ns, for each of the various data sets and the data set created by mean-combining the final images of the three data sets taken at favorable atmospheric conditions (i.e., the 2019-10-24, 2019-10-25A, and 2019-10-25B data sets; see Table 5.2). For each data set the measured q- and u-signals are within the uncertainties constant with aperture radius. We determined the final values of the polarization signals using apertures of radius 8 pixels, which is at, or close to, the radius where the S/N in q and u is maximized for the various data sets (see Sect. 5.4). As shown in Table 5.3, we detect significant polarization from DH Tau B, reaching S/Ns of around 10 for the three data sets taken at favorable atmospheric conditions. The measured degree and angle of polarization for the different data sets are overall consistent. From visual inspection of the images, we find that the small differences among the data sets are primarily due to small biases caused by incompletely removed bad pixels (see Appendix 5.B). These differences can additionally be caused by time-varying atmospheric conditions and AO performance, the limited accuracy of the Mueller matrix model with which the data have been corrected (see Chapter 2), and other unknown systematic effects. From the mean-combined images, we measure DH Tau B to have a degree and angle of polarization of $0.48 \pm 0.03\%$ and $58 \pm 2^\circ$ (east of north), respectively, with an S/N of 7.7 in q and 16.1 in u.

Table 5.3 also lists the stellar degrees and angles of polarization as measured with an annulus at the location of the AO residuals (see Sect. 5.3). For the mean-combined data set we determined the uncertainty on the stellar polarization by propagating the uncertainties from the individual data sets using a Monte Carlo calculation and assuming Gaussian statistics. The measurements of the stellar polarization are very likely affected by some systematic effects because the signals are less consistent than those of the companion and show differences among the data sets that are much larger than the calculated (statistical) uncertainties. The most likely explanation for these differences is that time-varying atmospheric conditions and AO performance cause the effective coronagraphic extinction to vary from frame to frame. Because the companion is not affected by the coronagraph,

Table 5.3: Degree and angle of linear polarization, including the uncertainties, of the parent star DH Tau A and the companion DH Tau B as measured in H-band for each of the five data sets and the data set created by mean-combining the final images of the 2019-10-24, 2019-10-25A, and 2019-10-25B data sets.

Data set	$P_{\rm star}$ (%)	$\chi_{\rm star}$ (°)	$P_{\rm com}$ (%)	$\chi_{\rm com}$ (°)	S/N $q_{\rm com}$	S/N $u_{\rm com}$
2019-08-17	0.08 ± 0.01	83 ± 10	0.4 ± 0.1	46 ± 9	0.1	3.1
2019-09-16	0.23 ± 0.01	114 ± 2	0.6 ± 0.2	51 ± 9	0.6	3.3
2019-10-24	0.11 ± 0.01	119 ± 3	0.51 ± 0.04	56 ± 3	4.3	10.6
2019-10-25A	0.16 ± 0.01	145 ± 2	0.49 ± 0.05	51 ± 3	2.1	9.9
2019-10-25B	0.27 ± 0.02	123 ± 2	0.48 ± 0.05	66 ± 3	6.4	7.4
Mean combined	0.172 ± 0.009	128 ± 1	0.48 ± 0.03	58 ± 2	7.7	16.1

Notes. $P_{\rm star}$ and $\chi_{\rm star}$ are the degree and angle of linear polarization of the parent star DH Tau A, respectively, and $P_{\rm com}$ and $\chi_{\rm com}$ are the degree and angle of polarization of the companion DH Tau B. S/N $q_{\rm com}$ and S/N $u_{\rm com}$ are the S/Ns with which the q- and u-signals of DH Tau B are detected.

this can also explain why the polarization measured for the companion is more consistent among the data sets. The stellar polarization measurements show that the star could be truly polarized because the angles of polarization for the three data sets taken at favorable conditions (2019-10-24, 2019-10-25A, and 2019-10-25B) are quite similar. Importantly, the measured polarization of the companion differs significantly from that of the star in all data sets, with the companion having a significantly larger degree of polarization and a very different angle of polarization.

DH Tau, at a distance of 135 pc[4], is located at the front side of the Taurus molecular cloud complex that extends from at least 126 pc to 163 pc (Galli et al., 2018). To determine whether DH Tau B is intrinsically polarized, we therefore need to determine the contribution of interstellar dust to the measured polarization. The interstellar polarization is a result of dichroism by elongated dust grains that are aligned with the local (galactic) magnetic field. Because interstellar dust creates the same polarization for the companion and the star, this contribution can often be determined from the measured stellar polarization (e.g., for 1RXS J1609, see Sect. 5.5.3, and ROXs 42B, see Jensen-Clem et al., 2020). However, we cannot do that in this case because the star hosts a disk that we spatially resolve in our images (see Sect. 5.5.5 and Fig. 5.12, top left) and therefore the stellar polarization is likely a combination of intrinsic and interstellar polarization.

To investigate the contribution of interstellar dust to the polarization of DH Tau B, we show in Fig. 5.8 a map of the polarization of DH Tau A and B and a few dozen nearby stars. The map is superimposed on a Herschel-SPIRE (Pilbratt et al., 2010) image at 350 µm that shows the concentrations of interstellar dust in the region. White lines show optical measurements of stars at the periphery of the B216-B217 dark cloud from Heyer et al. (1987). Yellow lines display measurements from Moneti et al. (1984) of the three nearest bright stars to DH Tau. Of these stars, HD 283704 (58 pc) is unpolarized as it is located in front of the clouds, whereas HD 283705 (170 pc) and HD 283643 (396 pc) are located behind the clouds and are both polarized with an angle of polarization of

[4] All distances in this chapter are retrieved from Bailer-Jones et al. (2018).

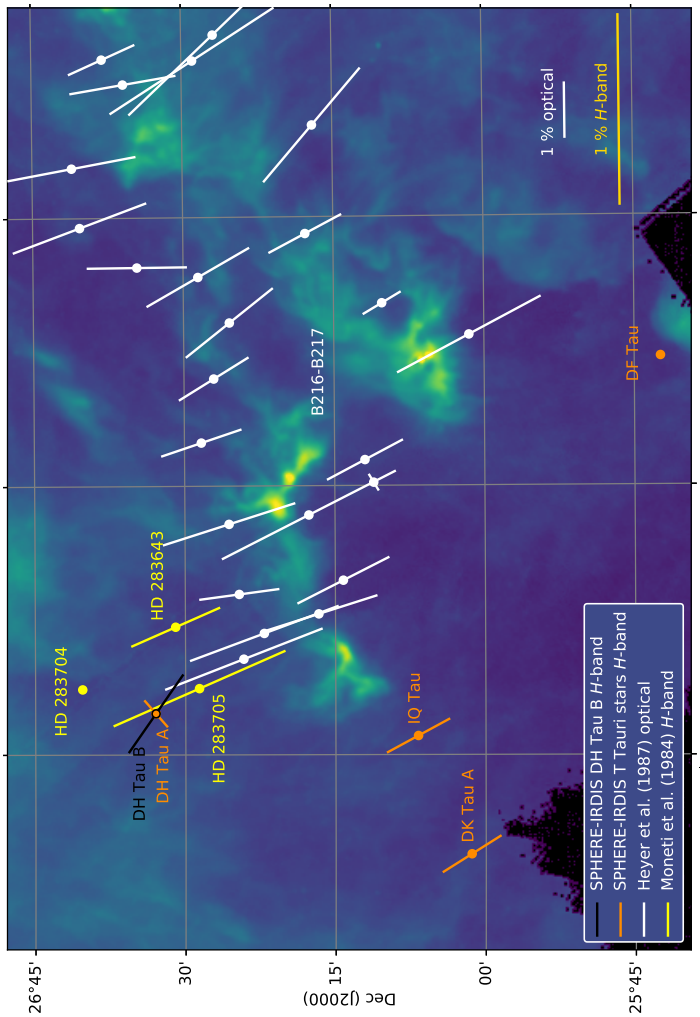


Figure 5.8: Map of the linear polarization of DH Tau B and nearby stars superimposed on a Herschel-SPIRE map at 350 µm. The length and orientation of the lines indicate the degree and angle of linear polarization, respectively. The black line shows the *H*-band polarization we measure for DH Tau B, and the orange lines display the SPHERE-IRDIS *H*-band measurements of DH Tau A and three other nearby T Tauri stars whose archival data we analyzed. White lines show optical measurements by Heyer et al. (1987). Yellow lines indicate the *H*-band polarization of three bright stars closest to DH Tau as derived from optical measurements by Moneti et al. (1984). The length of the *H*-band vectors are scaled by a factor of four with respect to the optical vectors.

$26 \pm 1°$. Because the stars from Heyer et al. (1987) and Moneti et al. (1984) are generally much older than DH Tau and are therefore not expected to have a circumstellar disk that significantly polarizes their light, their polarization must primarily originate from interstellar dust. Comparing the angles of polarization of DH Tau A ($128 \pm 1°$) and B ($58 \pm 2°$) with those of the reference stars in Fig. 5.8, we conclude that the polarization of both DH Tau A and B must include an intrinsic component.

We now set limits on the interstellar degree of polarization of the DH Tau system. To this end, we convert the optical measurements of the degree of polarization of the nearby stars HD 283705 and HD 283643 (2.48% and 1.27%) from Moneti et al. (1984) to *H*-band. For this conversion we use Serkowski's law of interstellar polarization (Serkowski et al., 1975):

$$P = P_{\max} \exp\left[-K \ln^2 (\lambda_{\max}/\lambda)\right], \tag{5.3}$$

where λ is the wavelength of the light, $P_{\max}$ is the maximum degree of polarization, and $\lambda_{\max}$ is the wavelength at which this maximum occurs. The parameter K is computed following Whittet et al. (1992):

$$K = 0.01 + 1.66\lambda_{\max}, \tag{5.4}$$

with $\lambda_{\max}$ in micrometers. Because the observations were taken without color filter, we retrieve the spectral response of a Ga-As photomultiplier tube similar to that used for the measurements[5] and multiply it with the transmission of the Earth's atmosphere. With the resulting spectral transmission, we can compute the degree of polarization that the instrument measures from the transmission-weighted average over the curve from Serkowski's law. Assuming $\lambda_{\max} = 0.55\,\mu$m, which is the average value for the 16 bright stars in Taurus observed by Whittet et al. (1992), we fit $P_{\max}$ for both stars. From the fitted curves we then compute the degree of polarization at *H*-band, yielding 0.9% for HD 283705 and 0.5% for HD 283643. Because DH Tau is located at the front side of the clouds (rather than behind the clouds as are the comparison stars), the interstellar polarization of DH Tau is most likely below 0.9%, probably below 0.5%. This is in agreement with the *H*-band degrees of polarization of three nearby T Tauri stars whose archival SPHERE-IRDIS polarimetric data we analyzed (see Fig. 5.8). Of these stars, DF Tau (125 pc) is unpolarized, and DK Tau A (128 pc), which does not have a disk, and IQ Tau (131 pc), which has a very faint disk, are 0.33% and 0.34% polarized, respectively, both with an angle of polarization of ~30°.

Although we do not know the exact interstellar degree of polarization for DH Tau, the angle of polarization is likely close to 26°, which is the angle of both HD 283705 and HD 283643. To see whether DH Tau B is intrinsically polarized, we take the polarization signal that we measured in the mean-combined images ($0.48 \pm 0.03\%$ at $58 \pm 2°$; see Table 5.3) and subtract interstellar polarization signals with an angle of polarization of 26° and a range of degrees of polarization. The resulting intrinsic degree and angle of polarization of DH Tau B versus the interstellar degree of polarization is shown in Fig. 5.9 (top). We see that the intrinsic polarization decreases for interstellar degrees of polarization between 0% and 0.2% and increases for larger interstellar polarizations. The

[5] RCA Photomultiplier Manual, http://www.decadecounter.com/vta/pdf/RCAPMT.pdf, consulted on June 2, 2020.

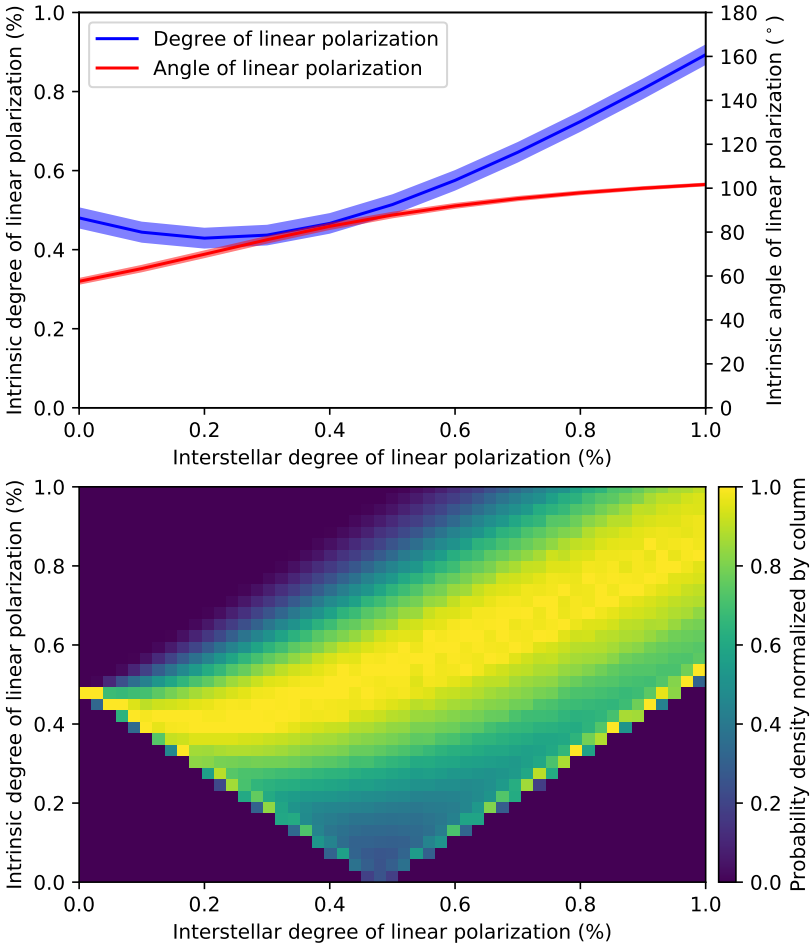


Figure 5.9: Intrinsic polarization of DH Tau B after subtracting interstellar polarization signals from the measured polarization of the companion. *Top*: Intrinsic degree and angle of linear polarization of DH Tau B as a function of the degree of polarization due to interstellar dust, assuming an angle of 26° for the interstellar polarization. The bands around the curves show the uncertainties of our measurements. *Bottom*: Probability distributions of the intrinsic degree of polarization of DH Tau B for a range of degrees of polarization due to interstellar dust, assuming the angle of the interstellar polarization to have the same distribution as that determined by Goodman et al. (1992) for the B216-B217 dark cloud adjacent to DH Tau. The probability distribution of each column is normalized to one.

intrinsic polarization increases because an ever larger interstellar polarization needs to be canceled to produce the measured polarization. For the range plotted, the intrinsic angle of polarization increases from 60° to 100°. Most importantly, the intrinsic degree of polarization is always higher than 0.4%, showing that DH Tau B should be intrinsically polarized if the interstellar polarization indeed has an angle of polarization of 26°.

From the measurements by Heyer et al. (1987) (white lines in Fig. 5.8), we see that there are slight variations in the angle of polarization of the stars in the region. Goodman et al. (1992) determined that the angles of polarization of these stars are Gaussian distributed with a mean of 27° and a standard deviation of 15°. Using this distribution of angles, we take a more probabilistic approach and perform a Monte Carlo simulation in which we compute for a range of interstellar degrees of polarization the probability distribution of the intrinsic polarization. The histograms of the resulting distributions for each value of the interstellar degree of polarization are displayed in Fig. 5.9 (bottom). In this figure we have normalized the distribution of each column to one. It follows that the curves of Fig. 5.9 (top) are in fact among the most probable scenarios. We also see that DH Tau B must be at least 0.2% intrinsically polarized for interstellar degrees of polarization between 0% and 0.3% or higher than 0.7%, regardless of the interstellar angle of polarization. Only for interstellar degrees of polarization between 0.3% and 0.7% there is a small possibility (~8%) that DH Tau B is not intrinsically polarized. Based on these findings, we conclude that DH Tau B is very likely intrinsically polarized.

5.5.2 Likely detection of intrinsic polarization of GSC 6214 B

In this section we present the likely detection of intrinsic polarization originating from GSC 6214 B. Figure 5.10 shows the reduced I_Q-, Q-, and U-images in H-band at the position of the companion of the data set created by mean-combining the final images of the three data sets. Table 5.4 shows the measured polarization of GSC 6214 B for the three individual data sets and the mean-combined one. Similar to the DH Tau data, the measured polarization signals of each data set are within the uncertainties constant with aperture radius. We select a final aperture radius of 4 pixels, corresponding to the (approximate) radius where the S/N in q and u is maximized in each of the data sets. Overall the measured degree and angle of polarization of the data sets are consistent within the uncertainties. The slightly different results of the 2019-02-22 data set compared to the other two data sets could be caused by the relatively strong time-varying atmospheric conditions that the observations were taken under (see Table 5.2). Whereas the q- and u-measurements of the three data sets individually do not reach the required 5σ-limit for a detection, the mean-combined measurement does, reaching an S/N of 5.2 in u. From the mean-combined data we therefore conclude that we detect significant polarization from GSC 6214 B, with a degree and angle of polarization of 0.23 ± 0.04% and 138 ± 5°, respectively.

Table 5.4 also shows the stellar degrees and angles of polarization. Because we do not spatially resolve a disk around GSC 6214 A, we used a star-centered aperture extending up to and including the AO residuals to maximize the S/N. The measured signals show significant differences and are overall inconsistent among the data sets. The signals average to a degree of polarization of only 0.10%. The measurements of the stellar polar-

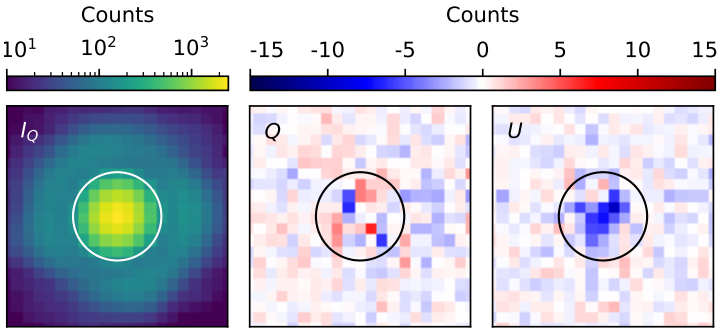


Figure 5.10: Reduced mean-combined I_Q-, Q-, and U-images (after applying the cosmetic correction described in Appendix 5.A) at the position of the companion GSC 6214 B, showing an aperture of radius 4 pixels centered on the companion. The I_U-image, which is not shown, is very similar to the I_Q-image.

Table 5.4: Degree and angle of linear polarization, including the uncertainties, of the parent star GSC 6214 A and the companion GSC 6214 B as measured in H-band for each of the three data sets and the data set created by mean-combining the final images of the three data sets.

Data set	$P_{\rm star}$ (%)	$\chi_{\rm star}$ (°)	$P_{\rm com}$ (%)	$\chi_{\rm com}$ (°)	S/N $q_{\rm com}$	S/N $u_{\rm com}$
2019-02-22	0.17 ± 0.05	27 ± 9	0.18 ± 0.07	143 ± 16	0.5	1.9
2019-08-06	0.18 ± 0.06	72 ± 13	0.26 ± 0.07	137 ± 8	0.2	3.6
2019-08-07	0.08 ± 0.04	70 ± 17	0.24 ± 0.07	139 ± 9	0.4	2.9
Mean combined	0.10 ± 0.03	54 ± 9	0.23 ± 0.04	138 ± 5	0.5	5.2

Notes. The meaning of the column headers is described in the notes of Table 5.3.

ization are therefore most likely dominated by spurious signals. To determine whether the companion is truly polarized, we need to investigate the potential origins of these spurious signals and the effect they have on the measurement of the companion polarization.

If the stellar polarization primarily results from uncorrected instrumental polarization, which to first order equally affects the star and the companion, we would need to subtract these signals from the images. Using the mean-combined images with the stellar polarization subtracted, we measure for the companion a degree and angle of polarization of 0.32 ± 0.04% and 141 ± 4°, respectively, with an S/N of 1.4 in q and 7.2 in u. This polarization signal is larger and more significant than that measured from the images without the stellar polarization subtracted (see Table 5.4). However, the measured signals are less consistent among the data sets, suggesting that uncorrected instrumental polarization may not be the principal cause of the stellar polarization.

A more likely scenario seems that the stellar polarization signals are dominated by systematic effects due to time-varying atmospheric conditions and AO performance in combination with the coronagraph, similar to the case of DH Tau (see Sect. 5.5.1). Also

in the case of GSC 6214, the systematic effects do not affect (as much) the companion measurements because those measurements are overall consistent among the data sets. This suggests that the measurements of the companion are more reliable than those of the star. Because the companion polarization is significantly different from the stellar polarization in all data sets, particularly in the angle of polarization (see Table 5.4), and we measure significant polarization from the companion for both the reduction with and without the stellar polarization subtracted (reaching S/Ns of 7.2 and 5.2 in u, respectively), we conclude that the companion is most likely truly polarized.

To determine whether the polarization of GSC 6214 B is intrinsic to the companion or caused by interstellar dust, we show in Fig. 5.11 a map of the angles of polarization of nearby bright stars from the catalog by Heiles (2000). The map is displayed over an IRAS (Neugebauer et al., 1984) 100 µm map that shows the dust concentrations in the region of the Ophiuchus molecular cloud complex where GSC 6214 is located. Comparing the angle of polarization of GSC 6214 B and the nearby stars, it may seem that the companion is polarized by interstellar dust. However, GSC 6214 is located at 109 pc, whereas estimates for the distance of the Ophiuchus molecular cloud complex range from approximately 120 to 150 pc (e.g., Mamajek, 2008; Lombardi et al., 2008; Ortiz-León et al., 2017; Yan et al., 2019). Indeed, the three stars closest to GSC 6214 in Fig. 5.11 are located at 128 to 131 pc. We therefore consider it more likely that GSC 6214 is located in front of the main concentrations of dust. In addition, if the companion were polarized by interstellar dust, we would expect to measure in all data sets a stellar polarization with the same angle of polarization as the companion (which is the case for 1RXS J1609; see Sect. 5.5.3). In principle it is possible that GSC 6214 A is not significantly polarized because the interstellar polarization is canceled by intrinsic polarization due to an unresolved circumstellar disk. However, this scenario seems very unlikely because Bowler et al. (2015) do not detect a disk with ALMA and put an upper limit on the disk's mass as low as 0.0015% of the mass of the star. Taking into account all considerations, we conclude that it is likely that the polarization we measure for GSC 6214 B is intrinsic to the companion, but we stress that we are less confident than for DH Tau B.

5.5.3 Detection of interstellar polarization from 1RXS J1609 B

In this section we present the detection of polarization in the 1RXS J1609 system. In all six data sets of 1RXS J1609, we consistently measure within the uncertainties the same degree and angle of polarization for the central star 1RXS J1609 A. In the mean-combined data set, which uses the four highest-quality data sets (2019-08-06, 2019-08-29, 2019-09-17B, and 2019-09-23), we measure for the star a degree and angle of polarization of 0.21 ± 0.01% and 97 ± 2°, respectively. In the same data set, we measure for the companion 0.2 ± 0.1% and 95 ± 26°, using an aperture radius of 5 pixels. Although the measurement of the companion polarization is not a significant detection, it is striking that it is within the uncertainties the same as the measured stellar polarization. In the six individual data sets we also measure the polarization of the companion to be consistent with that of the mean-combined data, although with higher uncertainties. Finally, using the mean-combined data, we measure for the relatively bright background object that is also visible in the field of view a degree and angle of polarization of 0.3 ± 0.1% and

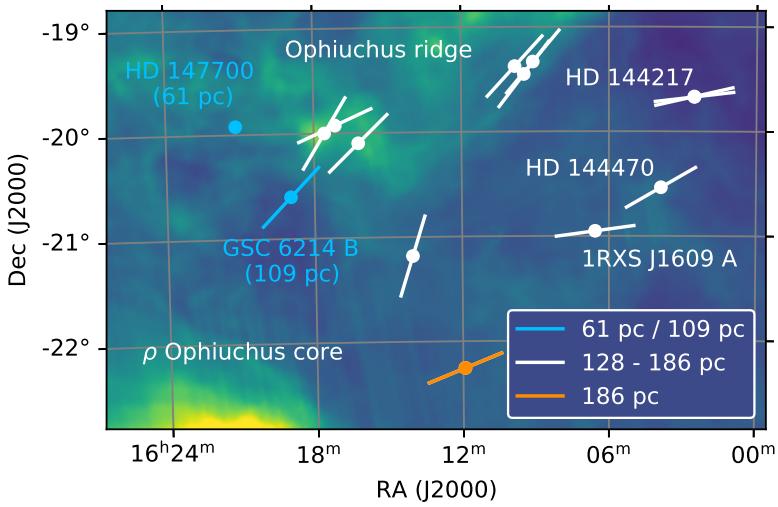


Figure 5.11: Map of the angle of linear polarization of the companion GSC 6214 B, the star 1RXS J1609 A, and other nearby bright stars superimposed on an IRAS map at 100 µm. The angles of GSC 6214 B and 1RXS J1609 A are from the SPHERE-IRDIS *H*-band measurements from this work, whereas for the other stars the angles are taken from the catalog of optical measurements by Heiles (2000). The length of the lines is arbitrary and contrary to Fig. 5.8 does not indicate the degree of polarization. White lines indicate stars at a distance between 128 pc and 142 pc, and blue and orange lines show objects closer or farther away, respectively. We note that the region shown is much larger than that of Fig. 5.8, and so the angular separation among the stars is much larger as well.

103 ± 50°, respectively. Because all three objects have within the uncertainties the same degree and angle of polarization, their polarization likely originates from the same source, that is, from interstellar dust.

To confirm this scenario, we turn to Fig. 5.11, which shows that 1RXS J1609 is located in the Ophiuchus molecular cloud complex a few degrees west from GSC 6214. Contrary to GSC 6214, 1RXS J1609, at a distance of 139 pc, is definitely located within the dust clouds that are located at a distance of approximately 120 to 150 pc (see Sect. 5.5.2). Indeed, the measured angles of polarization of 1RXS J1609 A, 1RXS J1609 B and the background object agree well with those of the nearby bright stars located at a similar distance (see Fig. 5.11). Serkowski et al. (1975) have fitted their multiwavelength optical measurements of the stars HD 144470 and HD 144217 (142 and 129 pc; see Fig. 5.11) to Serkowski's law of interstellar polarization (see Eq. (5.3)) and determined the values of $P_{\max}$ and $\lambda_{\max}$ for both stars. Using these values, we find that in *H*-band the degrees of polarization are equal to approximately 0.4% and 0.3%, respectively. These values are similar to the degree of polarization we measure for the star, the companion, and the background object in our images of 1RXS J1609, where the slight differences are likely due to the inhomogeneous spatial distribution of the interstellar dust. We conclude that the polarization we measure for 1RXS J1609 B originates from interstellar dust and therefore set an upper limit on the degree of polarization in Sect. 5.5.4.

5.5.4 Upper limits on polarization of other companions

In this section we present upper limits on the degree of polarization of the 18 companions for which we do not reach the 5σ-limit in q or u to claim a detection. For the majority of the companions, the S/N in q and u is typically $\lesssim$2–3 for any aperture radius. For four companions the maximum S/N in q or u reaches a value of almost 4. However, in these four cases the signals in the Q- and U-images (after the cosmetic correction described in Appendix 5.A) do not resemble scaled-down positive or negative versions of the total-intensity PSF as one would expect for real signals, but show strong pixel-to-pixel variations caused by incompletely removed bad pixels (see Appendix 5.B).

Table 5.5 shows for each target the upper limits determined from the 68.27% and 99.73% intervals, as described in Appendix 5.C. For targets for which we obtained multiple data sets, we computed the upper limits from the mean-combined images. For the majority of the companions, which are generally the fainter ones, we determined the upper limits using an aperture radius equal to half times the full width at half maximum (FWHM) of the stellar PSF. This aperture radius is on average 1.9 pixels in H-band and 2.6 pixels in K_s-band, and is at, or close to, the radius at which the upper limit is minimized. For seven, generally brighter companions (CD-35 2722 B, AB Pic b, HD 106906 b, GQ Lup B, GSC 8047 B, PZ Tel B in J-band, and 1RXS J1609 B) we used an aperture radius of 5 pixels to average out and suppress the spurious signals created by incompletely removed bad pixels (see Appendix 5.B). However, the bad pixels generally still create a bias in the q- and u-signals, and so we have to accept that this increases the upper limits. For the data sets where this bias is really strong (i.e., CD-35 2722, PZ Tel in J-band, and TYC 8998), we excluded from the data reduction those frames that contribute strong bad pixels at the position of the companion in the final images. Because HD 106906 b is located at an angular separation of 7.1″ from the central star, which is larger than the isoplanatic angle during the observations, its PSF is strongly elongated in the radial direction from the star. To account for this, we used an elliptically shaped aperture. Finally, for the companions of HR 8799, HD 206893, and β Pic, we computed the upper limits using the polarimetric images from the reduction with the added classical ADI step (see Appendix 5.C).

Table 5.5 also shows for each target the stellar degree and angle of polarization. For the majority of the stars the degree of polarization is around 0.1%. To be conservative and because we generally do not know the origin of these low polarization signals (intrinsic, interstellar dust or spurious), we interpret the signals as biases. For these targets we therefore computed the upper limits on the companion polarization from both the reductions with and without the stellar polarization subtracted, and show the highest values in Table 5.5. For three targets we measure a stellar polarization higher than approximately 0.1%. In the case of GQ Lup and PDS 70 this stellar polarization is caused by a circumstellar disk (see Keppler et al. 2018 and Sect. 5.5.5). Although GQ Lup is located in the Lupus I cloud, the contribution of interstellar dust is likely small because HD 141294, the nearest bright star to GQ Lup (at 14.3′ and a distance of 153 pc compared to 151 pc for GQ Lup), is unpolarized at optical wavelengths (Rizzo et al., 1998; Alves & Franco, 2006). For PDS 70 and GQ Lup we therefore determined the upper limits using only the images without the stellar polarization subtracted. For 1RXS J1609 on the other hand, the

Table 5.5: 68.27% and 99.73% upper limits on the degree of linear polarization of the companions (P_{com}), as well as the measured degree and angle of linear polarization of the central star (P_{star} and χ_{star}), for the targets for which we do not detect significant polarization.

Target	Filter	P_{star} (%)	χ_{star}(°)	68.27% upper limit on P_{com} (%)	99.73% upper limit on P_{com} (%)
HR 8799 b	BB_H	0.057 ± 0.006	126 ± 3	0.6	1.2
HR 8799 c	BB_H	0.057 ± 0.006	126 ± 3	0.5	1.1
HR 8799 d	BB_H	0.057 ± 0.006	126 ± 3	0.5	1.2
HR 8799 e	BB_H	0.057 ± 0.006	126 ± 3	0.6	1.3
PZ Tel B	BB_H	0.05 ± 0.03	17 ± 24	0.06	0.1
PZ Tel B	BB_J	0.13 ± 0.01	159 ± 2	0.1	0.2
HR 7672 B	BB_H	0.104 ± 0.007	138 ± 2	0.2	0.3
GSC 8047 B	BB_H	0.04 ± 0.02	160 ± 39	0.2	0.3
HD 19467 B	BB_H	0.054 ± 0.005	7 ± 3	0.4	1.0
GQ Lup B	BB_H	0.94 ± 0.02	83 ± 1	0.2	0.3
HD 206893 B	BB_K_s	0.15 ± 0.06	107 ± 15	0.8	1.7
HD 4747 B	BB_K_s	0.11 ± 0.02	71 ± 7	0.3	0.6
CD-35 2722 B	BB_H	0.15 ± 0.03	66 ± 6	0.1	0.3
AB Pic b	BB_H	0.05 ± 0.01	6 ± 8	0.07	0.2
HD 106906 b	BB_H	0.097 ± 0.008	68 ± 2	0.2	0.3
PDS 70 b	BB_K_s	1.1 ± 0.1	62 ± 3	5.0	12
PDS 70 b	BB_H	0.97 ± 0.02	65 ± 1	9.2	22
1RXS J1609 B	BB_H	0.21 ± 0.01	97 ± 2	0.2	0.5
β Pic b	BB_H	0.075 ± 0.008	163 ± 4	0.2	0.4
TYC 8998 b	BB_H	0.12 ± 0.09	0 ± 4	0.3	0.6

stellar polarization is caused by interstellar dust (see Sect. 5.5.3), and we therefore used the reduction where the stellar polarization is subtracted.

Examining the upper limits in Table 5.5, we see that for 11 companions the 68.27% upper limits are ≤0.3%, with the lowest upper limit equal to 0.06% for PZ Tel B in H-band. These low upper limits are in almost all cases dominated by the photon noise from the companion in the Q- and U-images or the bias due to incompletely removed bad pixels. The upper limits are still larger than the (minimum) polarimetric accuracy of the Mueller matrix model with which the data have been corrected (see Chapter 2). For the companions of HR 8799, HD 19467, and HD 206893, which are fainter or located at a much smaller separation than the other companions, the 68.27% upper limits are dominated by the uncertainty of the background in Q and U and have values between 0.4% and 0.8%. For the very close-in planet PDS 70 b we reach upper limits of 5.0% in K_s-band and 9.2% in H-band. These upper limits are so high because the comparison apertures contain signal from the inner circumstellar disk of PDS 70 A (see Fig. 5.12) and the Student's t-distribution imposes a large statistical penalty for the low number of available comparison apertures (see Appendix 5.C). We note that for PDS 70 c (Haffert et al., 2019), the circumstellar disk prevents us from measuring the polarization altogether. Finally, we reach the highest polarimetric point-source contrast in the mean-combined

data set of β Pic, with a 1σ-contrast of $3 \cdot 10^{-8}$ at a separations of 0.5″ and a contrast below 10^{-8} for separations >2.0″ (see Appendix 5.E). Overall, it follows that our measurements are sensitive to polarization signals of around a few tenths of a percent.

5.5.5 Detection of circumstellar disks of DH Tau, GQ Lup, PDS 70, β Pic, and HD 106906

In our survey we also detected the five circumstellar disks displayed in Fig. 5.12. Although the disks of DH Tau and GQ Lup have already been detected at mm-wavelengths (Wolff et al., 2017; MacGregor et al., 2017; Wu et al., 2017b), here we present the first images in polarized scattered light, revealing various interesting features. For PDS 70, HD 106906, and β Pic near-infrared polarimetric images already exist (Keppler et al., 2018; Hashimoto et al., 2012; Kalas et al., 2015; Millar-Blanchaer et al., 2015), but our images are generally deeper, reveal new features, or confirm features that were previously observed. In this section, we therefore briefly discuss these disks, although we consider a detailed analysis beyond the scope of this chapter.

Figure 5.12 (top left) shows the polarized intensity image of the DH Tau system, with the circumstellar disk visible in the top right corner of the panel. The relatively small disk has a diameter of approximately 0.50″ or 67 au at 135 pc. From ALMA measurements of the Keplerian rotation of the disk, Sheehan et al. (2019) have determined an inclination of 48° and a position angle of 2.5° (east of north), with the northern side of the disk rotating toward us (i.e., blue shifted). In our images the disk has a smooth intensity profile with no visible disk gap, rings, or spirals. A strong brightness asymmetry is visible between the eastern and western sides of the disk, which could be related to the viewing angle of the disk and the dust scattering properties. This asymmetry is compatible with the position angle derived from ALMA: if the side inclined toward the Earth appears brightest due to enhanced forward scattering, then the eastern side is the forward-scattering near side of the disk. Alternatively, this brightness asymmetry could result from shadowing by an unresolved inner disk component because the brightness changes quite abruptly with azimuth. The brightness asymmetry might extend toward the inner (coronagraphically masked) parts of the disk because the angle of polarization that we measure for the average stellar polarization (128°, see Table 5.3) agrees well with the angle of polarization one obtains when integrating over the non-obscured parts of the disk. In the bottom left corner of the panel the polarization signal of DH Tau B is visible, where the angle of polarization is indicated with the two lines protruding from the circle around the companion.

Figure 5.12 (top row, second column) shows the polarized intensity image of the circumstellar disk and companion of GQ Lup. From ALMA images (MacGregor et al., 2017; Wu et al., 2017b), which show a rather featureless disk, the disk inclination and position angle are known to be 60° and 346°, respectively. Our scattered light images show a remarkable north-south asymmetry in the circumstellar disk, with the southern part of the disk extending out to 0.84″ (127 au at 151 pc) and the northern part only out to 0.49″ (74 au). Two spiral-like features can be seen protruding eastward from the southern part of the disk. The disk asymmetry and spiral-like features are reminiscent of those of the disk around RY Lup (Langlois et al., 2018) and could be the result of periodic close passes of GQ Lup B (see e.g., Dong et al., 2016; Cuello et al., 2019, 2020). The orbital

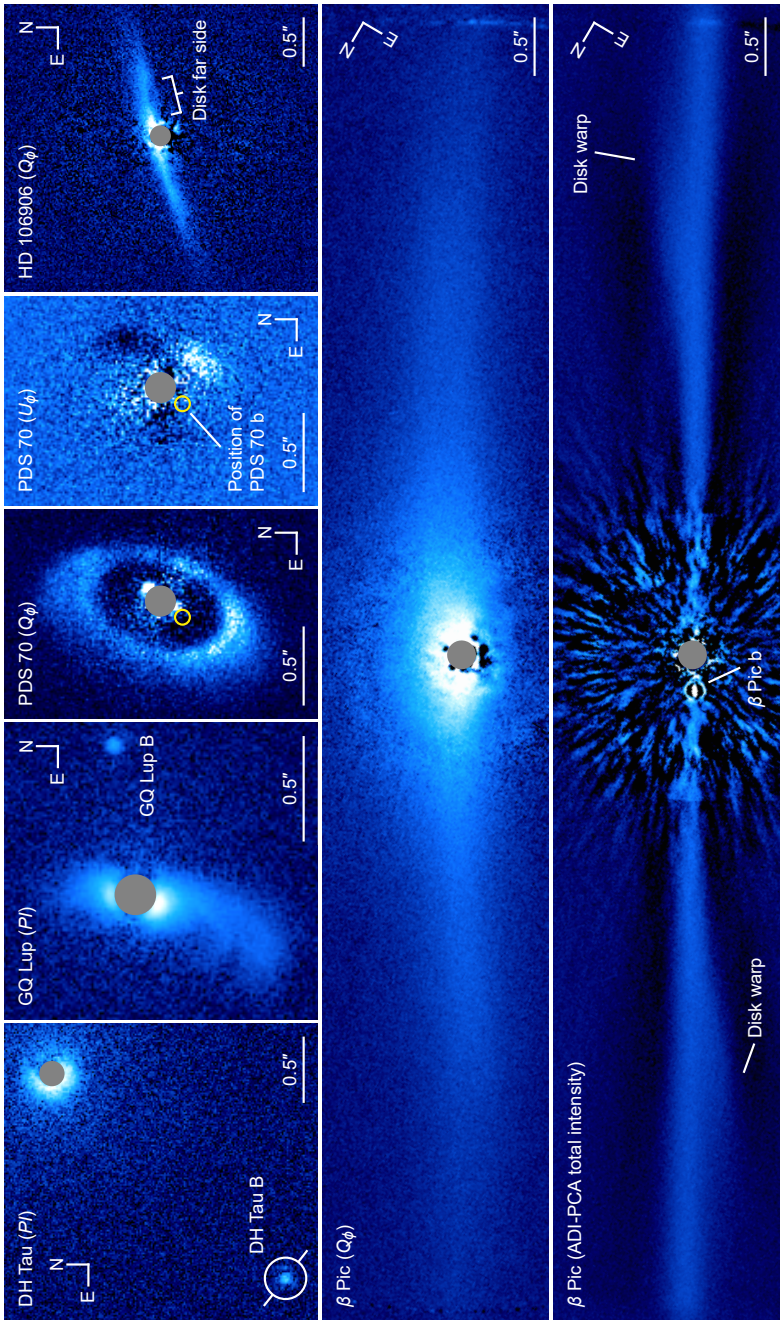


Figure 5.12: H-band images of the five circumstellar disks detected in our sample, showing the linearly polarized intensity (PI) for DH Tau and GQ Lup, Q_ϕ and U_ϕ for PDS 70, and Q_ϕ for HD 106906 and β Pic. A total-intensity image after applying ADI with PCA (subtracting four principal components) is additionally shown for β Pic. The U_ϕ-image of PDS 70 is shown on a linear scale, whereas all other images are shown on a logarithmic scale. All polarimetric images have the polarized stellar halo subtracted. The angular scale and sky orientation are indicated in each image. Gray circles mask regions obscured by the coronagraph.

analyses presented by Schwarz et al. (2016) and Wu et al. (2017b) indeed show that the orbit of GQ Lup B is almost certainly eccentric and that it is quite likely that the inclinations of the orbit and the disk are similar. However, Wu et al. (2017b) argue that although the inclinations may be similar, the disk and companion orbit are likely not in the same plane. We also find that the starlight of GQ Lup is polarized due to the unresolved part of the circumstellar disk, with an angle of polarization ($83 \pm 1°$; see Table 5.5) approximately perpendicular to the position angle of the disk. GQ Lup B appears to be polarized in Fig. 5.12 (top row, second column), but this polarization is spuriously created by subtracting the stellar polarization from the image. We will present a dynamical analysis of the complete system and detailed radiative transfer and hydrodynamical modeling of the circumstellar disk in a future paper.

Figure 5.12 (top row, third and fourth columns) show the H-band Q_ϕ- and U_ϕ-images of the circumstellar disk around PDS 70. The disk is seen at a position angle of 159° and an inclination of 50°, with the southwestern side being the near side (Hashimoto et al., 2012). The Q_ϕ-image clearly shows the known azimuthal brightness variations of the outer disk ring, as well as bright features close to the coronagraph's inner edge that most likely originate from the inner disk (see Keppler et al., 2018). The U_ϕ-image contains significant signal, with the maximum value equal to ~49% of the maximum in the Q_ϕ-image, revealing the presence of non-azimuthal polarization. The pattern in U_ϕ agrees well with the radiative transfer models by Canovas et al. (2015), indicating that part of the photons are scattered more than once. The Q_ϕ-image also shows a weak spiral-like feature extending toward the east from the northern ansa of the disk and perhaps a similar feature at the southern ansa. With these features the disk resembles the model images by Dong et al. (2016) for the inclination and position angle of the PDS 70 disk. We may therefore be seeing the effect of two spiral arms in the outer disk ring, potentially induced by PDS 70 b.

Figure 5.12 (top right) shows the Q_ϕ-image of the debris disk of HD 106906, which is viewed close to edge-on. The forward-scattering near side of the disk can be seen passing slightly to the north of the star. The image clearly shows the known east-west brightness asymmetry of the disk, which had until now only been detected in total intensity (Kalas et al., 2015; Lagrange et al., 2016). Because our data are particularly deep (i.e., 120 min total on-source exposure time), we detect the backward-scattering far side of the disk to the west of the star, just south of the brighter near side of the disk (see Kalas et al., 2015).

Finally, Fig. 5.12 (center) shows the Q_ϕ-image of the nearly edge-on-viewed debris disk of β Pic. The disk extends from one side of the $11'' \times 11''$ IRDIS field of view to the other. Earlier near-infrared scattered light images reported by Millar-Blanchaer et al. (2015) show the disk only to ~1.7″ or 33 au at 20 pc due to the smaller field of view of GPI. In our images we see the disk extending to at least 5.8″ or 115 au on both sides of the star. The disk midplane is seen slightly offset to the northwest of the star (up in Fig. 5.12 center) due to the disk's small inclination away from edge-on. Our image also shows the apparent warp in the disk (see Millar-Blanchaer et al., 2015, and references therein) that extends eastward (to the bottom left) in the northeastern (left) part of the disk and westward (to the upper right) in the southwestern (right) part of the disk. This warp is particularly well visible in Fig. 5.12 (bottom), which shows a total-intensity image after applying ADI with PCA using IRDAP.

5.6 Modeling of polarization from circumsubstellar disks

As discussed in Sects. 5.5.1 and 5.5.2, we (very) likely detected intrinsic polarization from DH Tau B and GSC 6214 B, with a degree of polarization of several tenths of a percent in H-band. The host stars of these two companions are among the youngest in our sample ($\lesssim$20 Myr) and the companions have indicators for the presence of circumsubstellar disks through hydrogen emission lines, red near-infrared colors, and excess emission at mid-infrared wavelengths (see Fig. 5.1 and Table 5.1). Therefore, the most plausible explanation for the polarization in these cases is scattering of the companion's thermal emission by dust within a spatially unresolved circumsubstellar disk. However, we note that the late M to early L spectral types of these low-mass companions (see Fig. 5.1 and Table 5.1) suggest their atmospheres could be dusty. As a result, the polarization could also originate from rotation-induced oblateness, an inhomogeneous cloud distribution, or a combination of these atmospheric asymmetries and a disk (see Stolker et al., 2017). Still, it seems reasonable to assume that the polarization is solely caused by a disk because the companions have low projected rotational velocities (Bryan et al., 2018; Xuan et al., 2020), and out of the 20 companions observed, we only detect intrinsic polarization for the companions that have hydrogen emission lines.

In this section we perform (spatially resolved) radiative transfer modeling of a representative example of a circumsubstellar disk to investigate whether our detections of polarization of several tenths of a percent can really be explained by such disks. To this end, we first describe the setup of the radiative transfer model in Sect. 5.6.1. We then examine the generation of an integrated (i.e., spatially unresolved) polarization signal in Sect. 5.6.2 and the dependence of the polarization on the properties of the disk in Sect. 5.6.3. We stress that we consider an isolated circumsubstellar disk (i.e., it is not embedded in a circumstellar disk) and that our models are general and not tailored to either DH Tau B or GSC 6214 B. Because we only study the degree and angle of polarization produced by the disk, the exact spectrum of the companion has little effect on the results. In Sects. 5.7.1 and 5.7.2 we use the results of our modeling to interpret and discuss our measurements.

5.6.1 Setup of the radiative transfer model

To quantify the expected near-infrared polarization from a self-luminous atmosphere with a circumsubstellar disk, we computed a radiative transfer model with `MCMax` (Min et al., 2009), which is a Monte Carlo radiative transfer code for axisymmetric disks that is optimized for the high optical depths in protoplanetary disks. The model considers a passive, irradiated disk around a self-luminous substellar atmosphere (the contribution from the light of the central star is negligible). We selected a synthetic spectrum from the `BT-Settl` atmospheric models (Allard et al., 2012) at an effective temperature $T_{\rm eff}$ = 2000 K and surface gravity $\log g$ = 4.0 dex. We then scaled the spectrum to a luminosity of 10^{-4} $L_{\odot}$ by assuming a radius for the atmosphere of 2 $R_{\rm Jup}$ at an age of ~10 Myr (e.g., Baraffe et al., 2015). We then modeled the circumsubstellar disk as a scaled down

version of a circumstellar disk (see e.g., Williams & Cieza, 2011). We parametrized the structure of the circumsubstellar disk with a profile for the dust surface density that is inversely proportional to the radius, $\Sigma \propto r^{-1}$. Using a surface density at the inner radius of $\Sigma_{\rm in} = 0.07$ g cm^{-2} and an inner and outer disk radius of $R_{\rm in} = 0.003$ au and $R_{\rm out} = 0.01$ au, we computed the total mass residing in the solids. For the pressure scale height, we used a linear dependence with the disk radius, $h \propto r$, with a (constant) aspect ratio of $h/r = 0.1$. The dust opacities contain by volume 60% silicates, 15% amorphous carbon, and 25% porosity (Woitke et al., 2016). Furthermore, we used a maximum hollow volume ratio of 0.8 for the distribution of hollow spheres, which approximates the irregularity of the dust grains (Min et al., 2016). The size distribution of the grains was chosen in the range of 0.05–3000 μm with a power-law exponent of −3.5. Dust settling is included with the prescription from Dubrulle et al. (1995), which assumes an equilibrium between turbulent mixing and gravitational settling. In this way, the dust scale height is a function of disk radius and grain size, which is controlled by the viscosity parameter $\alpha = 10^{-4}$.

5.6.2 Origin of the spatially integrated polarization

After setting up the disk and dust properties, we can now perform the radiative transfer computations to study the generation of a spatially integrated polarization signal from the disk. We propagate the Monte Carlo photons through the disk to compute the thermal structure and the local source function. We then run a monochromatic ray tracing at 1.62 μm (the central wavelength of the IRDIS H-band filter) to compute the synthetic total-intensity and Stokes Q- and U-images. Figure 5.13 displays an example image of the total-intensity surface brightness for a disk inclination of 70°. In this figure, the length and orientation of the lines indicate the local degree and angle of polarization, respectively. Finally, we compute the spatially integrated polarization using the sum of the pixel values in each of the Stokes images. In Fig. 5.13, this results in an integrated degree and angle of polarization of 0.24% and 0°, respectively. Indeed, the polarized flux is largest along the major axis of the disk, where scattering angles are closest to 90°, yielding a net polarization that is oriented perpendicular to the major axis of the disk. In fact, the angle of polarization is always perpendicular to the position angle of the disk, independent of the disk inclination.

For the interpretation of a nonzero integrated polarization, we need to consider various effects that are visible in the spatially resolved image of the disk in Fig. 5.13. To produce a measurable degree of polarization, the linearly polarized intensity should have a nonzero value while lowering the total intensity will further enhance the degree of polarization. In the example of Fig. 5.13, most of the polarized flux comes from the inner edge of the disk, where the flux in total intensity is about 10 to 100 times lower than the atmospheric emission. Part of the polarization signal is canceled because there is both horizontally and vertically polarized flux, but a net vertically polarized flux remains. The local degree of polarization increases along the major axis of the disk toward larger separations because of reduced multiple scattering. However, the total intensity is also lower in these regions such that the polarized intensity is also low there. This means that the integrated polarization depends primarily on the inner radius and the surface density, whereas the outer radius, and therefore the total disk mass, are much less relevant. Because the inner

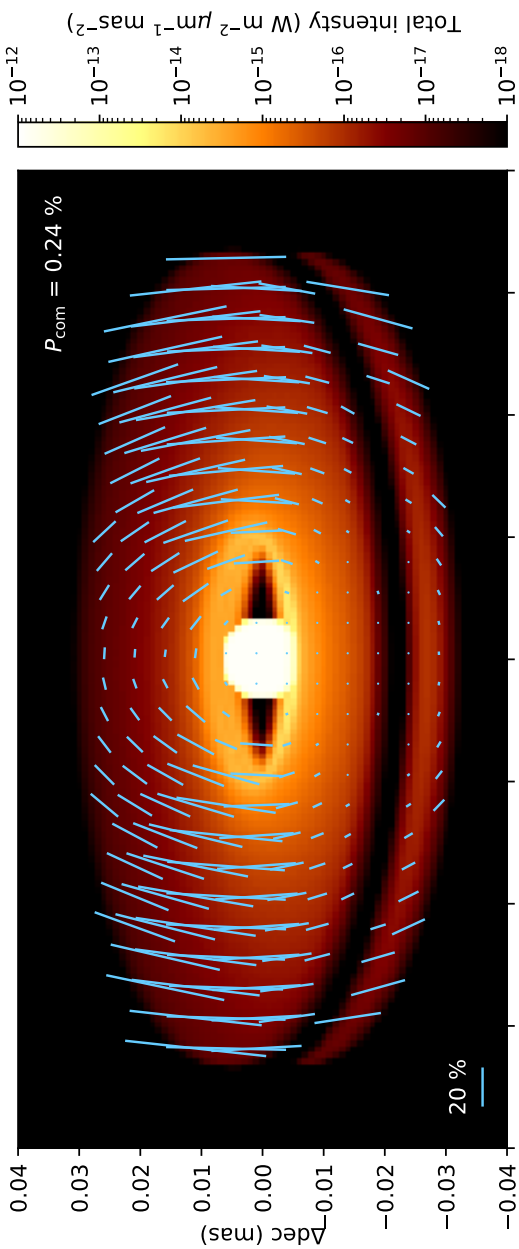


Figure 5.13: Synthetic image of a self-luminous companion ($T_{\rm eff}$ = 2000 K) with a compact circumsubstellar disk at a distance of 150 pc. The total intensity surface brightness is shown on a logarithmic scale and the lines indicate the local degree and angle of linear polarization. The spatially integrated degree of polarization is 0.24% and the angle of polarization is 0°, that is, the spatially unresolved light is linearly polarized along the minor axis of the disk.

radius of the disk is at ~6 $R_{\rm Jup}$ and the inclination is 70°, part of the photosphere of the central object is obscured by the near side of the disk. This reduces the total intensity of the system such that the net degree of polarization is enhanced compared to a situation in which the full atmosphere would be visible.

5.6.3 Dependence on the inner radius and surface density

We now investigate the dependence of the spatially integrated degree of polarization on the inner radius and the surface density at the inner radius. To this end, we run a grid of 10×10 radiative transfer models with a varying inner radius (5–41 $R_{\rm Jup}$) and dust surface density at the inner radius (10^{-2}–10^{2} g cm^{-2}). All other parameters are the same as in Sect. 5.6.1, except for the outer radius which we changed from 0.01 au to 0.4 au. In this way, the disk remains radially sufficiently extended even though the outer radius of the disk has a negligible impact on integrated degree of polarization because most of the polarized flux comes from the inner edge. Because the total disk mass depends on the inner radius and surface density, it is different for each model. We note that the estimated polarization may rely on additional properties of both the disk structure and the dust grains.

As discussed in Sect. 5.6.2, the integrated degree of polarization depends strongly on the fractional occultation of the substellar atmosphere by the disk. This effect occurs at a high enough inclination if the projected disk reaches close to the atmosphere and/or the vertical extend of the disk (which scales with the dust surface density) is sufficiently large. To resolve with a high precision the obscuration of the atmosphere, we perform the ray tracing at sufficient spatial resolution. We set the disk inclination i to 70° and 80° because for geometry reasons detections are biased toward highly inclined disks and, more importantly, a nonzero polarization from a circumsubstellar disk is only to be expected if the disk is sufficiently inclined. For example, we find that for $i < 45°$ and $i < 20°$, the degree of polarization is <0.15% and <0.03%, respectively. We calculate the integrated degree of polarization as before and present the results for each combination of disk inner radius and the surface density at the inner disk radius in Fig. 5.14.

At an inclination of 70° (see Fig. 5.14, top), the polarization reaches a maximum value of 0.4–0.5% when the inner radius is 5–10 $R_{\rm Jup}$ and the surface density is $\gtrsim$1 g cm^{-2}. At small inner radii, there is a correlation with the surface density because increasing the inner radius can be counteracted by an increase in surface density in order to maintain the same integrated degree of polarization. At a given surface density, the degree of polarization converges to a constant value at larger inner radii because the atmosphere is no longer obscured and most of the polarized flux originates from the cavity edge. For higher surface densities, this turnover point occurs at larger disk radii because the scattering surface is higher.

A more extreme picture emerges when the inclination is increased to 80° (see Fig. 5.14, bottom). Whereas for surface densities $\lesssim$0.1 g cm^{-1} the correlation with the inner radius is comparable to the $i = 70°$ case, at higher surface densities the substellar atmosphere becomes fully obscured by the disk. There is a peak in the degree of polarization when the vertically extended disk obscures the atmosphere along the minor axis of the disk while there is still some disk surface visible close to the major axis. As a result, the total intensity of the atmosphere is strongly reduced while the polarized flux at scattering an-

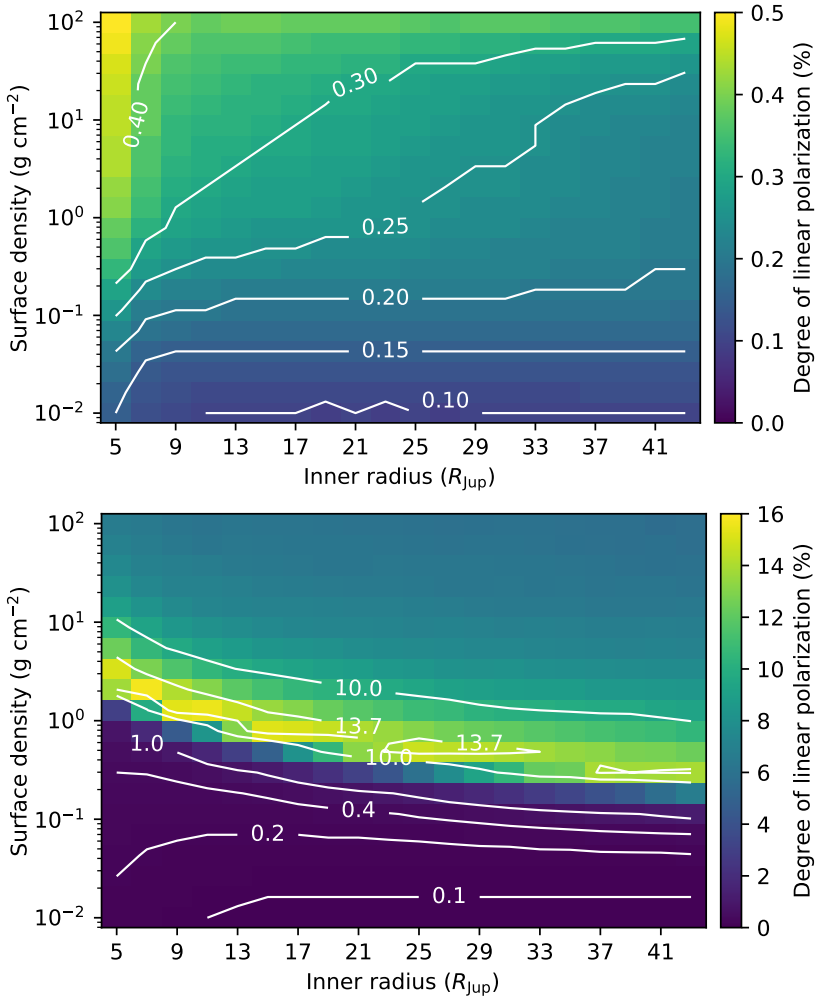


Figure 5.14: Dependence of the integrated degree of linear polarization on the inner radius of the circumsubstellar disk and the surface density of the dust at the inner radius. The grid of radiative transfer models is shown for a disk inclination of 70° (*top*) and 80° (*bottom*).

gles close to 90° is less attenuated, leading to a degree of polarization as high as ~15%. For even higher surface densities, the degree of polarization remains approximately constant at a value of ~8% because both the substellar atmosphere and the cavity edge are obscured by the vertical extent of the disk. In this case, only light that scatters through the surface layer of the disk will reach the observer, which is therefore no longer dependent on the surface density and the inner radius.

5.7 Discussion

In Sect. 5.6 we performed radiative transfer modeling of a generic circumsubstellar disk to study the origin of the integrated polarization and the dependence of this polarization on the disk properties. We use the results of our modeling in Sect. 5.7.1 to interpret our likely detections of polarization from DH Tau B and GSC 6214 B and our non-detection for GQ Lup B. In Sect. 5.7.2 we then briefly examine the non-detections of polarization for 1RXS J1609 B, HD 106906 b, and PDS 70 b, which also have evidence for the existence of a circumsubstellar disk. Subsequently, we outline the implications of our upper limits on the polarization of the other companions with respect to the presence of atmospheric asymmetries in Sect. 5.7.3. Finally, in Sect. 5.7.4, we discuss potential measurements with various instruments to confirm and further characterize the circumsubstellar disks of DH Tau B and GSC 6214 B.

5.7.1 Circumsubstellar disks, rotational periods, and formation of DH Tau B, GSC 6214 B, and GQ Lup B

As discussed in Sect. 5.6, the most plausible explanation for the polarization of DH Tau B and GSC 6214 B is the presence of a circumsubstellar disk. From the radiative transfer modeling in that same section, we see that the integrated degree of polarization of such a disk depends on many parameters and that estimating disk properties is therefore a degenerate problem. Nevertheless, we can still put constraints on the dust grain sizes and the disk's inclination and position angle, and through that constrain the rotational periods and formation mechanisms of the companions.

Whereas we most likely detect polarization signals from the disks of DH Tau B and GSC 6214 B, no emission has been detected from these companions at mm-wavelengths (Bowler et al., 2015; Wu et al., 2017a; Wolff et al., 2017; Wu et al., 2020). It is therefore possible that these disks contain mostly micrometer-sized dust grains and only little mm-sized grains, or, as suggested by Wu et al. (2017a), that the disks are compact and optically thick at mm-wavelengths. From our polarimetric measurements we cannot determine whether the disks are really compact because most of the polarized flux originates from the inner edge of the disk (see Sect. 5.6.2). Because we do not spatially resolve the disks, we can put a limit on the disk size from the measured FWHM of the PSF. The FWHM corresponds to a maximum disk radius of ~3 au for both companions. This radius is much smaller than one-third of the Hill radius (14–20 au, assuming the companions are on a circular orbit), which is the distance at which the disks are suspected to be truncated due to tidal interactions with the primary star (Ayliffe & Bate, 2009; Martin & Lubow,

2011; Shabram & Boley, 2013). However, it is possible that the disks extend beyond 3 au, but that we do not reach the sensitivity and contrast to detect the flux at the outer regions.

From the measured degree of polarization we can put constraints on the inclination of the disks. With degrees of polarization of a few to several tenths of a percent, the disks of DH Tau B and GSC 6214 B must have a high inclination because a low-inclination disk will have a very low, nearly zero degree of polarization below the sensitivity that we reach with our measurements (see Sect. 5.6.3). In fact, it could be that GQ Lup B hosts such a low-inclination disk because we do not detect significant polarization although the measured hydrogen emission lines are stronger than those of DH Tau B and GSC 6214 B (Zhou et al., 2014). We also see that the inclination of the disks of DH Tau B and GSC 6214 B cannot be close to edge-on so that disk completely obscures the companion's atmosphere because in that case we would measure polarization degrees of several to even ten percent. Such a high degree of polarization of 14% has been measured for CS Cha B in J- and H-band by Ginski et al. (2018), which the authors indeed interpret as being caused by a highly inclined and vertically extended disk. This interpretation was recently confirmed by Haffert et al. (2020) using medium-resolution optical spectroscopy with MUSE.

The projected rotational velocity, $v \sin i$, has been measured for DH Tau B, GSC 6214 B and GQ Lup B through high-resolution spectroscopic observations (Xuan et al., 2020; Bryan et al., 2018; Schwarz et al., 2016), finding values of 9.6 ± 0.7 km s^{-1}, $6.1^{+4.9}_{-3.8}$ km s^{-1}, and $5.3^{+0.9}_{-1.0}$ km s^{-1}, respectively. Assuming that the spin axes of the companions are perpendicular to the plane of their disks (the regular moons of our solar system's giant planets, which are believed to have formed in circumsubstellar disks, orbit near the equatorial plane of the planets) and taking the companion radii and uncertainties from Xuan et al. (2020) and Schwarz et al. (2016), we constrain the rotational period of the companions using a Monte Carlo calculation. We assume the inclination to be uniformly distributed in $\cos i$, with values between 60° and 80° for DH Tau B and GSC 6214 B and between 0° and 45° for GQ Lup B. We find rotational periods equal to 29–37 h for DH Tau B, 22–77 h for GSC 6214 B, and 19–64 h for GQ Lup B, within the 68% confidence interval. These estimates of the rotational periods are roughly an order of magnitude larger than the average periods expected from the period-mass relation as determined from observations of free-floating low-mass brown dwarfs of similar ages (e.g., Rodríguez-Ledesma et al., 2009; Scholz et al., 2015, 2018). This discrepancy can be explained by the companions hosting circumsubstellar accretion disks. The estimated slow rotation of the companions, which is at ~0.1% of their break-up velocities (see Xuan et al., 2020), is consistent with a scenario in which the companions lose angular momentum to their disks during accretion and should still spin up as they contract (see Takata & Stevenson, 1996; Bryan et al., 2018; Xuan et al., 2020). The long rotational periods we find also show that rotation-induced oblateness does not significantly contribute to the measured polarization because polarization >0.1% is generally expected only for rotational periods of ~6 h or less (Sengupta & Marley, 2010; Marley & Sengupta, 2011).

As we discussed in Sect. 5.6.2, the angle of polarization we measure from an unresolved disk is always oriented perpendicular to the position angle of the disk. Therefore, the position angle of the disk of DH Tau B is likely between 150° and 190° (see Fig. 5.9), whereas that of the disk of GSC 6214 B is around 48° (see Table 5.4). Because we already

found that both disks likely have large inclinations, we have strong constraints on the 3D orientation of the disks. The disk of DH Tau B is most likely misaligned with the circumstellar disk of DH Tau A, which has an inclination and position angle of 48° and 2.5°, respectively (see Sect. 5.5.5 and Fig. 5.12), although the position angles could possibly be aligned. Such a misalignment of disks is also found for CS Cha A and B (Ginski et al., 2018). Although GSC 6214 A is not known to host a circumstellar disk, orbital motion has been detected for GSC 6214 B (Pearce et al., 2019). However, the orbital elements are not sufficiently constrained to conclude on possible (mis)alignments of the disk and the orbit. If a low-inclination disk exists around GQ Lup B, it would be misaligned with the circumstellar disk that has an inclination of 60° (see Sect. 5.5.5 and Fig. 5.12) and the orbit of GQ Lup B that likely has a similar inclination. However, the circumsubstellar disk could be aligned with the spin axis of GQ Lup A that has an inclination of ~30° (Donati et al., 2012).

The misalignment of the disks of DH Tau A and B, and possibly also of GQ Lup A and B, suggests that the companions may have formed in situ through direct collapse in the molecular cloud, akin to the formation mechanism of binary stars. Indeed, CS Cha B, with its misaligned disk, was initially thought to be of substellar nature (Ginski et al., 2018), but was recently found to actually be a low-mass star (Haffert et al., 2020). However, formation through gravitational instabilities in the circumstellar disk is also possible because this mechanism can form companions at separations of up to at least 300 au (Tobin et al., 2016). Although one might expect the circumstellar and circumsubstellar disks to be coplanar in this scenario, misalignments can result if the companion formed away from the midplane of the original disk, the original disk was asymmetric, or the circumstellar disk or other objects disturbed the circumsubstellar disk (Stamatellos & Whitworth, 2009; Bryan et al., 2020). It seems unlikely, however, that DH Tau B, GSC 6214 B, and GQ Lup B formed close to their stars and were subsequently scattered to a higher orbit through dynamical encounters with massive inner bodies. This is because tidal interactions would most likely severely disturb or even destroy the circumsubstellar disks (see Stamatellos & Whitworth, 2009; Bailey et al., 2013; Bowler et al., 2011), and no massive objects at small separations, nor the gaps they would create in the circumstellar disks, have been detected (see Fig. 5.12; Pearce et al., 2019; Wu et al., 2017b).

5.7.2 Circumsubstellar disks of 1RXS J1609 B, HD 106906 b, and PDS 70 b

There is also evidence for disks around 1RXS J1609 B, HD 106906 b, and PDS 70 b (see Table 5.1), but we do not detect intrinsic polarization from these companions (see Sect. 5.5.4). It could be that these companions host a disk but that the properties and geometry of these disks is such that they do not produce a measurable degree of polarization. However, for 1RXS J1609 B no hydrogen emission lines are detected. Instead, the evidence for the existence of a disk is based on red near-infrared colors, weak mid-infrared excess that is spatially unresolved between the primary star and the companion, and a moderate extinction (Bailey et al., 2013; Wu et al., 2015). Because we find that the companion is polarized by interstellar dust (see Sect. 5.5.3), it seems more likely that these properties are caused by interstellar dust rather than a circumsubstellar disk.

As discussed in Sect. 5.5.4, we placed an upper limit of 0.2% on the degree of polarization of HD 106906 b, with a 68.27% confidence level. Because also no hydrogen emission lines are detected for this companion, a possible explanation for the non-detection is that the companion simply does not host a circumsubstellar disk. In the case of PDS 70 b we do not reach a very high sensitivity and placed a 68.27% upper limit of 5.0% on the degree of polarization in K_s-band. Therefore, we can conclude that if PDS 70 b hosts a disk, the inclination is probably not so high that it completely obscures the planet's atmosphere. Because we only detected polarization for companions with hydrogen emission lines, it seems that these lines are the best non-polarimetric indicators for the existence of a circumsubstellar disk.

5.7.3 Atmospheric asymmetries of the companions

Of the 18 companions for which we do not detect significant polarization, 14 show no clear evidence of hosting a circumsubstellar disk (see Fig. 5.1 and Table 5.1). Because the majority of the companions have late-M to mid-L spectral types and are therefore expected to have dusty atmospheres, we could expect to detect polarization due to rotation-induced oblateness or an inhomogeneous cloud distribution. Indeed, polarization between several tenths of a percent to a percent has been detected at near-infrared wavelengths (in particular in J-, Z-, and I-band) for more than a dozen late-M to mid-L field brown dwarfs (Miles-Páez et al., 2013, 2017). In our survey, we reached sensitivities (upper limits) $\leq$0.3% for 11 companions (see Sect. 5.5.4 and Table 5.5), and so we might have expected to detect polarization for a few of the companions. Because we do not detect polarization due to atmospheric asymmetries for any of the companions, these asymmetries either do not exists for the companions observed or they produce polarization below the sensitivity reached.

In the majority of cases, the polarization of field brown dwarfs is interpreted to be caused by rotation-induced oblateness. In that sense our non-detections are particularly surprising because the companions observed are generally young and have a low surface gravity (see Table 5.1), which should result in a more oblate atmosphere for a given rotation rate and therefore more polarization (Sengupta & Marley, 2010; Marley & Sengupta, 2011). It is important to note, however, that the field brown dwarfs observed by Miles-Páez et al. (2013) are old (ages 0.5–5 Gyr) and have measured projected rotational velocities $v \sin i > 30$ km s^{-1}. Indeed, in their sample of several dozen field brown dwarfs, Zapatero Osorio et al. (2006) found that about half of the very young field brown dwarfs (1–10 Myr) have $v \sin i \leq 10$ km s^{-1} whereas all old brown dwarfs ($\geq$ 1 Gyr) have $v \sin i \approx 30$ km s^{-1}. Very young brown dwarfs rotate slowly because they are still in the process of spinning up as they cool and contract. Looking at Fig. 5.1, we can divide our sample roughly into a large group of young, high-temperature companions with late-M to mid-L spectral types, and a smaller group of older, lower-temperature companions of mid-L to T spectral types. A possible explanation for our non-detections is that while the companions of the first group may have dusty atmospheres, they rotate too slowly to produce a measurable level of polarization. And on the other hand the second group may rotate faster, but due to their later spectral types their upper atmospheres may lack the scattering dust to produce polarization (Allard et al., 2001; Sengupta & Marley, 2009).

A more in-depth analysis of the degrees of polarization produced due to rotation-induced oblateness is presented in Jensen-Clem et al. (2020).

There could also be other explanations for our non-detections. It could be that the dust grains in the upper atmosphere are submicron sized, as also suggested by studies of the emission spectra of (field) brown dwarfs and planets (Hiranaka et al., 2016; Bonnefoy et al., 2016), and that we therefore need to observe at shorter wavelengths than H-band (i.e., in Y- or J-band). Miles-Páez et al. (2017) observed one of the field brown dwarfs in Z-, J-, and H-band and found that the degree of polarization decreases strongly with increasing wavelength, with the maximum polarization in Z-band and no detection in H-band. Another possibility, as suggested by Miles-Páez et al. (2017), is that the low-gravity atmospheres of young objects have thicker dust clouds, resulting in strong multiple scattering and therefore a low integrated degree of polarization. Finally, our non-detections may also indicate that the atmospheric dust clouds are homogeneously distributed, or that the inhomogeneities do not produce a measurable degree of polarization. Indeed, Millar-Blanchaer et al. (2020) recently detected polarization that is likely due to cloud banding on Luhman 16 A, but the measured degree of polarization is only 0.03% in H-band.

5.7.4 Confirmation and further characterization of the disks of DH Tau B and GSC 6214 B

To confirm that the polarization from DH Tau B and GSC 6214 B is truly intrinsic and not caused by interstellar dust, we should perform follow-up observations. For this we can use the recently implemented star-hopping technique for SPHERE-IRDIS to quasi-simultaneously measure the stellar polarization from nearby diskless reference stars. As a reference for DH Tau we can observe DI Tau, a very close neighbor to DH Tau located at a separation of only 15.3″ and at the same distance from Earth, and whose spectral-energy distribution (classified as class III; Luhman et al., 2010) and very low mass-accretion rate (Alonso-Martínez et al., 2017) indicate it very likely does not host a circumstellar disk that creates significant intrinsic stellar polarization. For GSC 6214 we can observe BD-20 4481, which is of similar spectral type as GSC 6214 A and is located at a separation of 13.3′ and at a distance of 113 pc (compared to 109 pc for GSC 6214). We can use the measurements of the stellar polarization of the reference stars to subtract the interstellar component of the companions' polarization, and with that accurately determine the intrinsic polarization of the companions. We can also measure the polarization of DH Tau A and GSC 6214 A with a different instrument than SPHERE, for example with the WIRC+Pol near-infrared spectropolarimeter (Tinyanont et al., 2019) on the Hale Telescope at Palomar Observatory. Using WIRC+Pol we can determine the stellar polarization as a function of wavelength, enabling us to quantify the interstellar polarization by comparing the measurements with Serkowski's law of interstellar polarization.

We can further characterize the circumsubstellar disks of DH Tau B and GSC 6214 B, as well as the companions themselves, by performing measurements with various current and future instruments. We can perform IRDIS polarimetric measurements in multiple filters to constrain the distribution of particle sizes in the disks. By combining these measurements with optical and near-infrared medium-resolution spectroscopy using MUSE and ERIS on the VLT, we can constrain the fundamental parameters of the companions. If

we are able to detect the disks with ALMA, we can derive their dust mass from the continuum emission, their gas mass from the CO spectral-line emission, and their effective temperature from the emission in two different wavelength bands. Similar to ALMA observations, the dust mass and effective temperature of the disk can be determined from mid-infrared photometric and spectroscopic observations, for example with MIRI on board the James Webb Space Telescope (JWST), METIS on the Extremely Large Telescope (ELT), or even VISIR on the VLT. Finally, with the sensitivity of MIRI and METIS we could detect silicate emission features at 10 and 18 μm.

5.8 Summary and conclusions

We measured the near-infrared linear polarization of 20 young planets and brown dwarf companions using SPHERE-IRDIS. We reduced the data using the IRDAP pipeline to correct for the instrumental polarization and crosstalk of the optical system with an absolute polarimetric accuracy <0.1% in the degree of polarization. To retrieve the polarization of the companions, we employed a combination of aperture photometry, ADI, and PSF fitting. We achieved a best 1σ polarimetric contrast of $3 \cdot 10^{-8}$ at an angular separation of 0.5″ from the star and a contrast $<10^{-8}$ for separations >2.0″.

We report the first detection of polarization originating from substellar companions, with a measured degree of polarization of several tenths of a percent for DH Tau B and GSC 6214 B in *H*-band. By comparing the measured polarization with that of nearby stars, we find that this polarization is unlikely to be caused by interstellar dust. Because the companions have previously measured hydrogen emission lines and red colors, we conclude that the polarization most likely originates from circumsubstellar accretion disks. Through radiative transfer modeling we constrain the position angles of the disks and find that the disks must have high inclinations to produce these measurable levels of polarization. For GQ Lup B, which has stronger hydrogen emission lines than DH Tau B and GSC 6214 B, we do not measure significant polarization. This implies that if GQ Lup B hosts a disk, this disk has a low inclination. Assuming that the spin axes of the companions are perpendicular to the plane of their disks, we use previously measured projected rotational velocities to constrain the rotational periods of DH Tau B, GSC 6214 B, and GQ Lup B to be 29–37 h, 22–77 h, and 19–64 h, respectively, within the 68% confidence interval. Finally, we find 1RXS J1609 B to be marginally polarized by interstellar dust, which suggests that the red colors and extinction that are thought to indicate the presence of a disk are more likely caused by interstellar dust.

The disk of DH Tau B, and possibly that of GQ Lup B, are misaligned with the disks around the primary stars. These misalignments suggest that these wide-separation companions have formed in situ through direct collapse in the molecular cloud, although formation through gravitational instabilities in the circumstellar disk cannot be excluded. Formation at close separations from the star followed by scattering to a higher orbit is unlikely because dynamical encounters with other bodies would most likely severely disturb or even destroy the circumsubstellar disks.

For 18 companions we do not detect significant polarization and place upper limits of typically <0.3% on their degree of polarization. These non-detections may indicate that

young companions rotate too slowly to produce measurable polarization due to rotation-induced oblateness, or that any inhomogeneities in the atmospheric clouds are limited. Another possibility is that the upper atmospheres of the companions contain primarily submicron-sized dust grains. This implies that we should perform future measurements in Y- or J-band, although these bands are more challenging in terms of companion-to-star contrast and contrast performance of the instrument.

In our survey, we also detected the circumstellar disks of DH Tau, GQ Lup, PDS 70, β Pic, and HD 106906, which for DH Tau and GQ Lup are the first disk detections in scattered light. The disk of DH Tau is compact and has a strong brightness asymmetry that may reveal the forward- and backward-scattering sides of the disk or may be caused by shadowing by an unresolved inner disk component. The disk of GQ Lup shows a pronounced asymmetry and two spiral-like features that could be the result of periodic close passes of GQ Lup B. The PDS 70 disk shows significant non-azimuthal polarization indicating multiple scattering. We also detect one or two weak spiral-like features protruding from the ansae of the disk that may be the result of two spiral arms in the outer disk ring, potentially induced by PDS 70 b.

Our measurements of the polarization of companions are reaching the limits of the instrument and the data-processing techniques. We find that incompletely corrected bad pixels can cause systematic errors of several tenths of a percent in the measured polarization. To minimize this effect, we recommend to use the field-tracking mode without dithering for future observations that aim to measure the polarization of companions. However, for companions at close separations or with large star-to-companion contrasts, pupil-tracking observations are still preferred to retrieve the companions' total intensity with ADI. These close-in companions can alternatively be observed in field-tracking mode when using the recently implemented star-hopping technique to enable reference star differential imaging. We also find that the measurements of the stellar polarization are affected by systematic errors related to the use of the coronagraph in combination with time-varying atmospheric conditions. We therefore recommend to take additional stellar polarization measurements without coronagraph.

To further characterize the circumsubstellar disks of DH Tau B and GSC 6214 B, as well as the companions themselves, we can perform follow-up observations with SPHERE-IRDIS, ALMA, JWST-MIRI, MUSE and ERIS on the VLT, and METIS on the ELT. Our polarimetric detections of the disks of DH Tau B and GSC 6214 B are a first step in building a complete picture of the companions, their formation, and evolution, and pave the way to detecting polarization of young planets with for example SPHERE+ (Boccaletti et al., 2020) and the future planet-characterization instrument EPICS (or PCS) on the ELT.

5.A Cosmetic correction of spurious structure in Q- and U-images

If a companion is polarized, we would expect the polarization signals in the Q- and U-images to resemble scaled-down positive or negative versions of the corresponding total-intensity images I_Q and I_U. However, for many data sets the Q- and U-images show spurious structure with adjacent positive and negative signals. For example, for the 2019-10-24 data set of DH Tau, as shown in Fig. 5.15 (first column), we see that the Q-image contains positive and negative signals and that the signal in U is offset from the center coordinates of the companion. These spurious structures result from imperfect relative centering of the images of IRDIS' left and right optical channels and image motion during the observations. For pupil-tracking observations the spurious structures can additionally originate from image rotation between the two measurements of the double difference.

In the case these spurious structures are visible in the Q- and U-images of a data set, we make to each image individually a (cosmetic) correction similar to that described in Snik et al. (2010). For this we retrieve a positive and negative copy of the I_Q- or I_U-image at the companion position and create a model image in which the two copies are symmetrically shifted in opposite directions from the center coordinates of the companion. We then subtract this model image from the Q- or U-image and fit the shifts in the x- and y-directions by minimizing the sum of squared residuals in an aperture of radius 8 pixels in the resulting image. Because the aperture sum in the model images is zero, subtracting these images only suppresses the spurious structures and does not alter the net polarization signals in Q and U.

For the data set of DH Tau, we find a total relative shift equal to 0.015 pixels for Q and 0.013 pixels for U. Only small relative shifts are needed because the maximum values of the total-intensity PSFs are more than 100 times larger than the maximum values of the positive and negative signals of the spurious structure. The model images and the corrected Q and U-images are shown in Fig. 5.15 (second and third column). The spurious structure has clearly disappeared in the corrected images, with the Q-image only having negative signal and the signal in U being positioned at the companion's center coordinates.

5.B Systematic errors due to bad pixels

A few percent of the pixels of the IRDIS Hawaii 2RG detector are bad, that is, they are dead, nonlinearly responding, or hot pixels. When preprocessing the raw frames with IRDAP, bad pixels are identified with a bad pixel map followed by sigma-filtering and then replaced by the median value of the surrounding pixels. These data-reduction steps correct the majority of the bad pixels, but some bad pixels remain uncorrected or are replaced by a value that is not accurate. This results in systematic errors of the pixel values. Whereas these small errors are not a real problem for photometry of point sources in total intensity or imaging of circumstellar disks in polarized light, they become quite problematic when trying to measure the polarization of point sources at a level as low as a few tenths of a percent of the total intensity.

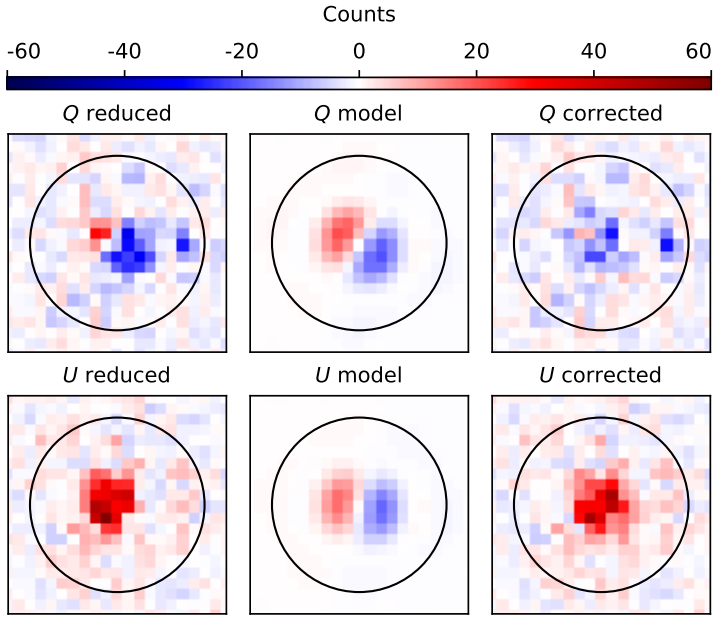


Figure 5.15: Reduced Q- and U-images (*first column*), model images of the spurious structures in Q and U (*second column*), and Q- and U-images corrected for the spurious structures (*third column*) at the position of the companion DH Tau B of the 2019-10-24 data set of DH Tau. An aperture of radius 8 pixels centered on the companion is shown superimposed on the images.

Incomplete correction of bad pixels only marginally affects data taken in field-tracking mode. This is because in field-tracking mode the PSF of the companion is approximately stationary on the detector and only moves very slightly due to variations in AO performance. The bad pixels, which are at a fixed position on the detector, are therefore replaced by approximately the same (median) value in consecutive frames, and so are strongly suppressed when computing the double difference. In addition, any uncorrected or incompletely corrected bad pixels that remain are further averaged out over the various HWP cycles. However, this averaging over HWP cycles only partially applies for our data because we generally observed in field-tracking mode with dithering in which case the detector moves by one to a few pixels each HWP cycle. We note that for total-intensity imaging, for which we compute the median over many exposures rather than differences of exposures, dithering does help suppress bad pixels.

Data taken in pupil-tracking mode are typically more strongly affected by incomplete correction of bad pixels. In pupil-tracking observations the companion moves over the detector, and so in each frame the bad pixels are at a different location with respect to the companion PSF. Therefore, the bad pixels are replaced by very different median values, and relatively large systematic errors remain after the double difference. For data sets with fast parallactic rotation (e.g., the data sets of GSC 8047 and TYC 8998), the bad pixels are more problematic than for data sets with only little rotation (e.g., GSC 6214).

For data sets with many HWP cycles the bad pixel effect averages out somewhat, but the systematic errors are still much larger than for field-tracking data.

We attempted to remove the systematic errors due to bad pixels by creating a more aggressive bad pixel map from the dark and flat frames, performing aggressive sigma-filtering, locally replacing the bad-pixel values with cubic spline interpolation rather than with the median filter, and computing the median over the Mueller-matrix-model-corrected Q- and U-images of each HWP cycle. Unfortunately, we were not able to identify all bad pixels in the data and completely remove the effect. This is primarily because part of the bad pixels cause systematic errors of only several percent or less of the total intensity. Such small deviations from the true value are practically impossible to detect in the images and only become evident when computing differences of images as we do in polarimetry.

Although we were not able to completely correct for the bad pixels, we can mitigate their effect by excluding those frames that contribute strong bad pixels to the final images or that show bad pixels at the position of the companion in the bad pixel map. In addition we can average out the systematic error due the bad pixels by mean-combining several data sets. We can also use large apertures to perform the photometry with, such that the bad pixels values (which are both positive and negative in polarimetric images) average out and sum to a lower spurious signal. Future observations aimed at measuring the polarization of companions should preferably be performed in field-tracking mode without dithering.

5.C Retrieval of total intensity through ADI: Upper limit on polarization of β Pic b

Companions at small separations or at large star-to-companion contrasts are swamped in the halo of starlight in total intensity. For data sets that were taken in pupil-tracking mode and have sufficient parallactic rotation, we have therefore slightly adapted the method described in Sect. 5.4 and determine the probability distribution of the total intensity of the companion by performing ADI with negative PSF injection. We still determine the distributions of Q and U using aperture photometry because the stellar speckle halo is almost completely removed in the polarimetric data-reduction steps, in particular for the reductions with the added classical ADI step (see Sect. 5.3). We applied this adapted method to the data sets of HR 8799, HD 206893, PDS 70, and β Pic. In this section we demonstrate the method with the 2019-11-26 H-band data set of β Pic and show how we calculate upper limits on the degree of polarization of the companion β Pic b. A total-intensity image of the data after applying classical ADI with IRDAP is shown in Fig. 5.16 (left).

To perform the ADI with negative PSF injection, we use the `PynPoint`[6] pipeline, version 0.8.2 (Amara & Quanz, 2012; Stolker et al., 2019), and closely follow the steps described in Stolker et al. (2020). In short, we fetch the preprocessed science frames and the stellar PSF image from the reduction with IRDAP in Sect. 5.3. Subsequently, we

[6] https://pynpoint.readthedocs.io

iteratively subtract scaled copies of the stellar PSF from the preprocessed science frames at the approximate position of the companion and apply ADI with PCA (in this case subtracting three principal components) to minimize the residuals at that same location. Using Markov chain Monte Carlo (MCMC) we then sample the posterior distributions of the companion's angular separation, position angle and contrast with respect to the star. We take the median of the posterior distribution of the contrast as the final contrast value and determine the corresponding statistical uncertainties from the 16th and 84th percentiles. We also estimate the systematic uncertainty on the contrast by injecting fake companions at various position angles (but the same separation and contrast as the real companion), retrieving them, and computing the distribution of the difference between the retrieved and injected contrasts. This systematic uncertainty accounts for the azimuthal variations of the noise around the central star and is generally 1 to 5 times larger than the statistical uncertainty (similar to the results of Wertz et al., 2017). Finally, we compute the overall uncertainty as the quadratic sum of the statistical and systematic uncertainties.

After these steps, we determine the probability distribution of the companion's total intensity (expressed in counts) for a range of aperture radii from 1 to 10 pixels. To this end, we draw 10^6 samples from a Gaussian distribution with the mean and standard deviation equal to the companion-to-star contrast and uncertainty we retrieved with PynPoint. We then sum the flux in the stellar PSF image using an aperture of the given radius and multiply the Gaussian samples by this summed flux. The resulting total-intensity distribution of the companion, which we use for both I_Q and I_U, is shown in Fig. 5.17 (left) for an aperture radius of 1.85 pixels. This radius is the final aperture radius we select at the end of this section and corresponds to half times the full width at half maximum (FWHM) we measure on the stellar PSF.

To determine the probability distributions in Q and U, we use the images from the reduction with the added classical ADI step. In the case of β Pic, the classical ADI step does not only further suppress the speckle noise, but also removes most of the signal from the nearly edge-on-viewed circumstellar disk that crosses the position of β Pic b (see Fig. 5.12, center and bottom). The classical ADI step suppresses the disk signal because the disk is broad and the parallactic rotation of the observations in only 19.8°. Indeed, as can be seen in Fig. 5.16 (right) for the Q-image, the disk is almost completely removed and there are only few speckles left at the separation of the companion. Any polarization originating from the companion should still be visible in the Q- and U-images because point sources are much less affected by ADI-induced self-subtraction.

We analyze the Q- and U-images by following the exact steps as described in Sect. 5.4, but with one exception. Before performing the aperture photometry, we quantify the throughput of the ADI procedure by performing a simulation in which we inject and retrieve an artificial source at the separation of the actual companion. We then correct the Q- and U-images for the self-subtraction by dividing them by the calculated throughput, which for this data set is 49%. After performing all the steps, we determine the companion's polarization for each of the defined aperture radii (as in Fig. 5.7 for DH Tau B). Contrary to the data of DH Tau, for this data set of β Pic we detect no signals with an S/N higher than 0.9 in Q and 1.9 in U for any aperture radius. Indeed, the reduced Q-image (see Fig. 5.16, right) and U-image contain only noise at the position of the companion. We thus conclude that we do not detect significant polarization originating from β Pic b.

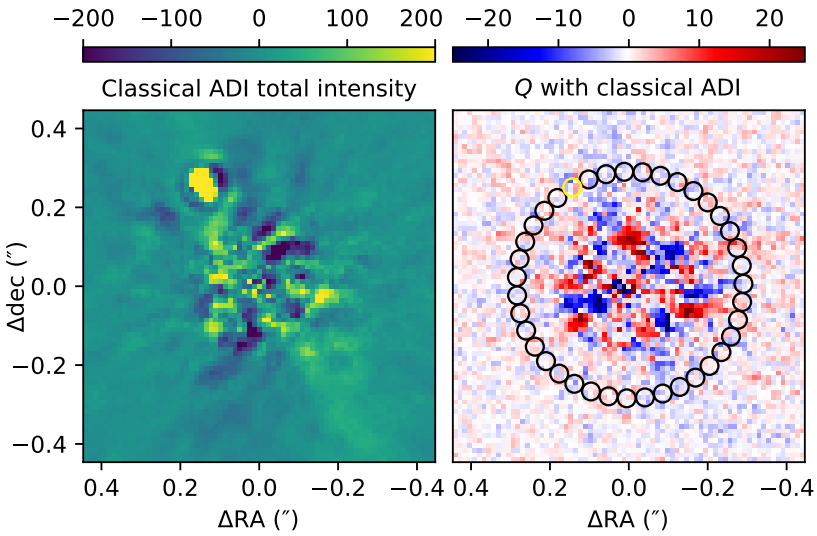


Figure 5.16: Reduced images of the 2019-11-26 data set of β Pic. *Left*: Total-intensity image after applying classical ADI with IRDAP to reveal the companion β Pic b. *Right*: Q-image after combining polarimetry with classical ADI, showing the aperture of radius 1.85 pixels at the position of the companion (yellow) and the ring of comparison apertures of the same radius around the star (black).

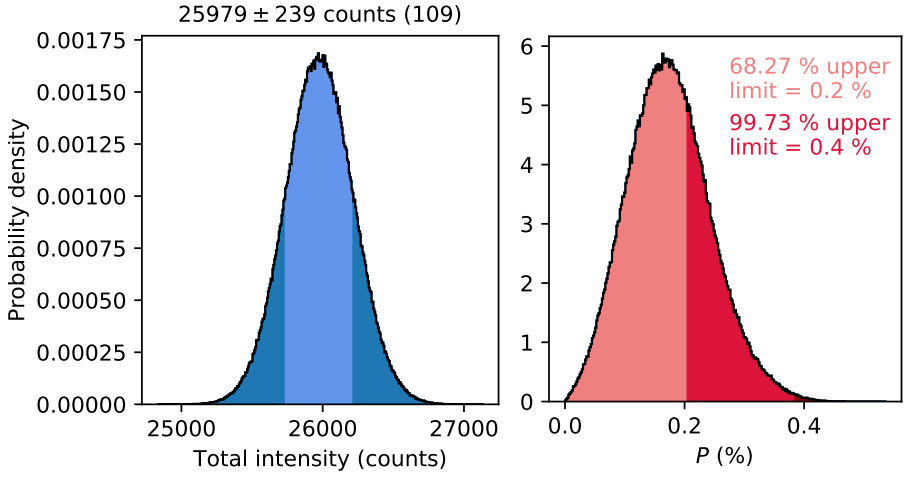


Figure 5.17: Final probability distributions of the signal of β Pic b from the 2019-11-26 data set of β Pic, using an aperture radius of 1.85 pixels. *Left*: Probability distribution of the total intensity. The mean and 68.27% uncertainties of the distribution are shown above the graph, with the latter also indicated by the light-blue shaded area. The S/N is shown within parentheses. *Right*: Probability distribution of the degree of linear polarization. The upper limits computed from the one-sided 68.27% and 99.73% intervals are indicated by the light-red and darker red shaded areas, respectively.

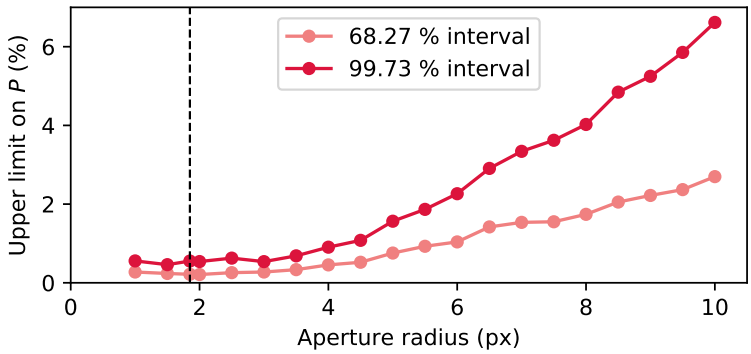


Figure 5.18: Upper limits on the degree of linear polarization of β Pic b computed from the one-sided 68.27% and 99.73% intervals as a function of aperture radius from the 2019-11-26 data set of β Pic. The final selected aperture radius of 1.85 pixels, equal to half times the FWHM of the stellar PSF, is indicated with the dashed vertical line.

We now proceed to set limits on the degree of polarization of the companion. To this end, we determine, for each defined aperture radius, two upper limits from the probability distribution of the degree of polarization. We compute these upper limits from the 68.27% and 99.73% intervals, which for a Gaussian distribution would correspond to the 1σ and 3σ confidence intervals, respectively. These intervals are calculated one-sided and starting at zero because the degree of linear polarization is computed as $P = \sqrt{(q^2 + u^2)}$ and therefore can only have positive values (see Sparks & Axon, 1999). Figure 5.17 (right) shows the distribution of the degree of polarization for an aperture radius of 1.85 pixels with the two intervals indicated. Figure 5.18 shows the two upper limits as a function of aperture radius. From this figure we see that the upper limits are relatively constant for an aperture radius smaller than approximately 3.5 pixels. For larger apertures, the upper limits increase as more noise is included in the companion aperture and the uncertainty of the background due to the low number of background samples increases. We select our final aperture radius to be 1.85 pixels, equal to half times the FWHM of the stellar PSF, and conclude that the 68.27% and 99.73% upper limits on the degree of polarization of β Pic b are equal to 0.2% and 0.4%, respectively. We note that while for this particular data set the upper limits monotonically increase with aperture radius, for several other data sets this is not the case due to incompletely removed bad pixels (see Sect. 5.5.4 and Appendix 5.B).

5.D Retrieval of total intensity through PSF fitting: Upper limit on polarization of HD 19467 B

Several observations of faint or close-in companions were not executed in pupil-tracking mode (i.e., they were executed in field-tracking mode) or have little parallactic rotation. For these observations we cannot retrieve the probability distribution of the companion's total intensity through ADI with negative PSF injection as described in Appendix 5.C. We also cannot use aperture photometry with comparison apertures as outlined in Sect. 5.4 because the spatially varying stellar halo at the separations of these companions prevents accurate determination of the background. We therefore use MCMC to fit the stellar PSF image to the I_Q- and I_U-images at the companion position and determine the corresponding probability distributions. We applied this method to the data sets of PZ Tel, HR 7682, HD 19467, GQ Lup, and HD 4747. To confirm that the PSF fitting is accurate, we also used the method to retrieve the total intensities of HR 8799 b, c, and d, and find that the results differ only 0.03 to 0.07 mag with those obtained with PynPoint (see Appendix 5.C). In this section we demonstrate the PSF fitting method with the 2018-08-07 H-band data set of HD 19467 and set upper limits on the degree of polarization of the companion HD 19467 B. Figure 5.19 shows the I_Q-image of this data set.

As the first step in our analysis, we obtain a rough estimate of the companion's contrast and x- and y-coordinates. To this end, we fit a model consisting of a 2D Moffat function and an inclined plane to the reduced I_Q-image at the companion position. The inclined plane accounts for the (approximately) linearly varying local background due to the stellar PSF and the stellar diffraction spikes (see Fig. 5.19) and is described by a constant (the z-intercept) and slopes in the x- and y-direction. We then fit a model containing the stellar PSF and an inclined plane to cropped versions of the I_Q and I_U-images, using the results from the Moffat fit for the initial estimates of the fit parameters. We use the Nelder-Mead method as implemented in the Python function `scipy.optimize.minimize` to minimize the sum of squared residuals (*SSR*):

$$SSR = \sum_{i=1}^{N} \left[\left(I_{Q,i} - \hat{I}_{Q,i} \right)^2 + \left(I_{U,i} - \hat{I}_{U,i} \right)^2 \right], \tag{5.5}$$

where $I_{Q,i}$ and $I_{U,i}$ are the flux values in the i-th pixel of the cropped I_Q- and I_U-images, $\hat{I}_{Q,i}$ and $\hat{I}_{U,i}$ are the corresponding modeled flux values, and N is the total number of pixels in each of the cropped images. We minimize the residuals in the I_Q- and I_U-images simultaneously to obtain a single set of x- and y-coordinates for the companion position. For the other parameters we fit separate values for I_Q and I_U.

We now repeat the PSF fitting using MCMC to obtain the final values of the fit parameters and the corresponding posterior distributions. We use the MCMC sampler from the Python package `emcee` (Foreman-Mackey et al., 2013) and let 32 walkers explore the probability space with 20,000 steps each (resulting in a total of 640,000 samples). We randomly generate the starting values of the walkers from Gaussian distributions centered on the best-fit parameter values from our previous fit. We use a Gaussian distribution for

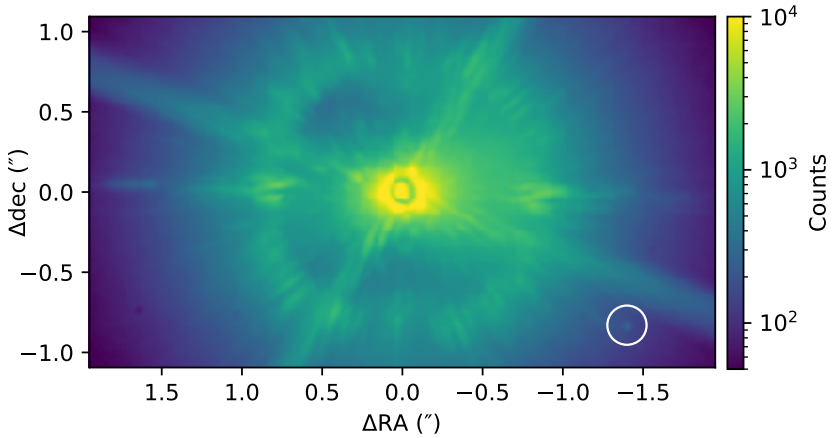


Figure 5.19: Reduced I_Q-image of the 2018-08-07 data set of HD 19467, showing the position of the companion HD 19467 B in the white circle. The asymmetric wind-driven halo and the stellar diffraction spikes are clearly visible.

the log-likelihood function:

$$\ln \mathcal{L} \propto -\frac{1}{2}\left[N \ln\left(2\pi\sigma^2\right) + \frac{SSR}{\sigma^2}\right], \tag{5.6}$$

where SSR is computed from Eq. (5.5) and σ is the standard deviation that accounts for the noise in the images. Because there is no region in the I_Q and I_U-images from which we can determine a representative value for σ, we include it among the parameters to be fitted (i.e., we treat σ as a nuisance parameter). We set the prior for σ proportional to $1/\sigma$, that is, Jeffrey's prior, to make sure it is non-informative. For the other parameters we use uniform priors. We remove the first 822 steps of each walker, equal to five times the maximum autocorrelation time, and check by visual inspection that the chains of all parameters have converged. The cropped I_Q- and I_U-images and the best-fit model and residual images are shown in Fig. 5.20. Figure 5.21 shows the resulting 1D- and 2D-projections of the posterior distribution of the fitted parameters. The distributions in Fig. 5.21 are visually very close to being Gaussian and show correlations only between the companion's contrast in I_Q or I_U and the corresponding z-intercept of the background.

We now determine the companion's probability distributions in I_Q and I_U (expressed in counts) for a range of aperture radii from 1 to 10 pixels. Similarly to the method described in Appendix 5.C, we sum the flux in the stellar PSF image using an aperture of the given radius and multiply the MCMC contrast samples in I_Q and I_U by this flux. For the remainder of the analysis we follow the steps described in Sects. 5.4 and Appendix 5.C, with the only exception that we sample the PDFs in Q and U with the same number of samples as used for the MCMC analysis. After performing the complete analysis, we detect no signals with an S/N higher than 1.4 in Q and 2 in U for any aperture radius. Finally, using an aperture radius of 1.86 pixels, equal to half times the FWHM of the stellar PSF, we determine the 68.27% and 99.73% upper limits on the degree of polarization of HD 19467 B to be equal to 1.0% and 2.0%, respectively.

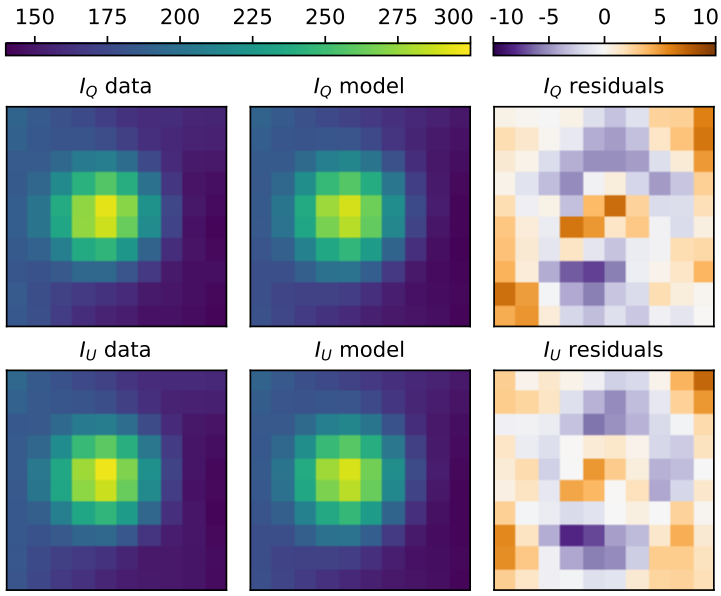


Figure 5.20: Data, best-fit model and residual images of the MCMC fitting of the stellar PSF at position of HD 19467 B to the reduced I_Q- and I_U-images of the 2018-08-07 data set of HD 19467.

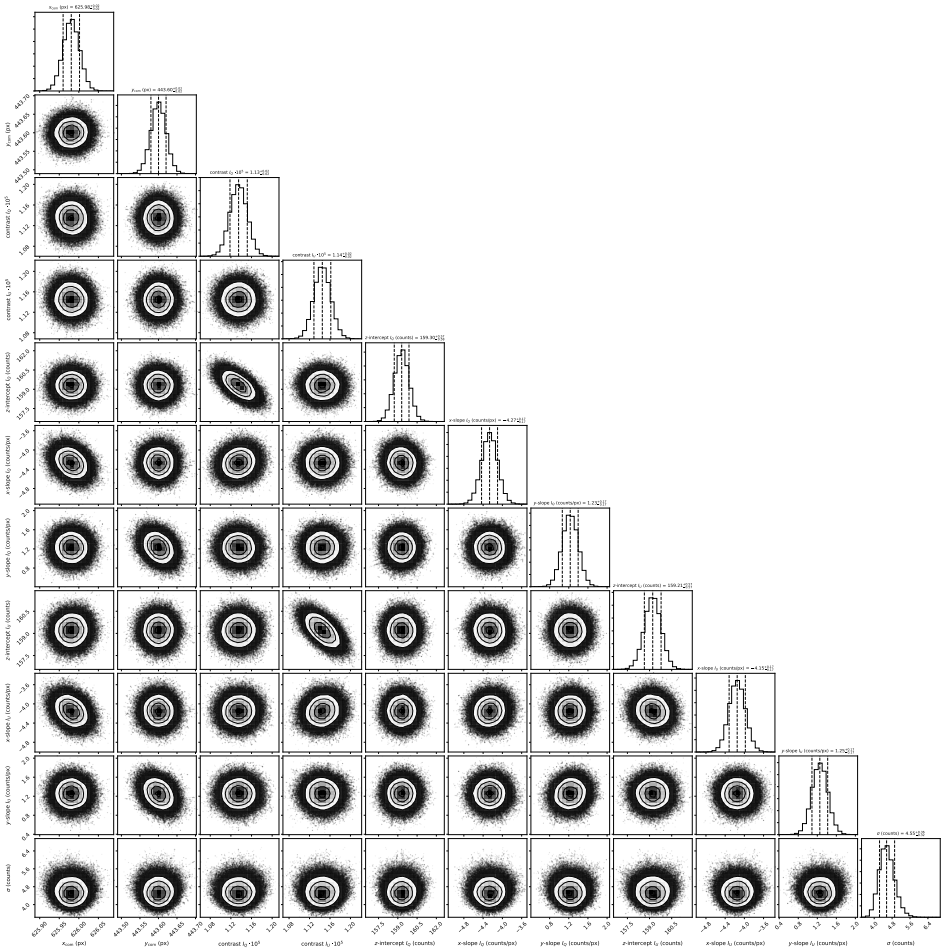


Figure 5.21: Posterior distributions after using MCMC to fit the stellar PSF at the position of the companion HD 19467 B to the reduced I_Q- and I_U-images of the 2018-08-07 data set of HD 19467. The fitted parameters are the companion position in x and y, the companion-to-star contrast in I_Q and I_U, the background's z-intercept and slopes in the x- and y-direction in I_Q and I_U, and the standard deviation σ that accounts for the noise in the images. The diagonal panels show the marginalized 1D distributions of the fitted parameters and the off-diagonal panels show the 2D projections of the posterior, revealing the covariance of the parameter pairs. The median and uncertainties (computed as the 18th and 84th percentiles) of the distributions are shown above the histograms and are indicated with the dashed vertical lines. The contours superimposed on the off-diagonal panels indicate the 1σ, 2σ and 3σ confidence levels assuming Gaussian statistics. The figure is created using the Python package `corner` (Foreman-Mackey, 2016).

5.E Contrast curve of β Pic data

Figure 5.22 shows the 1σ and 5σ point-source contrast in Q and U as a function of angular separation from the star for the mean-combined data set of β Pic as constructed with IRDAP. The curves are computed by summing the flux in rings of apertures around the star, computing the standard deviation over the aperture sums, and normalizing the result with the total stellar flux retrieved from the star flux frames. At small separations the correction for small-sample statistics is applied (see Mawet et al., 2014). For comparison the figure also shows the azimuthally averaged flux in the total-intensity I_Q- and I_U-images and the corresponding photon noise. At angular separations between ~0.2″ and 2.0″ the polarimetric sensitivity is close to the photon-noise limit, with a 1σ-contrast of $7 \cdot 10^{-8}$ to $1 \cdot 10^{-8}$ and a 5σ-contrast of $5 \cdot 10^{-7}$ to $5 \cdot 10^{-8}$. At separations larger than 2.0″ the sensitivity is limited by read noise or background noise and the 1σ- and 5σ-contrast are $<1 \cdot 10^{-8}$ and $<5 \cdot 10^{-8}$, respectively.

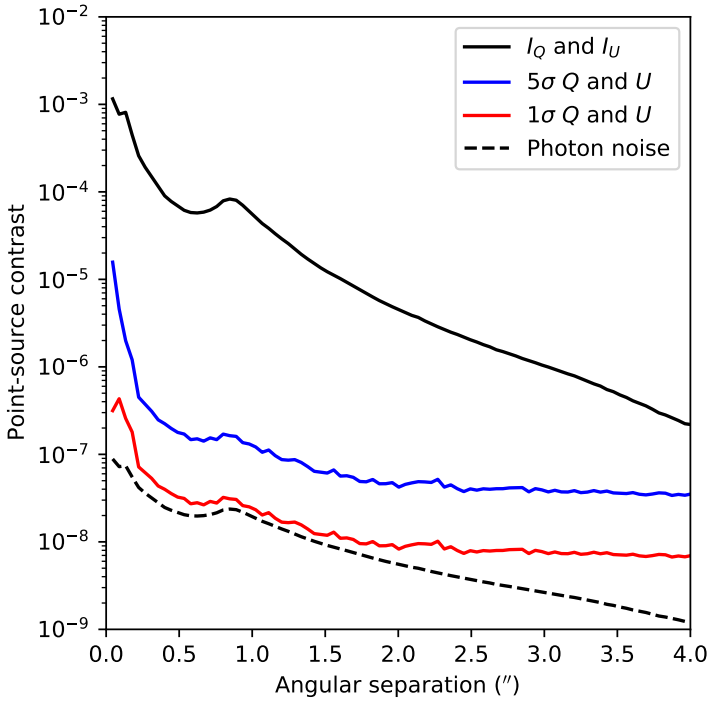


Figure 5.22: 1σ and 5σ point-source contrast in Q and U as a function of angular separation from the star for the mean-combined data set of β Pic. The azimuthally averaged flux in the total-intensity I_Q- and I_U-images and the corresponding photon noise are shown for comparison.

References

Ackerman, A. S., & Marley, M. S. 2001, Astrophysical Journal, 556, 872
Alibert, Y., Mordasini, C., Benz, W., & Winisdoerffer, C. 2005, Astronomy & Astrophysics, 434, 343
Allard, F., Hauschildt, P. H., Alexander, D. R., Tamanai, A., & Schweitzer, A. 2001, Astrophysical Journal, 556, 357
Allard, F., Homeier, D., & Freytag, B. 2012, Philosophical Transactions of the Royal Society of London Series A, 370, 2765
Alonso-Martínez, M., Riviere-Marichalar, P., Meeus, G., et al. 2017, Astronomy & Astrophysics, 603, A138
Alves, F. O., & Franco, G. A. P. 2006, Monthly Notices of the Royal Astronomical Society, 366, 238
Amara, A., & Quanz, S. P. 2012, Monthly Notices of the Royal Astronomical Society, 427, 948
Ayliffe, B. A., & Bate, M. R. 2009, Monthly Notices of the Royal Astronomical Society, 397, 657
Bailer-Jones, C. A. L., Rybizki, J., Fouesneau, M., Mantelet, G., & Andrae, R. 2018, Astronomical Journal, 156, 58
Bailey, V., Hinz, P. M., Currie, T., et al. 2013, Astrophysical Journal, 767, 31
Baraffe, I., Homeier, D., Allard, F., & Chabrier, G. 2015, Astronomy & Astrophysics, 577, A42
Bate, M. R. 2009, Monthly Notices of the Royal Astronomical Society, 392, 590
Bayo, A., Joergens, V., Liu, Y., et al. 2017, Astrophysical Journal Letters, 841, L11
Beuzit, J. L., Vigan, A., Mouillet, D., et al. 2019, Astronomy & Astrophysics, 631, A155
Boccaletti, A., Chauvin, G., Lagrange, A. M., & Marchis, F. 2003, Astronomy & Astrophysics, 410, 283
Boccaletti, A., Chauvin, G., Mouillet, D., et al. 2020, arXiv e-prints, arXiv:2003.05714
Bohn, A. J., Kenworthy, M. A., Ginski, C., et al. 2020, Monthly Notices of the Royal Astronomical Society, 492, 431
Bonnefoy, M., Chauvin, G., Lagrange, A. M., et al. 2014, Astronomy & Astrophysics, 562, A127
Bonnefoy, M., Chauvin, G., Rojo, P., et al. 2010, Astronomy & Astrophysics, 512, A52
Bonnefoy, M., Zurlo, A., Baudino, J. L., et al. 2016, Astronomy & Astrophysics, 587, A58
Boss, A. P. 1997, Science, 276, 1836
Bouvier, J., Chelli, A., Allain, S., et al. 1999, Astronomy & Astrophysics, 349, 619
Bowler, B. P. 2016, Publications of the Astronomical Society of the Pacific, 128, 102001
Bowler, B. P., Andrews, S. M., Kraus, A. L., et al. 2015, Astrophysical Journal Letters, 805, L17
Bowler, B. P., Liu, M. C., Kraus, A. L., Mann, A. W., & Ireland, M. J. 2011, Astrophysical Journal, 743, 148
Bryan, M. L., Benneke, B., Knutson, H. A., Batygin, K., & Bowler, B. P. 2018, Nature Astronomy, 2, 138
Bryan, M. L., Chiang, E., Bowler, B. P., et al. 2020, Astronomical Journal, 159, 181
Caceres, C., Hardy, A., Schreiber, M. R., et al. 2015, Astrophysical Journal Letters, 806, L22
Cameron, A. G. W. 1978, Moon and Planets, 18, 5
Canovas, H., Ménard, F., de Boer, J., et al. 2015, Astronomy & Astrophysics, 582, L7
Carbillet, M., Bendjoya, P., Abe, L., et al. 2011, Experimental Astronomy, 30, 39
Chauvin, G., Lagrange, A. M., Lacombe, F., et al. 2005a, Astronomy & Astrophysics, 430, 1027
Chauvin, G., Lagrange, A. M., Zuckerman, B., et al. 2005b, Astronomy & Astrophysics, 438, L29
Chilcote, J., Pueyo, L., De Rosa, R. J., et al. 2017, Astronomical Journal, 153, 182
Christiaens, V., Cantalloube, F., Casassus, S., et al. 2019, Astrophysical Journal Letters, 877, L33
Crepp, J. R., Johnson, J. A., Howard, A. W., et al. 2014, Astrophysical Journal, 781, 29

Crepp, J. R., Johnson, J. A., Fischer, D. A., et al. 2012, Astrophysical Journal, 751, 97
Crepp, J. R., Rice, E. L., Veicht, A., et al. 2015, Astrophysical Journal Letters, 798, L43
Crepp, J. R., Principe, D. A., Wolff, S., et al. 2018, Astrophysical Journal, 853, 192
Cuello, N., Dipierro, G., Mentiplay, D., et al. 2019, Monthly Notices of the Royal Astronomical Society, 483, 4114
Cuello, N., Louvet, F., Mentiplay, D., et al. 2020, Monthly Notices of the Royal Astronomical Society, 491, 504
Daemgen, S., Todorov, K., Quanz, S. P., et al. 2017, Astronomy & Astrophysics, 608, A71
de Boer, J., Langlois, M., van Holstein, R. G., et al. 2020, Astronomy & Astrophysics, 633, A63
de Kok, R. J., Stam, D. M., & Karalidi, T. 2011, Astrophysical Journal, 741, 59
Delorme, P., Schmidt, T., Bonnefoy, M., et al. 2017, Astronomy & Astrophysics, 608, A79
Dohlen, K., Langlois, M., Saisse, M., et al. 2008, in Society of Photo-Optical Instrumentation Engineers (SPIE) Conference Series, Vol. 7014, Proceedings of the SPIE, 70143L
Donati, J. F., Gregory, S. G., Alencar, S. H. P., et al. 2012, Monthly Notices of the Royal Astronomical Society, 425, 2948
Dong, R., Fung, J., & Chiang, E. 2016, Astrophysical Journal, 826, 75
Dubrulle, B., Morfill, G., & Sterzik, M. 1995, Icarus, 114, 237
Dupuy, T. J., Brandt, T. D., Kratter, K. M., & Bowler, B. P. 2019, Astrophysical Journal Letters, 871, L4
Foreman-Mackey, D. 2016, The Journal of Open Source Software, 1, 24
Foreman-Mackey, D., Hogg, D. W., Lang, D., & Goodman, J. 2013, Publications of the Astronomical Society of the Pacific, 125, 306
Gaia Collaboration, Brown, A. G. A., Vallenari, A., et al. 2018, Astronomy & Astrophysics, 616, A1
Galli, P. A. B., Loinard, L., Ortiz-Léon, G. N., et al. 2018, Astrophysical Journal, 859, 33
Ginski, C., Mugrauer, M., Neuhäuser, R., & Schmidt, T. O. B. 2014, Monthly Notices of the Royal Astronomical Society, 438, 1102
Ginski, C., Benisty, M., van Holstein, R. G., et al. 2018, Astronomy & Astrophysics, 616, A79
Goodman, A. A., Jones, T. J., Lada, E. A., & Myers, P. C. 1992, Astrophysical Journal, 399, 108
Gravity Collaboration, Lacour, S., Nowak, M., et al. 2019, Astronomy & Astrophysics, 623, L11
Gray, R. O., Corbally, C. J., Garrison, R. F., et al. 2006a, Astronomical Journal, 132, 161
—. 2006b, Astronomical Journal, 132, 161
Gray, R. O., Corbally, C. J., Garrison, R. F., McFadden, M. T., & Robinson, P. E. 2003, Astronomical Journal, 126, 2048
Grinin, V. P. 2000, in Astronomical Society of the Pacific Conference Series, Vol. 219, Disks, Planetesimals, and Planets, ASP Conference Proceedings, Vol. 219, edited by F. Garzón, C. Eiroa, D. de Winter, and T. J. Mahoney. Astronomical Society of the Pacific, ISBN 1-58381-051-X, 2000, p.216, ed. G. Garzón, C. Eiroa, D. de Winter, & T. J. Mahoney, 216
Guerri, G., Daban, J.-B., Robbe-Dubois, S., et al. 2011, Experimental Astronomy, 30, 59
Haffert, S. Y., Bohn, A. J., de Boer, J., et al. 2019, Nature Astronomy, 3, 749
Haffert, S. Y., van Holstein, R. G., Ginski, C., et al. 2020, Astronomy & Astrophysics, 640, L12
Hashimoto, J., Dong, R., Kudo, T., et al. 2012, Astrophysical Journal Letters, 758, L19
Heiles, C. 2000, Astronomical Journal, 119, 923
Herbig, G. H. 1977, Astrophysical Journal, 214, 747
Heyer, M. H., Vrba, F. J., Snell, R. L., et al. 1987, Astrophysical Journal, 321, 855
Hiranaka, K., Cruz, K. L., Douglas, S. T., Marley, M. S., & Baldassare, V. F. 2016, Astrophysical Journal, 830, 96
Houk, N., & Cowley, A. P. 1975, University of Michigan Catalogue of two-dimensional spectral types for the HD stars. Volume I.

Isella, A., Benisty, M., Teague, R., et al. 2019, Astrophysical Journal Letters, 879, L25
Jensen-Clem, R., Millar-Blanchaer, M., Mawet, D., et al. 2016, Astrophysical Journal, 820, 111
Jensen-Clem, R., Millar-Blanchaer, M. A., van Holstein, R. G., et al. 2020, Astronomical Journal, 160, 286
Kalas, P. G., Rajan, A., Wang, J. J., et al. 2015, Astrophysical Journal, 814, 32
Keppler, M., Benisty, M., Müller, A., et al. 2018, Astronomy & Astrophysics, 617, A44
Kharchenko, N. V., & Roeser, S. 2009, VizieR Online Data Catalog, I/280B
Kratter, K. M., Murray-Clay, R. A., & Youdin, A. N. 2010, Astrophysical Journal, 710, 1375
Kraus, A. L., Andrews, S. M., Bowler, B. P., et al. 2015, Astrophysical Journal Letters, 798, L23
Kraus, A. L., Ireland, M. J., Cieza, L. A., et al. 2014, Astrophysical Journal, 781, 20
Lagrange, A. M., Bonnefoy, M., Chauvin, G., et al. 2010, Science, 329, 57
Lagrange, A. M., Langlois, M., Gratton, R., et al. 2016, Astronomy & Astrophysics, 586, L8
Langlois, M., Pohl, A., Lagrange, A. M., et al. 2018, Astronomy & Astrophysics, 614, A88
Liu, M. C., Fischer, D. A., Graham, J. R., et al. 2002, Astrophysical Journal, 571, 519
Lombardi, M., Lada, C. J., & Alves, J. 2008, Astronomy & Astrophysics, 480, 785
Luhman, K. L., Allen, P. R., Espaillat, C., Hartmann, L., & Calvet, N. 2010, Astrophysical Journal Supplement, 186, 111
MacGregor, M. A., Wilner, D. J., Czekala, I., et al. 2017, Astrophysical Journal, 835, 17
Macintosh, B., Graham, J. R., Ingraham, P., et al. 2014, Proceedings of the National Academy of Science, 111, 12661
Maire, A. L., Bonnefoy, M., Ginski, C., et al. 2016a, Astronomy & Astrophysics, 587, A56
Maire, A.-L., Langlois, M., Dohlen, K., et al. 2016b, in Society of Photo-Optical Instrumentation Engineers (SPIE) Conference Series, Vol. 9908, Proceedings of the SPIE, 990834
Mamajek, E. E. 2008, Astronomische Nachrichten, 329, 10
Marley, M. S., & Sengupta, S. 2011, Monthly Notices of the Royal Astronomical Society, 417, 2874
Marois, C., Lafrenière, D., Doyon, R., Macintosh, B., & Nadeau, D. 2006, Astrophysical Journal, 641, 556
Martin, R. G., & Lubow, S. H. 2011, Monthly Notices of the Royal Astronomical Society, 413, 1447
Mawet, D., Milli, J., Wahhaj, Z., et al. 2014, Astrophysical Journal, 792, 97
Ménard, F., Bouvier, J., Dougados, C., Mel'nikov, S. Y., & Grankin, K. N. 2003, Astronomy & Astrophysics, 409, 163
Ménard, F., Delfosse, X., & Monin, J. L. 2002, Astronomy & Astrophysics, 396, L35
Miles-Páez, P. A., Zapatero Osorio, M. R., Pallé, E., & Peña Ramírez, K. 2013, Astronomy & Astrophysics, 556, A125
—. 2017, Monthly Notices of the Royal Astronomical Society, 466, 3184
Millar-Blanchaer, M. A., Graham, J. R., Pueyo, L., et al. 2015, Astrophysical Journal, 811, 18
Millar-Blanchaer, M. A., Perrin, M. D., Hung, L.-W., et al. 2016, in Society of Photo-Optical Instrumentation Engineers (SPIE) Conference Series, Vol. 9908, Proceedings of the SPIE, 990836
Millar-Blanchaer, M. A., Girard, J. H., Karalidi, T., et al. 2020, Astrophysical Journal, 894, 42
Milli, J., Hibon, P., Christiaens, V., et al. 2017, Astronomy & Astrophysics, 597, L2
Min, M., Dullemond, C. P., Dominik, C., de Koter, A., & Hovenier, J. W. 2009, Astronomy & Astrophysics, 497, 155
Min, M., Rab, C., Woitke, P., Dominik, C., & Ménard, F. 2016, Astronomy & Astrophysics, 585, A13
Miret-Roig, N., Galli, P. A. B., Brandner, W., et al. 2020, Astronomy & Astrophysics, 642, A179
Moneti, A., Pipher, J. L., Helfer, H. L., McMillan, R. S., & Perry, M. L. 1984, Astrophysical Journal, 282, 508

Montes, D., López-Santiago, J., Gálvez, M. C., et al. 2001, Monthly Notices of the Royal Astronomical Society, 328, 45
Mora, A., Wu, Y.-L., Bowler, B. P., & Sheehan, P. 2020, Research Notes of the American Astronomical Society, 4, 9
Müller, A., Keppler, M., Henning, T., et al. 2018, Astronomy & Astrophysics, 617, L2
Neugebauer, G., Habing, H. J., van Duinen, R., et al. 1984, Astrophysical Journal Letters, 278, L1
Nielsen, E. L., De Rosa, R. J., Macintosh, B., et al. 2019, Astronomical Journal, 158, 13
Ortiz-León, G. N., Loinard, L., Kounkel, M. A., et al. 2017, Astrophysical Journal, 834, 141
Pearce, L. A., Kraus, A. L., Dupuy, T. J., et al. 2019, Astronomical Journal, 157, 71
Pecaut, M. J., & Mamajek, E. E. 2016, Monthly Notices of the Royal Astronomical Society, 461, 794
Pérez, S., Marino, S., Casassus, S., et al. 2019, Monthly Notices of the Royal Astronomical Society, 488, 1005
Pilbratt, G. L., Riedinger, J. R., Passvogel, T., et al. 2010, Astronomy & Astrophysics, 518, L1
Pollack, J. B., Hubickyj, O., Bodenheimer, P., et al. 1996, Icarus, 124, 62
Ricci, L., Testi, L., Natta, A., et al. 2014, Astrophysical Journal, 791, 20
Ricci, L., Cazzoletti, P., Czekala, I., et al. 2017, Astronomical Journal, 154, 24
Rizzo, J. R., Morras, R., & Arnal, E. M. 1998, Monthly Notices of the Royal Astronomical Society, 300, 497
Rizzuto, A. C., Ireland, M. J., & Kraus, A. L. 2015, Monthly Notices of the Royal Astronomical Society, 448, 2737
Rodríguez-Ledesma, M. V., Mundt, R., & Eislöffel, J. 2009, Astronomy & Astrophysics, 502, 883
Rostopchina, A. N., Grinin, V. P., Okazaki, A., et al. 1997, Astronomy & Astrophysics, 327, 145
Schneider, J., Dedieu, C., Le Sidaner, P., Savalle, R., & Zolotukhin, I. 2011, Astronomy & Astrophysics, 532, A79
Scholz, A., Kostov, V., Jayawardhana, R., & Mužić, K. 2015, Astrophysical Journal Letters, 809, L29
Scholz, A., Moore, K., Jayawardhana, R., et al. 2018, Astrophysical Journal, 859, 153
Schwarz, H., Ginski, C., de Kok, R. J., et al. 2016, Astronomy & Astrophysics, 593, A74
Scott, D. W. 2015, Multivariate Density Estimation: Theory, Practice, and Visualization
Seifahrt, A., Neuhäuser, R., & Hauschildt, P. H. 2007, Astronomy & Astrophysics, 463, 309
Sengupta, S., & Krishan, V. 2001, Astrophysical Journal Letters, 561, L123
Sengupta, S., & Marley, M. S. 2009, Astrophysical Journal, 707, 716
—. 2010, Astrophysical Journal Letters, 722, L142
—. 2016, Astrophysical Journal, 824, 76
Serkowski, K., Mathewson, D. S., & Ford, V. L. 1975, Astrophysical Journal, 196, 261
Shabram, M., & Boley, A. C. 2013, Astrophysical Journal, 767, 63
Sheehan, P. D., Wu, Y.-L., Eisner, J. A., & Tobin, J. J. 2019, Astrophysical Journal, 874, 136
Snik, F., de Wijn, A. G., Ichimoto, K., et al. 2010, Astronomy & Astrophysics, 519, A18
Soummer, R., Pueyo, L., & Larkin, J. 2012, Astrophysical Journal Letters, 755, L28
Sparks, W. B., & Axon, D. J. 1999, Publications of the Astronomical Society of the Pacific, 111, 1298
Stamatellos, D., & Whitworth, A. P. 2009, Monthly Notices of the Royal Astronomical Society, 392, 413
Stolker, T., Bonse, M. J., Quanz, S. P., et al. 2019, Astronomy & Astrophysics, 621, A59
Stolker, T., Min, M., Stam, D. M., et al. 2017, Astronomy & Astrophysics, 607, A42
Stolker, T., Quanz, S. P., Todorov, K. O., et al. 2020, Astronomy & Astrophysics, 635, A182
Szulágyi, J., Mayer, L., & Quinn, T. 2017, Monthly Notices of the Royal Astronomical Society, 464, 3158

Takata, T., & Stevenson, D. J. 1996, Icarus, 123, 404
Tata, R., Martín, E. L., Sengupta, S., et al. 2009, Astronomy & Astrophysics, 508, 1423
Tinyanont, S., Millar-Blanchaer, M. A., Nilsson, R., et al. 2019, Publications of the Astronomical Society of the Pacific, 131, 025001
Tobin, J. J., Kratter, K. M., Persson, M. V., et al. 2016, Nature, 538, 483
Torres, C. A. O., Quast, G. R., da Silva, L., et al. 2006, Astronomy & Astrophysics, 460, 695
van der Plas, G., Ménard, F., Ward-Duong, K., et al. 2016, Astrophysical Journal, 819, 102
Veras, D., Crepp, J. R., & Ford, E. B. 2009, Astrophysical Journal, 696, 1600
Vigan, A., Fontanive, C., Meyer, M., et al. 2021, Astronomy & Astrophysics, 651, A72
Wahhaj, Z., Liu, M. C., Biller, B. A., et al. 2011, Astrophysical Journal, 729, 139
Wang, J. J., Graham, J. R., Dawson, R., et al. 2018, Astronomical Journal, 156, 192
Wertz, O., Absil, O., Gómez González, C. A., et al. 2017, Astronomy & Astrophysics, 598, A83
Whittet, D. C. B., Martin, P. G., Hough, J. H., et al. 1992, Astrophysical Journal, 386, 562
Wiktorowicz, S. J., Millar-Blanchaer, M., Perrin, M. D., et al. 2014, in Society of Photo-Optical Instrumentation Engineers (SPIE) Conference Series, Vol. 9147, Proceedings of the SPIE, 914783
Williams, J. P., & Cieza, L. A. 2011, Annual Review of Astronomy and Astrophysics, 49, 67
Woitke, P., Min, M., Pinte, C., et al. 2016, Astronomy & Astrophysics, 586, A103
Wolff, S. G., Ménard, F., Caceres, C., et al. 2017, Astronomical Journal, 154, 26
Wood, C. M., Boyajian, T., von Braun, K., et al. 2019, Astrophysical Journal, 873, 83
Wu, Y.-L., Close, L. M., Eisner, J. A., & Sheehan, P. D. 2017a, Astronomical Journal, 154, 234
Wu, Y.-L., & Sheehan, P. D. 2017, Astrophysical Journal Letters, 846, L26
Wu, Y.-L., Close, L. M., Males, J. R., et al. 2015, Astrophysical Journal Letters, 807, L13
Wu, Y.-L., Sheehan, P. D., Males, J. R., et al. 2017b, Astrophysical Journal, 836, 223
Wu, Y.-L., Bowler, B. P., Sheehan, P. D., et al. 2020, Astronomical Journal, 159, 229
Xuan, J. W., Bryan, M. L., Knutson, H. A., et al. 2020, Astronomical Journal, 159, 97
Yan, Q.-Z., Zhang, B., Xu, Y., et al. 2019, Astronomy & Astrophysics, 624, A6
Zapatero Osorio, M. R., Béjar, V. J. S., Goldman, B., et al. 2011, Astrophysical Journal, 740, 4
Zapatero Osorio, M. R., Caballero, J. A., & Béjar, V. J. S. 2005, Astrophysical Journal, 621, 445
Zapatero Osorio, M. R., Martín, E. L., Bouy, H., et al. 2006, Astrophysical Journal, 647, 1405
Zhou, Y., Herczeg, G. J., Kraus, A. L., Metchev, S., & Cruz, K. L. 2014, Astrophysical Journal Letters, 783, L17

6 Circular polarimetric imaging at planetary system scales by hacking SPHERE-IRDIS: Full-Stokes observations of the asymmetric nebula surrounding VY CMa[1]

K. N. Strelow, D. A. Abbink, R. G. van Holstein, S. P. Bos, and F. Snik

Context. Measuring near-infrared circular polarization at high spatial resolution is a promising method to characterize the dust and magnetic fields in protoplanetary disks and around evolved stars, and could even shed light on the emergence of homochirality in biomolecules. However, current high-contrast imaging polarimeters such as SPHERE-IRDIS at the Very Large Telescope are not designed to measure circular polarization.

Aims. We develop the observing scheme, data-reduction methods, and analysis tools to measure circular polarization with SPHERE-IRDIS.

Methods. The image derotator (K-mirror) of SPHERE acts as an almost perfect quarter-wave retarder in the H- and K_s-bands. We devised an observing scheme that uses the derotator as polarization modulator to convert incident circular polarization into measurable linear polarization. We tested the technique with H-band observations of the red hypergiant VY CMa and its surrounding asymmetric nebula, and reduced the data using our model of the instrumental polarization effects of SPHERE-IRDIS.

Results. We find that the efficiency of measuring circular polarization is close to 100% and that the instrument-induced circular polarization is small (<0.1%) and well corrected for with the instrument model. The accuracy of our measurements is limited by the less-well-calibrated linear-to-circular polarimetric crosstalk produced by the telescope and SPHERE's first mirror. To more accurately constrain this crosstalk, we use the spatial variation of the linear polarization in the nebula of VY CMa to distinguish between real astrophysical circular polarization and crosstalk-induced signal. We find that the light from VY CMa in H-band is 4.07 ± 0.05% linearly polarized and 0.14 ± 0.04% circularly polarized, in agreement with the literature. These polarization signals most likely originate from a spatially unresolved, asymmetric circumstellar structure located close to the star that is optically thick or contains magnetically aligned dust grains. We also detect several so-far-unresolved features in the nebula surrounding VY CMa in linearly polarized light, but do not conclusively detect spatially resolved circular polarization.

Conclusions. In order to maximize the accuracy of future measurements, the instrumental

[1] *Author contributions:* As part of their BSc research project, KS and DA modeled the polarization modulation and instrumental polarization effects, performed the data reduction, calibrated the retardances of the UT and M4, and developed the data visualizations. RGvH devised and implemented the measurement technique at SPHERE-IRDIS, carried out the observations, supervised the BSc students, interpreted the measurements of VY CMa and its nebula, and led the writing. SB and FS co-supervised the BSc research project. FS suggested the new circular-polarization mode and developed the science case. All authors contributed to discussions during the research project and the writing.

crosstalk should be further calibrated by observing a face-on-viewed circumstellar disk. Our observing scheme enables the first measurements of spatially resolved circular polarization in protoplanetary disks and the nebulae around evolved stars.

6.1 Introduction

Measuring scattering-induced near-infrared (NIR) circular polarization at high spatial resolution can provide unique diagnostics for the characterization of the dusty environments of protoplanetary disks and the nebulae around evolved stars. Contrary to NIR linear polarization that can be produced by single scattering of unpolarized starlight, circular polarization is created through higher-order scattering processes that break mirror symmetry and is therefore not very common. In fact, disregarding the possibility of chiral scattering particles with a single handedness, the creation of circular polarization through scattering requires that symmetry is broken twice. Typically, a first scattering event creates linearly polarized light from essentially unpolarized starlight, after which this linear polarization is (partially) converted into circular polarization by a second interaction that mimics the effect of a retarder (e.g., a quarter-wave plate at $\pm 45^{\circ}$ to the incident linear polarization for perfect conversion).

The first mechanism to create circular polarization is multiple scattering of anisotropic radiation off spherical dust grains (i.e., multiple Mie scattering; Shafter & Jura, 1980; Bastien & Ménard, 1990). In this mechanism, the linearly polarized light created by scattering off dust grains is re-scattered by other grains, which, for favorable 3D scattering angles and dust geometries, produces circular polarization. The second mechanism to create circular polarization is scattering off elongated dust grains that are aligned to a large-scale magnetic field (Gledhill & McCall, 2000). In this case, the circular polarization results from a multiple-scattering scenario in which linearly polarized light that is created elsewhere is scattered off grains that are aligned at an oblique angle with respect to the incoming linear polarization. Alternatively, if the grains are aligned at an oblique angle with respect to the scattering plane, circular polarization can be created by a single scattering event that combines the creation of linear polarization and retardance. Whereas multiple Mie scattering yields relatively modest degrees of circular polarization of $\lesssim 1\%$, scattering by aligned grains can produce circular-polarization signals of tens of percent (Hough, 2006). The higher-order scattering mechanisms can also produce non-azimuthally oriented linear polarization, that is, linear polarization that is not oriented orthogonal to the direction toward the central star (e.g., Canovas et al., 2015). Therefore, measurements of both the linear and circular polarization in protoplanetary disks and the nebulae around evolved stars can yield strong constraints on the distribution of the scattering material, scattering asymmetries, dust properties (e.g., size, shape, and texture), and magnetic-field geometries.

Detecting circular polarization in protoplanetary disks is especially interesting because circular polarization may be responsible for the emergence of biological homochirality, which is one of the most fundamental properties of life (Bailey et al., 1998; Lucas et al., 2005; Modica et al., 2014; Patty et al., 2018; Avnir, 2021). Biology primarily uses one of two mirror-image versions (enantiomers) of complex molecules such as

amino acids and sugars (the building blocks of biological macromolecules such as DNA), whereas pure chemistry does not have such biases (Nelson et al., 2008). Homochirality may originate from an initially small enantiomeric imbalance in these molecules that is then amplified by specific (bio)chemical or physical processes (Bonner, 1991). Bailey et al. (1998) suggest that circularly polarized ultraviolet radiation can create an enantiomeric imbalance in the organic molecules in star-forming regions and protoplanetary disks through selective destruction of enantiomers, after which these organic molecules are delivered to forming planets and moons by impacting planetesimals and dust. Unfortunately, the ultraviolet radiation in these systems is difficult to observe because it is mostly obscured from our view by dust. However, Bailey et al. (1998) show that circular polarization at ultraviolet wavelengths can be created through the same higher-order scattering processes that produce NIR circular polarization. Large-scale and strong NIR circular polarization has been detected in many star-forming regions with wide-field imaging polarimetry (e.g., Chrysostomou et al., 1997; Bailey et al., 1998; Chrysostomou et al., 2000; Ménard et al., 2000; Buschermöhle et al., 2005; Kwon et al., 2013, 2014, 2018). However, to really show that circular polarization can contribute to the origin of homochirality on forming planets, we need to measure the NIR circular polarization in protoplanetary disks.

The seeing-limited instruments that have so far been used to measure NIR circular polarization cannot reach the high contrast and subarcsecond resolutions required to image protoplanetary disks and the nebulae around evolved stars. The adaptive-optics-assisted high-contrast imaging instrument SPHERE-IRDIS (Beuzit et al., 2019; Dohlen et al., 2008) at the Very Large Telescope has a well-established NIR dual-beam polarimetric imaging mode (de Boer et al., 2020; Chapter 2) that is very successful at imaging and characterizing circumstellar disks and (sub)stellar companions with a high spatial resolution in linearly polarized light (see e.g., Garufi et al., 2017; Avenhaus et al., 2018; Ginski et al., 2018; Chapter 5). Although SPHERE-IRDIS is not designed to measure circular polarization, in Chapter 2 it is suggested that the instrument can be made sensitive to circular polarization without changing its optical components. The Mueller matrix model of the instrumental polarization effects of the complete optical path of SPHERE-IRDIS shows that at some orientations the image derotator of SPHERE produces very strong circular-to-linear polarimetric crosstalk in the H- and K_s-bands. The derotator can therefore be used as polarization modulator to convert incident circular polarization into linear polarization that can be measured with the linear polarizers in IRDIS.

In this chapter, we present an observing scheme with SPHERE-IRDIS that uses the derotator as a polarization modulator to measure NIR circular polarization at subarcsecond resolution. We test the new observing scheme with linear- and circular-polarization measurements of the evolved star VY Canis Majoris (VY CMa) and its surrounding nebula. Using the Mueller matrix model of Chapter 2, we examine the efficiency of measuring circular polarization and quantify the circular polarization induced by the telescope and instrument. To reduce the data, we adapt the publicly available `IRDAP` (IRDIS Data reduction for Accurate Polarimetry) pipeline that uses the Mueller matrix model of Chapter 2 to correct observations for instrumental polarization effects with an absolute polarimetric accuracy of $\lesssim 0.1\%$ in the degree of polarization. Because the accuracy of our circular-polarization measurements turns out to be limited by the uncertainty

of the polarimetric crosstalk produced by the telescope and SPHERE's first mirror, we use the data of VY CMa itself to more accurately constrain this crosstalk.

Our test target VY CMa is an 8.2 Myr-old red hypergiant star with a mass of $17 \pm 8 M_{\odot}$ and an effective temperature of 3490 ± 90 K (Wittkowski et al., 2012; Zhang et al., 2012). The star is located at a distance of 1.17 ± 0.08 kpc and has a radius of $1420 \pm 120 R_{\odot}$, making it one of the largest stars known. VY CMa is surrounded by a nebula that is several arcseconds wide and comprises dusty clumps of ejecta that are asymmetrically distributed around the star (e.g., Monnier et al., 1999; Smith et al., 2001; Humphreys et al., 2007; Jones et al., 2007; Smith et al., 2009; Shenoy et al., 2013, 2015; O'Gorman et al., 2015; Scicluna et al., 2015). Linear-polarization measurements at visible and NIR wavelengths show that these clumps contain micron-sized dust grains (Scicluna et al., 2015) and suggest that some of these clumps are optically thick (Jones et al., 2007; Shenoy et al., 2015). As a result, it is possible that the light from these clumps scattered multiple times and is therefore circularly polarized. Gehrels (1972) and Serkowski (1973) detect NIR circular polarization from VY CMa through aperture polarimetry on the central source (0.4% in *I*-, 0.2% in *H*-, and 0.1% in *K*-band), but because these observations do not spatially resolve the nebula it is unclear where in the nebula this circular polarization originates.

The outline of this chapter is as follows. We describe the observing scheme to measure circular polarization in Sect. 6.2 and outline the test observations of VY CMa in Sect. 6.3. Subsequently, we investigate the instrumental polarization effects of the circular-polarization measurements in Sect. 6.4. Next, we present the data reduction in Sect. 6.5 and use the test data of VY CMa itself to further constrain the polarimetric crosstalk in Sect. 6.6. In Sect. 6.7 we present and discuss the measured linear and circular polarization of VY CMa and its nebula. Finally, we present conclusions in Sect. 6.8.

6.2 Observing scheme for measuring circular polarization

In this section, we describe the observing scheme we developed to measure circular polarization with SPHERE-IRDIS. We build on the efforts described in de Boer et al. (2020) and Chapter 2 and adopt the same definitions for the (optical components') orientation angles and the Stokes parameters. Of these Stokes parameters, I is the total intensity and positive and negative Q describe vertical (north-south) and horizontal (east-west) linear polarization. When looking into the beam of light, positive and negative U describe linear polarization oriented 45° counterclockwise and clockwise from positive Q, and positive and negative V describe circular polarization with clockwise and counterclockwise rotation. We refer to positive and negative V as right-handed and left-handed circular polarization, respectively. In Sect. 6.2.1 we summarize the optical path of SPHERE-IRDIS' polarimetric mode and the measurement of linear polarization. For a detailed description of the mode we refer to de Boer et al. (2020) and Chapter 2. In Sect. 6.2.2 we discuss the observing scheme to measure circular polarization.

6.2.1 SPHERE-IRDIS' polarimetric mode for linear polarimetry

A schematic overview of the optical path of SPHERE-IRDIS for polarimetric measurements is shown in Fig. 6.1. Light is collected by the primary mirror of the altazimuth-mounted Unit Telescope (UT) and is subsequently refocused by the secondary mirror (M2) that is suspended at the top of the telescope. The inclined tertiary mirror (M3) of the UT then reflects the light to the Nasmyth platform on which SPHERE is installed. Within SPHERE, the light is reflected off another inclined mirror (M4) and passes a rotatable half-wave plate (HWP) and the image derotator, which is a rotatable assembly of three mirrors (a K-mirror). In field-tracking mode, the derotator follows a rotation law that keeps the image in a fixed orientation on the detector (de Boer et al., 2020, Appendix A):

$$\theta_{\mathrm{der}} = \frac{1}{2}\,(-p + a + \eta) + n \cdot 180^{\circ}, \tag{6.1}$$

where θ_{der} is the derotator angle, p the parallactic angle, a the telescope altitude angle, η a user-defined image-position-angle offset, and n an integer that is determined by the control software. After the derotator, the light passes the mirrors of the adaptive optics system and the coronagraphs (not shown in Fig. 6.1). Subsequently, the light enters IRDIS and is split into two beams by a nonpolarizing beamsplitter and a mirror. The beams then pass a pair of linear polarizers with orthogonal transmission axes oriented in the vertical and horizontal directions, that is, in the directions perpendicular and parallel to the Nasmyth platform. Finally, the beams fall on the detector and create two adjacent (left and right) images of the orthogonal linear-polarization states.

During observations in field-tracking mode, the HWP keeps the linear polarization incident on the telescope in a fixed orientation with respect to the detector. In addition, the HWP acts as a modulator and selects the incident linear polarization to be measured. To this end, the HWP follows the rotation law (de Boer et al., 2020, Appendix A):

$$\theta_{\mathrm{HWP}} = -p + a + \frac{1}{2}\,(\eta + \gamma) + \theta^{\mathrm{s}}_{\mathrm{HWP}}, \tag{6.2}$$

where θ_{HWP} is the HWP angle, γ is an additional position angle offset (in general $\gamma = 0^{\circ}$), and $\theta^{\mathrm{s}}_{\mathrm{HWP}}$ is the HWP switch angle. In one HWP cycle, the HWP switch angle takes on values equal to 0° and 45° to measure incident Stokes Q and 22.5° and 67.5° to measure incident Stokes U.

For each HWP switch angle, we subtract the right image from the left image (the single difference) to obtain the Q^{+}-, Q^{-}-, U^{+}-, and U^{-}-images, respectively. We then compute images of Stokes Q and U from these images using the double difference as:

$$Q = \frac{1}{2}\,(Q^{+} - Q^{-})\,, \tag{6.3}$$

$$U = \frac{1}{2}\,(U^{+} - U^{-})\,. \tag{6.4}$$

We also add the left and right images for each HWP switch angle (the single sum) to obtain the $I_{Q^{+}}$-, $I_{Q^{-}}$-, $I_{U^{+}}$-, and $I_{U^{-}}$-images. Finally, we calculate the total-intensity I_{Q}-

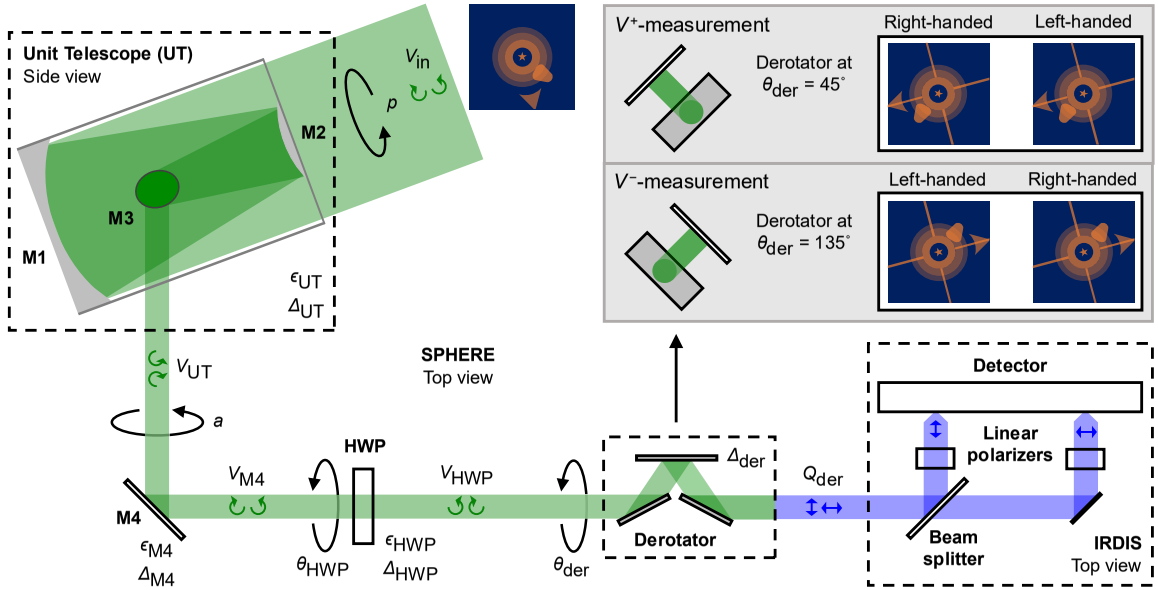


Figure 6.1: Overview of the optical path of the Unit Telescope (UT) and SPHERE-IRDIS, showing only the optical components relevant for polarimetric measurements, as well as a schematic depiction of the observing scheme to measure circular polarization. The names of the (groups of) components are indicated in boldface. The relevant diattenuations ϵ and retardances Δ of the components are shown as well. The black circular arrows indicate the parallactic angle p, the telescope altitude angle a, the half-wave plate (HWP) angle θ_{HWP}, and the derotator angle θ_{der}. Also indicated are the circularly polarized light (in green) incident on the telescope (V_{in}) and downstream of the UT (V_{UT}), M4 (V_{M4}), and the HWP (V_{HWP}) as well as the linearly polarized light (in blue) that the circularly polarized light is converted into downstream of the derotator (Q_{der}). The gray area at the top right of the image shows the circular-polarization V^+- and V^--measurements taken with the derotator (viewed as looking along the incident beam) at angles equal to 45° and 135°, respectively. The gray area also shows the orientation of the images on the detector (images of VY CMa with the diffraction patterns of the M2 support structure; see Fig. 6.4, left) and the handedness of the circular polarization (right-handed or left-handed) corresponding to these measurements. Image adapted from Fig. 2.2.

and I_U-images from the double sum as:

$$I_Q = \frac{1}{2}\left(I_{Q^+} + I_{Q^-}\right), \tag{6.5}$$

$$I_U = \frac{1}{2}\left(I_{U^+} + I_{U^-}\right). \tag{6.6}$$

The polarimetric measurements with IRDIS are affected by the instrumental polarization effects of the optical components, which, as discussed in Chapter 2, consist of instrumental polarization (IP) and polarimetric crosstalk. IP is the polarization signal produced by the optical components and can make unpolarized sources appear to be polarized. For a single component, IP is a linear-polarization signal created by that component's diattenuation ϵ, that is, the difference between the reflectances or transmittances of the orthogonal linearly polarized components of the light. Crosstalk is the mixing of polarization states induced by the optical components. The crosstalk of a single component converts (part of the) incident linear polarization into circular polarization and vice versa. This crosstalk is produced by the component's retardance Δ, that is, the induced relative phase shift of the orthogonal linearly polarized components of the light. By computing the double difference (Eqs. (6.3) and (6.4)), the IP produced by the non-rotating components downstream of the HWP is removed because this IP manifests itself as transmission differences between the two beams falling on the detector. In addition, the double difference suppresses flat-field errors and uncorrected bad pixels (see e.g., Canovas et al., 2011). The crosstalk as well as the IP created by the UT and M4, which are located upstream of the HWP, need to be corrected for during the data reduction using the Mueller matrix model as implemented in IRDAP.

Even though the instrumental polarization effects can be corrected for in the data reduction, the crosstalk produced by the derotator can still significantly lower the attainable signal-to-noise ratio of field-tracking observations. From the Mueller matrix model of Chapter 2, we know that the derotator has a retardance of $\Delta_{\text{der}} = 99.32 \pm 0.06°$ in H-band and $\Delta_{\text{der}} = 84.13 \pm 0.05°$ in K_s-band, close to the 90° retardance of an ideal quarter-wave plate. This means that in these filters the derotator induces a nearly 90° relative phase shift between linearly polarized components incident parallel and perpendicular to the derotator's plane of incidence. In other words, the derotator can produce very strong linear-to-circular and circular-to-linear polarimetric crosstalk. For linear-polarization measurements, this crosstalk is no problem when θ_{der} is close to 0°, 90°, 180°, or 270°, that is, when the plane of incidence of the derotator is oriented nearly horizontal or vertical. However, when θ_{der} is close to 45°, 135°, 225°, or 315°, the derotator converts a large fraction of the incident linear polarization into circular polarization that cannot be distinguished with the linear polarizers of IRDIS. This results in a significant loss of polarimetric signal and therefore a large decrease of polarimetric efficiency, that is, the fraction of the linear polarization incident on the telescope that is actually measured. To ensure a high polarimetric efficiency, the derotator angle can be manually offset (i.e., by setting $\eta \neq 0°$ in Eq. (6.1)) such that θ_{der} is close to 0°, 90°, 180°, or 270° at the time of the observations (de Boer et al., 2020).

6.2.2 Observing scheme for measuring circular polarization

In our observing scheme to measure circular polarization, we turn the nearly quarter-wave retardance of the derotator in the H- and K_s-bands to our advantage by using the derotator as polarization modulator. A schematic depiction of the observing scheme is included in Fig. 6.1. We employ the field-tracking mode and take two measurements for which we deliberately offset $\theta_{\rm der}$ to values close to 45° and 135°. At these angles, the derotator converts almost all incident circular polarization into vertically and horizontally oriented linear polarization that can then be distinguished with IRDIS' linear polarizers.

In the data reduction, we subtract for each of the two measurements the right image from the left image to obtain the single-difference V^+- and V^--images, respectively. Contrary to the linear-polarization Q^+-, Q^--, U^+-, and U^--images, the different derotator angles used for the V^+- and V^--images result in the images being rotated approximately 180° with respect to each other (see Fig. 6.1). We therefore derotate (e.g., using spline interpolation) the V^+- and V^--images and use the resulting images to compute the image of Stokes V from the double difference as:

$$V = \frac{1}{2}\left(V^+ - V^-\right). \tag{6.7}$$

We also add the left and right images of the two measurements to obtain the single-sum I_{V^+}- and I_{V^-}-images. Similarly to the V^+- and V^--images, we first derotate the I_{V^+}- and I_{V^-}-images after which we compute the total-intensity I_V-image from the double sum as:

$$I_V = \frac{1}{2}\left(I_{V^+} + I_{V^-}\right). \tag{6.8}$$

Because the polarization state of the light is encoded in the positive and negative signals of the V^+- and V^--images, the derotation of these images does not alter the polarization information contained in them. Therefore, the overall IP created downstream of the HWP is still removed when computing the double difference. However, contrary to the linear-polarization measurements, each image point in the left and right images of the V^+- and V^--measurements are recorded on different pixels of the detector. As a result, the double difference does not suppress flat-field errors, uncorrected bad pixels, and any spatial variations of the IP of the left and right beams incident on the detector. These effects can decrease the attainable polarimetric accuracy when measuring the degree of polarization of point sources at the level of a few tenths of a percent (see Chapter 5). However, the effects are generally small and are therefore not expected to significantly affect measurements of the polarization of bright circumstellar structures or the halo of the central star. After computing the double difference, the measurements of circular polarization are, similar to linear-polarization measurements, still affected by the crosstalk as well as the IP created by the UT and M4. Therefore, also the circular-polarization measurements need to be corrected for the instrumental polarization effects during the data reduction using the Mueller matrix model.

6.3 Test observations of VY CMa

To test our observing scheme, we observed VY CMa, which is one of only a few stars that are visible from the Paranal Observatory and for which circular polarization has previously been detected in H-band (Serkowski, 1973). We performed the observations during the morning twilight on January 13, 2020. We used the H-band filter and the apodized Lyot coronagraph with a mask diameter of 185 mas (Carbillet et al., 2011; Guerri et al., 2011). Because VY CMa has a high brightness (0.44 mag in H-band) we used a neutral-density filter that reduces the flux tenfold. At the start of the observations, we took sky frames to enable the subtraction of the sky background and star-center frames to enable the determination of the position of the star behind the coronagraph. We then performed 12 measurements of circular polarization and four regular measurements of linear polarization. Each of these 16 measurements consisted of 15 integrations (NDIT) of 2 s (DIT) each, summing to a total on-source exposure time of 8 min. The atmospheric conditions were excellent with an average seeing and coherence time of 0.4″ and 6.9 ms, respectively. An overview of the relevant (component) angles of the measurements is shown in Table 6.1.

For both the linear-polarization and circular-polarization measurements we used standard `SPHERE_irdis_dpi_obs` observation templates. We performed the measurements of linear polarization using a single conventional HWP cycle with HWP switch angles equal to 0°, 45°, 22.5°, and 67.5° (setting `SEQ.IRDIS.POL.STOKES` to "QU" in the observation template). To ensure a high (linear) polarimetric efficiency, we used an image position angle offset of $\eta = 249°$ to set $\theta_{\text{der}} \approx 270°$. These linear-polarization measurements are indicated in Table 6.1 as the Q^+-, Q^--, U^+-, and U^--measurements.

For the measurements of circular polarization, we employed a series of templates that each use a partial HWP cycle with HWP switch angles equal to 0° and 45° (setting `SEQ.IRDIS.POL.STOKES` to "Q"). For this series of templates, we alternately used derotator image-position-angle offsets of $\eta = 159°$ and $\eta = 339°$ to obtain measurements with derotator angles $\theta_{\text{der}} \approx 45°$ and $\theta_{\text{der}} \approx 135°$, respectively. These circular-polarization measurements are displayed in Table 6.1 as the V^+- and V^--measurements. From this table, we see that for the same value of η the derotator angle can have two values 180° apart, that is, θ_{der} is sometimes close to 225° instead of 45°, or 315° instead of 135°. This is not a problem because these derotator angles are effectively equivalent and result in the same image orientation and circular-to-linear polarimetric crosstalk. The two possible values of the derotator angle result from the control software choosing the value of n in Eq. (6.1) such that the derotator rotates to the closest angle that gives the desired image orientation. Finally, because the values of θ_{der} are not exactly equal to 45°, 135°, 225°, and 315°, the images of the V^+- and V^--measurements are only approximately 180° rotated with respect to each other.

We note that the HWP, and therefore also switching the HWP, is not necessary for measurements of circular polarization. However, there exists no template for IRDIS' polarimetric mode that allows to remove the HWP or use less than two HWP switch angles. We therefore accept the limitations and in the data reduction simply compute the double-difference V-images from the V^+- and V^--images with the same HWP switch angle.

Table 6.1: Overview of the linear and circular-polarization measurements of VY CMa in H-band.

File	Stokes	η (°)	p (°)	a (°)	θ_{der} (°)	$\theta^{\mathrm{s}}_{\mathrm{HWP}}$ (°)
1	V^-	339	102.9	35.5	135.8	0
2	V^-	339	103.0	35.3	135.6	45
3	V^+	159	103.1	35.0	225.5	0
4	V^+	159	103.1	34.8	225.3	45
5	Q^+	249	103.2	34.6	270.1	0
6	Q^-	249	103.3	34.4	270.0	45
7	U^+	249	103.4	34.2	269.9	22.5
8	U^-	249	103.4	34.0	269.8	67.5
9	V^-	339	103.5	33.7	314.6	0
10	V^-	339	103.6	33.5	314.5	45
11	V^+	159	103.7	33.3	44.3	0
12	V^+	159	103.7	33.1	44.1	45
13	V^-	339	103.8	32.8	134.0	0
14	V^-	339	103.9	32.6	133.8	45
15	V^+	159	104.0	32.3	223.6	0
16	V^+	159	104.1	32.1	223.5	45

Notes. In the header of the table, Stokes shows the single difference Stokes parameter corresponding to the measurement, η is the user-defined image-position-angle offset of the derotator, p is the parallactic angle, a is the telescope altitude angle, θ_{der} is the derotator angle, and $\theta^{\mathrm{s}}_{\mathrm{HWP}}$ is the half-wave plate switch angle.

6.4 Instrumental polarization effects of circular-polarization measurements

To understand the performance of our observing scheme for measuring circular polarization and enable accurate reduction and interpretation of the measurements of VY CMa, we need to investigate how these measurements are affected by instrumental polarization effects. To this end, we use the Mueller matrix model of Chapter 2 to compute the instrumental polarization effects of observations of VY CMa in H-band. Although the exact magnitude of the effects differs for measurements in K_s-band or observations of targets with declinations other than that of VY CMa, the main conclusions we draw in this section remain the same. In Sect. 6.4.1 we outline the Mueller matrix model and the setup of our calculations. Subsequently, we investigate and explain the polarimetric efficiency, IP, and polarimetric crosstalk in Sects. 6.4.2, 6.4.3, and 6.4.4, respectively. Finally, we discuss the effect of the uncertainty of the retardance of the UT and M4 on the instrumental polarization effects in Sect. 6.4.5.

6.4.1 Mueller matrix model and setup of calculations

The Mueller matrix model mathematically describes the instrumental polarization effects of the complete optical system as a function of the parallactic, altitude, HWP, and derotator angles, and is described in detail in Chapter 2. The model uses three principal reference frames: the celestial reference frame, with positive Q aligned with the north-south direction on the sky; the telescope reference frame, which is rotated with respect to the celestial reference frame with the parallactic angle; and the instrument reference frame, which is rotated with respect to the telescope reference frame with the altitude angle and where positive Q is aligned with the vertical direction. The parameters of the model that are most relevant for our discussion are (see Fig. 6.1) the diattenuation of the UT (ϵ_{UT}; which is ideally completely due to M3), the retardances of the UT, M4, the HWP, and the derotator (Δ_{UT}, Δ_{M4}, Δ_{HWP}, and Δ_{der}), and, to a lesser extent, the diattenuations of M4 and the HWP (ϵ_{M4} and ϵ_{HWP}). The retardances of the UT (assumed to be completely due to M3) and M4 have been computed analytically from the Fresnel equations using the complex refractive indices of aluminum retrieved from Rakić et al. (1998); all other model parameters have been experimentally determined from measurements with SPHERE's internal light source and observations of unpolarized stars.

To compute the instrumental polarization effects of measurements of VY CMa, we simulate idealized double-difference measurements for the period of time during which VY CMa is seen above the horizon from the Paranal Observatory. To this end, we first define the Stokes vector describing the polarization state of the light incident on the telescope, that is, we define $\boldsymbol{S}_{\mathrm{in}} = [I_{\mathrm{in}}, Q_{\mathrm{in}}, U_{\mathrm{in}}, V_{\mathrm{in}}]^{\mathrm{T}}$, where I_{in}, Q_{in}, U_{in}, and V_{in} are the incident Stokes parameters in the celestial reference frame. Subsequently, we define a series of points in time and compute for each of them the parallactic angle and altitude angle. For each point in time we also define a pair of V^+- and V^--measurements where we set the derotator angles of all V^+-measurements equal to 45° and those of all V^--measurements equal to 135°. Next, we compute the derotator image-position-angle offsets η to reach those derotator angles from Eq. (6.1). Using the values of η, we then compute the corresponding HWP angles from Eq. (6.2), setting $\gamma = 0°$ and $\theta^{\mathrm{s}}_{\mathrm{HWP}} = 0°$, where the latter corresponds to the V^+- and V^--measurements with odd file numbers in Table 6.1 (the results only differ marginally for $\theta^{\mathrm{s}}_{\mathrm{HWP}} = 45°$). After that, we use the Mueller matrix model to compute for each pair of V^+- and V^--measurements the intensities reaching the left and right sides of the detector. From these intensities, we calculate the double-difference and double-sum intensities, after which we compute the measured normalized Stokes parameter v (i.e., the degree of circular polarization) as the ratio of these two values. For the period that VY CMa is visible, these calculations thus yield a series of values of v, which, for specific incident Stokes vectors, we can interpret as the polarimetric efficiency, IP, and crosstalk.

6.4.2 Polarimetric efficiency

In Sect. 6.2.1 we defined the polarimetric efficiency in terms of linear polarization. For circular-polarization measurements, we adapt the definition and define the polarimetric efficiency as the fraction of the circular polarization incident on the telescope that is actu-

ally measured. To calculate the polarimetric efficiency, we simulate the double-difference measurements for the case of 100% circularly polarized light incident on the telescope, that is, we set $\boldsymbol{S}_{\rm in} = [1, 0, 0, 1]^T$. The polarimetric efficiency is then equal to the values of v resulting from the computations.

The calculated polarimetric efficiency as a function of altitude angle for observations of VY CMa in H-band is shown by the green curve in Fig. 6.2 (top). From this curve, we see that the polarimetric efficiency varies between 94.0% and 99.5%. Because these values are very close to the ideal value of 100%, we conclude that our observing scheme is very efficient at measuring circular polarization. Figure 6.2 (top) also shows the polarimetric efficiency of the six actual circular-polarization measurements of VY CMa (green data points) as computed using the angles from Table 6.1. The small offsets of these data points with respect to the green curve are due to the parallactic and altitude angles not being equal for the actual V^+- and V^--measurements, the derotator angles deviating slightly from their ideal values of 45° (225°) and 135° (315°), and, for half of the measurements, the HWP switch angles being equal to 45° instead of 0°. Finally, we note that in K_s-band the polarimetric efficiency ranges between 97.0% and 98.2% and is therefore slightly higher than in H-band. This is as expected because the retardance of the derotator in K_s-band is closer to 90° than the retardance in H-band.

The polarimetric efficiency is primarily determined by the retardances of the UT, M4, the HWP, and the derotator. Writing out part of the Mueller matrix model, we can summarize the main effect of these retardances as:

$$\begin{aligned} &V_{\rm in} \rightarrow V_{\rm UT} \rightarrow V_{\rm M4} \rightarrow V_{\rm HWP} \rightarrow Q_{\rm der} = \\ &-\cos\Delta_{\rm UT}\cos\Delta_{\rm M4}\cos\Delta_{\rm HWP}\sin\Delta_{\rm der} = 96.6\% \text{ in } H\text{-band}, \end{aligned} \tag{6.9}$$

where the first line of the equation shows the conversions of a Stokes parameter incident on the telescope (in this case $V_{\rm in}$, in the celestial reference frame) into different Stokes parameters downstream of the UT (in the telescope reference frame), M4, the HWP, and the derotator (all in the instrument reference frame). All these Stokes parameters are shown in Fig. 6.1. The retardances of the UT, M4, and the HWP ($\Delta_{\rm UT} = \Delta_{\rm M4} = 175.0°$ and $\Delta_{\rm HWP} = 170.7° \pm 0.1°$ in H-band) are close to the ideal value of 180°. Apart from inducing a change of handedness, these components therefore effectively reflect or transmit the circular polarization incident on the telescope. Contrary to the retardances of the UT, M4, and the HWP, the retardance of the derotator ($\Delta_{\rm der} = 99.32° \pm 0.06°$ in H-band) is close to the 90° of an ideal quarter-wave plate. When placed at an angle of 45° or 135°, the derotator therefore produces strong crosstalk that almost completely converts the circular polarization downstream of the HWP, $V_{\rm HWP}$, into a linear-polarization signal, $Q_{\rm der}$. Because the transmission axes of IRDIS' linear polarizers are aligned with the directions of positive and negative $Q_{\rm der}$, this $Q_{\rm der}$-signal can be distinguished with the polarizers. Whereas for $\theta_{\rm der} = 45°$ (the V^+-measurement) the $Q_{\rm der}$-signal has the opposite sign of $V_{\rm HWP}$, for $\theta_{\rm der} = 135°$ (the V^--measurement) the $Q_{\rm der}$-signal has the same sign. As a result, the single differences computed from the V^+- and V^--measurements have opposite signs, enabling the computation of the final value of Stokes V from the double difference (see Eq. (6.7)).

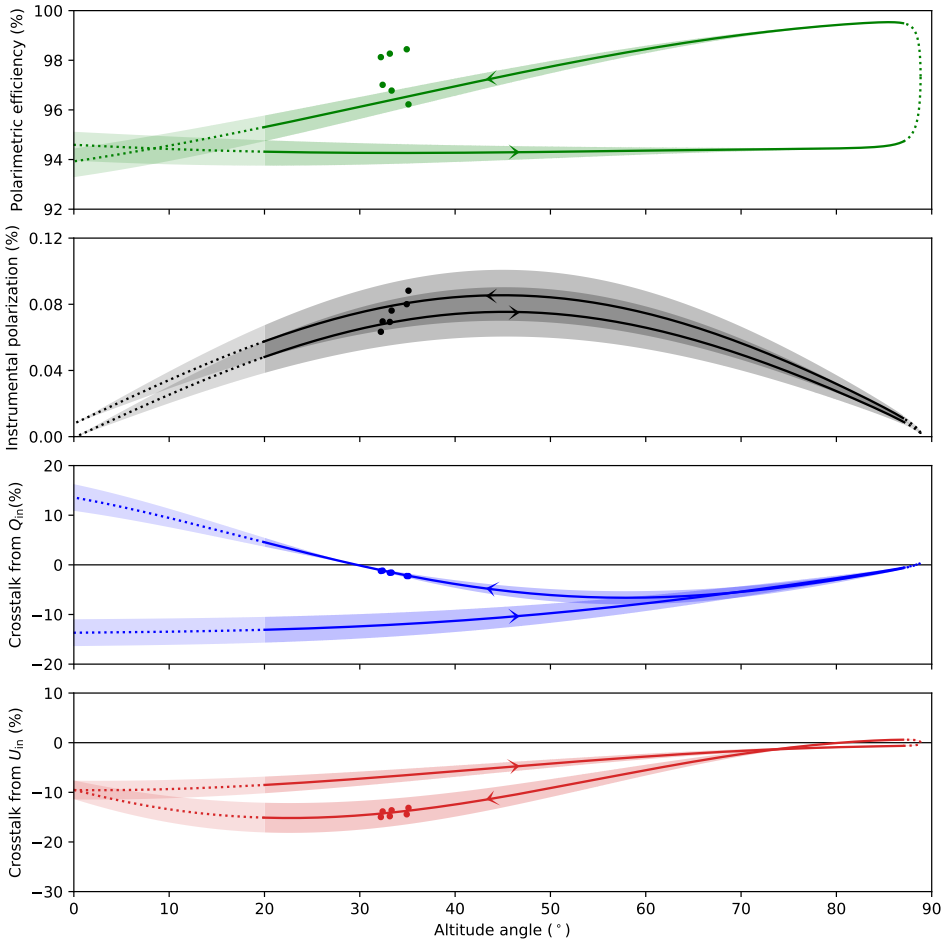


Figure 6.2: Polarimetric efficiency (*top*), instrumental polarization (*second row*), and crosstalk from incident Stokes Q (*third row*) and U (*bottom*) as a function of telescope altitude angle for circular-polarization measurements of VY CMa in H-band as computed from simulations of double-difference measurements with the Mueller matrix model of Chapter 2. The curves show the model values as calculated using ideal values of the parallactic, altitude, HWP, and derotator angles. In these curves, the arrowheads show the direction of increasing time and parallactic angle and the dotted parts indicate altitude angles that cannot actually be reached by the telescope. The data points show the model values of the six actual circular-polarization measurements of VY CMa as computed using the angles from Table 6.1. The data points deviate somewhat from the curves because the observations were performed with slightly different angles than the ideal angles used to compute the curves. The shaded areas indicate the uncertainty of the model values when assuming the retardances of the UT and M4 to have values between 174° and 176°.

The percentage on the right side of Eq. (6.9) is the polarimetric efficiency computed by substituting the H-band values of the model parameters (see Sect. 6.4.1) into the equation. This constant value of 96.6% is approximately equal to the average of the green curve in Fig. 6.2 (top). The small deviations from this value (i.e., those creating the loop in Fig. 6.2, top) are primarily due to the crosstalk of the HWP converting a small part of the incident circular polarization into linear polarization. Depending on the exact HWP angle (which in turn depends on the parallactic and altitude angle via Eqs. (6.1) and (6.2)), a fraction of this linear polarization is transmitted by the derotator (i.e., not converted to circular polarization) and contributes to the $Q_{\rm der}$-signal, thereby adding to the measured value of Stokes V.

6.4.3 Instrumental polarization

IP is the polarization signal produced by the optical components (see Sect. 6.2.1). For circular-polarization measurements, the IP refers specifically to the signal that contributes to the measurement of Stokes V. To compute the IP, we simulate the double-difference measurements for the case of completely unpolarized light incident on the telescope, that is, we set $\boldsymbol{S}_{\rm in} = [1,\ 0,\ 0,\ 0]^{\rm T}$. The IP is then equal to the values of v resulting from the calculations.

The computed IP as a function of altitude angle for observations of VY CMa in H-band is displayed with the black curve in Fig. 6.2 (second row). From the curve, it follows that the IP is (nearly) zero at an altitude angle of 0°, then increases to a maximum value of ∼0.08% at an altitude angle of 45°, and finally decreases toward zero again at an altitude angle of 90°. Compared to the maximum IP of more than 1% for linear-polarization measurements (Chapter 2), this IP is very small. Figure 6.2 (second row) also displays the IP of the six actual circular-polarization measurements of VY CMa (black data points) as calculated using the angles from Table 6.1. Similar to the polarimetric efficiency (see Sect. 6.4.2), the data points deviate somewhat with respect to the black curve because the observations were performed with slightly different angles than the ideal angles used to compute the curve. Finally, we note that in K_s-band the maximum IP is ∼0.04%, only half of that in H-band.

The IP is mainly produced by the combination of the diattenuation of the UT and the retardance of M4. Using the Mueller matrix model, we can write the principal process creating the IP as:

$$\begin{aligned} &I_{\rm in} \rightarrow Q_{\rm UT} \rightarrow V_{\rm M4} \rightarrow V_{\rm HWP} \rightarrow Q_{\rm der} = \\ &-\epsilon_{\rm UT} \sin(2a) \sin \Delta_{\rm M4} \cos \Delta_{\rm HWP} \sin \Delta_{\rm der} = \\ &\sin(2a) \cdot 0.077\% \text{ in } H\text{-band}, \end{aligned} \tag{6.10}$$

where in this case we take the total intensity as the Stokes parameter incident on the telescope. Initially, the diattenuation of the UT ($\epsilon_{\rm UT} = 0.0090 \pm 0.0001$ in H-band) produces a linear IP signal. Subsequently, a small part of this signal is converted into circular polarization by the crosstalk of M4. Besides the retardance of M4, the amount of circular polarization produced depends on the orientation of the linear polarization with respect

to M4, that is, it depends on the orientation of the telescope reference frame with respect to the instrument reference frame as defined by the altitude angle. The resulting circular polarization downstream of M4 is subsequently transmitted by the HWP (including a change of handedness) and converted to a measurable $Q_{\rm der}$-signal by the derotator (see Sect. 6.4.2). Interestingly, whereas for the IP of linear-polarization measurements the diattenuation of M4 ($\epsilon_{\rm M4} = 0.0092 \pm 0.0001$ in H-band) is equally important as the diattenuation of the UT (see Chapter 2), for circular-polarization measurements the diattenuation of M4 does not contribute at all.

The short expression on the right side of Eq. (6.10) is computed by substituting the values of the model parameters in H-band into the equation. This sinusoidal expression agrees well with the black curve in Fig. 6.2 (second row). However, from this figure we also see that for the same altitude angle the IP is slightly different for observations taken before or after passing the local meridian. These differences mainly result from the diattenuation of the HWP ($\epsilon_{\rm HWP} = -0.000297 \pm 7 \cdot 10^{-6}$ in H-band) that produces a small linear-polarization signal. Similar to the process described at the end of Sect. 6.4.2 and depending on the exact HWP angle, a small fraction of this signal is transmitted by the derotator and contributes to the $Q_{\rm der}$-signal, thus ending up in the measured value of Stokes V.

6.4.4 Crosstalk

As discussed in Sect. 6.2.1, polarimetric crosstalk is the mixing of polarization states induced by the optical components. For circular-polarization measurements, we are interested in the crosstalk that causes the linear polarization incident on the telescope to contribute to the measurement of Stokes V. We calculate the crosstalk by simulating the double-difference measurements for the cases of 100% Q- and U-polarized light incident on the telescope, that is, we perform the calculations twice, once with $\boldsymbol{S}_{\rm in} = [1,\ 1,\ 0,\ 0]^{\rm T}$ and once with $\boldsymbol{S}_{\rm in} = [1,\ 0,\ 1,\ 0]^{\rm T}$. In both cases the crosstalk is then equal to the values of v resulting from the computations.

The computed crosstalk for incident Q and U as a function of altitude angle for observations of VY CMa in H-band are shown in Fig. 6.2 (third row and bottom) with the blue and red curves, respectively. From these curves, it follows that the crosstalk is significant and can reach values of up to ∼15% at small altitude angles. At large altitude angles, the crosstalk reduces to a few percent. Figure 6.2 (third row and bottom) also shows the crosstalk of the six actual circular-polarization measurements of VY CMa (blue and red data points, respectively) as computed using the angles from Table 6.1. Similar to the polarimetric efficiency and IP (see Sects. 6.4.2 and 6.4.3), the data points show small deviations with respect to the curves because the angles from the observations are slightly different than the ideal angles used to calculate the curves. Finally, we note that the crosstalk in K_s-band has a maximum of ∼11%, somewhat lower than that in H-band.

The crosstalk is primarily produced by the retardances of the UT and M4. From the Mueller matrix model, we can derive the main process creating crosstalk from incident Q

as:

$$\begin{aligned} &Q_{\rm in}\rightarrow X_{\rm UT}\rightarrow V_{\rm M4}\rightarrow V_{\rm HWP}\rightarrow Q_{\rm der}\approx \\ &\quad[\sin(2p)\sin\Delta_{\rm UT}+\sin(2p-2a)\sin\Delta_{\rm M4}]\cos\Delta_{\rm HWP}\sin\Delta_{\rm der}= \\ &-[\sin(2p)+\sin(2p-2a)]\cdot 8.5\%\text{ in }H\text{-band}, \end{aligned} \tag{6.11}$$

where $X_{\rm UT}$ represents $Q_{\rm UT}$, $U_{\rm UT}$, and $V_{\rm UT}$ and we simplified the expression by assuming $\cos\Delta_{\rm UT}=\cos\Delta_{\rm M4}\approx -1$. Similarly, we can write the main process producing crosstalk from incident U as:

$$\begin{aligned} &U_{\rm in}\rightarrow X_{\rm UT}\rightarrow V_{\rm M4}\rightarrow V_{\rm HWP}\rightarrow Q_{\rm der}\approx \\ &-[\cos(2p)\sin\Delta_{\rm UT}+\cos(2p-2a)\sin\Delta_{\rm M4}]\cos\Delta_{\rm HWP}\sin\Delta_{\rm der}= \\ &\quad[\cos(2p)+\cos(2p-2a)]\cdot 8.5\%\text{ in }H\text{-band}. \end{aligned} \tag{6.12}$$

For both Q incident and U incident, the crosstalk is created following two distinct mechanisms. In the first mechanism, a small part of the incident Q- or U-polarization is converted to circular polarization by the crosstalk of the UT, after which this circular polarization is reflected by M4. In the second mechanism, the incident Q- or U-polarization is reflected by the UT, after which a fraction of the linear polarization is converted into circular polarization by the crosstalk of M4. Apart from the retardances of the UT and M4, the amount of circular polarization created in these two mechanisms depends on the orientation of the linear polarization in the telescope and instrument reference frames, respectively. Therefore, the crosstalk produced depends on the parallactic angle in the first mechanism and on both the parallactic and altitude angle in the second mechanism. In both mechanisms, the circular polarization created is subsequently transmitted by the HWP (including a change of handedness) and converted to a measurable $Q_{\rm der}$-signal by the derotator (see Sect. 6.4.2).

The expressions on the bottom lines of Eqs. (6.11) and (6.12) are calculated by substituting the H-band values of the model parameters into the equations. The two expressions are in good agreement with the blue and red curves in Fig. 6.2 (third row and bottom) and only show very small deviations that do not warrant further discussion. However, it is interesting to note that, even though the retardances of the HWP and the derotator are not ideal, these optical components do not cause additional crosstalk of the incident linear polarization (or the linear IP of the UT and M4) into the measurement of Stokes V. This is because the derotator as well as the HWP (following Eq. (6.2)) rotate 90° between the V^+- and V^--measurements. Due to the 90° rotations, the linear-polarization signals that are transmitted by the HWP-derotator combination and that contribute to the $Q_{\rm der}$-signal have the same sign in the V^+- and V^--measurements. As a result, these signals cancel when computing the double difference.

6.4.5 Effect of uncertainty of retardance of UT and M4

As discussed in Sects. 6.4.2–6.4.4, the polarimetric efficiency, IP, and crosstalk of circular-polarization measurements strongly depend on the retardances of the UT, M4, the HWP,

and the derotator. Of these retardances, the values of $\Delta_{\rm UT}$ and $\Delta_{\rm M4}$ have been computed from the Fresnel equations (see Sect. 6.4.1) and thus can differ significantly from the true values. As a result, the uncertainties of $\Delta_{\rm UT}$ and $\Delta_{\rm M4}$ can significantly decrease the achievable polarimetric accuracy after correcting for the instrumental polarization effects in the data reduction.

To examine the effect of the uncertainty of $\Delta_{\rm UT}$ and $\Delta_{\rm M4}$ on the instrumental polarization effects, we first make an estimate of the range of possible values of $\Delta_{\rm UT}$ and $\Delta_{\rm M4}$. To this end, we retrieve from several sources (Rakić, 1995; Rakić et al., 1998; McPeak et al., 2015; Ordal et al., 1988; Mathewson & Myers, 1971) the complex refractive indices of aluminum for the complete wavelength range of the H-band filter (1480–1770 nm). Assuming $\Delta_{\rm UT} = \Delta_{\rm M4}$, we then use the Fresnel equations to compute the retardance values from these refractive indices. From these calculations, we find $\Delta_{\rm UT}$ and $\Delta_{\rm M4}$ to have minimum and maximum values of approximately 174° and 176°, in agreement with the uncertainty due to the presence of oxide layers on aluminum mirrors (van Harten et al., 2009). Finally, we compute the polarimetric efficiency, IP, and crosstalk for $\Delta_{\rm UT} = \Delta_{\rm M4} = 174°$ and $\Delta_{\rm UT} = \Delta_{\rm M4} = 176°$ by repeating the calculations as described in Sects. 6.4.2–6.4.4 with these retardance values.

The resulting ranges of values for the polarimetric efficiency, IP, and crosstalk are displayed as shaded areas in Fig. 6.2. Figure 6.2 (top and second row) shows that the uncertainties in the polarimetric efficiency and IP are small. On the other hand, we see from Fig. 6.2 (third row and bottom) that the uncertainties in the crosstalk are significant and are largest for the points in time where the crosstalk is largest. Indeed, for the actual observations of VY CMa (data points in Fig. 6.2, third row and bottom) the large crosstalk from incident U (∼14%) is accompanied by an uncertainty of several percent. Whereas such large uncertainties in the crosstalk only marginally affect measurements of linear polarization, these uncertainties are very important for circular-polarization measurements. This is because the linear polarization in protoplanetary disks and the nebulae around evolved stars is expected to be generally much larger than the circular polarization. Therefore, if the value of 175.0° as used for $\Delta_{\rm UT}$ and $\Delta_{\rm M4}$ is slightly different from the true values, the part of the crosstalk that remains uncorrected in the data reduction can create large spurious signals in the images of Stokes V (see Sect. 6.6).

6.5 Data reduction

To reduce observations taken with our new observing scheme, we adapt the `IRDAP`[2] pipeline (version 1.2.3) that uses the Mueller matrix model to correct linear-polarization measurements for the instrumental polarization effects (Chapter 2). The most important adaptations concern the derotation of the images and the correction of the instrumental polarization effects. In this section, we describe the adapted data-reduction pipeline and apply it to the H-band observations of VY CMa.

The preprocessing of the raw files follows the exact same steps as used in the standard IRDAP. For each file, the pipeline subtracts the sky background, performs flat fielding, corrects for bad pixels, mean-combines the individual frames, and extracts the left

[2] https://irdap.readthedocs.io

and right images. Subsequently, it centers the left and right images using the star-center frames. For the observations of VY CMa, we exclude from the preprocessing the first three or four frames of the files that are taken after changing the image-position-angle offset (i.e., files 1, 3, 5, 9, 11, 13, and 15 in Table 6.1) because these frames show significant image smearing. The most likely cause of this smearing is that the rotation axis of the derotator is not exactly aligned with the position of the focal-plane mask of the coronagraph. As a result, the star moves away from the focal-plane mask with each large rotation of the derotator, after which the instrument needs several seconds to translate the image such that the star is placed behind the mask again.

After finishing the preprocessing, the pipeline subtracts the left and right images of each file, which in this case yields the single-difference Q^+-, Q^--, U^+-, U^--, V^+-, and V^--images. In addition, the pipeline adds the left and right images, thus creating the corresponding single-sum I_{Q^+}-, I_{Q^-}-, I_{U^+}-, I_{U^-}-, I_{V^+}-, and I_{V^-}-images. Contrary to the standard IRDAP, the pipeline then identifies the V^+-, V^-, I_{V^+}-, and I_{V^-}-images based on the derotator angle and derotates these images such that they have the same orientation with north upward. Finally, the pipeline computes cubes of double-difference Q-, U-, and V-images from Eqs. (6.3), (6.4), and (6.7) and cubes of double-sum I_Q-, I_U-, and I_V-images from Eqs. (6.5), (6.6), and (6.8).

As the next step, the pipeline uses the Mueller matrix model to correct the data for the instrumental polarization effects and computes the images of the Stokes parameters incident on the telescope. This model correction is very similar to that of the standard IRDAP because the Mueller matrix model simply depends on the (optical component) orientation angles and does not need to distinguish between the linear- and circular-polarization measurements. First, the pipeline subtracts the IP from each double-difference image. To this end, it scales the corresponding double-sum image with the computed IP and subtracts the resulting image from the double-difference image. Subsequently, the pipeline derotates the cubes of IP-subtracted Q- and U-images as well as the cubes of I_Q- and I_U-images such that north is upward (the IP-subtracted V-images and the I_V-images are already derotated). Next, the pipeline sets up a system of equations that describes for each derotated, IP-subtracted double-difference Q-, U-, or V-image the contribution of the crosstalk or transmission from incident Q, U, and V. The pipeline then computes the three images of incident Q, U, and V by solving, for every pixel individually, the system of equations using linear least squares (there are more than three measurements). The standard IRDAP differs from this in that it assumes the incident V to be zero and therefore solves the system of equations only for incident Q and U. Finally, the pipeline computes the three final I_Q-, I_U-, and I_V-images as the means of the cubes of derotated I_Q-, I_U-, and I_V-images, respectively.

From the three I_Q-, I_U-, and I_V-images, the pipeline subsequently computes the final total-intensity image by computing the mean of these images. Using the model-corrected Q- and U-images and following the definitions of de Boer et al. (2020), the pipeline also computes images of Q_ϕ and U_ϕ. In these images, positive and negative Q_ϕ show the linear polarization in the azimuthal and radial directions (i.e., orthogonal and parallel to the direction toward the central star), respectively, and positive and negative U_ϕ show the linear polarization at ±45° from these directions. Finally, the pipeline computes an image

of the linearly polarized intensity, $PI_{\rm L}$, as:

$$PI_{\rm L} = \sqrt{Q^2 + U^2}, \tag{6.13}$$

and an image of the angle of linear polarization, χ, as:

$$\chi = \frac{1}{2} \arctan\left(\frac{U}{Q}\right). \tag{6.14}$$

The final polarization images contain halos of polarized starlight that originate from interstellar dust and/or spatially unresolved circumstellar material located close to the star. In Fig. 6.3, which shows the central part of the linearly polarized intensity image of VY CMa, the halo is primarily visible as a star-centered ring (the adaptive-optics residuals) and four lines emanating from the center of the image (the diffraction patterns of the M2 support structure). With the pipeline we can determine the stellar polarization from the I_Q-, I_U-, I_V-, and model-corrected Q-, U-, and V-images by summing the flux in these images in a region that only contains light from the stellar halo and no signal from spatially resolved circumstellar material. From the summed fluxes, the pipeline then computes the normalized Stokes parameters of the stellar polarization as $q = Q/I_Q$, $u = U/I_U$, and $v = U/I_U$. For the data set of VY CMa, we select the region indicated with the dotted lines in Fig. 6.3. The measured values of q, u, and v do not significantly change when varying the size of the selected region, suggesting that the region indeed does not contain signal from circumstellar material. Subsequently, the pipeline determines the uncertainty of the measured stellar polarization. For the measurement of v, the pipeline solves the system of equations describing the crosstalk for each V-measurement separately, measures the stellar polarization from the resulting images, and computes the standard error of the mean over the measured values. Because we have taken only one HWP cycle to measure Q and U, the pipeline computes the uncertainty of q and u as the accuracy of the Mueller matrix model with which the data is corrected (see Chapter 2).

Finally, the pipeline creates an additional set of images with the stellar polarization subtracted by scaling the I_Q-, I_U-, and I_V-images with the measured stellar q, u, and v and subtracting the resulting images from the model-corrected Q-, U-, and V-images. In the remainder of this chapter we only consider the images with the stellar polarization subtracted. The final images of the total intensity as well as of the linearly polarized intensity and angle of linear polarization of VY CMa in H-band are shown in Fig. 6.4. In addition, the final Q-, U-, Q_ϕ−, and U_ϕ-images are shown in Fig. 6.8. Because the star-centered ring of the adaptive-optics residuals is not visible in the polarization images, we conclude that the stellar polarization is overall well subtracted. Indeed, when subtracting polarization signals that are slightly larger or smaller than the measured stellar q, u, and v, the ring of the adaptive-optics residuals becomes visible in the images with overall positive or negative signal. Still, spurious signals due to diffraction by the M2 support structure, the spiders of the coronagraph Lyot stop, and defective actuators of the deformable mirror of the adaptive-optics system (Cantalloube et al., 2019) remain (slightly) visible in the polarization images, but this is because the diffraction features produced by these components rotate during observations in field-tracking mode.

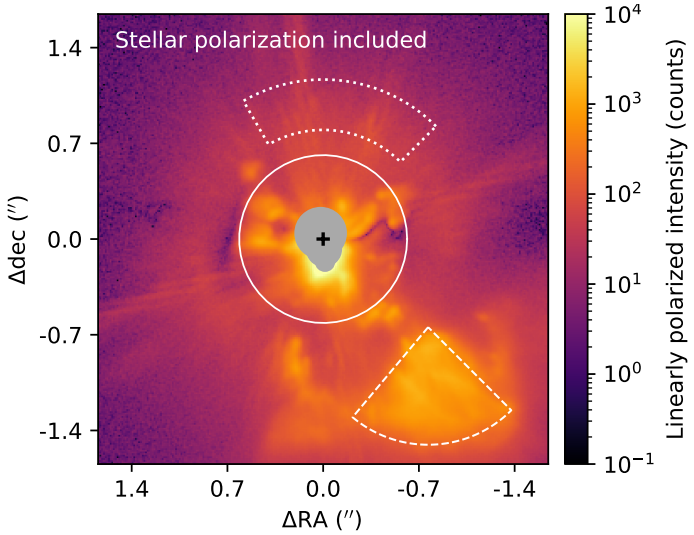


Figure 6.3: Central part of the linearly polarized intensity image of VY CMa in *H*-band before subtracting the stellar polarization. The three white shapes indicate the region used to measure the stellar polarization (dotted lines, Sect. 6.5) and the regions we denote the inner structure (solid line) and the southwest (SW) clump (dashed lines, Sect. 6.6). The position of the star is marked with the black plus sign. The gray area around this plus sign masks the region that is obscured by the focal-plane mask of the coronagraph and that contains saturated pixels and pixels with values in the nonlinear regime of the detector.

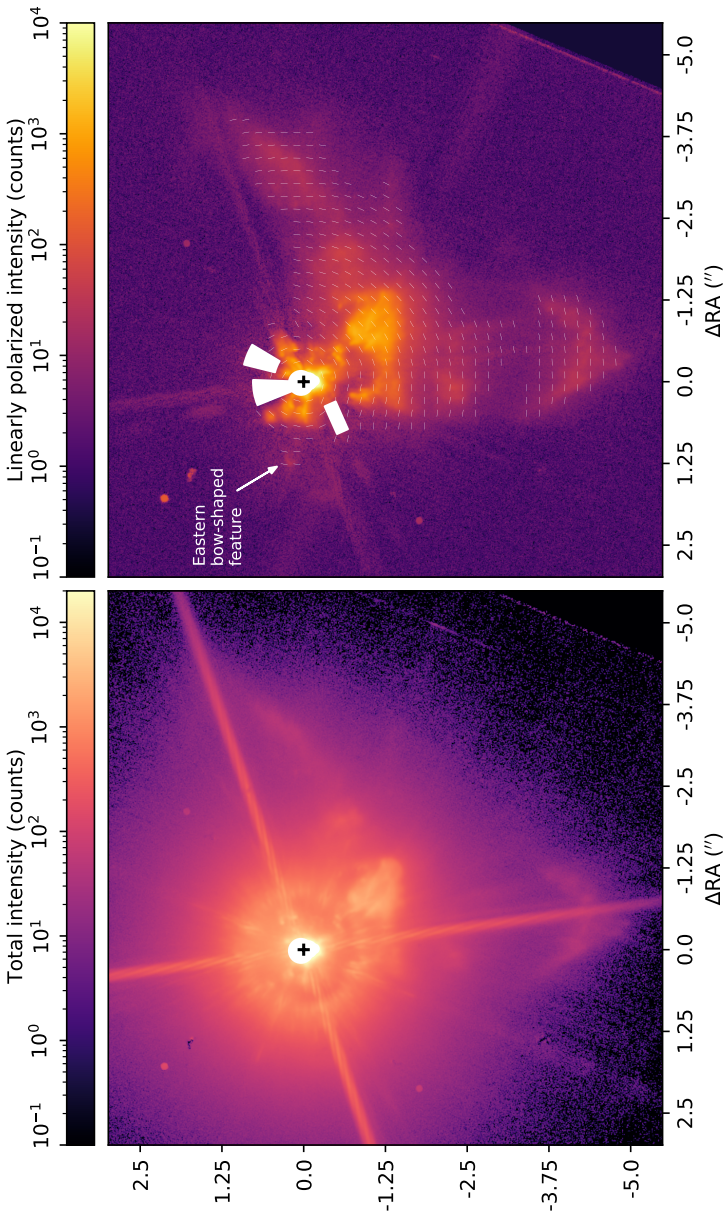


Figure 6.4: Images of the total intensity (*left*) as well as the linearly polarized intensity and angle of linear polarization after subtracting the stellar polarization (*right*) of VY CMa in *H*-band. The angle of linear polarization is indicated by white lines of arbitrary and constant length and is only shown where the average linearly polarized intensity in bins of 16×16 pixels is larger than 5 counts. The position of the star is marked with the black plus signs. The white areas around these plus signs mask the region that is obscured by the focal-plane mask of the coronagraph and that contains saturated pixels and pixels with values in the nonlinear regime of the detector. In the linearly polarized intensity image, several bright spurious features due to diffraction by the M2 support structure, Lyot stop, and deformable mirror are masked as well.

6.6 Calibration of crosstalk from data of VY CMa

As discussed in Sect. 6.4.5, the retardances of the UT and M4, $\Delta_{\rm UT}$ and $\Delta_{\rm M4}$, are relatively uncertain and therefore cause large uncertainties in the polarimetric crosstalk of circular-polarization measurements. As a result, it is not unlikely that part of the crosstalk from incident linear polarization remains uncorrected after the data reduction, thereby creating spurious signals in the image of Stokes V. In Sect. 6.6.1, we investigate whether the model-corrected V-image of VY CMa in H-band contains spurious signals. Subsequently, in Sect. 6.6.2, we use the data itself to constrain the H-band values of $\Delta_{\rm UT}$ and $\Delta_{\rm M4}$ that result in the best correction of the crosstalk.

6.6.1 Identification of spurious signals due to uncorrected crosstalk

To determine whether a model-corrected V-image contains spurious signals, we can examine the variation of the V-signals with time and position in the image. Whereas spurious V-signals vary with the parallactic and altitude angle as well as with the spatial distribution of incident Q- and U-signals (see Eqs. (6.11) and (6.12)), real incident V-signals are independent of these variables. Because the observations of VY CMa have very little variation in the parallactic and altitude angle (see Table 6.1), we need to rely on the spatial distribution of the incident Q- and U-signals (see Fig. 6.8, top) for the identification of spurious signals.

We can write the dependence of the spurious V-signals on the incident Q- and U-signals as:

$$V_{\rm CT} = (Q{\rightarrow}V) \cdot Q_{\rm in} + (U{\rightarrow}V) \cdot U_{\rm in}, \tag{6.15}$$

where $V_{\rm CT}$ is the spurious V-signal due to uncorrected crosstalk and $(Q{\rightarrow}V)$ and $(U{\rightarrow}V)$ are the parts of the crosstalk that remain uncorrected after the data reduction. We can rewrite Eq. (6.15) in terms of the linearly polarized intensity $PI_{\rm L}$ (Eq. (6.13)) and the angle of linear polarization χ (Eq. (6.14)). Substituting $Q_{\rm in} = PI_{\rm L}\cos(2\chi)$ and $U_{\rm in} = PI_{\rm L}\sin(2\chi)$ into Eq. (6.15) and rearranging, we obtain:

$$\frac{V_{\rm CT}}{PI_{\rm L}} = (Q{\rightarrow}V) \cdot \cos(2\chi) + (U{\rightarrow}V) \cdot \sin(2\chi). \tag{6.16}$$

This equation shows that when we compute an image of the ratio of Stokes V to the linearly polarized intensity, $V/PI_{\rm L}$, we can identify spurious signals from their variation with the angle of linear polarization. Figure 6.2 (third row and bottom) shows that for the observations of VY CMa the uncertainty of the crosstalk from incident U is much larger than that of the crosstalk from incident Q. As a result, the effect of $(U{\rightarrow}V)$ dominates over that of $(Q{\rightarrow}V)$ and we expect $V/PI_{\rm L}$ to vary with approximately $\sin(2\chi)$ if the V-signal is caused by uncorrected crosstalk. We should be able to identify such a sinusoidal signal in the data of VY CMa because in Fig. 6.4 (right) the angle of linear polarization covers the full range from 0° to 180°. Finally, we expect any spurious signal in the $V/PI_{\rm L}$-image to resemble a scaled version of the U-image (see Fig. 6.8, top right), either with the same or the opposite sign (see Eq. (6.15)).

To demonstrate that we can truly identify spurious V-signals from $V/PI_{\rm L}$-images, we repeat the data reduction as described in Sect. 6.5, but this time we set $\Delta_{\rm UT}$ and $\Delta_{\rm M4}$ to

the ideal value of 180° in the Mueller matrix model. In this way, the model-corrected V-image is not corrected for the crosstalk of the UT and M4 and therefore certainly contains spurious signal. After performing the data reduction, we bin the resulting V-, $PI_{\rm L}$-, and χ-images in bins of 2×2 pixels and compute the image of $V/PI_{\rm L}$. Subsequently, we create a scatter plot of the bins of $V/PI_{\rm L}$ as a function of χ. Because the ratio $V/PI_{\rm L}$ can become very noisy, we use only those bins for which both V and $PI_{\rm L}$ exceed 10 counts and for which $-0.5 \leq V/PI_{\rm L} \leq 0.5$. The resulting scatter plot and $V/PI_{\rm L}$-image are shown in Fig. 6.5 (top). The scatter plot exhibits a sinusoidal pattern and the $V/PI_{\rm L}$-image resembles the U-image of Fig. 6.8 (top right) with opposite sign. We therefore conclude that for the reduction with $\Delta_{\rm UT} = \Delta_{\rm M4} = 180°$ the V-signal is spurious, as expected.

Finally, we investigate whether the V-image of the original reduction of Sect. 6.5, with $\Delta_{\rm UT} = \Delta_{\rm M4} = 175.0°$, contains spurious signals. To this end, we perform the same analysis and show the results in Fig. 6.5 (center). In this case, the scatter plot exhibits only a slight hint of a sinusoidal pattern. However, the $V/PI_{\rm L}$-image quite clearly resembles the U-image of Fig. 6.8 (top right), although with much lower values of $V/PI_{\rm L}$ than in Fig. 6.5 (top). We thus conclude that the images of the original reduction contain some spurious signals due to uncorrected crosstalk, although much less than the images of the reduction with $\Delta_{\rm UT} = \Delta_{\rm M4} = 180.0°$.

6.6.2 Constraining retardance of UT and M4 from data

If we would reduce the data of VY CMa with the true values of $\Delta_{\rm UT}$ and $\Delta_{\rm M4}$, the $V/PI_{\rm L}$-image should ideally only show the real incident V-signal (if present) and no signals resembling the U-image of Fig. 6.8 (top right). To constrain the true value of $\Delta_{\rm UT}$ and $\Delta_{\rm M4}$ in H-band, we perform a series of data reductions in which we vary $\Delta_{\rm UT}$ and $\Delta_{\rm M4}$ from 170° to 180° in steps of 0.1°. In these reductions, we assume that $\Delta_{\rm UT} = \Delta_{\rm M4}$ because the observations of VY CMa do not have sufficient variation in parallactic and altitude angle to distinguish the two retardances. However, it is not unlikely that $\Delta_{\rm UT}$ and $\Delta_{\rm M4}$ are truly (nearly) equal because the measured diattenuations of the UT and M4 in H-band are very similar (see Sect. 6.4.3). After performing all the reductions, we compute the $V/PI_{\rm L}$-images and identify by eye the reductions with the least spurious signal.

A gallery of $V/PI_{\rm L}$-images for retardances between 170.5° and 180° in steps of 0.5° is shown in Fig. 6.9. Most images in this figure resemble a scaled version of the U-image of Fig. 6.8 (top right) and thus contain spurious signal. For retardances from 170.5° to 172.5°, the spurious signals have the same sign as the U-image, whereas for retardances from 174.5° to 180° the sign is opposite. Because the sign of the crosstalk from incident U is negative (see Fig. 6.2, bottom), the crosstalk is overcorrected for retardances from 170.5° to 172.5° and undercorrected for retardances from 174.5° to 180°. For retardances between 172.5° and 174.5°, the images in Fig. 6.9 exhibit less resemblance to the U-image and thus contain little spurious signal. The true H-band value of $\Delta_{\rm UT}$ and $\Delta_{\rm M4}$ therefore most likely lies between 172.5° and 174.5°.

To more quantitatively constrain the true value of $\Delta_{\rm UT}$ and $\Delta_{\rm M4}$, we compute for each reduction over some specified region the sum of squared normalized Stokes v-signal, which we denote $|v|^2$. For the computation of $|v|^2$, we first square the I_V- and model-corrected V-images. Subsequently, we sum the flux over the specified region in the re-

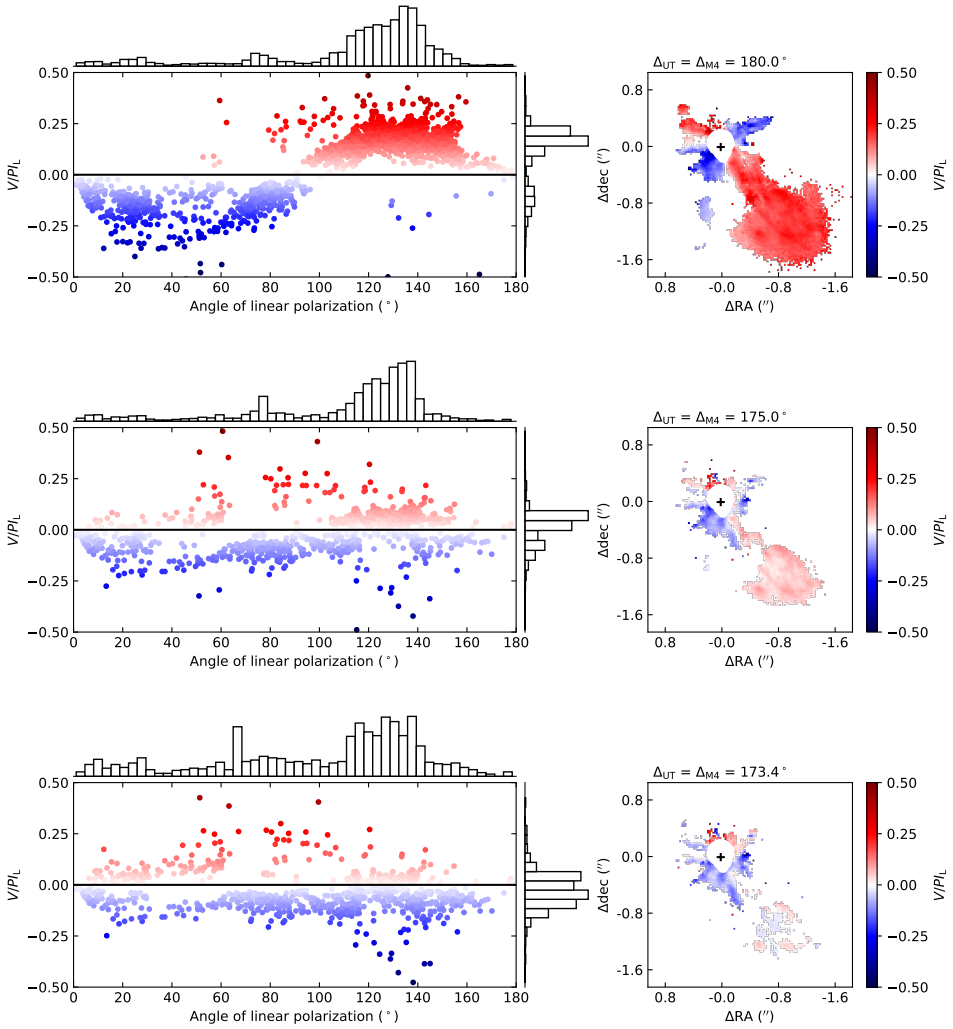


Figure 6.5: Scatter plots of the ratio of circular polarization to linearly polarized intensity $V/PI_{\rm L}$ as a function of angle of linear polarization χ (*left column*) and the corresponding images of $V/PI_{\rm L}$ (*right column*) for reductions of the H-band data of VY CMa using retardances of both the UT and M4 equal to 180° (*top*), 175° (*center*) and 173.4° (*bottom*). The data points in the scatter plots correspond to bins of 2×2 pixels in the images for which both V and $PI_{\rm L}$ exceed 10 counts and for which $-0.5 \leq V/PI_{\rm L} \leq 0.5$. The histograms on the top and right sides of the scatter plots show the distributions of the data points as a function of χ and $V/PI_{\rm L}$. The position of the star is marked with the black plus signs in the images. The white areas around these plus signs mask the region that is obscured by the focal-plane mask of the coronagraph and that contains saturated pixels and pixels with values in the nonlinear regime of the detector.

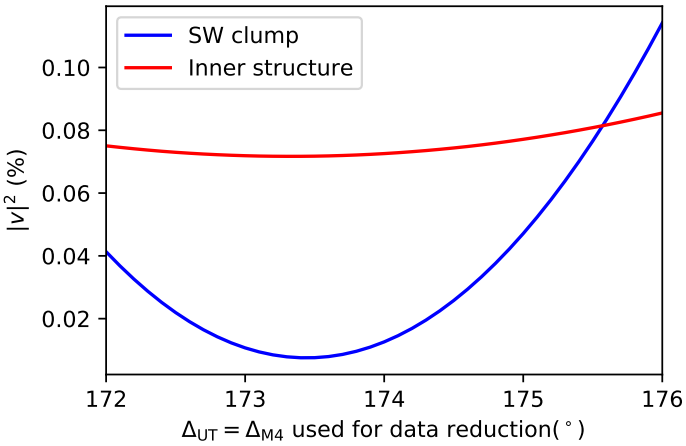


Figure 6.6: Sum of squared normalized Stokes v-signal, $|v|^2$, computed over the southwest (SW) clump and the inner structure as a function of the retardance of the UT and M4 used in the data reduction. The regions we denote the SW clump and inner structure are shown in Fig. 6.3.

sulting V^2- and I_V^2-images and compute $|v|^2$ as the ratio of the summed fluxes. The value of $|v|^2$ thus quantifies the total amount of (positive and negative) circular-polarization signal present in the specified region. We compute $|v|^2$ over the two brightest regions of the nebula of VY CMa that we resolve: the inner structure of circumstellar material close to the star and the clump to the southwest (SW) of star. These regions, which we denote the inner structure and the SW clump, are indicated in Fig. 6.3.

The $|v|^2$-values of the inner structure and the SW clump for reductions with retardances between 172° and 176° are shown in Fig. 6.6. From this figure, we see that the $|v|^2$-values of both regions reach a minimum for the reduction with $\Delta_{UT} = \Delta_{M4} = 173.4°$, suggesting that with this retardance the crosstalk is best corrected. The scatter plot and V/PI_L-image for the reduction with $\Delta_{UT} = \Delta_{M4} = 173.4°$ are shown in Fig. 6.5 (bottom). From this figure, the crosstalk indeed seems to be well corrected because the scatter plot does not exhibit a sinusoidal pattern and the V/PI_L-image shows only a slight resemblance to the U-image. However, significant signal is still visible close to the star, which is also reflected by the nonzero minimum of $|v|^2$ for the inner structure in Fig. 6.6. A large fraction of this signal is most likely spurious in nature and results from imperfect centering of the star behind the focal-plane mask of the coronagraph in combination with the rotations of the images; the diffraction patterns of the M2 support structure, Lyot stop, and deformable mirror; imperfect relative centering of the left and right images; the speckle field changing in time; and image motion during the observations. Such spurious structures are also consistently visible in images of regular linear-polarization measurements (see e.g., Chapter 4). Contrary to the inner structure, the SW clump contains only very small positive and negative signals in the V/PI_L-image of Fig. 6.5 (bottom). These signals almost completely cancel each other out, resulting in a nearly zero minimum of $|v|^2$ for the SW clump in Fig 6.6. This very low minimum may suggest that the crosstalk is almost completely

corrected. However, the range of angles of linear polarization in the SW clump is limited (see Fig. 6.4, right) and so the U-signal is locally very uniform (see Fig. 6.8, top right). Therefore, we cannot exclude the possibility that a real incident V-signal at the location of the SW clump cancels out a spurious V-signal due to uncorrected crosstalk from incident U. It is unfortunate that the only sufficiently bright region at a large separation from the star has a strong U-signal and that we took the observations at a time when the uncertainty in crosstalk from incident U is large. We conclude that we cannot be completely certain that for $\Delta_{\mathrm{UT}} = \Delta_{\mathrm{M4}} = 173.4°$ the crosstalk is best corrected. Nevertheless, under the assumption that there is no real incident V-signal in the SW clump, we conclude that the most likely value of Δ_{UT} and Δ_{M4} in H-band is 173.4°.

6.7 Linear and circular polarization of VY CMa and its nebula

Now that we have determined the more accurate value of 173.4° for Δ_{UT} and Δ_{M4} in H-band, we perform a final reduction of our measurements of VY CMa using this value. Whereas for this final reduction the image of Stokes V differs from the image obtained in the original reduction (see Sect. 6.6), the linear-polarization images exhibit no significant differences. In this section, we present and briefly discuss the resulting images and measurements. Our measurements, especially when combined with the polarimetric images in V- and I-band from Scicluna et al. (2015), can in principle be used for a detailed quantitative study of grain-size distributions, optical depths, and scattering geometries, but we consider such a detailed analysis beyond the scope of this chapter. In Sect. 6.7.1, we analyze the measured linear and circular stellar polarization and compare these measurements to measurements of VY CMa from the literature. Subsequently, in Sect. 6.7.2, we examine the spatially resolved linear and circular polarization of the nebula of VY CMa.

6.7.1 Spatially unresolved stellar polarization

As discussed in Sect. 6.5, we have measured the stellar polarization of VY CMa, expressed in terms of the normalized Stokes parameters q, u, and v, from the halo of polarized starlight visible in the final images. For the linear polarization of the star, we measure $q = -3.99 \pm 0.05\%$ and $u = 0.80 \pm 0.04\%$. These values translate to a degree of linear polarization, $P_{\mathrm{L}} = \sqrt{(q^2 + u^2)}$, equal to $P_{\mathrm{L}} = 4.07 \pm 0.05\%$ and an angle of linear polarization (see Eq. (6.14)) of $\chi = 84.3 \pm 0.3°$, where we have propagated the uncertainties using a Monte Carlo calculation and assuming Gaussian statistics. For the circular polarization, we measure $v = 0.14 \pm 0.04\%$, corresponding to right-handed circular polarization in our definitions (see Sect. 6.2). We also measure the stellar q, u, and v from reductions with Δ_{UT} and Δ_{M4} ranging from 172.5° to 174.5° and find that the variations in the measured normalized Stokes parameters are within the quoted uncertainties. This is also the case for the measurement of v because the starlight is predominantly polarized in q and the uncertainty of the crosstalk from incident Q is very small at the time of the observations (see Fig. 6.2, third row).

The measurements of the stellar q and u can contain a contribution from interstellar polarization. This interstellar polarization is almost exclusively linear and results from dichroic absorption (diattenuation) by elongated dust grains that are aligned with the magnetic field in the interstellar medium. To estimate the interstellar polarization, we compare our measurements to the known linear polarization of HD 58011, a background star located 15′ from VY CMa at a distance of ∼4 kpc (Bailer-Jones et al., 2018). From the catalog by Klare et al. (1972), we find that HD 58011 has a degree of linear polarization of $P_{\rm L} = 0.36 \pm 0.05\%$ in the spectral range from approximately 370 to 490 nm. We convert this degree of linear polarization to H-band using Serkowski's law of interstellar polarization (Serkowski et al., 1975; Whittet et al., 1992). Assuming that the degree of linear polarization is maximum at a wavelength of 590 nm, which is the average value for the 105 stars observed by Whittet et al. (1992), we find a degree of linear polarization of ∼0.1% in H-band. This degree of linear polarization of ∼0.1% for the interstellar polarization is negligible compared to the stellar q and u that we measure. We therefore conclude that the measured linear polarization of VY CMa, as well as the circular polarization, most likely originate from spatially unresolved circumstellar material located close to the star.

From aperture-masking interferometry with the 10-m Keck telescope, Monnier et al. (1999) show that the NIR flux within 0.1″ around VY CMa is dominated by an asymmetric structure with a projected major axis of ∼170° (east of north) located south of the star. Assuming single scattering only, such a structure would create an integrated polarization signal with an angle of linear polarization of ∼80°, in close agreement with our measured $\chi = 84.3 \pm 0.3°$. Because we also detect circular polarization, this inner circumstellar material likely causes some multiple scattering due to being optically thick and/or contains magnetically aligned dust grains. The latter is plausible because there is observational evidence for a magnetic field throughout the nebula of VY CMa (Humphreys et al., 2007).

The linear and circular polarization of VY CMa in H-band have been measured before from aperture polarimetry on seeing-limited observations by (among others) Serkowski (1973), Maihara et al. (1976), and Takami et al. (1992). Contrary to our measurements of the stellar polarization, which only contain the contributions from the innermost regions around the star, the measurements from the literature encompass the complete nebula. Before comparing our results with those from the literature, we therefore need to check that the parts of the nebula that are excluded from our measurements of stellar polarization (i.e., the parts we spatially resolve in the images) do not significantly contribute to the measurements from the literature. To this end, we use the IRDIS exposure-time calculator[3] to estimate the peak flux of the non-coronagraphic stellar point-spread function (PSF). Subsequently, we determine the peak fluxes of the SW clump and the non-saturated parts of the inner structure in the total-intensity image (see Fig. 6.4, left). Dividing the resulting values by the peak flux of the star, we find that the SW clump and the inner structure, which are the brightest regions in our images, have contrasts of $\sim 10^{-4}$ and $\sim 4 \cdot 10^{-3}$. We conclude that the circumstellar material we spatially resolve in our images does not significantly contribute to the measurements from the literature and that we can thus compare the measurements.

[3] https://www.eso.org/observing/etc/bin/gen/form?INS.NAME=SPHERE+INS.MODE=IRDIS

From H-band observations of VY CMa, Serkowski (1973) measured $P_L = 5 \pm 0.1\%$ and $\chi = 75°$ for the linear polarization and $v = 0.24 \pm 0.05\%$ (right-handed) for the circular polarization, which both agree reasonably well with our measurements of the stellar polarization. However, similar measurements of the linear polarization by Maihara et al. (1976) and Takami et al. (1992) yielded $P_L = 2.3\%$ and $\chi = 85°$, and $P_L = 8.3\%$ and $\chi = 98°$, respectively. Therefore, the degree of linear polarization, and possibly also the degree of circular polarization, vary significantly over the years (see also Maihara et al., 1976). Such variability has also been detected on shorter time scales by Serkowski (1969), who found that within four months the degree of linear polarization of VY CMa changed approximately 0.5%-point in V-band and 1%-point in B-band. Contrary to the degree of linear polarization, the angle of linear polarization seems to have remained relatively constant over the past 50 years. A possible explanation for these observations is that the overall asymmetric structure in the inner region around VY CMa is quite stable with time (resulting in a more or less constant χ), but that the distribution of scattering material located at even smaller separations from the star exhibits significant variations (causing changes in P_L). Such variations of the innermost scattering material could indicate recent ejections of dust from the star.

6.7.2 Spatially resolved polarization of nebula

The images of the total intensity and linearly polarized intensity of VY CMa in H-band are shown in Fig. 6.4. From IRDIS H-band data taken under similar atmospheric conditions (see Chapter 5), we estimate that our images have a spatial resolution (i.e., a full width at half maximum of the PSF) of ~47 mas, making them the highest-resolution NIR images of VY CMa to date. In the linearly polarized intensity image (Fig. 6.4, right), the asymmetric nebula of VY CMa is clearly visible and many of the well-known features can be discerned (see e.g., Monnier et al., 1999; Smith et al., 2001; Humphreys et al., 2007; Shenoy et al., 2013). To the south of the star, we distinguish the SW clump and the adjacent south knot (both at ~1.3″ from the star), the south arc (2.3″), and the bow-shaped feature known as arc 2 (4.3″). To the west of the star we discern the elongated arc-like feature known as the curved nebulous tail or northwest arc (2.5–4.4″) as well as part of the west arc (2.0″) located between this feature and the SW clump. We also detect the radially oriented northwest knot (0.6″) in the inner structure and the ridge connecting the SW clump and the inner structure. Due to the high spatial resolution, our linearly polarized intensity image shows the substructures within most of these features and reveals so-far-unresolved radial plumes of ejecta (similar to the northwest knot) in the inner structure. We also detect a relatively small and faint bow-shaped feature 1.2″ to the east of the star that has not been previously observed. Finally, we note that most of the observed features are so bright that they are also visible in the total-intensity image (see Fig. 6.4, left), even though this image is strongly contaminated by the ring of the adaptive-optics residuals and the diffraction pattern of the M2 support structure.

In addition to the linearly polarized intensity, Fig. 6.4 (right) displays the angle of linear polarization in the nebula of VY CMa. The angle of linear polarization largely follows a centrosymmetric pattern of azimuthal polarization, in agreement with the polarization maps of VY CMa at visible and NIR wavelengths from Jones et al. (2007), Shenoy et al.

(2015), and Scicluna et al. (2015). The pattern of azimuthal polarization can also be deduced from the Q_ϕ- and U_ϕ-images (see Fig. 6.8, bottom) which show most of the flux as positive Q_ϕ-signal. The predominantly azimuthal polarization is indicative of single scattering of the light from the central star and shows that most scattering material is optically thin in H-band.

Figure 6.4 (right) shows that the angle of linear polarization in the inner structure is not azimuthal everywhere. From the U_ϕ-image (see Fig. 6.8, bottom right), it follows that not only the inner structure, but also the SW clump exhibits non-azimuthal linear polarization. However, these U_ϕ-signals are probably artifacts of the finite-sized PSF (see Heikamp & Keller, 2019). In addition, at the smallest separations from the star the measurements may be affected by the spurious signals described in Sect. 6.6.2. Nevertheless, part of the U_ϕ-signals could be due to real non-azimuthal polarization, which would indicate that the circumstellar material in these regions is optically thick in H-band (as already found for the SW clump by Shenoy et al. (2013) and Shenoy et al. (2015)) and therefore scatters part of the light multiple times (see e.g., Canovas et al., 2015). From the region indicated with the dashed lines in Fig. 6.3, and following the same methods as used to determine the stellar polarization and its uncertainty (see Sects. 6.5 and 6.7.1), we find that the SW clump has an integrated degree and angle of linear polarization of $P_\mathrm{L} = 38.5 \pm 0.2\%$ and $\chi = 125.9 \pm 0.1^\circ$ in H-band. Because the degree of linear polarization is relatively large, any depolarization due to multiple scattering is most likely limited in the SW clump (Shenoy et al., 2015). Finally, we note that the images from Scicluna et al. (2015) show much stronger non-azimuthal polarization than Fig. 6.4 (right), but this is because the images from Scicluna et al. (2015) still contain the halo of polarized starlight. Indeed, the regions to the north and east of the star in these images have an angle of linear polarization of ~90°, close to the $\chi = 84.3 \pm 0.3^\circ$ we measured for the stellar polarization (see Sect. 6.7.1).

The final V-image of the central part around VY CMa in H-band as obtained from the reduction with a value of 173.4° for Δ_UT and Δ_M4 is shown in Fig. 6.7. In this image, we see relatively strong signals close to the star (in the inner structure), which, as discussed in Sect. 6.6.2, are most likely spurious in nature. Still, we cannot exclude the possibility that part of the signals are real incident V-signals. Figure 6.7 also shows signals at the position of the SW clump. These signals average to ~0%, which is as expected because we selected the value of Δ_UT and Δ_M4 used for this reduction under the assumption that there is no real incident V-signal in the SW clump (see Sect. 6.6.2). However, we are not certain about the exact value of Δ_UT and Δ_M4 and so the SW clump could in reality be circularly polarized. Using the same method as we used to determine the linear polarization of the SW clump, we find that for the data reductions with Δ_UT and Δ_M4 between 172.5° and 174.5° (the most likely range of values, see Sect. 6.6.2), the integrated normalized Stokes v in the SW clump lies between −1.0% and 1.2%. Overall, we cannot conclusively prove or disprove the presence of real incident V-signal in the spatially resolved parts of the nebula surrounding VY CMa. However, we can conclude that we do not detect the large circular-polarization signals on the order of 10% or more that are frequently found in star-forming regions and that result from magnetically aligned elongated dust grains (e.g., Bailey et al., 1998; Chrysostomou et al., 2000; Ménard et al., 2000; Buschermöhle et al., 2005; Kwon et al., 2013, 2014).

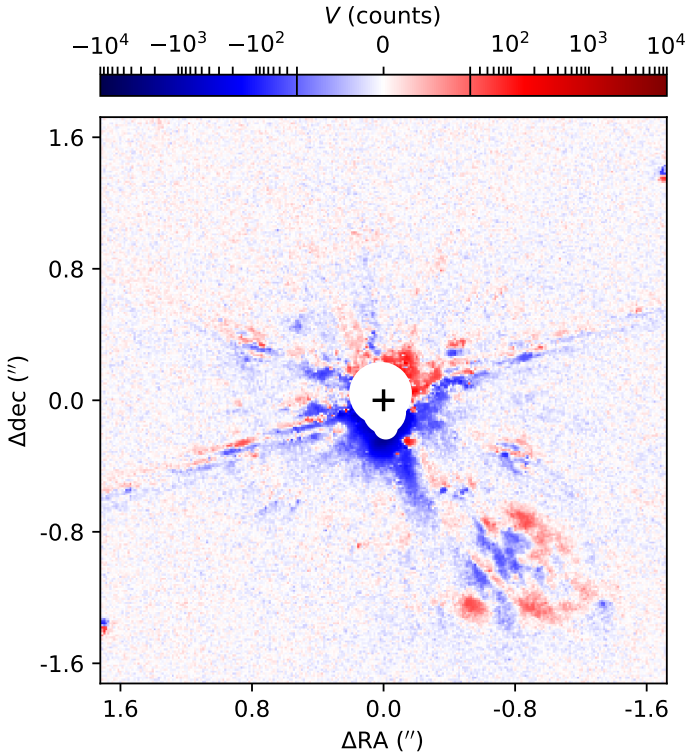


Figure 6.7: Central part of the image of Stokes V of VY CMa in H-band as obtained from the data reduction using a retardance of the UT and M4 equal to 173.4° and after subtracting the stellar polarization. Values smaller than -30 counts or larger than 30 counts are shown on a logarithmic scale, whereas values between -30 and 30 counts are shown on a linear scale. The position of the star is marked with the black plus sign. The white area around this plus sign masks the region that is obscured by the focal-plane mask of the coronagraph and that contains saturated pixels and pixels with values in the nonlinear regime of the detector.

6

6.8 Conclusions

We developed the observing scheme, data-reduction methods, and analysis tools to measure NIR circular polarization at sub-arcsecond resolution with SPHERE-IRDIS at the Very Large Telescope. We use SPHERE's image derotator, which acts as an almost perfect quarter-wave retarder in the H- and K_s-bands, as a polarization modulator to convert incident circular polarization into measurable linear polarization. We tested our observing scheme with linear- and circular-polarization measurements of the red hypergiant VY CMa and its asymmetric nebula in H-band. To reduce the observations, we adapted the IRDAP pipeline that uses the Mueller matrix model of Chapter 2 to correct for instrumental polarization effects.

Using this Mueller matrix model, we investigated the instrumental polarization effects of circular-polarization measurements. For both the H- and K_s-bands, we find that the polarimetric measurement efficiency is close to 100%, that the IP is <0.1%, and that the polarimetric crosstalk from incident linear polarization can reach values of up to ~15%. However, the crosstalk can have an uncertainty of several percent due to uncertainties in $\Delta_{\rm UT}$ and $\Delta_{\rm M4}$, the retardances of the UT and M4. Such large uncertainties in the crosstalk can create large spurious signals in the images after the data reduction. We therefore reduced the test data of VY CMa using a series of values for both $\Delta_{\rm UT}$ and $\Delta_{\rm M4}$ to find the value that minimizes the spurious signals. Assuming that there is no real incident circular polarization in one of the brightest regions of the nebula (the SW clump), the most likely value of $\Delta_{\rm UT}$ and $\Delta_{\rm M4}$ in H-band is 173.4°.

With this new value of $\Delta_{\rm UT}$ and $\Delta_{\rm M4}$, we performed a final reduction of the measurements of VY CMa. We find that the light from the star is polarized with a degree and angle of linear polarization of 4.07 ± 0.05% and 84.3 ± 0.3°, respectively, and a degree of circular polarization of 0.14 ± 0.04% (right-handed) in H-band. These polarization signals most likely originate from a spatially unresolved, asymmetric circumstellar structure located close to the star that is optically thick or contains magnetically aligned dust grains. Variations of the stellar polarization over the past 50 years may indicate recent ejections of dust from the star. From the linearly polarized intensity image, we detect so-far-unresolved radial plumes of ejecta close to the star as well as a faint bow-shaped feature to the east. We also find that the SW clump and the structures close to the star exhibit non-azimuthal linear polarization. However, these non-azimuthal polarization signals are probably artifacts of the finite-sized PSF, although part of the signals could be real and indicate multiple scattering. Finally, due to the uncertainty in $\Delta_{\rm UT}$ and $\Delta_{\rm M4}$, we cannot conclusively prove or disprove the presence of circular polarization in the nebula.

To enable accurate measurements of circular polarization and improve the accuracy of the IRDAP pipeline, we need to determine the true value of $\Delta_{\rm UT}$ and $\Delta_{\rm M4}$. To this end, we plan to observe a large, bright, nearly face-on viewed circumstellar disk (e.g., TW Hya; van Boekel et al., 2017). For such a disk we only expect azimuthally oriented linear polarization and no circular polarization, so that any circular polarization we measure should originate from uncorrected polarimetric crosstalk. We then perform a series of data reductions in which we vary the value of both $\Delta_{\rm UT}$ and $\Delta_{\rm M4}$ and find the value for which the total amount of (positive and negative) circular polarization in the disk (i.e., $|v|^2$) is minimized. Ideally, we would repeat these measurements at different parallactic and altitude angles so that we can fit separate values for $\Delta_{\rm UT}$ and $\Delta_{\rm M4}$. An alternative strategy for determining $\Delta_{\rm UT}$ and $\Delta_{\rm M4}$ would be to perform linear- and circular-polarization measurements of the highly linearly polarized twilight sky, for which the angle of linear polarization can be easily predicted using a single-Rayleigh-scattering model (see e.g., Harrington et al., 2011; de Boer et al., 2014; Harrington et al., 2017).

We stress that any future measurements taken with our observing scheme should also include regular linear-polarization measurements to enable the correction of the polarimetric crosstalk in the final image of Stokes V. We recommend to perform multiple integrations for each individual measurement (i.e., NDIT > 1) so that the frames that are smeared after a change of image-position-angle offset can be discarded without losing all data of a HWP cycle. Finally, we could in principal create an observation template for

circular-polarization measurements in which the HWP is not inserted. However, this is not really necessary because the contribution of the HWP to the polarimetric efficiency, IP, and crosstalk is small and these effects are corrected for in the data reduction.

Our observing scheme enables the first high-contrast, high-spatial-resolution measurements of NIR circular polarization in protoplanetary disks and the nebulae around evolved stars. Circular-polarization measurements can yield strong constraints on the distribution of scattering material, scattering asymmetries, dust properties, and magnetic-field geometries in these systems, and could even shed light on the emergence of homochirality in biomolecules. We plan to observe multiple young stars with bright, complex disks to explore the range of circular-polarization signatures in protoplanetary disks. If these observations are successful, we could add high-quality quarter-wave plates to SPHERE and implement dedicated circular-polarimetric modes for SPHERE-IRDIS at NIR wavelengths and SPHERE-ZIMPOL at visible wavelengths.

6.A Additional figures

Figure 6.8 shows the final images of Q, U, Q_ϕ, and U_ϕ of VY CMa in H-band after subtracting the stellar polarization. In addition, Fig. 6.9 displays images of the ratio of circular polarization to linearly polarized intensity $V/PI_{\rm L}$ for reductions of the H-band data of VY CMa using retardances of both the UT and M4 ranging from 170.5° to 180°.

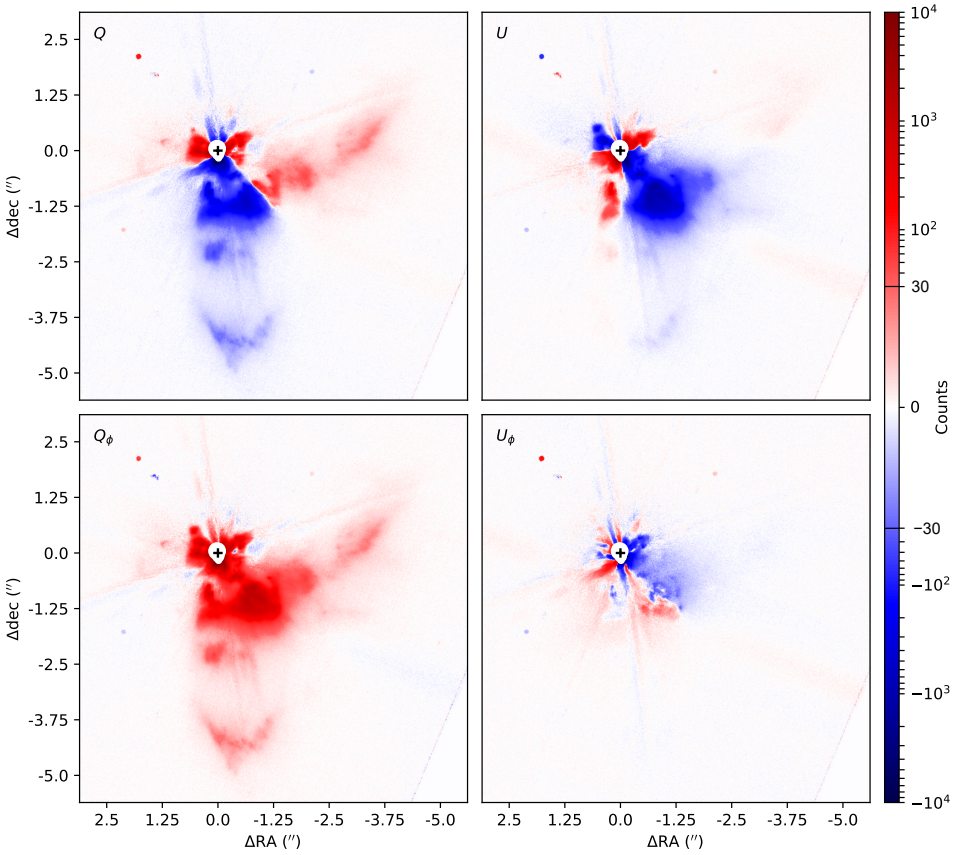


Figure 6.8: Images of Q (*top left*), U (*top right*), Q_ϕ (*bottom left*), and U_ϕ (*bottom right*) of VY CMa in H-band after subtracting the stellar polarization. In all images, values smaller than -30 counts or larger than 30 counts are shown on a logarithmic scale, whereas values between -30 and 30 counts are shown on a linear scale. The position of the star is marked with the black plus signs. The white areas around these plus signs mask the region that is obscured by the focal-plane mask of the coronagraph and that contains saturated pixels and pixels with values in the nonlinear regime of the detector.

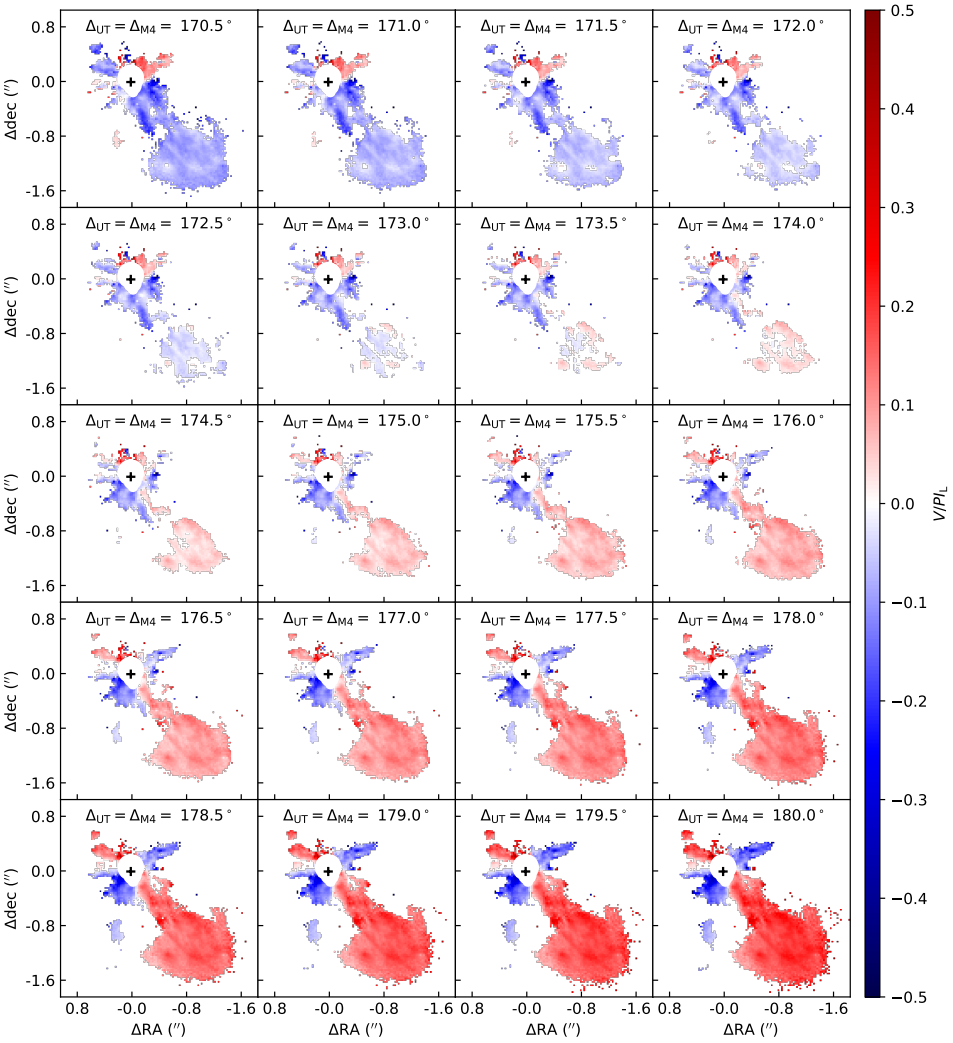


Figure 6.9: Images of the ratio of circular polarization to linearly polarized intensity $V/PI_{\rm L}$ for reductions of the H-band data of VY CMa using retardances of both the UT and M4 ranging from 170.5° to 180° in steps of 0.5°. The images show bins of 2×2 pixels for which both V and $PI_{\rm L}$ exceed 10 counts and for which $-0.5 \leq V/PI_{\rm L} \leq 0.5$. The position of the star is marked with the black plus signs. The white areas around these plus signs mask the region that is obscured by the focal-plane mask of the coronagraph and that contains saturated pixels and pixels with values in the nonlinear regime of the detector.

References

Avenhaus, H., Quanz, S. P., Garufi, A., et al. 2018, Astrophysical Journal, 863, 44
Avnir, D. 2021, New Astronomy Review, 92, 101596
Bailer-Jones, C. A. L., Rybizki, J., Fouesneau, M., Mantelet, G., & Andrae, R. 2018, Astronomical Journal, 156, 58
Bailey, J., Chrysostomou, A., Hough, J. H., et al. 1998, Science, 281, 672
Bastien, P., & Ménard, F. 1990, Astrophysical Journal, 364, 232
Beuzit, J. L., Vigan, A., Mouillet, D., et al. 2019, Astronomy & Astrophysics, 631, A155
Bonner, W. A. 1991, Origins of Life and Evolution of the Biosphere, 21, 59
Buschermöhle, M., Whittet, D. C. B., Chrysostomou, A., et al. 2005, Astrophysical Journal, 624, 821
Canovas, H., Ménard, F., de Boer, J., et al. 2015, Astronomy & Astrophysics, 582, L7
Canovas, H., Rodenhuis, M., Jeffers, S. V., Min, M., & Keller, C. U. 2011, Astronomy & Astrophysics, 531, A102
Cantalloube, F., Dohlen, K., Milli, J., Brandner, W., & Vigan, A. 2019, arXiv preprint arXiv:1907.03624
Carbillet, M., Bendjoya, P., Abe, L., et al. 2011, Experimental Astronomy, 30, 39
Chrysostomou, A., Gledhill, T. M., Ménard, F., et al. 2000, Monthly Notices of the Royal Astronomical Society, 312, 103
Chrysostomou, A., Menard, F., Gledhill, T. M., et al. 1997, Monthly Notices of the Royal Astronomical Society, 285, 750
de Boer, J., Girard, J. H., Mawet, D., et al. 2014, in Society of Photo-Optical Instrumentation Engineers (SPIE) Conference Series, Vol. 9147, Ground-based and Airborne Instrumentation for Astronomy V, 914787
de Boer, J., Langlois, M., van Holstein, R. G., et al. 2020, Astronomy & Astrophysics, 633, A63
Dohlen, K., Langlois, M., Saisse, M., et al. 2008, in Society of Photo-Optical Instrumentation Engineers (SPIE) Conference Series, Vol. 7014, Proceedings of the SPIE, 70143L
Garufi, A., Benisty, M., Stolker, T., et al. 2017, The Messenger, 169, 32
Gehrels, T. 1972, Astrophysical Journal Letters, 173, L23
Ginski, C., Benisty, M., van Holstein, R. G., et al. 2018, Astronomy & Astrophysics, 616, A79
Gledhill, T. M., & McCall, A. 2000, Monthly Notices of the Royal Astronomical Society, 314, 123
Guerri, G., Daban, J.-B., Robbe-Dubois, S., et al. 2011, Experimental Astronomy, 30, 59
Harrington, D. M., Kuhn, J. R., & Ariste, A. L. 2017, Journal of Astronomical Telescopes, Instruments, and Systems, 3, 018001
Harrington, D. M., Kuhn, J. R., & Hall, S. 2011, Publications of the Astronomical Society of the Pacific, 123, 799
Heikamp, S., & Keller, C. 2019, Astronomy & Astrophysics, 627, A156
Hough, J. 2006, Astronomy and Geophysics, 47, 3.31
Humphreys, R. M., Helton, L. A., & Jones, T. J. 2007, Astronomical Journal, 133, 2716
Jones, T. J., Humphreys, R. M., Helton, L. A., Gui, C., & Huang, X. 2007, Astronomical Journal, 133, 2730
Klare, G., Neckel, T., & Schnur, G. 1972, Astronomy & Astrophysics Supplement, 5, 239
Kwon, J., Tamura, M., Lucas, P. W., et al. 2013, Astrophysical Journal Letters, 765, L6
Kwon, J., Tamura, M., Hough, J. H., et al. 2014, Astrophysical Journal Letters, 795, L16
Kwon, J., Nakagawa, T., Tamura, M., et al. 2018, Astronomical Journal, 156, 1
Lucas, P. W., Hough, J. H., Bailey, J., et al. 2005, Origins of Life and Evolution of the Biosphere, 35, 29

Maihara, T., Noguchi, K., Oishi, M., Okuda, H., & Sato, S. 1976, Nature, 259, 465
Mathewson, A., & Myers, H. 1971, Physica Scripta, 4, 291
McPeak, K. M., Jayanti, S. V., Kress, S. J., et al. 2015, ACS photonics, 2, 326
Ménard, F., Chrysostomou, A., Gledhill, T., Hough, J. H., & Bailey, J. 2000, in Astronomical Society of the Pacific Conference Series, Vol. 213, Bioastronomy 99, ed. G. Lemarchand & K. Meech, 355
Modica, P., Meinert, C., de Marcellus, P., et al. 2014, Astrophysical Journal, 788, 79
Monnier, J. D., Tuthill, P. G., Lopez, B., et al. 1999, Astrophysical Journal, 512, 351
Nelson, D. L., Lehninger, A. L., & Cox, M. M. 2008, Lehninger principles of biochemistry (Macmillan)
O'Gorman, E., Vlemmings, W., Richards, A. M. S., et al. 2015, Astronomy & Astrophysics, 573, L1
Ordal, M. A., Bell, R. J., Alexander, R. W., Newquist, L. A., & Querry, M. R. 1988, Applied optics, 27, 1203
Patty, C. L., ten Kate, I. L., Sparks, W. B., & Snik, F. 2018, in Chiral Analysis (Second Edition), second edition edn., ed. P. L. Polavarapu (Elsevier), 29–69
Rakić, A. D. 1995, Applied optics, 34, 4755
Rakić, A. D., Djurišić, A. B., Elazar, J. M., & Majewski, M. L. 1998, Applied Optics, 37, 5271
Scicluna, P., Siebenmorgen, R., Wesson, R., et al. 2015, Astronomy & Astrophysics, 584, L10
Serkowski, K. 1969, Astrophysical Journal Letters, 158, L107
—. 1973, Astrophysical Journal Letters, 179, L101
Serkowski, K., Mathewson, D. S., & Ford, V. L. 1975, Astrophysical Journal, 196, 261
Shafter, A., & Jura, M. 1980, Astronomical Journal, 85, 1513
Shenoy, D. P., Jones, T. J., Packham, C., & Lopez-Rodriguez, E. 2015, Astronomical Journal, 150, 15
Shenoy, D. P., Jones, T. J., Humphreys, R. M., et al. 2013, Astronomical Journal, 146, 90
Smith, N., Hinkle, K. H., & Ryde, N. 2009, Astronomical Journal, 137, 3558
Smith, N., Humphreys, R. M., Davidson, K., et al. 2001, Astronomical Journal, 121, 1111
Takami, H., Shiba, H., Sato, S., Yamashita, T., & Kobayashi, Y. 1992, Publications of the Astronomical Society of the Pacific, 104, 949
van Boekel, R., Henning, T., Menu, J., et al. 2017, Astrophysical Journal, 837, 132
van Harten, G., Snik, F., & Keller, C. 2009, Publications of the Astronomical Society of the Pacific, 121, 377
Whittet, D. C. B., Martin, P. G., Hough, J. H., et al. 1992, Astrophysical Journal, 386, 562
Wittkowski, M., Hauschildt, P. H., Arroyo-Torres, B., & Marcaide, J. M. 2012, Astronomy & Astrophysics, 540, L12
Zhang, B., Reid, M. J., Menten, K. M., & Zheng, X. W. 2012, Astrophysical Journal, 744, 23

7 | Polarization-dependent beam shifts upon metallic reflection in high-contrast imagers and telescopes

R. G. van Holstein, C. U. Keller, F. Snik, and S. P. Bos

Context. To directly image rocky exoplanets in reflected (polarized) light, future space- and ground-based high-contrast imagers aim to reach extreme contrasts at close separations from the star. However, the achievable contrast will be limited by reflection-induced polarization aberrations. While polarization aberrations can be modeled with numerical codes, these computations provide little insight into the full range of effects, their origin, and possible ways to mitigate them.
Aims. We aim to understand polarization aberrations produced by reflection off flat metallic mirrors at the fundamental level.
Methods. We use polarization ray tracing to numerically compute polarization aberrations and interpret the results in terms of the polarization-dependent spatial and angular Goos-Hänchen (GH) and Imbert-Federov (IF) shifts of the beam of light as described in the physics literature.
Results. We find that all four beam shifts are fully reproduced by polarization ray tracing. We study the origin of the shifts as well as the dependence of their size and direction on the beam intensity profile, incident polarization state, angle of incidence, mirror material, and wavelength. Of the four beam shifts, only the spatial GH and IF shifts are relevant because they are visible in the focal plane and create polarization structure in the point-spread function that reduces the performance of coronagraphs and the polarimetric speckle suppression close to the star.
Conclusions. The beam shifts in an optical system can be mitigated by keeping the f-numbers large and angles of incidence small. Most importantly, mirror coatings should not be optimized for maximum reflectivity, but should be designed to have a retardance close to 180°. Our insights can be applied to improve the performance of SPHERE-ZIMPOL at the VLT and future telescopes and instruments such as the Roman Space Telescope, HabEx, LUVOIR, PSI at the TMT, and PCS (or EPICS) at the ELT.

7.1 Introduction

To directly image rocky exoplanets in (polarized) reflected visible and near-infrared light, future space telescopes and extremely large ground-based telescopes and instruments aim to reach extreme planet-to-star contrast ratios at diffraction-limited angular separations from the star. Even though the optical systems of these high-contrast imagers will minimize scalar aberrations, the coronagraphic performance and achievable contrast will still be limited by polarization aberrations (e.g., Chipman, 1989; McGuire & Chipman, 1990; Sanchez Almeida & Martinez Pillet, 1992; McGuire & Chipman, 1994a,b; Breckinridge et al., 2015). Polarization aberrations are minute, polarization-dependent variations of the amplitude and phase of the electromagnetic field across a beam of light that result in polarization structure in the point-spread function (PSF). Polarization aberrations are predominantly caused by reflection off oblique and/or curved metallic mirrors and originate directly from the Fresnel reflection coefficients. The first-order polarization aberrations, that is, the sub-wavelength, polarization-dependent shifts of the beam of light, most negatively affect the achievable contrast. Because polarization aberrations are different for orthogonal polarization components of unpolarized light, adaptive optics cannot fully correct these aberrations (Breckinridge et al., 2015).

Recently, it has become clear that high-angular-resolution polarimeters are also affected by polarization aberrations. The polarimetric speckle suppression of the high-contrast imaging polarimeter SPHERE-ZIMPOL at the Very Large Telescope, which is specifically designed to search for the reflected, polarized visible light of giant exoplanets, is limited by reflection-induced, polarization-dependent beam shifts (Schmid et al., 2018). Such shifts also affect interferometric polarization measurements with the SPeckle Polarimeter at the Sternberg Astronomical Institute 2.5-m telescope (Safonov et al., 2019). The beam shifts become apparent for these instruments due to the unprecedented polarimetric sensitivity and spatial resolution they achieve.

The polarization aberrations of an astronomical telescope and instrument can be numerically computed with polarization ray tracing (Breckinridge et al., 2015). First, the paths of the rays of light are traced through the optical system using geometrical optics, but instead of the intensity, the electric field components of the rays are computed upon each reflection or transmission (e.g., Waluschka, 1989; Chipman, 1989; Yun et al., 2011a,b). Each point in the exit pupil is then associated with a Jones matrix. In this way, the Jones pupil, which maps the changes in the electric fields between the entrance and exit pupils of the system, is calculated (Totzeck et al., 2005). Finally, the intensity in the focal plane (i.e., the PSF) is computed, in the Fraunhofer approximation, through spatial Fourier transforms over the Jones pupil. Several studies have used polarization ray tracing to model the polarization aberrations of future high-contrast imagers and telescopes, such as the Roman Space Telescope (Krist et al., 2017), HabEx (Davis et al., 2018; Breckinridge et al., 2018), LUVOIR (Sabatke et al., 2018; Will & Fienup, 2019), PICTURE-C (Mendillo et al., 2019), and the Thirty Meter Telescope (Anche et al., 2018). However, these numerical computations give little insight into the full range of aberrations and their origin, or the relative importance of amplitude and phase effects.

Breckinridge et al. (2015) use polarization ray tracing to analyze a three-mirror system consisting of a Cassegrain telescope followed by a flat fold mirror, and find two beam-

shift effects that both originate from the oblique reflection off the flat mirror. The authors find phase gradients (i.e., wavefront tilts) in the Jones pupil that have opposite directions for the linearly polarized components parallel and perpendicular to the plane of incidence of the fold mirror. In the focal plane, these gradients cause the orthogonally polarized components of the PSF to shift in opposite directions, thereby broadening the resulting PSF in intensity. Furthermore, the authors find PSF components that couple the light from one orthogonal polarization into the other. These PSF components, which they call ghost PSFs, have two peaks, one on either side of the plane of incidence.

Sub-wavelength, polarization-dependent shifts of a beam of light induced by reflection off a flat metallic mirror are also extensively described in the physics literature (for overviews, see Aiello & Woerdman, 2008; Götte & Dennis, 2012; Bliokh & Aiello, 2013). These shifts are referred to as the Goos-Hänchen (GH) and Imbert-Federov (IF) shifts and occur in the directions parallel and perpendicular to the plane of incidence, respectively. Both shifts are further divided into a spatial and an angular shift. The spatial shifts are displacements of the entire beam of light upon reflection, and the angular shifts refer to angular deviations of the beam upon reflection. As such, the four shifts are considered first-order corrections to the laws of geometrical optics due to diffraction within a beam of light of finite width; the Fresnel equations only apply to infinitely extended interfaces, and a correct description of light reflected off an interface must therefore take into account the finite beam size. The GH and IF shifts are derived from first principles through full diffraction calculations and are described using closed-form mathematical expressions specifying the centroid of the intensity of a reflected Gaussian beam (e.g., Aiello & Woerdman, 2007, 2008). All four shifts have been experimentally validated for metallic reflections (Merano et al., 2007; Aiello et al., 2009; Hermosa et al., 2011). Schmid et al. (2018) show in their analysis of the beam shifts of SPHERE-ZIMPOL that the spatial GH shift is likely the same as the shift arising from phase gradients in the Jones pupil as described by Breckinridge et al. (2015).

The two views of the beam shifts from polarization ray tracing and full diffraction calculations in the physics literature raise many questions. Are the GH and IF shifts reproduced by polarization ray tracing or are they additional effects that we need to take into account for astronomical instruments? What is the origin of the shifts? How do the size and direction of the shifts depend on the beam intensity profile, incident polarization state, angle of incidence, mirror material, and wavelength? How do these shifts affect the performance of high-contrast imagers and how can we mitigate them in (future) diffraction-limited astronomical telescopes and instruments? This chapter answers these questions. To this end, we determine the beam shifts from the polarization ray tracing of the reflection of a beam of light with a uniform (or top-hat) intensity profile (as applies to astronomical telescopes and instruments), and compare the resulting shifts to the spatial and angular GH and IF shifts as predicted by the closed-form expressions derived for Gaussian beams.

The outline of this chapter is as follows. In Sect. 7.2 we describe the conventions and definitions of the mathematics used throughout the chapter. Subsequently, in Sect. 7.3, we outline the polarization ray tracing of the reflection of a beam of light off a flat metallic mirror and the determination of the beam shifts. In Sect. 7.4 we then explain the origin of the spatial and angular GH and IF shifts and their relation to shifts found using polar-

ization ray tracing. We also show the dependence of the size and direction of the shifts on the incident polarization state and angle of incidence. In Sect. 7.5, we investigate the polarization structure in the PSF induced by the beam shifts and the effect of the beam shifts on polarimetric measurements. In the same section we also examine the size of the beam shifts for various mirror materials and wavelengths, and discuss and refine the approaches to mitigate the beam shifts. Finally, we present conclusions in Sect. 7.6.

7.2 Conventions and definitions

In this section, we outline the conventions and definitions used throughout this chapter. In the literature, the mathematical definitions underlying the descriptions of polarization aberrations and beam shifts are often incomplete and not consistent among different studies. This can lead to errors in the physical interpretation, for example with the handedness of the circular polarization or the direction of the beam shifts. We therefore describe our definitions quite extensively and have carefully checked our equations for consistency. To enable easy comparison of our results with those from the physics literature, we use the same definitions as Aiello & Woerdman (2007), Merano et al. (2007), Aiello & Woerdman (2008), Aiello et al. (2009), and Hermosa et al. (2011). For the description of the polarization of light, these definitions are consistent with the definitions adopted by the International Astronomical Union (see e.g., Hamaker & Bregman, 1996). We present the mathematics to describe light and its polarization in Sect. 7.2.1 and discuss metallic reflection in Sect. 7.2.2.

7.2.1 Polarization of light

Consider a monochromatic, polarized light wave propagating in the positive z-direction of a Cartesian reference frame (or basis) xyz as shown in Fig. 7.1. The transverse electric field components of this light wave in the vertical x- and horizontal y-directions can then be described as (see e.g., Born & Wolf, 2013):

$$\tilde{E}_x(z,t) = A_x \cos\left(kz - \omega t + \varphi_x\right) = \mathrm{Re}\left[A_x \mathrm{e}^{\mathrm{i}\varphi_x} \mathrm{e}^{\mathrm{i}(kz-\omega t)}\right], \tag{7.1}$$

$$\tilde{E}_y(z,t) = A_y \cos\left(kz - \omega t + \varphi_y\right) = \mathrm{Re}\left[A_y \mathrm{e}^{\mathrm{i}\varphi_y} \mathrm{e}^{\mathrm{i}(kz-\omega t)}\right], \tag{7.2}$$

where t is time, $\omega > 0$ is the angular frequency, $k = 2\pi/\lambda$ is the wave number with λ the wavelength, A_x and A_y are the amplitudes, φ_x and φ_y are the initial phases, Re[...] denotes the real part, and i is the imaginary unit. On the right side of Eqs. (7.1) and (7.2), the factor $\exp\left[\mathrm{i}(kz - \omega t)\right]$ only describes the propagation of the light wave. The polarization of the wave can therefore be described by a Jones vector $\boldsymbol{E}$ defined as:

$$\boldsymbol{E} = \begin{bmatrix} E_x \\ E_y \end{bmatrix} = \begin{bmatrix} A_x \mathrm{e}^{\mathrm{i}\varphi_x} \\ A_y \mathrm{e}^{\mathrm{i}\varphi_y} \end{bmatrix}, \tag{7.3}$$

where E_x and E_y are the complex electric field components.

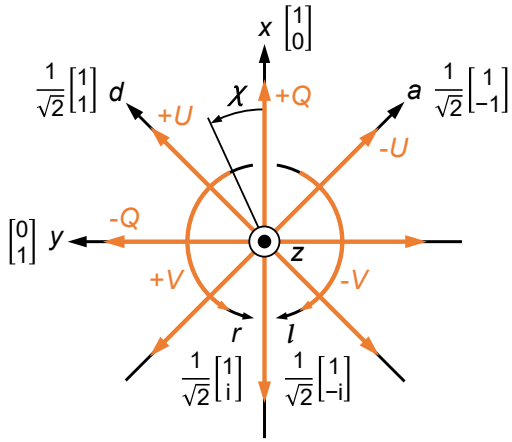


Figure 7.1: Definition of the three reference frames (or bases) and the Stokes parameters to describe the electric field components and polarization of an electromagnetic wave. The light propagates along the z-axis out of the paper toward the reader. In the xyz-basis, the x-axis (y-axis) is oriented in the vertical (horizontal) direction. In the daz-basis, the d-axis (a-axis) is oriented in the diagonal (antidiagonal) direction, at 45° counterclockwise (clockwise) from the x-axis. In rlz-basis, r and l represent the right-handed and left-handed circularly polarized components. For each reference frame, the basis Jones vectors, expressed in the xyz-bases, are indicated. The Stokes parameters are shown in orange with the plus sign (minus sign) indicating that the Stokes parameter is positive (negative) in that direction. The angle of linear polarization χ is defined positive for a counterclockwise rotation from the x-axis.

As an alternative way to describe the polarization, we can define a set of Stokes parameters as (see Fig. 7.1):

$$I = E_x E_x^* + E_y E_y^* \quad = A_x^2 + A_y^2 \quad = I_x + I_y = I_d + I_a$$
$$= I_r + I_l = 1, \tag{7.4}$$

$$Q = E_x E_x^* - E_y E_y^* \quad = A_x^2 - A_y^2 \quad = I_x - I_y, \tag{7.5}$$

$$U = E_x E_y^* + E_y E_x^* \quad = 2A_x A_y \cos\delta = I_d - I_a, \tag{7.6}$$

$$V = \mathrm{i}\left(E_x E_y^* - E_y E_x^*\right) = 2A_x A_y \sin\delta \; = I_r - I_l, \tag{7.7}$$

where * denotes the complex conjugate, $\delta = \varphi_y - \varphi_x$ is the phase difference between the y- and x-components of the electric field, and I_x and I_y are the intensities of the x- and y-components of the electric field. The variables I_d and I_a are the intensities of the d- and a-components in the basis of the diagonal and antidiagonal polarizations, daz, and I_r and I_l are the intensities of the r- and l-components in the basis of the right-handed and left-handed circular polarizations, rlz (see Fig. 7.1). Stokes I is the total intensity, positive (negative) Stokes Q describes linear polarization in the vertical x-direction (hor-

izontal y-direction), positive (negative) Stokes U describes linear polarization in the diagonal (antidiagonal) direction, 45° counterclockwise (clockwise) from the x-direction, and positive (negative) Stokes V describes right-handed (left-handed) circular polarization. Whereas the xyz-basis is the natural basis of Stokes Q, the daz- and rlz-bases are the natural bases of Stokes U and V, respectively. Because we normalize the total intensity, that is, we set $I = 1$ in Eq. (7.4), Q, U, and V have values between 1 and -1. We note that Eqs. (7.4)–(7.7) are strictly speaking only valid for 100% polarized, monochromatic light. However, for quasi-monochromatic light, whether 100% polarized, partially polarized, or unpolarized, we simply need to take the time averages over the terms in the equations.

From Eqs. (7.4) and (7.5) we can derive expressions for the intensities of the x- and y-components of the electric field:

$$I_x = \frac{1+Q}{2}, \tag{7.8}$$

$$I_y = \frac{1-Q}{2}. \tag{7.9}$$

Although these two equations are simple, they are important, and we use them in all closed-form expression for the beam shifts in Sect. 7.4. Finally, we assemble the Stokes parameters in a Stokes vector $\boldsymbol{S}$:

$$\boldsymbol{S} = \begin{bmatrix} I \\ Q \\ U \\ V \end{bmatrix}, \tag{7.10}$$

and define the degree of linear polarization P (which for $I = 1$ is equal to the linearly polarized intensity) and angle of linear polarization χ (see Fig. 7.1) as:

$$P = \sqrt{Q^2 + U^2}, \tag{7.11}$$

$$\chi = \frac{1}{2}\arctan\left(\frac{U}{Q}\right). \tag{7.12}$$

7.2.2 Metallic reflection

Using this mathematically consistent description of light and its polarization, we can describe the reflection of light using the Fresnel equations in the geometric polarization ray-tracing approximation. Consider the central ray of a beam of light incident on a flat metallic mirror as shown in Fig. 7.2. Describing this ray as a plane electromagnetic wave, we decompose the incident electric field into the p- and s-polarized components that are parallel and perpendicular to the plane of incidence, respectively. For this central ray, the p- and s-directions correspond to the x- and y-directions, respectively. Assuming the refractive index of the incident medium (air) to be equal to 1, we compute the complex

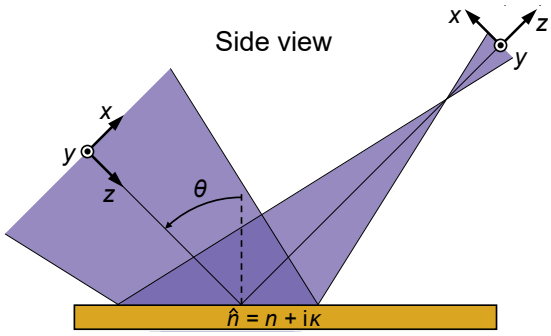


Figure 7.2: Schematic of the reflection of a beam of light off a flat metallic mirror with complex refractive index $\hat{n} = n + \mathrm{i}\kappa$. The central ray of the beam hits the mirror at an angle of incidence θ measured with respect to the normal to the surface of the mirror. The orientation of the *xyz* reference frame before and after reflection is indicated.

Fresnel reflection coefficients r_p and r_s as (see e.g., Born & Wolf, 2013):

$$r_p = \frac{\hat{n}^2 \cos\theta - \sqrt{\hat{n}^2 - \sin^2\theta}}{\hat{n}^2 \cos\theta + \sqrt{\hat{n}^2 - \sin^2\theta}} = R_p \mathrm{e}^{\mathrm{i}\phi_p}, \tag{7.13}$$

$$r_s = \frac{\cos\theta - \sqrt{\hat{n}^2 - \sin^2\theta}}{\cos\theta + \sqrt{\hat{n}^2 - \sin^2\theta}} = R_s \mathrm{e}^{\mathrm{i}\phi_s}, \tag{7.14}$$

where θ is the central angle of incidence (see Fig. 7.2) and $\hat{n} = n + \mathrm{i}\kappa$ is the complex refractive index of the mirror material, with n and κ the real and complex parts, respectively. The amplitudes $R_{p/s} = |r_{p/s}|$ specify the ratios of the amplitudes of the reflected and incident electric fields, while the phases $\phi_{p/s} = \arg(r_{p/s})$ describe the phase shifts between the reflected and incident electric fields.

Two important quantities related to the reflection coefficients are the diattenuation and the retardance, which can be considered to be the zeroth-order polarization aberrations. The diattenuation ϵ is defined as:

$$\epsilon = \frac{R_s^2 - R_p^2}{R_s^2 + R_p^2}, \tag{7.15}$$

which ideally equals 0. When unpolarized light is incident on the mirror, a nonzero value of the diattenuation quantifies the amount of linearly polarized light that is created, that is, the instrumental polarization (IP). The retardance Δ is defined as:

$$\Delta = \phi_s - \phi_p \ , \tag{7.16}$$

which ideally equals 180°. The latter value comes from the requirement that the electromagnetic wave before and after reflection is described by a right-handed triplet in terms of the electric field, the magnetic field, and the wave vector. For values other than 180°,

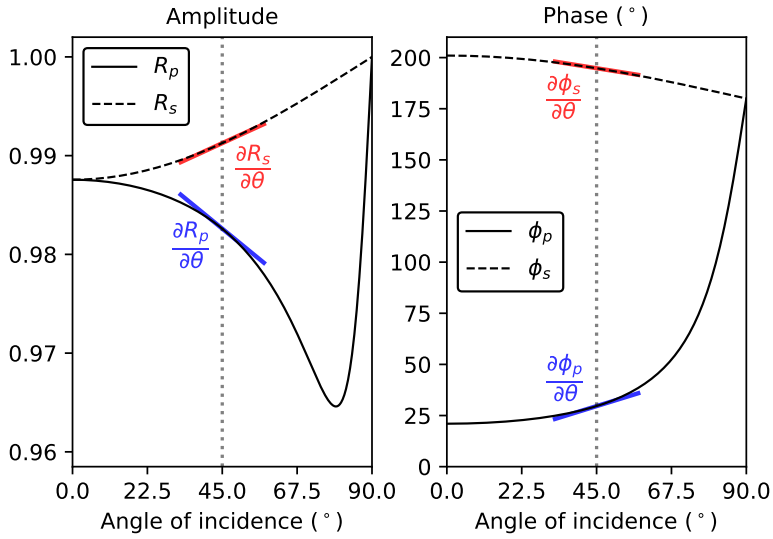


Figure 7.3: Amplitude (*left*) and phase (*right*) of the Fresnel reflection coefficients in the *p*- and *s*-directions as a function of angle of incidence for gold with $\hat{n} = 0.188 + i5.39$ at a wavelength of 820 nm. The gradients in the amplitude and phase for an angle of incidence of 45° are indicated in blue for the *p*-direction and in red for the *s*-direction.

retardance results in the conversion of incident linearly polarized light into circularly polarized light and vice versa, that is, it produces polarimetric crosstalk.

The physics of the beam shifts as described in Sect. 7.4 depends on the diattenuation and retardance as well as on the gradients of the amplitude and phase of the reflection coefficients with the angle of incidence. Figure 7.3 shows the amplitude and phase of the reflection coefficients as a function of angle of incidence for gold with $\hat{n} = 0.188 + i5.39$ at a wavelength of 820 nm, corresponding to the configuration studied in Sects. 7.3–7.5. From Fig. 7.3 (left) it follows that the diattenuation, which is roughly the difference between the curves of R_s and R_p (see Eq. (7.15)), is zero at $\theta = 0°$, increases with increasing angle of incidence until it reaches a maximum around $\theta = 80°$, and then decreases again to zero at $\theta = 90°$. In Fig. 7.3 (right) we see that the retardance, which is the difference between the curves of ϕ_s and ϕ_p (see Eq. (7.16)), is 180° at $\theta = 0°$ and remains close to this value for small values of θ. For large θ, the retardance decreases rapidly to 0° at $\theta = 90°$. Fig. 7.3 (left and right) also show the gradients in amplitude and phase at $\theta = 45°$ (similar to the phase gradients shown by Breckinridge et al. 2015). Whereas the amplitude gradient $\partial R_s/\partial\theta$ is always positive for $\theta > 0°$, $\partial R_p/\partial\theta$ is initially negative, then becomes zero, and finally is positive for very large angles of incidence. Lastly, for $\theta > 0°$ the phase gradients $\partial\phi_s/\partial\theta$ and $\partial\phi_p/\partial\theta$ are negative and positive, respectively, and monotonically decrease and increase with increasing angle of incidence.

7.3 Beam shifts from polarization ray tracing

In this section, we describe the polarization ray tracing of a beam of light that reflects off a metallic mirror, following the methodology outlined in Breckinridge et al. (2015), and the determination of the beam shifts that result. In Sect. 7.4, we compare the resulting shifts for various incident polarization states and angles of incidence to the predicted spatial and angular GH and IF shifts as derived for Gaussian beams. We determine the centroid shifts of both the focal-plane intensity (i.e., the PSF) and the intensity in the exit-pupil plane because these planes are where the spatial shifts (shifts of the complete beam) and angular shifts (angular deviations as measured from the focus) should be visible. To enable a direct comparison of our results with the experimental measurements of the GH and IF shifts by Merano et al. (2007), Aiello et al. (2009), and Hermosa et al. (2011), we consider a (practically) identical configuration to the one used in those studies: a converging, monochromatic beam of light with an f-number of 61.3 that reflects off a flat golden mirror at a wavelength of 820 nm and with a focal distance of 11.9 cm. Our configuration differs in that the beam of light is not Gaussian but has a uniform intensity profile across the entrance pupil as is the case for astronomical telescopes and instruments.

As the first step in our analysis, we compute the Jones pupil that describes the electric-field response in the exit pupil upon reflection. We only describe this computation briefly here (for detailed descriptions see e.g., Waluschka, 1989; Götte & Dennis, 2012). We use the definitions as shown in Fig. 7.2 and decompose the beam of light into a set of rays that each can be described by a plane electromagnetic wave. For each ray, we compute the angle of incidence and, using Eqs. (7.13) and (7.14), the corresponding Fresnel reflection coefficients in the local p- and s-directions. Subsequently, we calculate the orientation of the local plane of incidence for each ray. Finally, we compute the Jones pupil as the set of Jones matrices describing the reflection of each ray, taking into account the orientation of the local plane of incidence and the change of sign of the x-coordinate of the ray upon reflection. The resulting Jones pupil J_{xyz}, which is expressed in the xyz-basis, can be written as:

$$J_{xyz} = \begin{bmatrix} J_{xx} & J_{xy} \\ J_{yx} & J_{yy} \end{bmatrix} = \begin{bmatrix} R_{xx}\mathrm{e}^{\mathrm{i}\phi_{xx}} & R_{xy}\mathrm{e}^{\mathrm{i}\phi_{xy}} \\ R_{yx}\mathrm{e}^{\mathrm{i}\phi_{yx}} & R_{yy}\mathrm{e}^{\mathrm{i}\phi_{yy}} \end{bmatrix}, \tag{7.17}$$

where J_{xx} to J_{yy} are the complex Jones-pupil elements describing the contribution of the x- or y-polarized components of the incident electric field (in the entrance pupil) to the x- or y-polarized components of the reflected electric field (in the exit pupil). The amplitudes and phases of the Jones-pupil elements, which define the ratios of the amplitudes and the phase shifts of the reflected and incident electric fields, are denoted R_{xx} to R_{yy} and ϕ_{xx} to ϕ_{yy}, respectively. The Jones pupil J_{xyz} for reflection with an angle of incidence of 45° is shown in Fig. 7.4 (top).

The Jones pupil is a crucial ingredient for our understanding of the beam shifts in Sect. 7.4. In that context, it is useful to also express the Jones pupil in the basis of the diagonal and antidiagonal polarizations, *daz*, and the basis of the right-handed and left-handed circular polarizations, *rlz*, as defined in Fig. 7.1. The Jones pupils in the *daz*- and

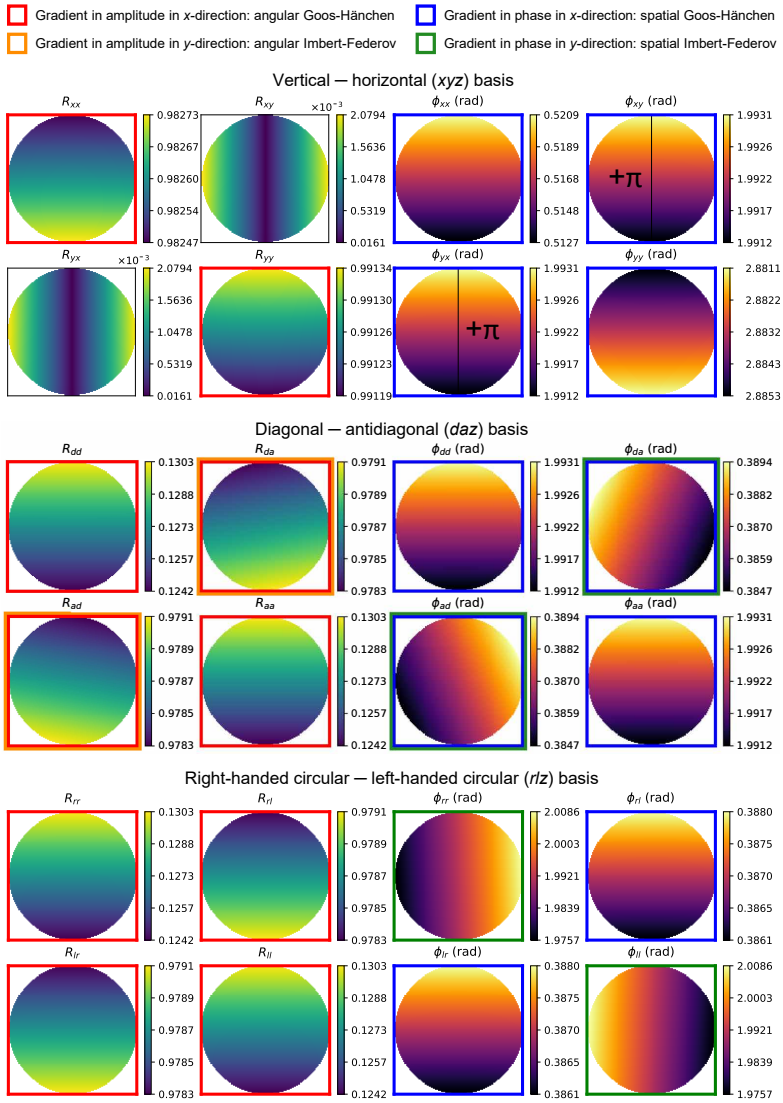


Figure 7.4: Jones pupil expressed in the *xyz*- (*top*), *daz*- (*center*), and *rlz*-bases (*bottom*) at a wavelength of 820 nm for a converging beam of light with an f-number of 61.3 that reflects off gold at an angle of incidence of 45°. The panels in the first and second (third and fourth) columns show the amplitude (phase) of the Jones-pupil elements. The positive x- and y-directions are upward and to the left, respectively. The values of the color maps are different among the panels. The red, orange, blue, and green borders around the panels indicate the gradients that are visible and the specific beam shifts that these gradients cause (see the legend above the top panels). To reveal the gradient in the panels of ϕ_{xy} and ϕ_{yx}, π has been added to the phase in the left and right halves of the pupil, respectively.

rlz-bases, J_{daz} and J_{rlz}, are defined as:

$$J_{daz} = T_{daz} J_{xyz} T_{daz}^{-1} = \begin{bmatrix} R_{dd} e^{i\phi_{dd}} & R_{da} e^{i\phi_{da}} \\ R_{ad} e^{i\phi_{ad}} & R_{aa} e^{i\phi_{aa}} \end{bmatrix}, \tag{7.18}$$

$$J_{rlz} = T_{rlz} J_{xyz} T_{rlz}^{-1} = \begin{bmatrix} R_{rr} e^{i\phi_{rr}} & R_{rl} e^{i\phi_{rl}} \\ R_{lr} e^{i\phi_{lr}} & R_{ll} e^{i\phi_{ll}} \end{bmatrix}, \tag{7.19}$$

where R_{dd} to R_{ll} and ϕ_{dd} to ϕ_{ll} are the amplitudes and phases of the Jones-pupil elements and $^{-1}$ denotes the inverse of a matrix. The matrices T_{daz} and T_{rlz} describe the transformations from the *xyz*-basis to the *daz*- and *rlz*-bases, respectively, and are defined as:

$$T_{daz} = \frac{1}{\sqrt{2}} \begin{bmatrix} 1 & 1 \\ 1 & -1 \end{bmatrix}, \tag{7.20}$$

$$T_{rlz} = \frac{1}{\sqrt{2}} \begin{bmatrix} 1 & -i \\ 1 & i \end{bmatrix}. \tag{7.21}$$

The Jones pupils J_{daz} and J_{rlz} for reflection with an angle of incidence of 45° are shown in Fig. 7.4 (center) and Fig. 7.4 (bottom), respectively.

Next, we compute the amplitude-response matrix, *ARM*, specifying the electric-field response in the focal plane. The *ARM* is computed as:

$$ARM = \begin{bmatrix} \mathscr{F}(J_{xx}) & \mathscr{F}(J_{xy}) \\ \mathscr{F}(J_{yx}) & \mathscr{F}(J_{yy}) \end{bmatrix}, \tag{7.22}$$

where $\mathscr{F}(\dots)$ denotes the spatial Fourier transform over a Jones-pupil element. For the computation of the *ARM* we therefore assume that the Fraunhofer approximation to diffraction applies, which is the case for beams with absolute f-numbers larger than ~5 (see e.g., McGuire & Chipman, 1990). Subsequently, we calculate the point-spread matrix, *PSM*, which is the Mueller-matrix representation of the PSF and describes the intensity response in the focal plane for any incident Stokes vector, whether 100% polarized, partially polarized, or unpolarized. The *PSM* is calculated as:

$$PSM = C(ARM \otimes ARM^*)C^{-1} \tag{7.23}$$

where $\otimes$ denotes the Kronecker product, * indicates the element-wise complex conjugate, and the matrix C is defined as (see e.g., Espinosa-Luna et al., 2008):

$$C = \begin{bmatrix} 1 & 0 & 0 & 1 \\ 1 & 0 & 0 & -1 \\ 0 & 1 & 1 & 0 \\ 0 & i & -i & 0 \end{bmatrix}. \tag{7.24}$$

The *PSM* can be written as:

$$PSM = \begin{bmatrix} I \to I & Q \to I & U \to I & V \to I \\ I \to Q & Q \to Q & U \to Q & V \to Q \\ I \to U & Q \to U & U \to U & V \to U \\ I \to V & Q \to V & U \to V & V \to V \end{bmatrix}, \tag{7.25}$$

where each element $A \rightarrow B$ describes the contribution of the incident Stokes parameter A to the resulting Stokes parameter B. The *PSM* for reflection with an angle of incidence of 45° is shown in Fig. 7.5. We note that the same *PSM* can also be obtained from the Jones pupil expressed in the *daz*- or *rlz*-bases when replacing the matrix C in Eq. (7.24) with the appropriate matrix corresponding to those bases.

As the final step, we determine the beam shifts in the exit pupil and the focal plane. To this end, we define an incident Jones vector or Stokes vector with a uniform intensity profile and polarization state. For the determination of the shift in the exit pupil, we right-multiply the Jones pupil by the incident Jones vector to obtain the Jones vector in the pupil plane. Subsequently, we compute the intensity distribution in the pupil plane as the sum of squares of the amplitudes of the latter Jones vector. Finally, we calculate the beam shift as the offset of the centroid of the intensity distribution with respect to the beam position in the absence of diffraction and aberrations. To determine the beam shift in the focal plane, we compute the Stokes vector after reflection by right-multiplying the *PSM* by the incident Stokes vector. We then retrieve the intensity image from the first element of the resulting Stokes vector and determine the shift as the offset of the centroid with respect to the beam position in the absence of diffraction and aberrations.

7.4 Explanation of beam shifts and comparison to polarization ray tracing

In this section, we explain the spatial and angular GH and IF shifts and compare them to the shifts found using polarization ray tracing. We analytically describe the four shifts using the closed-form expressions from Aiello & Woerdman (2008). These expressions are derived (see Aiello & Woerdman, 2007) by decomposing an incident, uniformly polarized Gaussian beam of light into the angular spectrum of plane waves (e.g., Born & Wolf, 2013) and computing the effect of the reflection on each wave. Because the plane waves are infinitely extended, the Fresnel equations can be applied without making any approximations. The decomposition into plane waves is equivalent to a Fourier transform of the electric field at the mirror interface. The resulting reflected plane waves are then integrated over, and the shift is calculated as the shift of the centroid of the intensity of the beam. The expressions depend on the Fresnel reflection coefficients at the central angle of incidence and the complex electric-field components of the incident beam. We have rewritten the expressions in terms of the more familiar Stokes parameters to make the expressions easier to understand and enable the computation of the shifts for any incident polarization state.

For each of the four shifts, which generally occur simultaneously, we explain the origin and analytically compute the size and direction as a function of angle of incidence for different incident polarization states. We consider 100% linearly polarized light with angles of linear polarization χ ranging from 0° to 180° in steps of 22.5°, 100% right-handed and left-handed circularly polarized light (i.e., $V = 1$ and $V = -1$, respectively), and unpolarized light. For these same polarization states, we numerically compute the shifts from the polarization ray tracing as outlined in Sect. 7.3 and compare the results to the analytical computations. We also explain the shifts using the Jones pupil and the *PSM*.

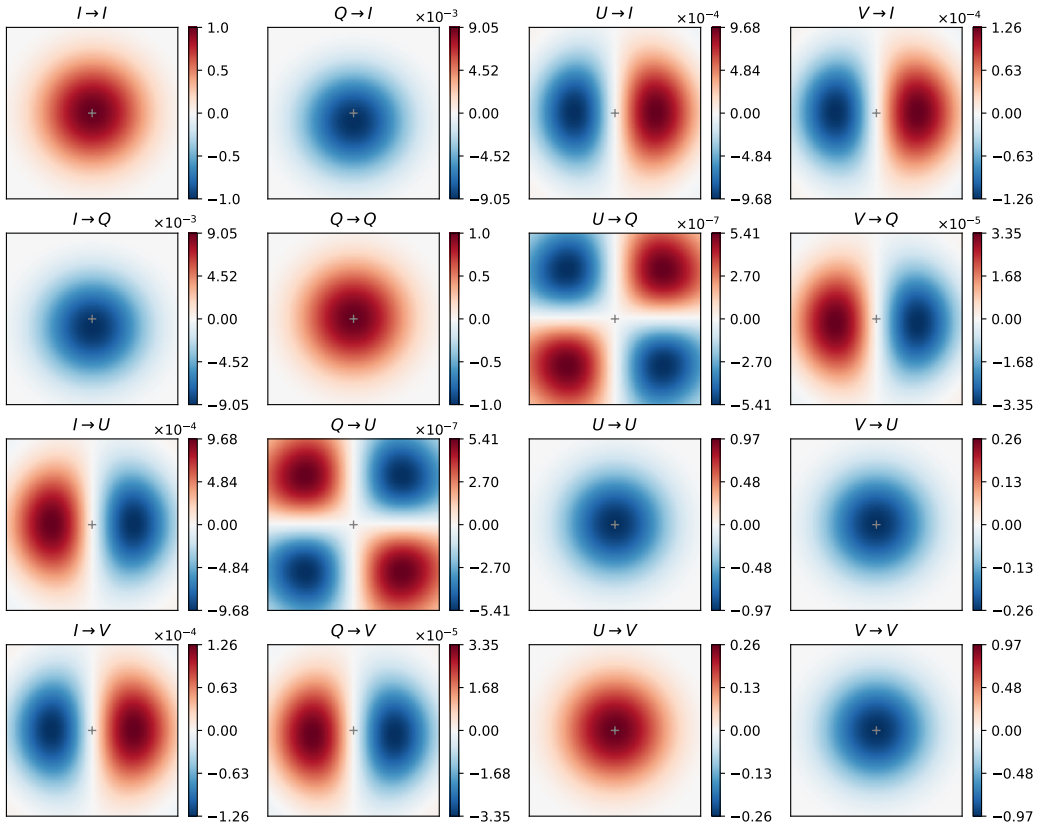


Figure 7.5: Point-spread matrix (*PSM*) at a wavelength of 820 nm for a converging beam of light with an f-number of 61.3 that reflects off gold at an angle of incidence of 45°. The positive x- and y-directions are upward and to the left, respectively. The gray plus signs indicate the beam position in the absence of diffraction and aberrations. The values of the color maps differ between elements.

We discuss the spatial and angular GH shifts in Sects. 7.4.1 and 7.4.2 and the spatial and angular IF shifts in Sects. 7.4.3 and 7.4.4.

7.4.1 Spatial Goos-Hänchen shift

The spatial GH shift, X_{sGH}, is a displacement of the entire beam of light upon reflection and occurs in the plane of incidence (e.g., Goos & Hänchen, 1947; Merano et al., 2007; Aiello & Woerdman, 2008; Aiello et al., 2009; Götte & Dennis, 2012; Bliokh & Aiello, 2013). Figure 7.6 (top) shows a schematic with the definition of the spatial GH shift. The shift is independent of the divergence angle of the incident beam (i.e., the f-number) and does not depend on whether the reflection occurs in the focus or the converging or diverging parts of the beam. From the perspective of the plane-wave decomposition, the spatial GH shift can be understood from a 2D picture of the beam of light, looking from a direction perpendicular to the plane of incidence (i.e., the side view as shown in Fig. 7.6, top). Each plane wave of the beam has a different angle of incidence and therefore acquires a correspondingly different phase shift upon reflection. This results in a gradient in phase over the range of angles of incidence (see Fig. 7.3, right). Integrating over all reflected plane waves, this then results in a shift of the entire beam parallel to the plane of incidence. The integration is equivalent to an inverse Fourier transform, which explains how a phase gradient is equivalent to a shift of the entire beam on the mirror.

The spatial GH shift can be analytically computed as:

$$X_{\mathrm{sGH}} = \frac{\lambda}{2\pi} \frac{\frac{\partial \phi_p}{\partial \theta} R_p^2 I_x + \frac{\partial \phi_s}{\partial \theta} R_s^2 I_y}{R_p^2 I_x + R_s^2 I_y}, \tag{7.26}$$

where R_p and R_s (from Eqs. (7.13) and (7.14)) and the phase gradients $\partial\phi_p/\partial\theta$ and $\partial\phi_s/\partial\theta$ (see Fig. 7.3, right) are computed at the central angle of incidence of the beam, and I_x and I_y are the intensities of the components of the light polarized in the x- and y-direction, respectively. These intensities only depend on the incident Stokes Q and follow from Eqs. (7.8) and (7.9). The factor $R_p^2 I_x + R_s^2 I_y$ in Eq. (7.26) is the intensity of the reflected beam and returns in the expressions of all shifts. The spatial GH shift is produced by the phase gradients, whereas R_p and R_s can be considered to be small corrections. Indeed, if we set either I_x or I_y equal to zero in Eq. (7.26), we obtain:

$$X_{\mathrm{sGH},x/y} = \frac{\lambda}{2\pi} \frac{\partial \phi_{p/s}}{\partial \theta}, \tag{7.27}$$

which shows that the spatial GH shift consists of two components: $X_{\mathrm{sGH},x}$ for the light polarized in the x-direction and $X_{\mathrm{sGH},y}$ for the light polarized in the y-direction. The total spatial GH shift as computed from Eq. (7.26) can then be understood as the intensity-weighted average of these two shifts.

Figure 7.7 shows the spatial GH shift as a function of angle of incidence for different incident polarization states as computed from Eq. (7.26). The figure also shows the shifts in the focal plane (data points) as obtained from the numerical computations using the polarization ray tracing as outlined in Sect. 7.3. The close agreement between the analytical

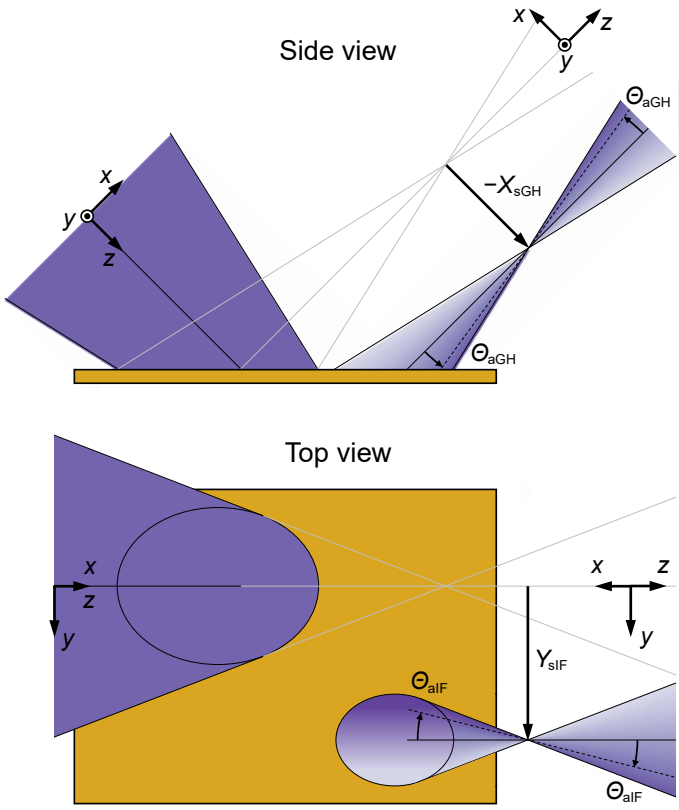


Figure 7.6: Schematic showing the definitions of the spatial and angular GH shifts, X_{sGH} and Θ_{aGH} (*top*), and the spatial and angular IF shifts, X_{sIF} and Θ_{aIF} (*bottom*), for an (initially converging) beam of light incident on a metallic mirror. Darker colors within the reflected beam indicate a higher relative intensity. The orientation of the *xyz* reference frame before and after reflection is indicated. Positive spatial GH and IF shifts are directed in the positive *x*- and *y*-directions, respectively, after reflection (the spatial GH shift is shown in the negative direction). The angular GH and IF shifts are positive for a right-handed rotation around the *y*-axis and a left-handed rotation around the *x*-axis, respectively. For clarity the size of the shifts is extremely exaggerated.

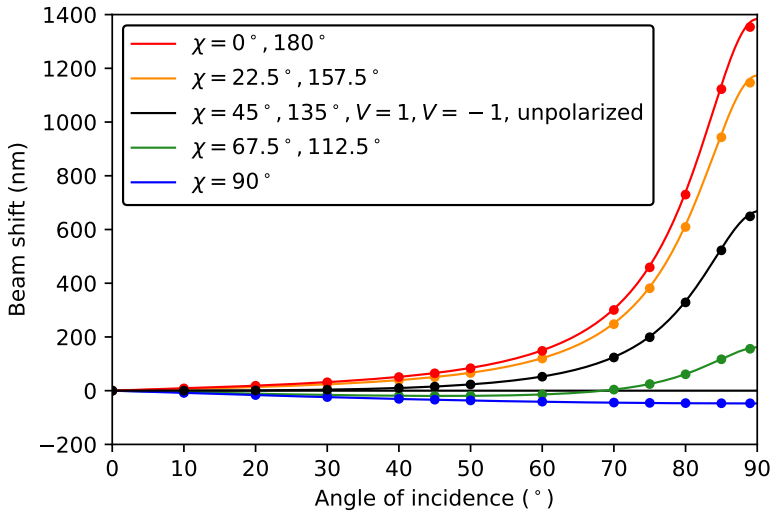


Figure 7.7: Spatial GH shift as a function of angle of incidence for reflection off gold at a wavelength of 820 nm as obtained from the closed-form expression of Eq. (7.26) (curves) and polarization ray tracing (data points). The shift is shown for an incident beam of light that is completely unpolarized, 100% linearly polarized with various angles of linear polarization χ, and 100% right-handed ($V = 1$) or left-handed ($V = -1$) circularly polarized.

and numerical results shows that the spatial GH shift is reproduced very closely by the polarization ray tracing and that Eq. (7.26) is not only valid for Gaussian beams, but is also accurate for beams with a uniform intensity profile. Small deviations between the analytical and numerical results are only visible for very large angles of incidence ($\theta \gtrsim 80°$). These deviations are higher-order effects due to the beam intensity profile deviating from a Gaussian profile. Indeed, when performing the polarization ray tracing for a Gaussian beam, the data points agree exactly with the analytical curves for all angles of incidence.

Figure 7.7 shows that, although the size of the spatial GH shift is generally less than the wavelength, the shift can be larger than a wavelength for large angles of incidence and certain incident polarization states. At normal incidence, the shift is always zero. The spatial GH shift is largest for light polarized in the x-direction (i.e., for $\chi = 0°$ and $\chi = 180°$, or $Q = 1$) and increases with increasing angle of incidence. Because the shift for light polarized in the x-direction is directly proportional to $\partial\phi_p/\partial\theta$ (see Eq. (7.27)), this behavior can be understood from the increasing gradient seen in Fig. 7.3 (right). For incident light polarized in the y-direction (i.e., for $\chi = 90°$ or $Q = -1$), the shift is much smaller and in the opposite direction, which also agrees with $\partial\phi_s/\partial\theta$ being smaller than and opposite to $\partial\phi_p/\partial\theta$ in Fig. 7.3 (right). In case of light with $Q = 0$ (e.g., for unpolarized light or 100% polarized light with $\chi = 45°$, $\chi = 135°$, $V = 1$, or $V = -1$), the intensities of the light polarized in the x- and y-directions are equal and the resulting shift is the intensity-weighted average of the shifts of the x- and y-polarizations. Finally, for light

with $0 < |Q| < 1$ (e.g., for 100% polarized light with $\chi = 22.5°, \chi = 67.5°, \chi = 112.5°$, or $\chi = 157.5°$, and also partially polarized light), the resulting shift is in between the three aforementioned shifts.

As can be seen from Fig. 7.4 (top), which shows the Jones pupil expressed in the xyz-basis, the spatial GH shift produces gradients in the phase of all Jones-pupil elements (blue borders). These phase gradients represent wavefront tilts in the exit pupil and as such result in shifts of the centroid of the PSF in the focal plane. This confirms the claim by Schmid et al. (2018) that the spatial GH shift is the shift that arises from the phase gradient in the x-direction in the Jones pupil as described by Breckinridge et al. (2015). However, we note that Fig. 27 of Schmid et al. (2018) suggests that the spatial GH shift is caused by both a shift on the mirror and a directional change of the beam due to a wavefront tilt induced upon reflection. This depiction is inaccurate: The spatial GH shift is a shift of the entire beam that occurs on the mirror surface, which, in the Fraunhofer approximation, can be described as a wavefront tilt in the exit pupil.

From the Jones pupil, it may seem that the spatial GH shift depends on the f-number, but this is not the case. Although a two times smaller f-number gives a two times larger phase gradient in the pupil plane, the focal distance is also two times smaller, resulting in the same shift in the focal plane. Similarly, for a diverging beam (i.e., a beam with a negative f-number) the phase gradients have the opposite sign but then the focal plane is imaginary and located in front of the mirror (i.e., the focal distance is negative), again yielding the same shift. A more mathematical approach to showing the independence of the shift from the f-number is presented in Schmid et al. (2018). We note that the size of the shift (which scales with λ, see Eq. (7.26)) relative to the size of the PSF (which scales with $\lambda|F|$, with F the f-number) does depend on the f-number and is proportional to $1/|F|$. This means that a more strongly converging or diverging beam results in a larger shift relative to the PSF.

Finally, we show that the spatial GH shift is visible in the *PSM* as well (see Fig. 7.5). As described in Sect. 7.3, the focal-plane shifts are determined from the intensity image constructed by right-multiplying the *PSM* by the incident Stokes vector. In other words, the shifts are determined from the image constructed as a linear combination of the *PSM*-elements in the top row, weighted with the incident Stokes parameters. Whereas both the $(I \to I)$- and $(Q \to I)$-elements have their centroids shifted in the x-direction, the $(U \to I)$- and $(V \to I)$-elements do not exhibit such shifts. For incident light with $Q = 0$, the shift we find is that of the $(I \to I)$-element. On the other hand, for light with $Q \neq 0$, a scaled version of the $(Q \to I)$-element, which shows a relatively large shift, is added to or subtracted from the $(I \to I)$-element. This results in either a larger or smaller shift than that of the $(I \to I)$-element, in agreement with the curves of Fig. 7.7.

7.4.2 Angular Goos-Hänchen shift

The angular GH shift, Θ_{aGH}, is an angular deviation of the beam of light upon reflection and, similar to the spatial GH shift, occurs in the plane of incidence (e.g., Aiello & Woerdman, 2008; Aiello et al., 2009; Götte & Dennis, 2012; Bliokh & Aiello, 2013). The definition of the angular GH shift is shown in Fig. 7.6 (top). Similar to the spatial GH shift, the angular GH shift can be understood from a 2D picture of the beam of light.

Each ray in the incident beam hits the mirror at a different angle of incidence and therefore experiences a different reflection coefficient. Over the range of angles of incidence this results in a gradient in the amplitude across the reflected beam (see Fig. 7.3, left), which translates into a shift of the centroid in intensity. Contrary to the spatial GH shift, the size of the angular shift depends on the divergence angle, and thus the f-number, of the incident beam. This is because a more strongly converging or diverging beam covers a larger range of angles of incidence and therefore yields a larger gradient. The angular GH shift is truly a deflection of the beam centroid as described by an angle, which is the same whether the reflection occurs in the focus or the converging or diverging part of the beam (see Fig. 7.6, top). The resulting physical displacement of the beam centroid vanishes in the focus and increases with distance from the focus. That the physical displacement of the beam centroid is zero in the focus can easily be understood in the Fraunhofer approximation: The amplitude gradient in the exit pupil will lead to a point-symmetric change in the PSF, which cannot change the centroid of the intensity distribution.

The angular GH shift can be computed as:

$$\Theta_{\mathrm{aGH}} = \frac{-\alpha^2}{2} \frac{R_p \dfrac{\partial R_p}{\partial \theta} I_x + R_s \dfrac{\partial R_s}{\partial \theta} I_y}{R_p^2 I_x + R_s^2 I_y}, \tag{7.28}$$

where, similar to the spatial GH shift, I_x and I_y are functions of Stokes Q (see Eqs. (7.8) and (7.9)), and R_p, R_s, and the amplitude gradients $\partial R_p/\partial\theta$ and $\partial R_s/\partial\theta$ (see Fig. 7.3, left) are evaluated at the central angle of incidence. The divergence angle of the beam, α, is computed as:

$$\alpha = \arctan\left(\frac{1}{2|F|}\right), \tag{7.29}$$

with F the f-number of the beam. Contrary to the spatial GH shift, the angular GH shift only depends on the amplitude of the reflection coefficients, and not on the phase. The angular GH shift is produced by the amplitude gradients, whereas R_p and R_s only have a small effect. The structure of Eq. (7.28) is quite similar to that of Eq. (7.26), which describes the spatial GH shift. Indeed, when setting $I_x = 0$ or $I_y = 0$ in Eq. (7.28), we see that the angular GH shift also consists of two components for the light polarized in the x- and y-directions:

$$\Theta_{\mathrm{aGH},x/y} = \frac{-\alpha^2}{2} \frac{1}{R_{p/s}} \frac{\partial R_{p/s}}{\partial \theta}. \tag{7.30}$$

Equation (7.28) therefore constitutes the intensity-weighted average of these two shifts. Finally, the physical displacement of the beam centroid at a distance z_f from the focus of the beam is given by:

$$X_{\mathrm{aGH}} = z_\mathrm{f}\, \Theta_{\mathrm{aGH}}, \tag{7.31}$$

where $z_\mathrm{f} > 0$ in the diverging part of the beam and $z_\mathrm{f} < 0$ in the converging part. We can compute the physical displacement of the centroid of the intensity in the pupil plane by

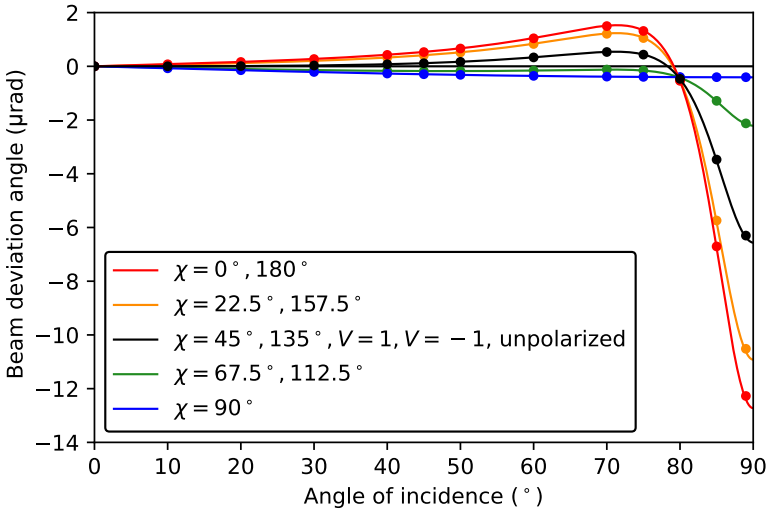


Figure 7.8: Angular GH shift as a function of angle of incidence at a wavelength of 820 nm for a beam of light with an f-number of 61.3 that reflects off gold as obtained from the closed-form expression of Eq. (7.28) (curves) and polarization ray tracing (data points). The shift is shown for an incident beam that is completely unpolarized, 100% linearly polarized with various angles of linear polarization χ, and 100% right-handed ($V = 1$) or left-handed ($V = -1$) circularly polarized.

inserting $z_f = -f$ in Eq. (7.31), where f is the focal distance ($f > 0$ in a converging beam and $f < 0$ in a diverging beam).

Figure 7.8 shows the angular GH shift as a function of angle of incidence for different polarization states as computed from Eq. (7.28). The figure also shows the shifts as obtained from the exit pupil (data points) using the polarization ray tracing as explained in Sect. 7.3. We have computed these numerical shifts by dividing the physical displacements of the centroid in the pupil plane by the negative value of the focal distance (see Eq. (7.31)). Contrary to the analytically computed shifts, we have computed the numerical shifts only for 100% polarized light (i.e., not for unpolarized light), because the Jones calculus used cannot describe unpolarized or partially polarized light. Similar to the spatial GH shift, the analytical and numerical results in Fig. 7.8 agree closely and small deviations are only visible for very large angles of incidence. These deviations are due to the angular GH shift depending on the precise beam intensity profile and vanish when performing the polarization ray tracing for a Gaussian beam.

Figure 7.8 indicates that the angular GH shift is on the order of microradians for the particular configuration studied. For normal incidence, the shift is zero. The largest shifts are found for light polarized in the x-direction (i.e., for $\chi = 0°$ and $\chi = 180°$, or $Q = 1$), whereas the shifts of the light polarized in the y-direction (i.e., for $\chi = 90°$ or $Q = -1$) are much smaller. The curves can be understood from the amplitude gradients governing the angular GH shift as shown in Fig. 7.3 (left): Whereas $\partial R_s/\partial\theta$ increases monotonically

with increasing angle of incidence, $\partial R_p/\partial\theta$ is initially negative, reaches a value of zero, and then attains large positive values. The curves in Fig. 7.8 follow a similar pattern as those of the spatial GH shift (see Fig. 7.7), with the shifts for incident light that is not 100% x- or y-polarized being an intensity-weighted average of the shifts of the x- and y-polarizations.

As shown in the R_{xx}- and R_{yy}-elements of Fig. 7.4 (top; red borders), the amplitude gradients associated with the angular GH shift are visible in the Jones pupil expressed in the xyz-basis. In the antidiagonal elements R_{xy} and R_{yx} these amplitude gradients also exist, but they are overshadowed by the left-right symmetric structure visible in those elements. For a diverging rather than converging beam, the amplitude gradients have opposite signs (see also Fig. 7.6, top). Because a diverging beam implies a negative focal distance, that is, the focal plane is virtual and located in front of the mirror, the signs of the angular shifts themselves do not change (see Eq. (7.31)). Finally, the angular GH shift is not visible in the *PSM* (Fig. 7.5) because it is zero in the focus.

7.4.3 Spatial Imbert-Federov shift

The spatial IF shift, Y_{sIF}, is a displacement of the entire beam of light upon reflection and occurs in the direction perpendicular to the plane of incidence (e.g., Federov, 1955; Imbert, 1972; Bliokh & Bliokh, 2006; Aiello & Woerdman, 2008; Hermosa et al., 2011; Götte & Dennis, 2012; Bliokh & Aiello, 2013; Bliokh et al., 2015). A schematic with the definition of the spatial IF shift is shown in Fig. 7.6 (bottom). Similar to the spatial GH shift, the spatial IF shift is independent of the f-number of the beam and the position within the beam where the reflection occurs. To understand the spatial IF shift from a plane-wave decomposition, it is necessary to consider the full 3D picture (e.g., Aiello & Woerdman, 2008; Bliokh & Aiello, 2013). Each plane wave in the incident beam has a different (3D) propagation direction. Therefore, not only the angles of incidence (and thus the reflection coefficients) are different among the waves, but also the orientations of the local planes of incidence. These rotations of the planes of incidence induce different geometric (Berry) phases among the circularly polarized components of the waves. This results in a gradient of the geometric phases in the direction perpendicular to the plane of incidence, with the gradient having opposite sign for the right-handed and left-handed circular polarizations. Accounting for the reflection coefficients of each wave as well as the geometric phases within the reflected beam, the reflected beam is found to be shifted in the direction perpendicular to the plane of incidence when integrating over all waves.

The spatial IF shift is more easily understood in terms of conservation of total angular momentum (e.g., Bliokh & Bliokh, 2006; Bliokh & Aiello, 2013; Bliokh & Nori, 2015; Bliokh et al., 2015). Disregarding vortex beams, the total angular momentum of a beam of light consists of the spin angular momentum (SAM) and the external orbital angular momentum. In the quantum-mechanical description of light, photons carry one of two spin states that correspond to right-handed and left-handed circular polarization. The SAM of a beam of light is a vector quantity pointing in the direction of propagation that is proportional to the difference between the number of right-handed and left-handed photons, that is, it is proportional to Stokes V. The external orbital angular momentum is given by the cross product of the radius vector of the beam centroid with respect to some

origin and the (linear) momentum of the beam, with the latter pointing in the direction of propagation. Upon reflection, the total angular momentum in the direction normal to the surface of the mirror is conserved. As a result, any change in the SAM of the beam, that is, in the circular polarization, must be compensated for by a shift of the beam in the direction perpendicular to the plane of incidence. This shift is the spatial IF shift, which is therefore considered to be a spin-orbit interaction of light.

The spatial IF shift can be calculated as:

$$Y_{\mathrm{sIF}} = \frac{-\lambda}{2\pi} \frac{\cot\theta}{R_p^2 I_x + R_s^2 I_y} \left[V \left(\frac{R_p^2 + R_s^2}{2} \right) + R_p R_s \left(V \cos\Delta + U \sin\Delta \right) \right], \tag{7.32}$$

where R_p, R_s, and the retardance Δ (see Eq. (7.16) and Fig. 7.3) are evaluated at the central angle of incidence θ, and $\cot\theta$ is the transverse gradient of the induced geometric phase. Although the spatial IF shift has a weak dependence on Stokes Q through I_x and I_y (see Eqs. (7.8) and (7.9)), the shift depends primarily on the incident Stokes U and V. So, whereas the GH shift consists of two separate shifts for light polarized in the x- and y-directions, the spatial IF shift comprises separate and opposite shifts for the diagonally and antidiagonally polarized components (because $U = I_d - I_a$, see Eq. (7.6)) as well as for the right-handed and left-handed circularly polarized components (because $V = I_r - I_l$, see Eq. (7.7)). For metallic reflections, the spatial IF shift results primarily from the retardance, whereas R_p and R_s can be considered to be small corrections. Indeed, we can simplify Eq. (7.32) by assuming that the incident beam is totally reflected. Setting $R_p = R_s = 1$ and inserting $I_x + I_y = 1$ (see Eq. (7.4)), we obtain:

$$Y_{\mathrm{sIF}} = \frac{-\lambda}{2\pi} \cot\theta \left[V \left(1 + \cos\Delta \right) + U \sin\Delta \right]. \tag{7.33}$$

In this equation, the factor $[V(1+\cos\Delta)+U\sin\Delta]$ is proportional to the change of the SAM upon reflection, with $V(1)$ proportional to the incident SAM and $-(V\cos\Delta + U\sin\Delta)$, which gives Stokes V after reflection, proportional to the SAM of the reflected beam. The spatial IF shift thus depends on the crosstalk from U to V ($U\sin\Delta$) and the crosstalk from V to U or even the crosstalk creating a change of handedness of the circular polarization ($V\cos\Delta$).

Figure 7.9 shows the spatial IF shift as a function of angle of incidence for different incident polarization states as computed from Eq. (7.32). Also shown are the shifts in the focal plane (data points) as numerically determined using polarization ray tracing (see Sect. 7.4), which agree closely with the analytical computations. The small deviations among the results vanish when performing the polarization ray tracing with a Gaussian beam.

Figure 7.9 illustrates that the spatial IF shift is (somewhat) smaller than the spatial GH shift and is always smaller than the wavelength. At normal incidence, where $\Delta = 180°$ (see Fig. 7.3), the spatial IF shift is zero. For nonzero angles of incidence, where $\Delta \neq 180°$, changes in the SAM occur for incident U- or V-polarized light, thus leading to spatial IF shifts. The spatial IF shifts are in opposite directions for opposite signs of U (e.g., for $\chi = 45°$ and $\chi = 135°$) and V (for right-handed and left-handed circular polarization). The shifts initially become larger with increasing angle of incidence

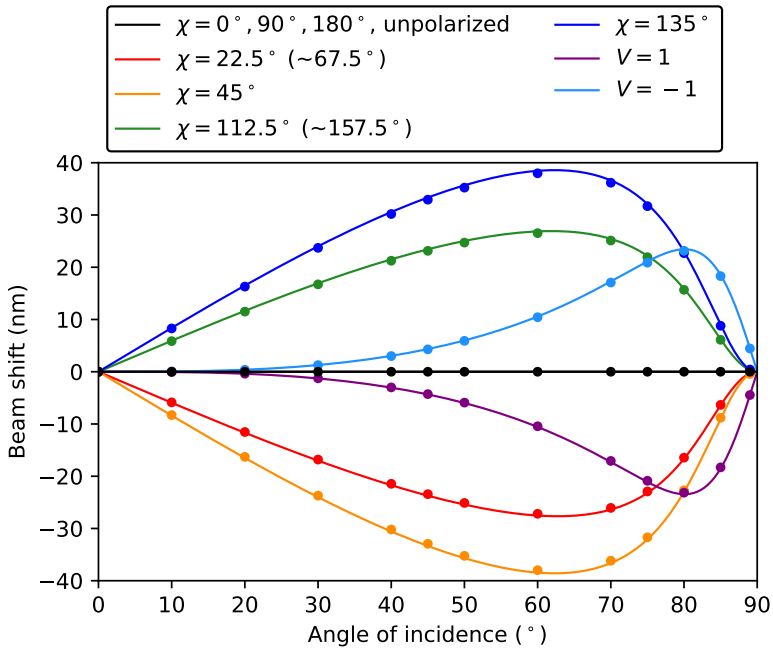


Figure 7.9: Spatial IF shift as a function of angle of incidence for reflection off gold at a wavelength of 820 nm as obtained from the closed-form expression of Eq. (7.32) (curves) and polarization ray tracing (data points). The shift is shown for an incident beam of light that is completely unpolarized, 100% linearly polarized with various angles of linear polarization χ, and 100% right-handed ($V = 1$) or left-handed ($V = -1$) circularly polarized. The shifts for $\chi = 67.5°$ and $\chi = 157.5°$ are not shown, but are very close to the shifts for $\chi = 22.5°$ and $\chi = 112.5°$, respectively. The colors indicate different polarization states than in Figs. 7.7 and 7.8.

(because Δ monotonically decreases), but then become smaller again for (very) large angles of incidence as $\cot\theta \to 0$ when $\theta \to 90°$, resulting in no shift at $\theta = 90°$. The spatial IF shift for U ($\chi = 45°$ and $\chi = 135°$) reaches larger values than that of V with the maximum of U occurring at a smaller angle of incidence than the maximum of V. The maxima of the curves are lower for partially polarized light or light with both Q and U nonzero (e.g., $\chi = 22.5°, \chi = 67.5°, \chi = 112.5°$ or $\chi = 157.5°$). Although the light with $\chi = 22.5°$ and $\chi = 67.5°$ (and similar for $\chi = 112.5°$ and $\chi = 157.5°$) have the same value for U, small differences in the size of the shifts occur due to the dependence on Q via I_x and I_y. The curves of incident light with both U and V nonzero are combinations of the curves for the individual Stokes parameters. Finally, for unpolarized light or light polarized in the x- or y-direction (i.e., Q-polarized light), the spatial IF shift is always zero because the incident beam carries no SAM and no SAM can be created upon reflection.

Similar to the spatial GH shift, the spatial IF shift is expected to create gradients in phase in the Jones pupil. However, in the Jones pupil expressed in the xyz-basis (see

Fig. 7.4, top), phase gradients in the y-direction are not visible. This is because the spatial IF shift primarily depends on Stokes U and V (see Eq. (7.33)), and therefore results from the complex linear combination of all four Jones-pupil elements in this basis. Nevertheless, a hint of a gradient in the y-direction is visible in the R_{xy}-, R_{yx}-, ϕ_{xy}-, and ϕ_{yx}-elements when considering that a phase difference of π between the left and right sides of the pupil implies that the reflection coefficients on either side have opposite signs. Actual phase gradients in the y-direction naturally appear in the Jones pupils expressed in the bases of Stokes U and V, that is, in the Jones pupils expressed in the *daz*- and *rlz*-bases (see Fig. 7.4, center and bottom). The gradients are visible in the ϕ_{da}-, ϕ_{ad}-, ϕ_{rr}-, and ϕ_{ll}-elements (green borders). The Jones pupils also show the phase gradient in the x-direction produced by the spatial GH shift (blue borders), with the ϕ_{da}- and ϕ_{ad}-elements exhibiting a combination of gradients in the x- and y-directions. In Fig. 7.4 (center and bottom), the amplitude gradient in the x-direction due to the angular GH is visible as well (red borders). Lastly, we note that although the spatial IF shift does not depend on the f-number, its size relative to the PSF scales as $1/|F|$, analogous to the spatial GH shift (see Sect. 7.4.1).

Finally, we show how the spatial IF shift is visible in the *PSM* (see Fig. 7.5). As explained in Sect. 7.4.1, the focal-plane shifts are determined from the image created as a linear combination of the *PSM*-elements in the top row, weighted with the incident Stokes parameters. Because the $(I\rightarrow I)$- and $(Q\rightarrow I)$-elements are symmetric with respect to the x-axis (i.e., they are left-right symmetric in Fig. 7.5), no shift results for unpolarized light or light that is polarized in the x- or y-direction. The $(U\rightarrow I)$- and $(V\rightarrow I)$-elements on the other hand are asymmetric, with positive and negative signals on opposite sides of the x-axis. For incident light with nonzero U and/or V, scaled versions of these elements are added to or subtracted from the $(I\rightarrow I)$-element, producing a PSF with the centroid shifted in the y-direction. We note that the relative intensity of the $(U\rightarrow I)$-element is larger than that of the $(V\rightarrow I)$-element, in agreement with the spatial IF shift being larger for U than for V at an angle of incidence of 45° (see Fig. 7.9).

7.4.4 Angular Imbert-Federov shift

The angular IF shift, Θ_{aIF}, is an angular deviation of the beam of light upon reflection directed away from the plane of incidence (e.g., Bliokh & Bliokh, 2007; Aiello & Woerdman, 2008; Hermosa et al., 2011; Götte & Dennis, 2012; Bliokh & Aiello, 2013). The definition of the angular IF shift is shown in Fig. 7.6 (bottom). Similar to the angular GH shift, the size of the angular IF shift depends on the f-number of the incident beam and is the same whether the beam is reflected in the focus or in the converging or diverging parts of the beam. The physical displacement of the centroid of the beam is zero in the focus and increases with distance from the focus. The angular IF shift is related to the conservation of (linear) momentum in the direction perpendicular to the plane of incidence, and, similar to the spatial IF shift, results from the differences in induced geometric phase across the beam.

The angular IF shift can be calculated as:

$$\Theta_{\mathrm{aIF}} = \frac{\alpha^2}{4} \frac{\cot\theta}{R_p^2 I_x + R_s^2 I_y} U \left(R_p^2 - R_s^2\right), \tag{7.34}$$

where R_p and R_s are computed at the central angle of incidence, and the divergence angle α is given by Eq. (7.29). Similar to the angular GH shift, the angular IF shift does not depend on the phases of the reflection coefficients, but only on the amplitudes. The angular IF shift depends primarily on the incident Stokes U, although small Q-dependent corrections take place through I_x and I_y (see Eqs. (7.8) and (7.9)). If $Q = 0$, that is, $I_x = I_y = {}^1/_2$, Eq. (7.34) reduces to:

$$\Theta_{\mathrm{aIF}} = \frac{-\alpha^2}{2} U \epsilon \cot\theta, \tag{7.35}$$

with ϵ the diattenuation from Eq. (7.15). Finally, the physical displacement of the centroid of the beam is computed as:

$$Y_{\mathrm{aIF}} = z_{\mathrm{f}}\, \Theta_{\mathrm{aIF}}, \tag{7.36}$$

with z_{f} the distance from the focus, similar to Eq. (7.31).

Figure 7.10 shows the angular IF shift as a function of angle of incidence for various polarization states as computed from Eq. (7.34). The shifts as obtained from the exit pupil (data points) using polarization ray tracing (see Sect. 7.3) are also shown. These numerical shifts are computed using Eq. (7.36) and are only calculated for 100% polarized light, similarly to the angular GH shifts (see Sect. 7.4.2). The analytical and numerical results agree closely, with the small deviations vanishing when performing the polarization ray tracing for a Gaussian beam.

Figure 7.10 shows that the angular IF shift is on the order of less than a microradian for the particular configuration considered. For incident light with U nonzero, angular IF shifts occur that are in the opposite direction for opposite signs of U. The shifts are zero for angles of incidence of 0° and 90°. The shape of the curves is related to the diattenuation (roughly the difference between R_s and R_p in Fig. 7.3), which initially increases with increasing angle of incidence, reaches a maximum, and then decreases again to zero at $\theta = 90°$. For incident light with $U = 0$ (i.e., $\chi = 0°$, $\chi = 90°$, $\chi = 180°$, $V = 1$, $V = -1$, or unpolarized light), the shift is zero for any angle of incidence.

Finally, the amplitude gradients in the y-direction associated with the angular IF shift are visible in the R_{da}- and R_{ad}-elements of the Jones pupil expressed in the *daz*-basis (see Fig. 7.4, center). The gradients of these elements are a combination of gradients in the y-direction and the x-direction, with the latter due to the angular GH shift (red borders). Because the angular IF shift is zero in the focus, it is not visible in the *PSM*.

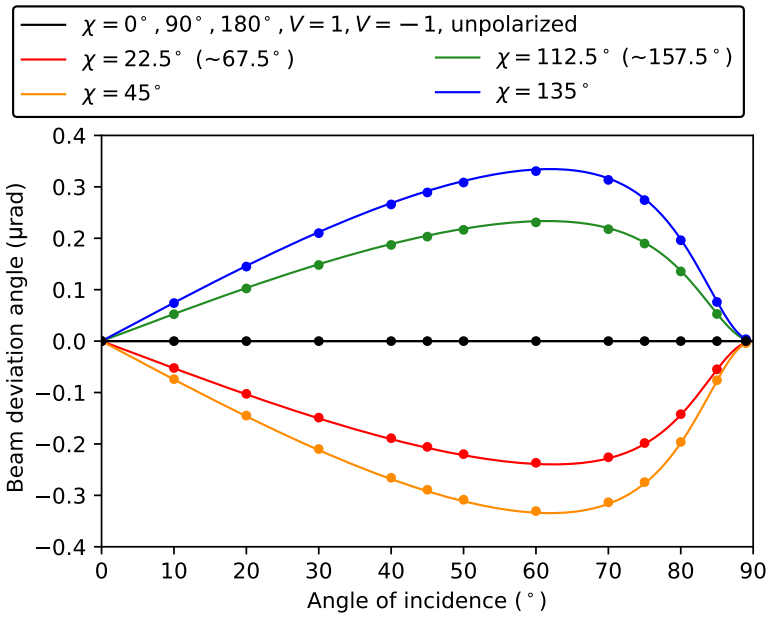


Figure 7.10: Angular IF shift as a function of angle of incidence at a wavelength of 820 nm for a beam of light with an f-number of 61.3 that reflects off gold as obtained from the closed-form expression of Eq. (7.34) (curves) and polarization ray tracing (data points). The shift is shown for an incident beam that is completely unpolarized, 100% linearly polarized with various angles of linear polarization χ, and 100% right-handed ($V = 1$) or left-handed ($V = -1$) circularly polarized. The shifts for $\chi = 67.5°$ and $\chi = 157.5°$ are not shown, but are very close to the shifts for $\chi = 22.5°$ and $\chi = 112.5°$, respectively. Except for the circular polarization, the colors used indicate the same polarization states as in Fig. 7.9.

7.5 Discussion

In Sect. 7.4 we explained the origin of the spatial and angular GH and IF shifts and investigated their size and direction as a function of angle of incidence and incident polarization state. We also showed that these four beam shifts are fully reproduced by polarization ray tracing as described in Sect. 7.3 and that the exact beam intensity profile (i.e., whether it is Gaussian or uniform) has a negligible effect. Of the four beam shifts, only the spatial GH and IF shifts are relevant for high-contrast imagers because they are visible in the focal plane; the angular GH and IF shifts are not important because, besides a small point-symmetric deformation of the PSF for angles of incidence close to grazing incidence (which do not occur in high-contrast imagers), they have no effect in the focus. We thus find that the polarization structure in the PSF that limits the performance of coronagraphs and the speckle suppression of polarimetric imagers is created by the spatial GH and IF shifts. In Sect. 7.5.1, we investigate the polarization structure in the PSF created

by the spatial GH and IF shifts. Subsequently, in Sect. 7.5.2, we examine the effect of the spatial GH and IF shifts on polarimetric measurements. In Sect. 7.5.3, we then briefly discuss the size of the spatial GH and IF shifts for various mirror materials and wavelengths. Finally, we use our understanding of the spatial GH and IF shifts to discuss and refine the approaches to mitigate the shifts in Sect. 7.5.4.

7.5.1 Polarization structure in the PSF due to beam shifts

In this section, we investigate the polarization structure in the PSF created by the spatial GH and IF shifts. This polarization structure must be taken into account when designing the coronagraphs of high-contrast imagers that aim to detect planets in reflected light (Breckinridge et al., 2015). For our analysis, we consider the reflection off a single flat mirror at an angle of incidence of 45°, using the same configuration as examined in Sects. 7.3 and 7.4.

The observed light of the stars around which high-contrast imagers search for planets is unpolarized or has a degree of polarization of only several percent (see e.g., Heiles, 2000). For this case of (nearly) unpolarized incident light, the Stokes vector after reflection off a flat mirror is given by the elements in the left column of the *PSM* in Fig. 7.5, that is, the $(I \rightarrow I)$-, $(I \rightarrow Q)$-, $(I \rightarrow U)$-, and $(I \rightarrow V)$-elements. These elements are the same as those in the top row of the *PSM*, except for the $(I \rightarrow U)$-element which has opposite sign. Because the spatial GH and IF shifts follow from these top-row elements (see Sects. 7.4.1 and 7.4.3), the polarization-dependent structures visible in the Stokes vector for reflection of incident unpolarized light must be created by the spatial GH and IF shifts. In the following, we refer to the $(I \rightarrow I)$-, $(I \rightarrow Q)$-, $(I \rightarrow U)$-, and $(I \rightarrow V)$-elements as the intensity image and the Q-, U-, and V-images, respectively.

As outlined in Sect. 7.4.1, the spatial GH shift is described by two opposite shifts of different size for the incident light polarized in the x- and y-directions, that is, for the incident I_x- and I_y-components of the light. Because unpolarized light can be described as the sum of equal amounts of the I_x- and I_y-components (see Eqs. (7.4), (7.8), and (7.9)), the intensity image consists of two PSF components that are slightly shifted in opposite directions along the x-axis. As a result, the PSF in intensity is not only shifted (see Fig. 7.7, black curve), but also broadened in the x-direction. The Q-image is equal to the difference of the I_x- and I_y-components (see Eq. (7.5)). Due to the diattenuation (see Eq. (7.15)), the two components are not reflected by an equal amount. Therefore, an overall negative signal with a minimum of ~0.9% remains in the image, which constitutes the IP. But because the I_x- and I_y-components are also shifted in opposite directions, this IP signal itself also has a large shift (see also Breckinridge et al., 2015).

As explained in Sect. 7.4.3, the spatial IF shift is opposite for incident diagonally (d) and antidiagonally (a) polarized light (i.e., for positive and negative 100% U-polarized light) as well as for incident right-handed (r) and left-handed (l) circularly polarized light (i.e., for positive and negative 100% V-polarized light). Unpolarized light can be described as the sum of equal amounts of these I_d- and I_a-components as well as the sum of equal amounts of the I_r- and I_l-components (see Eqs. (7.4), (7.6), and (7.7)). Therefore, the intensity image consists of PSF components that are slightly shifted by equal amounts in opposite direction parallel to the y-axis. So although the PSF in intensity is

not shifted (see Fig. 7.9, black curve), it is broadened in the y-direction in addition to the broadening in the x-direction (due to the spatial GH shift). The opposite shifts of the I_d- and I_a-components and the I_r- and I_l-components can also be seen in the U- and V-images, respectively, where for the configuration considered they create structures below 0.1% of the intensity (with the U-image having larger values than the V-image as can be expected from Fig. 7.9). Breckinridge et al. (2015) refer to these structures as ghost PSFs (see Sect. 7.1), although the authors describe them as components of the *ARM*. Our results show that these ghost PSFs are created by the spatial IF shifts and are elliptically polarized. Finally, we note that due to the splitting of the orthogonal circular polarization states in the V-image, the spatial IF shift is often also referred to as the spin Hall effect of light (e.g., Hermosa et al., 2011; Bliokh & Aiello, 2013; Bliokh & Nori, 2015; Bliokh et al., 2015).

The *PSM* in Fig. 7.5 as calculated with polarization ray tracing includes all orders of polarization aberrations. Still, we find that the polarization structure in the PSF for the case of unpolarized incident light is adequately described by the diattenuation and the first-order polarization aberrations in the focus, that is, the spatial GH and IF shifts. We therefore conclude that only for curved mirrors the higher-order polarization aberrations, such as polarization-dependent astigmatism (Breckinridge et al., 2015), come into play. For a discussion on the combined effect of a series of flat mirrors and the polarization aberrations of curved mirrors with normal incidence, we refer to Breckinridge et al. (2015).

7.5.2 Effect of beam shifts on polarimetric measurements

In this section, we investigate the effect of the spatial GH and IF shifts on polarimetric measurements with high-contrast imagers. The physics literature does not describe beam shifts for the case of incident unpolarized light measured by a polarimeter following the mirror reflection. However, our approach enables us to understand that case based on our insight into the beam shifts as well as our results from the polarization ray tracing.

Consider placing a rotatable linear polarizer behind the mirror that we analyzed in Sect. 7.5.1. In that case, the Stokes vector incident on the polarizer is the same Stokes vector as examined in Sect. 7.5.1: It is equal to the left column of the *PSM* in Fig. 7.5. If we then align the transmission axis of the polarizer with the x-, y-, d-, and a-directions, we measure the I_x-, I_y-, I_d-, and I_a-components of the beam. Also, if we replace the polarizer with a right-handed or left-handed circular polarizer, we measure the I_r- and I_l-components of the beam. As a result, these six measurements are sensitive to exactly the same spatial GH and IF shifts of these components as described in Sect. 7.5.1. Therefore, when we compute the differences of the x- and y-, d- and a-, and r- and l-measurements, we obtain the Q-, U-, and V-images of the Stokes vector after reflection.

Because stars are generally unpolarized, polarimetric measurements strongly suppress the light from the star, thereby making the detection of planets in reflected light easier. However, the maximum gain in contrast from polarimetry is limited by the spatial GH and IF shifts and the polarization structure that they create. Although the IP is a larger aberration, this effect is routinely subtracted in the data reduction and/or removed by using a half-wave plate in front of the optical path in current high-contrast imaging polarimeters

(Witzel et al., 2011; Canovas et al., 2011; Wiktorowicz et al., 2014; Millar-Blanchaer et al., 2016; de Boer et al., 2020; Chapters 2 and 3).

To quantify the maximum gain in contrast from polarimetry as limited by the spatial GH and IF shifts, we compute the mirror-induced fractional polarization in Q, U, and V over the PSF. To this end, we convolve the intensity image and the Q-, U-, and V-images using a top-hat kernel with a diameter equal to the full width at half maximum of the PSF in the intensity image. This diameter is equal to the diameter of the apertures one would use to extract the fluxes of detected planets and determine the noise level in the images (e.g., Mawet et al., 2014). After convolving the images, we compute the IP in the Q-image by dividing the total flux in the Q-image by the total flux in the intensity image. We then subtract the IP from the Q-image by multiplying the intensity image by the IP and subtracting the resulting image from the Q-image. Subsequently, we compute the images of the normalized Stokes $q = Q/I$, $u = U/I$, and $v = V/I$ by dividing the (IP-subtracted) Q-, U-, and V-images by the intensity image. The resulting images as well as the images of the intensity and the degree and angle of linear polarization P and χ (see Eqs. (7.11) and (7.12)) are shown in Fig. 7.11.

Figure 7.11 (top) shows that the spatial GH and IF shifts create polarization structures with significant fractional-polarization levels in the PSF. Whereas the structure in the q-image is produced by the spatial GH shift, the orthogonally oriented structures in the u- and v-images are induced by the spatial IF shift. In all images the PSF core and the Airy rings contain successive positively and negatively polarized regions. The fractional-polarization levels are largest in the q-image and smallest in the v-image. The relative strength of the fractional polarizations in the q-, u-, and v-images are directly related to the relative sizes of the spatial GH and IF shifts at an angle of incidence of 45° (see Figs. 7.7 and 7.9). Figure 7.11 (bottom) indicates that the degree of linear polarization in the PSF reaches a maximum of 0.56%. Finally, we see that the angle of linear polarization rotates 180° when moving in a circle around the center of the PSF and that it differs by 90° between the inner and outer regions of the Airy rings.

The fractional polarizations in the q-, u-, and v-images limit the local gain in contrast achievable with polarimetry. The degree of (linear) polarization is several tenths of a percent on average; hence the average contrast gain is a factor of ~350, which is the gain compared to the contrast in intensity including the effects of seeing. This is because any speckles due to the seeing are also polarized at approximately this level. We stress that the exact numerical values presented in Fig. 7.11 are only valid for the specific configuration considered. For example, for a series of mirrors and/or beams with smaller f-numbers, the fractional-polarization levels are much higher and therefore the gain in contrast due to polarimetry is much lower.

Finally, as discussed in Sect. 7.1, the polarimetric speckle suppression of the high-contrast imaging polarimeter SPHERE-ZIMPOL is limited by polarization-dependent beam shifts (Schmid et al., 2018). Indeed, the structures visible in the on-sky polarimetric images of Fig. 26 of Schmid et al. (2018) agree very well with those in the q- and u-images of Fig. 7.11 (top). Therefore, the polarimetric contrast of SPHERE-ZIMPOL at small angular separations from the star is clearly limited by both the spatial GH and IF shifts.

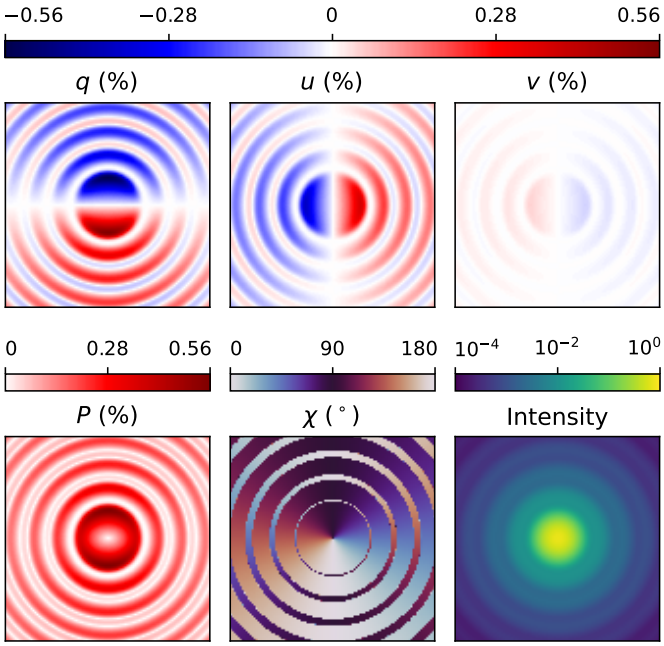


Figure 7.11: Images of the PSF structures visible in normalized Stokes q (without IP), u, and v (*top*), degree of linear polarization P, angle of linear polarization χ, and intensity (*bottom*) at a wavelength of 820 nm for a converging beam of light with an f-number of 61.3 that reflects off gold at an angle of incidence of 45°. The images are convolved with a top-hat kernel with a diameter equal to the full width at half maximum of the PSF in intensity. The images show the core of the PSF and the first three complete Airy rings. The positive x- and y-directions are upward and to the left, respectively.

7.5.3 Size of beam shifts for various mirror materials and wavelengths

So far we have only considered the beam shifts for reflection off gold at a wavelength of 820 nm. Here we briefly discuss the maximum size of the spatial GH and IF shifts as a function of wavelength from the ultraviolet to the near-infrared for the three most common (bulk) mirror materials used in astronomical telescopes and instruments. We note, however, that actual mirrors in astronomical telescopes and instruments are likely to consist of a stack of thin films and so the exact sizes of the shifts will be different. To compute the shifts, we use the complex refractive indices of gold, silver, and aluminum for the range of wavelengths from Rakić et al. (1998). The spatial GH shift for x-polarized light (from Eq. (7.26)) and the spatial IF shift for anti-diagonally polarized light (from Eq. (7.32)) for angles of incidence θ of 45° and 70°, normalized with the wavelength, are shown in Fig. 7.12.

We conclude that the spatial GH shift is larger than the spatial IF shift for all mirror materials, that the size of the shifts is always less than the wavelength, and that the shifts

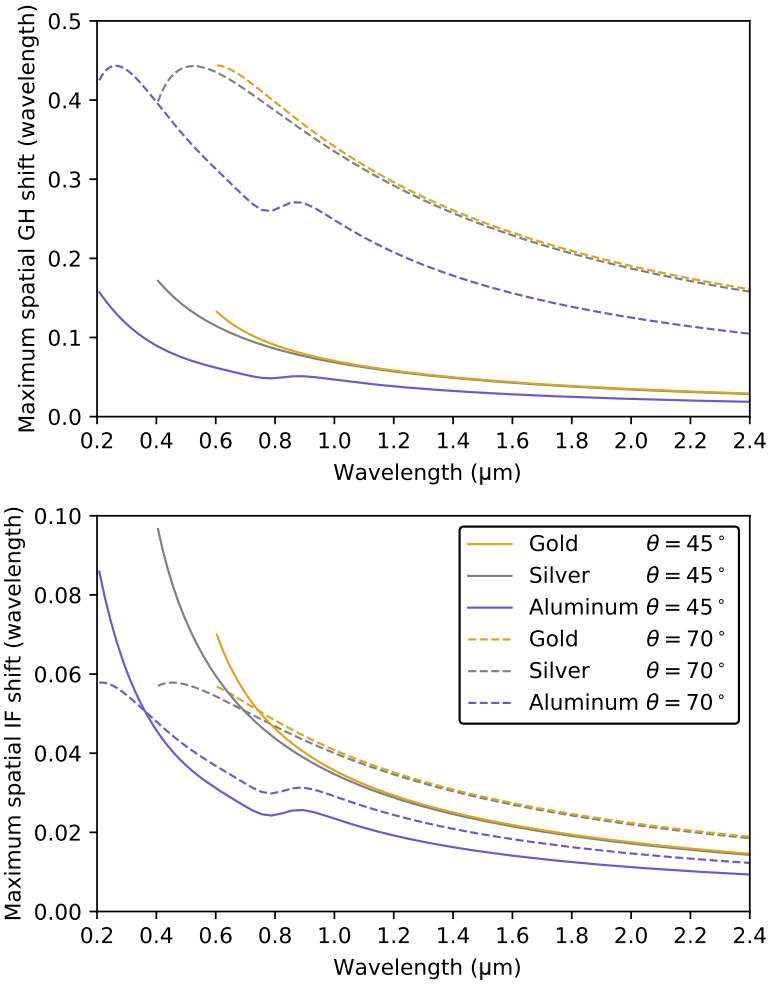


Figure 7.12: Maximum wavelength-normalized spatial GH (*top*) and IF (*bottom*) shifts as a function of wavelength at an angle of incidence θ of 45° and 70° for reflection off gold, silver, and aluminum. The legend in the bottom panel is valid for both panels. The shifts for gold and silver are only shown for wavelengths longer than 600 nm and 400 nm, respectively, because the reflectivity drops below 90% at shorter wavelengths.

relative to the wavelength are larger for shorter wavelengths. Of the three materials, aluminum produces the smallest shifts, whereas gold and silver create larger shifts. For all materials and wavelengths, the spatial GH shift is smaller for $\theta = 45°$ than for $\theta = 70°$. The same is true for the spatial IF shift, except for the shortest wavelengths where the shift for $\theta = 45°$ becomes larger than that of $\theta = 70°$.

7.5.4 Mitigation of beam shifts

Breckinridge et al. (2015) provide an overview of possible approaches to mitigate polarization aberrations in optical systems, which includes using beams with large f-numbers, keeping the angles of incidence small, and tuning the coatings of the mirrors. In this section, we discuss and refine these approaches based on our fundamental understanding of the beam shifts. Breckinridge et al. (2015) also discuss the use of possible optical devices that could compensate polarization aberrations (see also Clark & Breckinridge, 2011; Sit et al., 2017; Dai et al., 2019), but a discussion of these devices is beyond the scope of this chapter. We also note that Schmid et al. (2018) and Hunziker et al. (2020) are able to correct the beam shifts of SPHERE-ZIMPOL by measuring them in on-sky data. This correction significantly reduces the speckle noise at angular separations >0.6″ from the star, but residuals remain at separations <0.6″. These residuals are particularly strong for broadband data because the beam shifts are wavelength dependent and thus cannot be corrected with a simple shift for a broad wavelength range. Therefore, mitigating the beam shifts already during the optical design is the preferred approach.

The size of the spatial GH and IF shifts relative to the size of the PSF is inversely proportional to the f-number F of the beam of light incident on a mirror (see Sect. 7.4.1). Therefore, to limit the effect of beam shifts, the absolute f-numbers of the beams falling onto the mirrors in the optical system should be large; the beams should converge or diverge slowly. In the limit of a perfectly collimated beam ($F = \infty$) incident on a flat mirror followed by a focusing optical element, the spatial GH and IF shifts even vanish in the focal plane. Because any beam of finite extent corresponds to an angular spectrum of plane waves, the spatial GH and IF shifts still occur, independent of the f-number, but shifts in the pupil plane do not lead to shifts in the focal plane. We find the same result with polarization ray tracing: A perfectly collimated incident beam has the same angle of incidence for all rays, and therefore in the Jones pupil there are no phase gradients (for the spatial GH shift) or rotations of the planes of incidence (for the spatial IF shift). Unfortunately, placing mirrors in collimated beams is generally not possible because the limited number of collimated beams in astronomical instruments are used for other optical components such as coronagraphs and pupil stops. Finally, we note that magnifications in the optical system after the reflection off the mirror do not affect the size of the beam shifts relative to the PSF, because magnifications change the size of the shifts and the PSF by an equal amount.

The spatial GH and IF shifts are created by respectively the phase gradient and the retardance of the mirror at the central angle of incidence of the beam; the amplitudes of the reflection coefficients have only a marginal effect and are therefore not important. Hence, to minimize the spatial GH and IF shifts, the phase gradient should be kept small and the retardance should have a value close to 180° (see Eqs. (7.26) and (7.33)). Fortu-

nately, the values of the phase gradient and the retardance are closely related: A retardance close to 180° automatically implies small phase gradients in both the *p*- and *s*-directions. Figure 7.3 shows that this situation occurs at small angles of incidence. Therefore, to minimize the spatial GH and IF shifts, the central angle of incidence of the beams should be kept small.

Keeping the f-numbers large and the central angles of incidence small may not always be possible because optical systems need to fit in a limited volume. Therefore, also the design of the coatings of the mirrors should be considered to minimize the spatial GH and IF shifts. In general, mirror coatings are optimized for large reflectivity to maximize the throughput of the optical system. However, highly reflective coatings almost always have retardances significantly different from 180° and therefore such coatings produce large spatial GH and IF shifts. But for high-contrast imaging, a high system throughput is of little use when one cannot attain the contrast to image exoplanets. Therefore, a paradigm shift in the design of the mirror coatings for high-contrast imagers is necessary: Rather than maximizing the reflectivity, the retardance should be optimized to have values close to 180° for the central angle of incidence of the mirror and the wavelength range of interest. For linear polarimeters such a design philosophy has the added advantage that it also prevents large losses of signal due to strong polarimetric crosstalk, such as those found for the image derotators of SPHERE and SCExAO-CHARIS (de Boer et al., 2020; Chapters 2 and 3). The larger IP resulting from the suboptimal reflectivity is not an issue because it can be easily removed by adding a half-wave plate to the optical path or subtracting it in the data reduction.

7.6 Conclusions

We used polarization ray tracing to numerically compute the beam shifts for reflection off a flat metallic mirror and compared the resulting shifts to the closed-form expressions of the spatial and angular GH and IF shifts from the physics literature. We find that all four beam shifts are fully reproduced by polarization ray tracing. In particular, we find that the phase gradients in the Jones pupil and the ghost PSFs as described by Breckinridge et al. (2015) are produced by the spatial GH and IF shifts, respectively. We also studied the origin of the four shifts and the dependence of their size and direction on the beam intensity profile, incident polarization state, angle of incidence, mirror material, and wavelength.

Whereas the spatial GH and IF shifts depend on the phase of the Fresnel reflection coefficients, the angular GH and IF shifts depend on the amplitude. Only the spatial GH and IF shifts are relevant for astronomical telescopes and instruments because they are visible in the focal plane. The angular GH and IF shifts on the other hand are not important because they only change the intensity distribution across the reflected beam. As such, the angular shifts have no significant effect in the focus and only create a small point-symmetric deformation of the PSF. We thus conclude that only phase aberrations are important; amplitude aberrations have an almost negligible effect.

The spatial GH and IF shifts create polarization structure in the PSF that reduces the performance of coronagraphs. In fact, we find that the polarization structure for the case of unpolarized light incident on a flat metallic mirror is adequately described by

the diattenuation (i.e., the IP) and the spatial GH and IF shifts. The spatial GH and IF shifts can also significantly reduce the speckle suppression of polarimetric measurements, thereby limiting the maximum attainable gain in contrast from polarimetry. To mitigate the spatial GH and IF shifts in optical systems, the beams of light reflecting off the mirrors should have large f-numbers and small central angles of incidence. Most importantly, mirror coatings should not be optimized for maximum reflectivity, but should instead be designed to have a retardance close to 180°.

Our study provides a fundamental understanding of the polarization aberrations resulting from reflection off flat metallic mirrors in terms of beam shifts. In addition, we have created the analytical and numerical tools to describe these shifts. The next step is to study the combined effect and wavelength dependence of the beam shifts of complete optical paths of (polarimetric) high-contrast imaging instruments and telescopes with multiple inclined components with varying orientation as well as rotating half-wave plates. In particular, we plan to use our tools to create a detailed model of the beam shifts affecting the polarimetric mode of SPHERE-ZIMPOL and enable accurate corrections of on-sky observations. The insights from our work can be applied to understand and improve the performance of many future space- and ground-based high-contrast imagers and polarimeters, such as the Roman Space Telescope, HabEx, LUVOIR, PSI at the Thirty Meter Telescope, and PCS (or EPICS) at the Extremely Large Telescope.

References

Aiello, A., Merano, M., & Woerdman, J. 2009, Physical Review A, 80, 061801
Aiello, A., & Woerdman, H. 2007, arXiv preprint arXiv:0710.1643
Aiello, A., & Woerdman, J. 2008, Optics Letters, 33, 1437
Anche, R. M., Anupama, G., Sriram, S., Sankarasubramanian, K., & Skidmore, W. 2018, in Adaptive Optics Systems VI, Vol. 10703, International Society for Optics and Photonics, 107034K
Bliokh, K. Y., & Aiello, A. 2013, Journal of Optics, 15, 014001
Bliokh, K. Y., & Bliokh, Y. P. 2006, Physical Review Letters, 96, 073903
—. 2007, Physical Review E, 75, 066609
Bliokh, K. Y., & Nori, F. 2015, Physics Reports, 592, 1
Bliokh, K. Y., Rodríguez-Fortuño, F. J., Nori, F., & Zayats, A. V. 2015, Nature Photonics, 9, 796
Born, M., & Wolf, E. 2013, Principles of optics: electromagnetic theory of propagation, interference and diffraction of light (Elsevier)
Breckinridge, J., Kupinski, M., Davis, J., Daugherty, B., & Chipman, R. 2018, in Space Telescopes and Instrumentation 2018: Optical, Infrared, and Millimeter Wave, Vol. 10698, International Society for Optics and Photonics, 106981D
Breckinridge, J. B., Lam, W. S. T., & Chipman, R. A. 2015, Publications of the Astronomical Society of the Pacific, 127, 445
Canovas, H., Rodenhuis, M., Jeffers, S., Min, M., & Keller, C. 2011, Astronomy & Astrophysics, 531, A102
Chipman, R. A. 1989, Optical Engineering, 28, 280290
Clark, N., & Breckinridge, J. B. 2011, in Uv/Optical/Ir Space Telescopes and Instruments: Innovative Technologies and Concepts V, Vol. 8146, International Society for Optics and Photonics, 81460O
Dai, Y., He, C., Wang, J., & Booth, M. 2019, in Adaptive Optics and Wavefront Control for Biological Systems V, Vol. 10886, International Society for Optics and Photonics, 1088609

Davis, J., Kupinski, M. K., Chipman, R. A., & Breckinridge, J. B. 2018, in Space Telescopes and Instrumentation 2018: Optical, Infrared, and Millimeter Wave, Vol. 10698, International Society for Optics and Photonics, 106983H
de Boer, J., Langlois, M., van Holstein, R. G., et al. 2020, Astronomy & Astrophysics, 633, A63
Espinosa-Luna, R., Rodríguez-Carrera, D., Bernabeu, E., & Hinojosa-Ruíz, S. 2008, Optik, 119, 757
Federov, F. 1955, in Doklady Akademii Nauk USSR, Vol. 105, 465
Goos, F., & Hänchen, H. 1947, Annalen der Physik, 436, 333
Götte, J. B., & Dennis, M. R. 2012, New Journal of Physics, 14, 073016
Hamaker, J., & Bregman, J. 1996, Astronomy & Astrophysics Supplement, 117, 161
Heiles, C. 2000, Astronomical Journal, 119, 923
Hermosa, N., Nugrowati, A., Aiello, A., & Woerdman, J. 2011, Optics Letters, 36, 3200
Hunziker, S., Schmid, H. M., Mouillet, D., et al. 2020, Astronomy & Astrophysics, 634, A69
Imbert, C. 1972, Physical Review D, 5, 787
Krist, J., Riggs, A., McGuire, J., et al. 2017, in Techniques and Instrumentation for Detection of Exoplanets VIII, Vol. 10400, International Society for Optics and Photonics, 1040004
Mawet, D., Milli, J., Wahhaj, Z., et al. 2014, Astrophysical Journal, 792, 97
McGuire, J. P., & Chipman, R. A. 1990, Journal of the Optical Society of America A, 7, 1614
—. 1994a, Applied Optics, 33, 5080
—. 1994b, Applied Optics, 33, 5101
Mendillo, C. B., Howe, G. A., Hewawasam, K., et al. 2019, Journal of Astronomical Telescopes, Instruments, and Systems, 5, 025003
Merano, M., Aiello, A., Van Exter, M., et al. 2007, Optics Express, 15, 15928
Millar-Blanchaer, M. A., Perrin, M. D., Hung, L.-W., et al. 2016, in Ground-based and Airborne Instrumentation for Astronomy VI, Vol. 9908, International Society for Optics and Photonics, 990836
Rakić, A. D., Djurišić, A. B., Elazar, J. M., & Majewski, M. L. 1998, Applied Optics, 37, 5271
Sabatke, D., Knight, J. S., & Bolcar, M. R. 2018, in Optical Modeling and Performance Predictions X, Vol. 10743, International Society for Optics and Photonics, 1074307
Safonov, B., Lysenko, P., Goliguzova, M., & Cheryasov, D. 2019, Monthly Notices of the Royal Astronomical Society, 484, 5129
Sanchez Almeida, J., & Martinez Pillet, V. 1992, Astronomy & Astrophysics, 260, 543
Schmid, H. M., Bazzon, A., Roelfsema, R., et al. 2018, Astronomy & Astrophysics, 619, A9
Sit, A., Giner, L., Karimi, E., & Lundeen, J. S. 2017, Journal of Optics, 19, 094003
Totzeck, M., Graupner, P., Heil, T., et al. 2005, in Optical Microlithography XVIII, Vol. 5754, International Society for Optics and Photonics, 23–37
Waluschka, E. 1989, Optical Engineering, 28, 280286
Wiktorowicz, S. J., Millar-Blanchaer, M., Perrin, M. D., et al. 2014, in Ground-based and Airborne Instrumentation for Astronomy V, Vol. 9147, International Society for Optics and Photonics, 914783
Will, S. D., & Fienup, J. R. 2019, in Techniques and Instrumentation for Detection of Exoplanets IX, Vol. 11117, International Society for Optics and Photonics, 1111710
Witzel, G., Eckart, A., Buchholz, R., et al. 2011, Astronomy & Astrophysics, 525, A130
Yun, G., Crabtree, K., & Chipman, R. A. 2011a, Applied Optics, 50, 2855
Yun, G., McClain, S. C., & Chipman, R. A. 2011b, Applied Optics, 50, 2866

English summary

High-contrast imaging polarimetry of exoplanets and circumstellar disks

Understanding the formation and evolution of planetary systems is one of the most fundamental challenges in astronomy. The formation of planets is closely related to the formation of stars. Stars form inside massive clouds of molecular gas and dust that are located in the interstellar medium. Parts of such a molecular cloud fragment and collapse under their own gravity, resulting in the formation of dense cores that further collapse to form stars. Because the collapsing core has a net angular momentum, a rotating disk of dust and gas forms around the forming star. This circumstellar disk is often called a protoplanetary disk because planets as well as brown dwarfs are believed to form in this disk. Together these planets and brown dwarfs are called substellar companions, that is, objects that are less massive than stars and that orbit around a star. Substellar companions may form through the coagulation of the dust in the circumstellar disk into kilometer-sized planetesimals and the subsequent accretion of planetesimals and gas, the local collapse of part of the disk, or the direct collapse of a separate core in the molecular cloud. In all these scenarios the companions are expected to have their own disks from which in turn moons may form. As time progresses, the circumstellar disk disperses through various mechanisms, leaving a planetary system similar to our own Solar System.

To study the formation and evolution of planetary systems, we can directly image exoplanets (planets around stars other than the Sun), brown dwarf companions, and circumstellar disks by spatially separating the near-infrared or visible light from these objects from the light from the central star. However, this is a very challenging task because substellar companions and circumstellar disks are generally located very close to their star and are orders of magnitude fainter than the star. To overcome this challenge, dedicated high-contrast imaging instruments are built. These instruments are installed on the largest ground-based telescopes and have complex optical systems designed to suppress the light from the star and create images with a spatial resolution close to the theoretical limit of the telescope.

Several of the high-contrast imaging instruments have polarimetric modes. With polarimetry, we measure the polarization state of the light, that is, the direction of the oscillation (in case of linear polarization) or rotation (in case of circular polarization) of the electric fields of the light. Polarimetry is particularly powerful to reach the large contrasts required to directly image circumstellar disks and substellar companions. The direct light from the central star is generally unpolarized: The light is a mixture of equal amounts of all possible polarization states. As this starlight scatters off dust grains in the circumstellar disk or off the companion's atmosphere, it becomes linearly polarized. Therefore, when taking an image in linearly polarized light, the direct starlight is strongly suppressed, while the polarized light from the circumstellar disk or companion is revealed. Polarimetry can also be used for characterization because polarimetric images contain information on the physical properties of the scattering particles. Measurements of polarization can, for instance, be used to constrain the composition, size, and shape of the dust grains

in circumstellar disks and to determine the properties of the atmospheres or surfaces of companions. However, performing polarimetry on a high-contrast imaging instrument is not straightforward because many different instrumental effects can limit the attainable sensitivity and accuracy of the measurements.

This thesis

The goals of this thesis are to improve the sensitivity, accuracy, and capabilities of high-contrast imaging polarimeters for the detection and characterization of substellar companions and circumstellar disks. In addition, this thesis presents the first direct detections of linear polarization from substellar companions. The focus of this thesis is mostly on ground-based high-contrast imaging polarimetry, in particular with the instrument SPHERE-IRDIS at the Very Large Telescope.

In Chapter 2 we characterize the instrumental polarization effects of the near-infrared polarimetric mode of SPHERE-IRDIS using measurements with SPHERE's internal light source and observations of unpolarized stars. We find that the telescope and SPHERE's first mirror produce significant polarization. In addition, we find that the image derotator (a rotating assembly of three mirrors that is used to rotate the image) causes severe loss of signal at some orientations and wavelengths as it converts incident linearly polarized light into circularly polarized light that cannot be measured. We develop a data-reduction method that corrects these effects and apply it to observations of a circumstellar disk. We have incorporated the correction method in a highly automated end-to-end data-reduction pipeline called `IRDAP`, which we made publicly available[1]. IRDAP enables us to accurately measure the polarized intensity and angle of polarization of circumstellar disks and substellar companions. As such, IRDAP is the go-to pipeline for IRDIS polarimetric data and laid the foundation for many scientific publications.

In Chapter 3 we perform a preliminary characterization of the instrumental polarization effects of the near-infrared spectropolarimetric mode of SCExAO-CHARIS at the Subaru Telescope. From measurements with the internal light source we find that the image derotator can cause significant loss of signal at some wavelengths. We calculate the polarization produced by the telescope using theoretical models. We plan to measure the telescope polarization with observations of an unpolarized star and add a correction method similar to that of IRDAP to the existing CHARIS data-reduction pipeline. Once finished, these calibrations will enable unique quantitative polarimetric studies of circumstellar disks and substellar companions at a spectral resolution beyond that possible with SPHERE-IRDIS' broadband filters.

In Chapter 4 we introduce an observing scheme that combines high-contrast imaging polarimetry with the angular-differential-imaging data-reduction technique to reach the sensitivity required to characterize substellar companions that are located at small angular separations from their stars. We have implemented this scheme for SPHERE-IRDIS and developed the corresponding observing strategies and data-reduction approaches. Using this technique, we observed the planets of HR 8799 and the substellar companion PZ Tel B. We do not detect near-infrared polarization from these companions and estimate upper limits on their degree of polarization. The achieved sensitivity and accuracy

[1] https://irdap.readthedocs.io

of the measurements show that our technique enables the characterization of faint substellar companions located close to their stars.

In Chapter 5 we use SPHERE-IRDIS to measure the near-infrared linear polarization of 20 known, directly imaged exoplanets and brown dwarf companions. We report the first direct detection of polarization originating from substellar companions, with a polarization of several tenths of a percent for DH Tau B and GSC 6214-210 B. Because these companions have previously measured hydrogen emission lines and red colors, the polarization most likely originates from disks around these companions. Through radiative transfer modeling, we constrain the position angles of the disks and find that the disks must have high inclinations. The presence of the disks around DH Tau B and GSC 6214-210 B as well as the misalignment of the disk of DH Tau B with the disk around its host star suggest in-situ formation of the companions. For the 18 other companions, we do not detect significant polarization and place upper limits on their degree of polarization. These non-detections may indicate the absence of disks around the companions, a slow rotation rate of young companions, the upper atmospheres containing primarily submicron-sized dust grains, and/or limited inhomogeneity of the atmospheric clouds. Our work shows that the polarization of substellar companions can indeed by detected and that polarimetry can be used to characterize these objects.

In Chapter 6 we develop the observing scheme, data-reduction methods, and analysis tools to measure near-infrared circular polarization with SPHERE-IRDIS. Because the instrument is not designed to measure circular polarization, we use the image derotator to convert incident circular polarization into measurable linear polarization. We tested the technique with observations of the red hypergiant VY CMa and its surrounding nebula. To accurately measure the circular polarization, we use the spatial variation of the linear polarization around VY CMa to distinguish between real, astrophysical circular polarization and instrument-induced signal. We find that the light from VY CMa is circularly polarized, in agreement with the literature, but do not conclusively detect circular polarization in the nebula surrounding VY CMa. Our observing scheme enables the first measurements of circular polarization at high spatial resolution. The method is promising for the characterization of the dust and magnetic fields in circumstellar disks, and could even shed light on the emergence of homochirality in biomolecules.

In Chapter 7 we investigate polarization aberrations produced by reflection off flat metallic mirrors at the fundamental level. Polarization aberrations are polarization-dependent variations of the electromagnetic field across a beam of light. These aberrations create polarization structure in the images that limits the sensitivity of the most sensitive high-contrast imagers. We numerically compute the polarization aberrations and interpret the results in terms of the Goos-Hänchen and Imbert-Federov shifts of the beam of light as described in the physics literature. We find that the beam shifts are fully reproduced by our numerical calculations and study the origin, size, and direction of the shifts. The beam shifts in an optical system can be mitigated by keeping the focal ratios large and angles of incidence small as well as by designing mirror coatings to have a retardance close to 180° rather than maximum reflectivity. Our insights can be applied to improve the performance of current and future ground- and space-based high-contrast imagers that aim to reach the extreme contrasts required to directly image exoplanets in reflected, and thus polarized, visible light.

Nederlandstalige samenvatting

Polarimetrische observaties van exoplaneten en circumstellaire schijven

Het begrijpen van het ontstaan en de ontwikkeling van planetenstelsels is een van de meest fundamentele uitdagingen in de sterrenkunde. De vorming van planeten is nauw verwant aan de vorming van sterren. Sterren worden gevormd in enorme wolken van moleculair gas en stof die zich in het interstellaire medium bevinden. Delen van zo een moleculaire wolk fragmenteren en storten onder invloed van hun eigen zwaartekracht ineen, wat resulteert in de vorming van dichte kernen die verder ineenstorten tot sterren. Omdat de instortende kern een netto impulsmoment heeft, vormt zich een ronddraaiende schijf van stof en gas rond de vormende ster. Deze circumstellaire schijf wordt vaak een protoplanetaire schijf genoemd omdat we denken dat planeten alsook bruine dwergen zich in deze schijf vormen. Deze planeten en bruine dwergen noemen we samen substellaire begeleiders, oftewel objecten die lichter zijn dan sterren en die in een baan rond een ster draaien. Substellaire begeleiders kunnen zich vormen door de samenklontering van het stof in de circumstellaire schijf tot kilometersgrote planetesimalen en de daaropvolgende samentrekking van planetesimalen en gas, de lokale ineenstorting van een deel van de schijf, of de directe ineenstorting van een afzonderlijke kern in de moleculaire wolk. In al deze scenario's verwachten we dat de substellaire begeleiders hun eigen schijven hebben waaruit op hun beurt manen kunnen worden gevormd. Naarmate de tijd vordert, drijft de circumstellaire schijf door verschillende processen uiteen, waarna een planetenstelsel vergelijkbaar met ons eigen zonnestelsel overblijft.

Om het ontstaan en de ontwikkeling van planetenstelsels te bestuderen, kunnen we exoplaneten (planeten rond andere sterren dan de Zon), begeleidende bruine dwergen en circumstellaire schijven direct afbeelden door het nabij-infrarode of zichtbare licht van deze objecten ruimtelijk te scheiden van het licht van de centrale ster. Dit is echter een zeer uitdagende taak omdat substellaire begeleiders en circumstellaire schijven zich over het algemeen zeer dicht bij hun ster bevinden en vele malen lichtzwakker zijn dan de ster. Om deze uitdaging het hoofd te bieden worden speciale hoogcontrast-instrumenten gebouwd. Deze instrumenten zijn geïnstalleerd op de grootste telescopen en hebben geavanceerde optische systemen die zijn ontworpen om het licht van de ster te onderdrukken en afbeeldingen te maken met een ruimtelijke resolutie die dicht bij de theoretische limiet van de telescoop ligt.

Verschillende hoogcontrast-instrumenten hebben polarimetrische modi. Met polarimetrie meten we de polarisatietoestand van het licht, oftewel de trillingsrichting (bij lineaire polarisatie) of rotatierichting (bij circulaire polarisatie) van de elektrische velden van het licht. Polarimetrie is bijzonder krachtig om de hoge contrasten te bereiken die nodig zijn om circumstellaire schijven en substellaire begeleiders direct af te beelden. Het directe licht van de centrale ster is over het algemeen ongepolariseerd: het licht is een mengsel van gelijke hoeveelheden van alle mogelijke polarisatietoestanden. Dit sterlicht wordt door stofdeeltjes in de circumstellaire schijf of de atmosfeer van de begeleider verstrooid, en raakt daarbij gedeeltelijk lineair gepolariseerd. Op deze manier wordt in afbeeldingen

van lineair gepolariseerd licht het directe sterlicht sterk onderdrukt, terwijl het gepolariseerde licht van de circumstellaire schijf of begeleider zichtbaar wordt. Polarimetrie kan ook worden gebruikt om circumstellaire schijven en begeleiders te karakteriseren omdat polarimetrische afbeeldingen informatie bevatten over de fysieke eigenschappen van de verstrooiende deeltjes. Metingen van polarisatie kunnen bijvoorbeeld worden gebruikt om de samenstelling, grootte en vorm van de stofdeeltjes in circumstellaire schijven te bepalen en om de eigenschappen van de atmosferen of oppervlakken van begeleiders vast te stellen. Het meten van polarisatie met een hoogcontrast-instrument is echter niet eenvoudig, omdat veel verschillende instrumentele effecten de gevoeligheid en nauwkeurigheid van de metingen kunnen verminderen.

Dit proefschrift

Het doel van dit proefschrift is het verbeteren van de gevoeligheid, nauwkeurigheid en mogelijkheden van polarimetrische hoogcontrast-instrumenten om substellaire begeleiders en circumstellaire schijven te detecteren en te karakteriseren. Daarnaast presenteert dit proefschrift de eerste directe detecties van lineaire polarisatie van substellaire begeleiders. De focus van dit proefschrift ligt voornamelijk op polarimetrische hoogcontrast-instrumenten, in het bijzonder het instrument SPHERE-IRDIS op de Very Large Telescope.

In Hoofdstuk 2 karakteriseren we de instrumentele polarisatie-effecten van de nabij-infrarode polarimetrische modus van SPHERE-IRDIS met behulp van metingen met SPHERE's interne lichtbron en waarnemingen van ongepolariseerde sterren. Uit onze metingen blijkt dat de telescoop en SPHERE's eerste spiegel significante polarisatie produceren. Bovendien zien we dat de beeldderotator (een roterend samenstel van drie spiegels dat wordt gebruikt om de afbeelding te roteren) bij sommige oriëntaties en golflengtes ernstig signaalverlies veroorzaakt omdat dit onderdeel invallend lineair gepolariseerd licht omzet in circulair gepolariseerd licht dat niet gemeten kan worden. We ontwikkelen een dataverwerkingsmethode die deze effecten corrigeert en passen deze toe op waarnemingen van een circumstellaire schijf. We hebben de correctiemethode in een geautomatiseerd dataverwerkingsprogramma genaamd `IRDAP` ingebouwd en dat programma openbaar beschikbaar gemaakt[2]. IRDAP stelt ons in staat om de gepolariseerde intensiteit en polarisatiehoek van circumstellaire schijven en substellaire begeleiders met een hoge nauwkeurigheid te meten. Als zodanig is IRDAP het primaire dataverwerkingsprogramma voor polarisatiemetingen met IRDIS en staat het aan de basis van vele wetenschappelijke publicaties.

In Hoofdstuk 3 presenteren we de voorlopige resultaten van de karakterisatie van de instrumentele polarisatie-effecten van de nabij-infrarode spectropolarimetrische modus van SCExAO-CHARIS op de Subaru telescoop. Uit metingen met de interne lichtbron blijkt dat de beeldderotator bij sommige golflengtes aanzienlijk signaalverlies kan veroorzaken. Met behulp van theoretische modellen berekenen we de polarisatie die de telescoop produceert. We zijn van plan om de polarisatie van de telescoop met waarnemingen van een ongepolariseerde ster te meten en een correctiemethode vergelijkbaar aan die van

[2] https://irdap.readthedocs.io

IRDAP toe te voegen aan het bestaande CHARIS-dataverwerkingsprogramma. Omdat CHARIS een hogere spectrale resolutie heeft dan IRDIS, zullen deze kalibraties unieke kwantitatieve polarimetrische studies van circumstellaire schijven en substellaire begeleiders mogelijk maken.

In Hoofdstuk 4 introduceren we een observatietechniek die polarimetrische metingen combineert met de angulaire differentiële beeldverwerkingsmethode om de gevoeligheid te bereiken die nodig is om substellaire begeleiders op kleine hoekafstanden van hun ster te kunnen karakteriseren. We hebben deze techniek voor SPHERE-IRDIS geïmplementeerd en hebben de bijbehorende observatiestrategieën en data-analysemethodes ontwikkeld. Met behulp van de techniek hebben we de planeten van HR 8799 en de substellaire begeleider PZ Tel B waargenomen. We detecteren geen nabij-infrarode polarisatie van deze begeleiders en schatten bovenlimieten op hun polarisatiegraad. De gevoeligheid en nauwkeurigheid van de metingen laten zien dat onze techniek geschikt is om lichtzwakke substellaire begeleiders die zich dicht bij hun sterren bevinden te karakteriseren.

In Hoofdstuk 5 gebruiken we SPHERE-IRDIS om de nabij-infrarode lineaire polarisatie van twintig bekende, direct afgebeelde exoplaneten en begeleidende bruine dwergen te meten. We presenteren de eerste directe detecties van polarisatie afkomstig van substellaire begeleiders, met een polarisatie van enkele tienden van een procent voor DH Tau B en GSC 6214-210 B. Omdat voor deze begeleiders eerder al waterstofemissielijnen en rode kleuren zijn gemeten, is de polarisatie hoogstwaarschijnlijk afkomstig van schijven rond deze begeleiders. Door middel van stralingstransportmodellen bepalen we de positiehoeken van de schijven en stellen we vast dat de schijven hoge glooiingshoeken moeten hebben. De aanwezigheid van de schijven rond DH Tau B en GSC 6214-210 B, alsook de ongelijke oriëntaties van de schijven rond DH Tau B en de centrale ster, wijzen er op dat de begeleiders op ongeveer de huidige afstand van de ster gevormd moeten zijn. Voor de achttien andere begeleiders detecteren we geen significante polarisatie en bepalen we bovenlimieten op de polarisatiegraad. Deze non-detecties kunnen wijzen op de afwezigheid van schijven rond de begeleiders, een lage rotatiesnelheid van jonge begeleiders, bovenste atmosferen met hoofdzakelijk stofdeeltjes kleiner dan een micrometer en/of beperkte inhomogeniteit van de wolken in de atmosferen van de begeleiders. Ons werk laat zien dat de polarisatie van substellaire begeleiders inderdaad kan worden gedetecteerd en dat polarimetrie kan worden gebruikt om deze objecten te karakteriseren.

In Hoofdstuk 6 ontwikkelen we de observatietechniek en data-analysemethodes om nabij-infrarode circulaire polarisatie te meten met SPHERE-IRDIS. Omdat het instrument niet is ontworpen om circulaire polarisatie te meten, gebruiken we de beeldderotator om invallende circulaire polarisatie om te zetten in meetbare lineaire polarisatie. We hebben de techniek getest met waarnemingen van de rode hyperreus VY CMa en de omringende nevel. Om de circulaire polarisatie nauwkeurig te meten, gebruiken we de ruimtelijke variatie van de lineaire polarisatie rond VY CMa om onderscheid te maken tussen werkelijke, astrofysische circulaire polarisatie en signaal dat is geïnduceerd door het instrument. We vinden dat het licht van VY CMa circulair gepolariseerd is, in overeenstemming met de literatuur, maar we detecteren geen circulaire polarisatie in de nevel rond VY CMa. Onze observatietechniek maakt de eerste circulaire polarisatiemetingen met een hoge ruimtelijke resolutie mogelijk. De techniek is veelbelovend om het stof en de magne-

tische velden in circumstellaire schijven te karakteriseren en zou zelfs kunnen helpen om de oorsprong van de homochiraliteit van biologische moleculen te ontrafelen.

In Hoofdstuk 7 onderzoeken we op fundamenteel niveau de polarisatie-aberraties die geproduceerd worden door reflectie van platte metalen spiegels. Polarisatie-aberraties zijn polarisatie-afhankelijke variaties van het elektromagnetische veld over een lichtbundel. Deze aberraties creëren polarisatiestructuur in de uiteindelijke afbeeldingen die de gevoeligheid van de meest gevoelige hoogcontrast-instrumenten beperkt. We berekenen de polarisatie-aberraties met een numerieke code en vergelijken de resultaten met de Goos-Hänchen en Imbert-Federov verschuivingen van de lichtbundel zoals beschreven in de natuurkundige literatuur. We constateren dat deze bundelverschuivingen volledig worden gereproduceerd door onze numerieke berekeningen en bestuderen de oorsprong, grootte en richting van de verschuivingen. De effecten van de bundelverschuivingen in een optisch systeem kunnen worden beperkt door grote f-getallen en kleine invalshoeken te gebruiken, en door de coatings van de spiegels niet te ontwerpen voor maximale reflectiviteit maar voor een retardatie dicht bij 180°. De inzichten van ons werk kunnen worden gebruikt voor de verbetering van de prestaties van huidige en toekomstige hoogcontrast-instrumenten die als doel hebben om exoplaneten direct af te beelden in gereflecteerd, en dus gepolariseerd, zichtbaar licht.

List of publications

Refereed publications

1. *New constraints on the disk characteristics and companion candidates around T Chamaeleontis with VLT/SPHERE*
   Pohl, A., Sissa, E., Langlois, M., et al.
   Astronomy and Astrophysics, 605, A34 (2017)

2. *DZ Chamaeleontis: a bona fide photoevaporating disc*
   Canovas, H., Montesinos, B., Schreiber, M. R., et al.
   Astronomy and Astrophysics, 610, A13 (2018)

3. *First direct detection of a polarized companion outside a resolved circumbinary disk around CS Chamaeleonis*
   Ginski, C., Benisty, M., van Holstein, R. G., et al.
   Astronomy and Astrophysics, 616, A79 (2018)

4. *Discovery of a planetary-mass companion within the gap of the transition disk around PDS 70*
   Keppler, M., Benisty, M., Müller, A., et al.
   Astronomy and Astrophysics, 617, A44 (2018)

5. *Resolving faint structures in the debris disk around TWA 7. Tentative detections of an outer belt, a spiral arm, and a dusty cloud*
   Olofsson, J., van Holstein, R. G., Boccaletti, A., et al.
   Astronomy and Astrophysics, 617, A109 (2018)

6. *SPHERE/ZIMPOL high resolution polarimetric imager. I. System overview, PSF parameters, coronagraphy, and polarimetry*
   Schmid, H. M., Bazzon, A., Roelfsema, R., et al.
   Astronomy and Astrophysics, 619, A9 (2018)

7. *Spatially resolved spectroscopy of the debris disk HD 32297. Further evidence of small dust grains*
   Bhowmik, T., Boccaletti, A., Thébault, P., et al.
   Astronomy and Astrophysics, 630, A85 (2019)

8. *Polarimetric imaging mode of VLT/SPHERE/IRDIS. I. Description, data reduction, and observing strategy*
   de Boer, J., Langlois, M., van Holstein, R. G., et al.
   Astronomy and Astrophysics, 633, A63 (2020)

9. *Polarimetric imaging mode of VLT/SPHERE/IRDIS. II. Characterization and correction of instrumental polarization effects*
van Holstein, R. G., Girard, J. H., de Boer, J., et al.
Astronomy and Astrophysics, 633, A64 (2020)

10. *Disks Around T Tauri Stars with SPHERE (DARTTS-S). II. Twenty-one new polarimetric images of young stellar disks*
Garufi, A., Avenhaus, H., Pérez, S., et al.
Astronomy and Astrophysics, 633, A82 (2020)

11. *RefPlanets: Search for reflected light from extrasolar planets with SPHERE/ZIMPOL*
Hunziker, S., Schmid, H. M., Mouillet, D., et al.
Astronomy and Astrophysics, 634, A69 (2020)

12. *Spirals inside the millimeter cavity of transition disk SR 21*
Muro-Arena, G. A., Ginski, C., Dominik, C., et al.
Astronomy and Astrophysics, 636, L4 (2020)

13. *Detection of Polarization due to Cloud Bands in the Nearby Luhman 16 Brown Dwarf Binary*
Millar-Blanchaer, M. A., Girard, J. H., Karalidi, T., et al.
The Astrophysical Journal, 894, 42 (2020)

14. *A low-mass stellar companion to the young variable star RZ Psc*
Kennedy, G. M., Ginski, C., Kenworthy, M. A., et al.
Monthly Notices of the Royal Astronomical Society, 496, L75 (2020)

15. *Gap, shadows, spirals, and streamers: SPHERE observations of binary-disk interactions in GG Tauri A*
Keppler, M., Penzlin, A., Benisty, M., et al.
Astronomy and Astrophysics, 639, A62 (2020)

16. *Ongoing flyby in the young multiple system UX Tauri*
Ménard, F., Cuello, N., Ginski, C., et al.
Astronomy and Astrophysics, 639, L1 (2020)

17. *Dynamical Evidence of a Spiral Arm-driving Planet in the MWC 758 Protoplanetary Disk*
Ren, B., Dong, R., van Holstein, R. G., et al.
The Astrophysical Journal, 898, L38 (2020)

18. *CS Cha B: A disc-obscured M-type star mimicking a polarised planetary companion*
Haffert, S. Y., van Holstein, R. G., Ginski, C., et al.
Astronomy and Astrophysics, 640, L12 (2020)

19. *The circumstellar environment of EX Lupi: SPHERE and SINFONI views*
Rigliaco, E., Gratton, R., Kóspál, Á., et al.
Astronomy and Astrophysics, 641, A33 (2020)

20. *Disk Evolution Study Through Imaging of Nearby Young Stars (DESTINYS): A close low-mass companion to ET Cha*
Ginski, C., Ménard, F., Rab, C., et al.
Astronomy and Astrophysics, 642, A119 (2020)

21. *A triple star in disarray. Multi-epoch observations of T Tauri with VLT-SPHERE and LBT-LUCI*
Kasper, M., Santhakumari, K. K. R., Herbst, T. M., et al.
Astronomy and Astrophysics, 644, A114 (2020)

22. *A Search for Polarized Thermal Emission from Directly Imaged Exoplanets and Brown Dwarf Companions to Nearby Stars*
Jensen-Clem, R., Millar-Blanchaer, M. A., van Holstein, R. G., et al.
The Astronomical Journal, 160, 286 (2020)

23. *Disk Evolution Study Through Imaging of Nearby Young Stars (DESTINYS): Late Infall Causing Disk Misalignment and Dynamic Structures in SU Aur*
Ginski, C., Facchini, S., Huang, J., et al.
The Astrophysical Journal, 908, L25 (2021)

24. *A survey of the linear polarization of directly imaged exoplanets and brown dwarf companions with SPHERE-IRDIS. First polarimetric detections revealing disks around DH Tau B and GSC 6214-210 B*
van Holstein, R. G., Stolker, T., Jensen-Clem, R., et al.
Astronomy and Astrophysics, 647, A21 (2021)

25. *HD 142527: quantitative disk polarimetry with SPHERE*
Hunziker, S., Schmid, H. M., Ma, J., et al.
Astronomy and Astrophysics, 648, A110 (2021)

26. *How many suns are in the sky? A SPHERE multiplicity survey of exoplanet host stars. I. Four new close stellar companions including a white dwarf*
Ginski, C., Mugrauer, M., Adam, C., et al.
Astronomy and Astrophysics, 649, A156 (2021)

27. *The HD 206893 planetary system seen with VLT/SPHERE. Upper limit on the dust albedo and constraints on additional companions*
Romero, C., Milli, J., Lagrange, A.-M., et al.
Astronomy and Astrophysics, 651, A34 (2021)

Non-refereed publications

1. *Combining angular differential imaging and accurate polarimetry with SPHERE/IRDIS to characterize young giant exoplanets*
   van Holstein, R. G., Snik, F., Girard, J. H., et al.
   Society of Photo-Optical Instrumentation Engineers (SPIE) Conference Series, 10400, 1040015 (2017)

2. *A Planet with a Disc? A Surprising Detection in Polarised Light with VLT/SPHERE*
   Ginski, C., van Holstein, R. G., Juhász, A., et al.
   The Messenger, 172, 27 (2018)

3. *Lessons for WFIRST CGI from ground-based high-contrast systems*
   Bailey, V. P., Bottom, M., Cady, E., et al.
   Space Telescopes and Instrumentation 2018: Optical, Infrared, and Millimeter Wave, 10698, 106986P (2018)

4. *Original use of MUSE's laser tomography adaptive optics to directly image young accreting exoplanets*
   Girard, J. H., de Boer, J., Haffert, S., et al.
   arXiv e-prints, arXiv:2003.02145 (2020)

5. *SPHERE+: Imaging young Jupiters down to the snowline*
   Boccaletti, A., Chauvin, G., Mouillet, D., et al.
   arXiv e-prints, arXiv:2003.05714 (2020)

6. *Calibration of the instrumental polarization effects of SCExAO-CHARIS' spectropolarimetric mode*
   van Holstein, R. G., Bos, S. P., Ruigrok, J., et al.
   Society of Photo-Optical Instrumentation Engineers (SPIE) Conference Series, 11447, 114475B (2020)

7. *Planet formation with all flavors of adaptive optics: VLT/MUSE's laser tomography adaptive optics to directly image young accreting exoplanets*
   Girard, J. H., Haffert, S. Y., Bae, J., et al.
   Society of Photo-Optical Instrumentation Engineers (SPIE) Conference Series, 11448, 1144808 (2020)

8. *Full characterization of the instrumental polarization effects of the spectropolarimetric mode of SCExAO-CHARIS*
   't Hart, G. J. J., van Holstein, R. G., Bos, S. P., et al.
   Society of Photo-Optical Instrumentation Engineers (SPIE) Conference Series, 11833, 118330O (2021)

Curriculum vitae

I was born on December 10, 1990 in Delft, the Netherlands. In 2009 I received my secondary education diploma at the ISW Tiendweg in Naaldwijk. Subsequently, I started the Bachelor Aerospace Engineering at the Delft University of Technology. During the third year, I took astronomy and physics courses at the University of Amsterdam as part of the minor program. I received my bachelor's degree with distinction in 2013 and continued with the Master Aerospace Engineering in Delft, specializing in spaceflight. For my master internship project, I visited the European Southern Observatory (ESO) in Santiago, Chile, where, under supervision of Julien Girard and Jos de Boer, I worked on the commissioning and calibration of the polarimetric mode of SPHERE-IRDIS at the Very Large Telescope. I then visited the Leiden Observatory where I continued the calibration of SPHERE-IRDIS as part of my master thesis supervised by Daphne Stam, Frans Snik, and Jos de Boer. I obtained my master's degree with distinction in 2016 and received the NvVL (Dutch Society of Aeronautical Engineering) Wittenberg-award for best aerospace-engineering-related MSc thesis. After my graduation, I started a PhD at the Leiden Observatory with Christoph Keller and Frans Snik, of which this thesis is the result. During the PhD, I spent 20 months at ESO in Santiago as part of the studentship program under supervision of Julien Milli and Zahed Wahhaj. At the end of 2021, I will start as a fellow at ESO in Santiago where I will continue my work on high-contrast imaging polarimetry, in particular with SPHERE-IRDIS.

Acknowledgments

This thesis would not have been possible without the support of many people and I would therefore like to thank everyone who directly or indirectly contributed to this thesis. There are several persons and groups of people that I would like to thank in particular. First off, I would like to thank Christoph Keller and Frans Snik for supervising me during the PhD project and supporting me in spending a considerable part of my PhD in Chile. In addition, I am grateful to Linda Schmidtobreick and Itziar de Gregorio-Monsalvo for offering me a studentship at the European Southern Observatory in Santiago, Chile, and to Julien Milli and Zahed Wahhaj for supporting and guiding me in my projects there. I also thank the members of the SPHERE consortium and the SCExAO team as well as the (support) staff in Leiden, in Santiago, and at Paranal. Furthermore, I would like to thank Christian Ginski and Jos de Boer for helping me get started in the world of observations and data reduction and for advising and helping me whenever I needed it. You have been real mentors to me. I thank Joost, Jasper, Kira, and Daphne for their enthusiasm and commitment during their bachelor and master research projects that I (co-)supervised. I would also like to thank all the friends and colleagues in Leiden and Santiago for the very pleasant working environment. I have very much enjoyed all the fun conversations, coffee times, lunches, football matches, drinks, pizza nights, and conference visits. I am grateful to Steven, David, and Alex for supporting me during the more challenging times of my PhD. Natuurlijk wil ik ook mijn familie en vrienden bedanken voor jullie steun, afleiding en gezelligheid. Finalmente, agradezco a Sophia, mi compañera, por su apoyo, paciencia y comprensión durante la redacción de esta tesis. No hubiera podido terminar esta tesis sin ti.